

UNIVERSITY OF
BIRMINGHAM

DEVELOPMENT OF NEW MICRO-CHANNELS SEGMENTED REGENERATOR FOR V-TYPE ALPHA STIRLING ENGINE

By

Ahmad Khalid Boubaker Almajri

A thesis submitted to the University of Birmingham for the Degree of

Doctor of Philosophy

Department of Mechanical Engineering
College of Engineering and Physical Sciences
The University of Birmingham
January - 2019

UNIVERSITY OF
BIRMINGHAM

University of Birmingham Research Archive

e-theses repository

This unpublished thesis/dissertation is copyright of the author and/or third parties. The intellectual property rights of the author or third parties in respect of this work are as defined by The Copyright Designs and Patents Act 1988 or as modified by any successor legislation.

Any use made of information contained in this thesis/dissertation must be in accordance with that legislation and must be properly acknowledged. Further distribution or reproduction in any format is prohibited without the permission of the copyright holder.

بِسْمِ اللَّهَّ الرَّحْمَٰنِ الرَّحِيمِ

﴿دَعْوَاهُمْ فِيهَا سُبْحَانَكَ اللَّهُمَّ وَتَحِيَّتُهُمْ فِيهَا سَلَامٌ ۚ وَآخِرُ دَعْوَاهُمْ أَنِ الْحَمْدُ لِلَّهِ رَبِّ الْعَالَمِينَ (10)﴾ .

صَدَقَ الله العَظيم

سورة يونس الآيـــــه 10

ABSTRACT

With the increased world population, fossil fuel consumption and Co2 emissions, solutions are being sought to provide for the increase in energy demands and to reduce emission levels. One promising approach is the use of renewable energy and waste heat sources to drive thermo-mechanical conversion systems, such as Stirling engines. Recently, interest in developing efficient and cost effective Stirling engine technology has increased, particularly in many academic and industrial organizations. In this context, this thesis has first focused on the development of thermodynamic and numerical simulations for the V-type alpha Stirling engine. Secondly, the development of efficient regenerator that can improve the engine performance, it is a new non-annulus segmented micro-channels regenerator of parallel geometry. Using non-ideal adiabatic analysis approach, a successful thermodynamic model was developed for a V-type alpha Stirling engine, and it was validated using published experimental data available for the engine prototype. Also, the development of a detailed 3D CFD model for V-type alpha Stirling engine was carried out and its results were validated using the developed thermodynamic model. The results have shown good agreement in the estimation of the engine indicated power. The combination of the thermodynamic analysis with the 3D CFD modelling to predict the engine performance was an advantage of this work.

The effects of different design parameters and operating conditions have been investigated on the performance of a V-alpha type Stirling engine by using the developed CFD model. Those parameters including the dead volume, cold/hot ends temperatures, charge pressure, porosity and matrix wire diameter of regenerator. The PV diagram for the engine was used to predict the power output contributed by each parameter. The maximum power output in this parametric study was achieved 162 W by using a wire matrix diameter of 0.02 mm, porosity of 80%, cold side temperature of 20 ^{0}C, and hot side temperature of 600 ^{0}C. Also, results predicted that,

further increase of the heater and the cooler heights (up to 140 mm) pushed the power output to reach 170 W.

A detailed 3D CFD model for segmented micro-channel regenerator was developed and its results were validated against experimental measurements showing maximum deviation of 10.6% and 6.03% for both unidirectional and oscillatory flows respectively in terms of measuring the outlet temperature. The validated CFD model was used to carry out an investigation on the effect of increasing the number of segmentations on the regenerator effectiveness and engine performance. The effects of changing the micro-channel diameter on the regenerator performance in terms of heat transfer and pressure loss was also investigated. The micro- channels regenerator with diameter of 0.5 mm and 32 segments performed better than all other configurations investigated in this study including the Random Fibre matrix.

In order to reduce the time and cost for Stirling engine development, this work investigated the route to upgrade commercially available V-type compressor to develop V-type alpha Stirling engine through detailed 3D CFD modelling. The correlations of Nusselt number and friction factor for the developed segmented regenerator were used as porous media parameters in the CFD model for the developed Stirling engine. Also, a new concept for the engine cooler design was modelled and integrated in the overall engine model, showing improved performance for the engine due to lowering of the coolant temperature. The maximum indicated power observed from the developed engine using the 32-segmented regenerator with 0.5 mm micro-channel diameter was 132.89 W. This is higher by 18.33% and 44.4% than those of the two commercial matrix regenerators, namely the Random fibre and the Screen woven respectively.

DEDICATED TO:

*My beloved **parents** for all their love and support.*

*My beloved wife (**Amira**), my children (**Khaled** and **Mohammad**) and all of my **brothers** and **sisters**.*

*My lovely city **Derna**….*

Ahmad Almajri

January 2019

ACKNOWLEDGEMENTS

All praises are due to Allah (whom we praise Him, seek His help and ask for His forgiveness) for his guidance, blessing and helping me to complete this research project. May His Mercy and blessing be upon our noble Prophet Mohamed (SAWA) and his households and his companions.

I would like to express the deepest gratitude to my supervisor **Dr. Saad Mahmoud**, for his continuous support of my PhD research, his patience, his motivation and his immense knowledge. His guidance helped me in the entire time of my research, writing research papers, and writing of my thesis. Dr. Saad has supported me by providing not only research guidance, but also academically and emotionally during the difficult times to finish this research by giving support and the freedom I needed to develop.

I would also like to express my thanks to my second supervisor **Dr. Raya Al-Dadah** who mentored and trusted me during the whole period of this project.

My special thanks to all my colleagues especially **Dr. Peter Youssef** for his help and support for setting up the test rig for this work.

Many thanks to **Mr Lee** and **Mr Peter** for their support with some technical issues needed in the workshop.

Finally, I would like to acknowledge the Ph.D. sponsorship received from **Derna** Polytechnic Institute and the **Libyan Ministry** of Higher Education and Scientific Research.

TABLE OF CONTENTS

ABSTRACT I

ACKNOWLEDGEMENTS IV

TABLE OF CONTENTS V

LIST OF TABLES XVIII

NOMENCLATURE XIX

LIST OF PUBLICATIONS XXIV

1. CHAPTER 1 1

1.1 General background 1

1.2 V-type alpha Stirling engine 5

1.3 Research objectives 6

1.4 Thesis outlines 7

2. CHAPTER 2 9

2.1 Introduction 9

2.2 Stirling engine analysis techniques 9

2.2.1 The zeroth-order analysis 10

2.2.2 The first-order analysis (Schmidt analysis) 11

2.2.3 The second-order analysis 14

2.2.4 The third-order analysis 18

2.2.5 The forth-order analysis (CFD analysis)....19
2.2.6 Maximum deviation:....22
2.3 Design of V-type alpha Stirling engine prototype....23
2.4 Review of previous work on regenerators....25
2.5 Review summary and knowledge gap....35
3. CHAPTER 3....36
3.1 Introduction....36
3.2 Thermodynamic analysis model....39
3.2.1 Losses modelling....45
3.2.2 Thermodynamic model validation....48
3.3 Engine CFD modelling....49
3.3.1 Heat transfer in porous media....49
3.3.2 Moving mesh....52
3.3.3 Governing equations and solution methodology....53
3.3.4 Boundary conditions....58
3.3.5 Sequence of meshing and solver scheme....60
3.3.6 Model Validation....65
3.4 Parametric study using the developed CFD model....66
3.4.1 Effect of Cold Temperature....66
3.4.2 Effect of Charge Pressure....67
3.4.3 Effect of Matrix Wire Diameter....67

3.4.4 Effect of Porosity 69
3.4.5 Effect of Geometrical Parameters 69
3.4.6 Comparison between the original and the new Stirling engine 71
3.5 Conclusion 73
4. CHAPTER 4 74
4.1 Introduction 74
4.2 Parallel-Geometry Regenerators 75
4.3 Micro-Channel Regenerator 76
4.4 Regenerator Three-Dimensional CFD Modelling 78
4.4.1 Boundary conditions and solver scheme 80
4.4.2 Regenerator Test Facility Layout 89
4.5 Instruments and Measuring Devices 93
4.5.1 Flow meter 93
4.5.2 Heater 94
4.5.3 Electrical control box 94
4.5.4 Flow control valves 95
4.5.5 Thermocouples 98
4.5.6 Pressure transducers 100
4.5.7 Data taker 101
4.6 Devices Calibration: 101
4.6.1 Thermocouple calibration 101

4.6.2 Pressure transducers calibration 103
4.7 Measurement Accuracy 104
4.8 Test Procedure 106
4.9 Experimental Results 107
4.9.1 Results of one direction flow 107
4.9.2 Results of two direction flow 119
4.10 Conclusion 138
5. CHAPTER 5 140
5.1 Introduction 140
5.2 Experimental and CFD comparison for unidirectional flow 141
5.3 Experimental and CFD comparison for two directional flows 148
5.4 Regenerator segmentation 158
5.5 Effect of channels diameter 166
5.6 Conclusion 172
6. CHAPTER 6 173
6.1 Introduction 173
6.2 Engine development from air compressor 174
6.3 Developed engine CFD modelling 176
6.4 Results and discussion 178
6.5 Design improvement of the engine cooler 184
6.6 Conclusion 191

7. CHAPTER 7 192

REFERENCES 197

APPENDIX A 204

A.1 Historical Background of Stirling engine 204

A.1.1 Invention 204

A.1.2 Second engine model 205

A.1.3 The Philips Stirling engine 205

A.1.4 The efficient Stirling engine 206

A.2 Working Principles of Stirling Engine 207

A.2.1 Theoretical cycle of Stirling Engine 208

A.2.2 Carnot and Stirling cycles 211

A.2.3 Real cycle of Stirling Engine 212

APPENDIX B 213

APPENDIX C 233

APPENDIX D 241

LIST OF FIGURES

Figure 1.1 Air engine model built by Robert Stirling in 1816 [1] 2

Figure 1.2 Three main part of Stirling engine: Heater, Cooler and Regenerator..... 2

Figure 1.3 “Schematic diagram of the operation of a regenerator in a thermal system”[4] 3

Figure 1.4 Stirling regenerator shapes, [a]woven screen [7],[b]random fibre [6], ... 4

Figure 1.5 Engine classification [12] 4

Figure 1.6,[a]: yoke drive mechanism, [b]: rhombic drive mechanism, [c]: crank drive mechanism [9] 5

Figure 1.7 [a]:Dual -arrangement, [b]: V -arrangement 6

Figure 2.1 Different order techniques for Stirling engine 10

Figure 2.2 “Beale number for a range of heater temperature” [10] 11

Figure 2.3 “Compressor used for pistons of the Stirling engine” [11] 25

Figure 2.4 “Experimental apparatus” [73] 28

Figure 2.5 “Stacked woven wire matrices: friction factor vs. Reynolds number” [75] 30

Figure 2.6 “Stacked woven wire matrices for 110 μm wire diameter: Nusselt number versus” Reynolds number [7] 31

Figure 2.7 “Schematic diagram of the segmented parallel wire regenerator” [79] 34

Figure 3.1: “[a] Schematic diagram [b] Pictorial diagram taken from [61]” 37

Figure 3.2 Schematic diagram of the adiabatic model with seven engine parts 39

Figure 3.3 Flow chart for the Matlab code 40

Figure 3.4 Linear temperature profile of regenerator 41

Figure 3.5 Forced work [87] 47

Figure 3.6 Comparison of shaft power between the mathematical model and experiment at fixed charge pressure and different engine speed 48

Figure 3.7 Symmetric view showing the solid and fluid domains of the engine 53
Figure 3.8 Symmetric view showing moving and fixed domains of the engine.....59
Figure 3.9 Symmetric view showing the computational domains of the engine.....60
Figure 3.10 Grid independence Vs. Engine power.....61
Figure 3.11 Engine model mesh distribution.....61
Figure 3.12 Temperature contours at various sections in the heater domains during the cycle at (t= 0.48s).....62
Figure 3.13 CFD results of Stirling engine of the temperature contours (^{0}C) at different [Theta] crank angels (^{o}) at ([a] t= 0.46s and [b] t= 0.48s).....63
Figure 3.14 Pressure contours of the whole engine during the cycle at (t= 0.48s).....63
Figure 3.15 Variation of total, compression and expansion volumes versus crank angle within an engine cycle at 555 r.p.m 64
Figure 3.16 PV diagrams for compression and expansion volumes within an engine cycle at 555 r.p.m.....64
Figure 3.17 Comparison of indicated power between the mathematical model and CFD model at fixed charge pressure and different engine speed.....65
Figure 3.18 Cold temperatures Vs. Power at different hot temperatures (^{0}C) 66
Figure 3.19 Effect of Charge Pressure on the engine performance at different hot temperature (^{0}C) 67
Figure 3.20 Effect of regenerator matrix on engine performance at different hot temperature (^{0}C).....68
Figure 3.21 Effect of Porosity on engine performance at different hot temperature.....69
Figure 3.22 The selected geometric parameters 70
Figure 3.23 Effect of geometrical parameters on the engine performance:.....71
Figure 4.1 [a]Non-segmented micro-channel regenerator.....77

Figure 4.2 Distance between channels of regenerator 77

Figure 4.3 Thermal penetration depth vs. engine speed [100].....78

Figure 4.4 3D sector view showing the solid and fluid Domains of the regenerator 79

Figure 4.5 3D Sector view showing the computational domains Regenerator.....83

Figure 4.6. Regenerator model mesh distribution.....85

Figure 4.7 Temperature faces contours (^{0}C) for the 4-segmented regenerator at time of 360 s and one direction flow 86

Figure 4.8 Heat flux Vs. flow rates.....88

Figure 4.9 Validation of Nusselt number.....88

Figure 4.10 CAD drawing of the test section: 90

Figure 4.11: [a] Exploded view of the micro-channels regenerative heat exchanger and their housing ,[b] Micro-channels heat exchanger and [c] Random fibre regenerative heat exchanger 91

Figure 4.12 schematic of the Regenerator test rig 92

Figure 4.13 Pictorial figure of the whole regenerator test rig.....93

Figure 4.14 Omega FLMG-10050AL.....93

Figure 4.15 Electric heater wraps around inlet line 94

Figure 4.16 [a]Temperature Control box, [b] Inkbird Dual Digital PID with 25A SSR Solid State Relay and K Sensor probe" [102] 94

Figure 4.17 Solenoid valve, 'Steam- SAH HH' 96

Figure 4.18 control board by National Instruments, 'NI 6008' 96

Figure 4.19 'Labview' software user interface 96

Figure 4.20 The control of solenoid valves electric circuit 97

Figure 4.21 RTD sensors 98

Figure 4.22 Positions of thermocouples at the inlet, outlet and on the surface of the test section 99
Figure 4.23 Pressure transducers at the cold side of the test section 100
Figure 4.24 [a] Pressure transducer electrical wiring diagram [b] the DC power supply 100
Figure 4.25 Data taker.....101
Figure 4.26 Thermocouples calibration 102
Figure 4.27 Thermocouple calibration chart for T1.....102
Figure 4.28 Pressure transducers calibration 103
Figure 4.29 Pressure transducer calibration chart.....103
Figure 4.30 Surface temperature vs. Time (Th= 90 °C & SLPS=3).....108
Figure 4.31 Surface temperature vs. Time (Th= 90 °C & SLPS=5).....109
Figure 4.32 Inlet and outlet Temperature vs. Time (Th = 70 ^{0}C & SLPS=3).....111
Figure 4.33 Inlet and outlet Temperature vs. Time (Th = 90 ^{0}C & SLPS=3).....112
Figure 4.34 Inlet and outlet Temperature vs. Time (Th = 90 ^{0}C & SLPS=5).....113
Figure 4.35 Temperature Difference (ΔT) vs. Flow rate 114
Figure 4.36 Pressure Drop (ΔP) vs. Flow rate 116
Figure 4.37 The inlet and outlet pressure vs. Time (Th = 70 ^{0}C & SLPS=5).....117
Figure 4.38 The inlet and outlet pressure vs. Time (Th = 90 ^{0}C & SLPS=5).....118
Figure 4.39 Example of Temperature (Thi and Tci) vs. Time at (90 ^{0}C, SLPS=3& r.p.m=3) (Random fibre matrix) 120
Figure 4.40 Example of Temperature (Thi and Tci) vs. Time at (90 ^{0}C, SLPS=3& r.p.m=3) (Non-aligned Micro-channels matrix) 121
Figure 4.41 Example of Temperature (Thi and Tci) vs. Time at (90 ^{0}C, SLPS=3& r.p.m=3) (Micro-channels matrix) 122

Figure 4.42 Example of Temperature (Thi and Tci) vs. Time at (90 ^{0}C, SLPS=5& r.p.m=6) (Random fibre matrix) 123

Figure 4.43 Example of Temperature (Thi and Tci) vs. Time at (90 ^{0}C, SLPS=5& r.p.m=6) (Micro-channels matrix) 124

Figure 4.44 Example of Temperature (Thi and Tci) vs. Time at (90 ^{0}C, SLPS=5& r.p.m=30) (Random fibre matrix) 125

Figure 4.45 Example of Temperature (Thi and Tci) vs. Time at a (90 ^{0}C, SLPS=5& r.p.m=30) (micro-channels matrix).....126

Figure 4.46 Temperature Difference (ΔT) vs. r.p.m with SLPS=5.....127

Figure 4.47 Example of Pressure drop vs. Time in the oscillating flow.....131

Figure 4.48 Pressure Drop (ΔP) vs. Flow rate with (r.p.m=3).....132

Figure 4.49 Pressure Drop (ΔP) vs. Flow rate with (r.p.m=6).....133

Figure 4.50 Pressure Drop (ΔP) vs. Flow rate with (r.p.m=30).....134

Figure 4.51 Pressure Drop (ΔP) vs. r.p.m at different flow rate (Th=90 ^{0}C).....137

Figure 5.1Micro-channel regenerator geometry for the CFD model.....141

Figure 5.2: [a] to [h] Micro-channel regenerator temperature contours at t=360 s and SLPS=3 143

Figure 5.3 [a]to[d] Surface temperature CFD values compared with experimentally measured for SLPS = 3 and 5.....146

Figure 5.4 CFD and experimental time variation for the (T_{ci}) temperature at Th= 90 with SLPS=3 and 5. 147

Figure 5.5 comparison of pressure drop across the micro-channels regenerator between experiment and CFD.....147

Figure 5.6 Regenerator temperature contours (^{0}C) at (t=720s, SLPS=3& r.p.m=30) 150

Figure 5.7 Comparison of surface temperature from CFD simulations and experiments for two directional flow at SLPS=3 & r.p.m=30. 152
Figure 5.8 Comparison of inlet and outlet temperatures (Th_i &Tc_i) from CFD simulations and experiments for two directional flow at SLPS=3 & r.p.m=30 (cycle 359 & 360).....153
Figure 5.9 Comparison of inlet and outlet temperatures (Th_i &Tc_i) from CFD simulations and experiments for two directional flow at SLPS=5 & r.p.m=30 (cycle 359 & 360).....154
Figure 5.10 Pressure drop across the regenerator channels: 155
Figure 5.11 Friction factor versus Reynolds number for the micro-channels regenerator 156
Figure 5.12 Reynolds number versus average Nusselt number for the micro-channels regenerator. 157
Figure 5.13 Exploded view for the different micro- channels regenerator.....159
Figure 5.14 Interfaces temperature contours (^{0}C) for the non-segmented regenerator.....160
Figure 5.15 Interfaces temperature contours (^{0}C) for the 4-segmented regenerator.....160
Figure 5.16 Interfaces temperature contours (^{0}C) for the 8-segmented regenerator.....160
Figure 5.17 Interfaces temperature contours (^{0}C) for the 16-segmented regenerator.....160
Figure 5.18 Interfaces temperature contours (^{0}C) for the 32-segmented regenerator.....160
Figure 5.19 Positions of the axial temperature measurement (centre, middle and top).....161
Figure 5.20 Axial temperature for the micro-channels regenerator.....162
Figure 5.21 Comparison of inlet and outlet temperatures (Th_i &Tc_i) from CFD simulations for the segmented-regenerator with experiments at SLPS=3 & r.p.m=30 (cycle 359 & 360) 164
Figure 5.22 Relation between Reynolds number and average Nusselt number for the three segmented-regenerators 165
Figure 5.23 Inlet surface temperature contours (^{0}C) for the 0.5 mm regenerator.....167
Figure 5.24 Inlet surface temperature contours (^{0}C) for the 1 mm regenerator.....167
Figure 5.25 Inlet surface temperature contours (^{0}C) for the 1.5 mm regenerator.....167

Figure 5.26 Relation between Reynolds number and Friction factor for the three Channels 168

Figure 5.27 Inlet and outlet temperatures (Th_i &Tc_i) from CFD simulations for the 0.5,1 and 1.5mm / 32-segmented-regenerator at SLPS=3 & r.p.m = 30 (cycle 359 & 360) 169

Figure 5.28 Reynolds number vs. average Nusselt number for the three channels regenerators 170

Figure 6.1 V-type compressor “Clark Air Compressor Pump 9 CFM- CE20” [105]..... 174

Figure 6.2 [a] V-type compressor [b] Converted Stirling engine 175

Figure 6.3 Definition of engine geometrical parameters 175

Figure 6.4:[a]to[d] Geometry domains and mesh 178

Figure 6.5 Heater inner diameter Vs. Power..... 179

Figure 6.6 Cooler inner diameter Vs. Power 179

Figure 6.7 Heater outer diameter Vs. Power..... 180

Figure 6.8 Cooler outer diameter Vs. Power 180

Figure 6.9 Heater length Vs. Power..... 180

Figure 6.10 Cooler length Vs. Power..... 181

Figure 6.11 Regenerator length Vs. Power..... 181

Figure 6.12: [a] to [d] CFD Temperature contours at different [Theta]crank angels during 5^{th} cycle 183

Figure 6.13: [a] and [b] Cooler of Stirling engine cooling system 184

Figure 6.14 Three dimensional view of the finned-cooler..... 185

Figure 6.15 Symmetrical view of the finned-cooler 185

Figure 6.16 Boundary conditions of the finned-cooler..... 186

Figure 6.17 Axial temperature for the finned cooler with different lengths..... 187

Figure 6.18 Axial temperature for the finned cooler with different diameters..... 188

Figure 6.19: Water velocity magnitude (m/s) [a]Non finned and [b]Finned cooler 188

Figure 6.20 [a] and [b] Temperature distribution (^{0}C).....189

Figure 6.21 V-type alpha Stirling engine with Finned-cooler 189

Figure 6.22 Indicated power for channels, Screen woven and random fibre matrix regenerators 190

LIST OF TABLES

Table 2.1 “Estimated parameters (a1, a2, a3) for Woven Screens” [74] 29

Table 2.2 “Estimated parameters (a1, a2, a3) for Metal Felts” [74] 30

Table 2.3 “Comparison between current testing technique and single-blow method” [78] 33

Table 3.1 “Stirling engine specifications and operating conditions [61]” 38

Table 3.2 Matrix woven wire diameter 68

Table 3.3 New Stirling Engine design parameters and operating conditions 72

Table 4.1 Summery of the main proprieties of the selected regenerator material 77

Table 4.2 Grid independence and CFD results 84

Table 4.3 Summery of thermocouple calibration and uncertainties 105

Table 4.4 Summery of pressure transducers calibration and uncertainties 105

Table 4.5 Effectiveness of the Random fibre regenerator at different r.p.m and flow rates: 129

Table 4.6 Effectiveness of the micro-channels regenerator at different r.p.m and flow rates: 129

Table 4.7 Darcy friction factor comparison for the regenerator matrixes: Micro-channels, Screen woven and Random fibre at different Reynolds numbers 139

Table 5.1 Regenerators configurations and parameters. 166

Table 5.2 Equivalent porous media characteristics of segmented micro-channel regenerator matrix 171

Table 6.1 Stirling engine specifications and operating conditions 182

Table 6.2 Value of the boundary conditions: 186

NOMENCLATURE

Symbols	Description	Unit
A_{k1}	Internal wetted area of the connecting pipe	(m^2)
A_{k2}	Internal wetted area of the cooler	(m^2)
C_p	Heat capacity of the gas at constant pressure	(J/kg. K)
C_v	Heat capacity of the gas at constant volume	(J/kg. K)
CVC	Clearance volumes in the compression space	(m^3)
CVE	Clearance volumes in the expansion space	(m^3)
Dh_i	Inner diameter of the heater	(mm)
D_d	Piston diameter	(m)
Dh_o	Outer diameter of the heater	(mm)
Dk_i	Inner diameter of the cooler	(mm)
Dk_o	Outer diameter of the cooler	(mm)
d_h	Hydraulic diameter	(m)
d_w	Mesh wire diameter	(m)
E	Mechanism effectiveness	(m)
eff	Effective volumetric heat capacity	[-]
f_D	Darcy friction factor	[-]
f_r	Reynolds friction factor	[-]
J_d	Cylinder annular gap	(m)

h_{h1}	Hot pipe heat transfer coefficient	(W/m^2. K)
h_{h2}	Heater heat transfer coefficient	(W/m^2. K)
h_{k1}	Cooler transfer coefficient	(W/m^2. K)
h_{k2}	Cold pipe heat transfer coefficient	(W/m^2. K)
K	Permeability	(W/m^2. K)
k	Thermal conductivity of the gas	(W/m. K)
k_{eff}	Effective thermal conductivity	(W/m. K)
k_p	Thermal conductivity of porous matrix	(W/m. K)
k_d	Displacer thermal conductivity	(W/m. K)
k_r	Regenerator thermal conductivity	(W/m. K)
l_r	Regenerator effective length	(m)
m	Total mass of gas	(kg)
$\dot{m}$	Mass flow rate	(kg/s)
n	Engine speed	(rpm)
NTU	Number of transfer units	(W/m. K)
p	Instantaneous gas pressure	(Pa)
p_{ch}	Charge pressure	(Pa)
q	Heat Flux	(W/m^2)
Q_h	Heat absorbed by the heater	(J)
Q_k	Heat rejected by the cooler	(J)

Q_r	Heat transfer to the regenerator	(J)
$Q_{r,loss}$	Heat losses in the regenerator	(J)
$Q_{r,max}$	Maximum heat losses in the regenerator	(J)
$Q_{r,min}$	Minimum heat losses in the regenerator	(J)
Q_p	Work done by pressure changes	(J)
Q_{vd}	Viscous dissipation	[-]
R	Gas constant	(J/kg. K)
Re	Reynolds number	[-]
T_h	Ideal gas temperature in the heater	(K)
T_k	Ideal gas temperature in the cooler	(K)
T_r	Ideal gas temperature in the regenerator	(K)
T_e	Temperature of the expansion space	(K)
T_c	Temperature of the compression space	(K)
T_{h2e}	Conditional temperature (heater)	(K)
T_{ck1}	Conditional temperature (cooler)	(K)
T_{wk}	Cooler wall temperature	(K)
u	Velocity of the gas	(m/s)
T_k	Ideal gas temperature in the cooler	(K)
V_c	Volume variation in the compression space	(m^3)
V_e	Volume variation in the expansion space	(m^3)

V_{h1}	Void volume of the heater	(m^3)
V_{h2}	Void volume of the connecting pipe (hot side)	(m^3)
V_{k1}	Void volume of the connecting pipe (cold side)	(m^3)
V_{k2}	Void volume of the cooler	(m^3)
V_r	Void volume of the regenerator	(m^3)
V_{SC}	Swept volumes in the compression space	(m^3)
V_{SE}	Swept volumes in the expansion space	(m^3)
W_{loss}	Pumping loss	(W)
$\dot{W}_s$	Shaft power	(W)
W_s	Shaft work	(J)
$\bar{W}$	Forced work	(J)
Z_d	Piston stroke	(m)
Greek letters	**Description**	**Unit**
ε	Regenerator effectiveness	[-]
ϵ_p	Porosity	[-]
γ	Specific heat ratios	[-]
α	Phase angle, rad	(rad)
μ	fluid dynamic viscosity	(Pa. s)
ρ	Gas density	(kg/m^3)
I	The identity matrix	[-]

β_F	Forcheimer coefficient	(m^2/s)
θ_p	Volume Fraction	[-]
α_p	Coefficient of thermal expansion	[-]

Acronyms	**Description**
2D	Two dimensional
3D	Three dimensional
CFD	Computational fluid dynamics
SLPS	Standard liter per second

LIST OF PUBLICATIONS

1. **A. K. Almajri**, S. Mahmoud, and R. Al-Dadah, S. Alfarawi, H Jayakody. “CFD Parametric Study of Alpha Stirling Engine Performance”. the 17th International Stirling Engine Conference, Northumbria University, Newcastle, 2016.

2. **A. K. Almajri**, S. Mahmoud, and R. Al-Dadah, “Modelling and parametric study of an efficient Alpha type Stirling engine performance based on 3D CFD analysis,” *Energy Convers. Manag.*, vol. 145, 2017.

3. H. Ahmed, **A. K. Almajri**, S. Mahmoud, R. Al-Dadah, and A. Ahmad, “CFD modelling and parametric study of small scale Alpha type Stirling Cryocooler,” *Energy Procedia*, vol. 142, pp. 1668–1673, Dec. 2017.

CHAPTER 1

INTRODUCTION

1.1 General background

Nowadays with the current levels of fossil fuels consumption and CO2 emissions, the global warming effects have reached concerning levels. The use of Stirling engines for electrical power generation offers the potential of exploiting the vast amount of waste heat available from industrial processes, thus reducing the use of fossil fuels and carbon emissions. The development of efficient Stirling engines is essential for the effective exploitation of industrial waste heat.

Robert Stirling, in 1816 built the first Stirling engine based on the processes of the expansion and compression that occurs when heat is added to or taken from a closed system of air. After more than 150 years, precisely in 1971, the first attempt to analyse the engine mathematically was made. Since then, improved engine models have emerged through the process of improving and mastering the theory of Stirling engines [1].

According to the industrial revolution in the 19th century, which was known as the golden era of the development in science and technology, the management of these industrial applications required a huge need for mechanical engines and thermal energy. Stirling engine, a safe external combustion engine, was one of the engines in competition with the steam engine which was commonly used during the early 19^{th} century. Stirling engine was initially used to pump water from a stone quarry producing two horse-power for almost 2 years [2].

Figure 1.1 shows the first engine model, which used air as the working fluid. (The working principles of Stirling engine is provided in Appendix A)



Figure 1.1 Air engine model built by Robert Stirling in 1816 [1]

However, Stirling engine suffered from lower power output compared to the steam engine, and the need for higher temperatures in order to maximize its power output, which caused frequent materials failure.

The regenerator, as a major part of the engine, is a heat exchanger placed between two heat sources, the cooler, and the heater as on Figure 1.2.

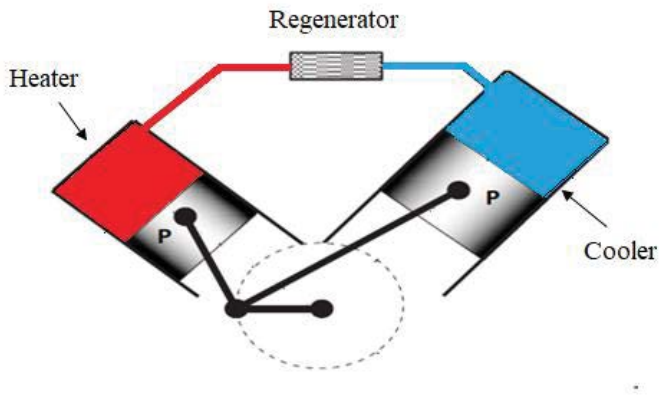


Figure 1.2 Three main part of Stirling engine: Heater, Cooler and Regenerator

The working gas transfers from the heater through the regenerator to the cooler in the first half of the engine cycle, the regenerator matrix absorbs the heat from the hot gas during this stage.

In the second half of the cycle, the working gas is sent back through the regenerator from the cold side to the hot side, the cold gas absorbs the stored heat from the regenerator matrix. Thus, as the regenerator acts as thermal storage, this minimizes the amount of energy that needs to be added in the heater. In the cooler, after the gas leaves the regenerator, the gas loses part of its temperature and arrives in the cooler at a lower temperature; this then minimizes the heat rejection compared to cases where there is no regenerator. (See Figure 1.3).

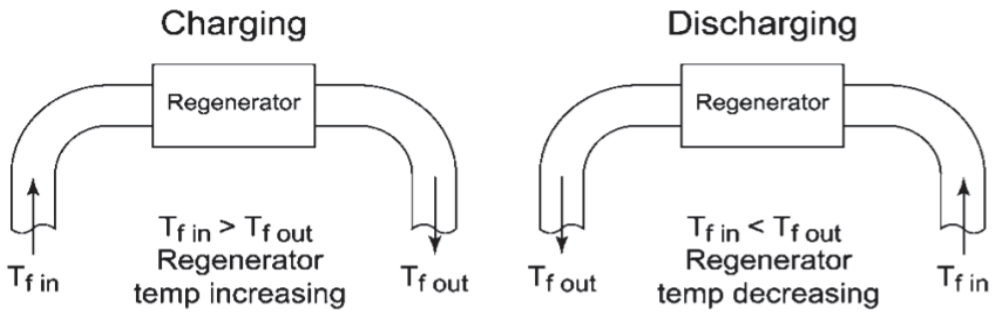


Figure 1.3 “Schematic diagram of the operation of a regenerator in a thermal system”[3]

The regenerator was considered as an added value to Stirling engine performances to be more capable in comparison to the other exciting engines. Moreover, the engine with a regenerator can reduce five times the demands of heat that applied to the heater compared to the case of the engine without a regenerator [4], [5].

There are several regenerator types that can be used in Stirling engines such as woven-wire screens mesh, packed-sphere, random-fibre, metal foam, wrapped-foil, parallel plate and tube-bundles regenerator [5] . The most common types that are widely used in Stirling engines are the random fibre and wire mesh, known as the conventional type of regenerators. (See Figure 1.4).

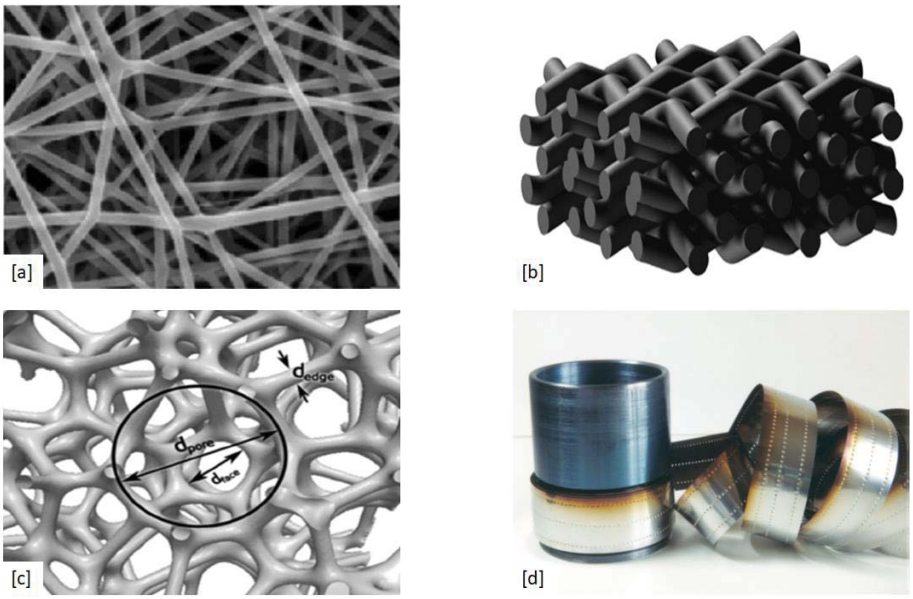


Figure 1.4 Stirling regenerator shapes, [a]woven screen [6],[b]random fibre [5], [c] metal foam [7], [d]wrapped-foil [8]

Alpha, Beta and Gamma are the three types of Stirling engine, which differ in the way the working fluid is transferred between the heat exchangers but have similar thermodynamic cycles. (See Figure 1.5).

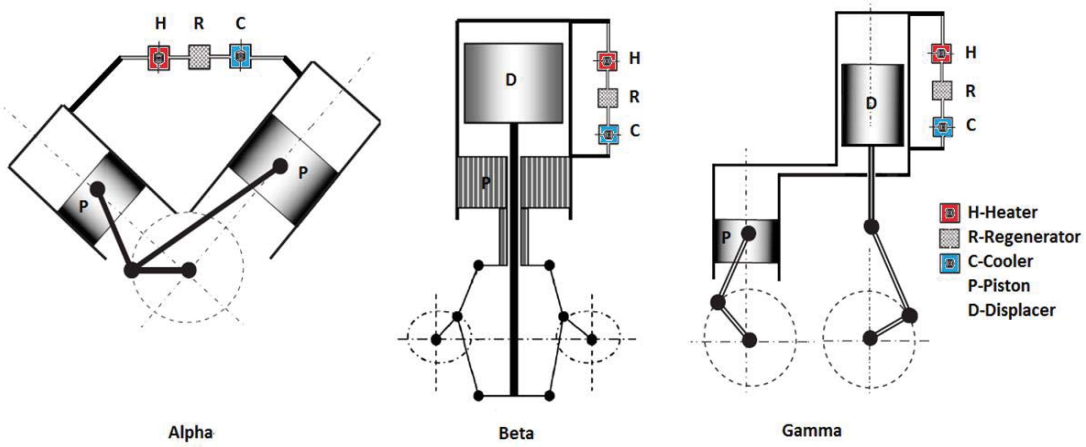


Figure 1.5 Engine classification [9]

The alpha Stirling engine consists of hot and cold cylinders located separately on two pistons with connecting tubes that are used to connect the cold and hot cylinders, while a regenerator

is positioned between the two sides. The drive mechanism in Figure 1.6 (a) shows the yoke drive arrangement (Ross linkage) for an alpha type. In a Beta Stirling engine, one cylinder contains a compression piston on the cold side and a displacer on the hot and cold side. The rhombic drive is often applied to this type of engine as shown in Figure 1.6 (b). The Gamma Stirling engine has two individual cylinders, a displacer disposed in the hot cylinder, while the cold cylinder comprises a power piston [10]. The standard crank drive is often applied to this type of engine as shown in Figure 1.6 (b). In the comparison between the three classifications, alpha-type is the simplest design in terms of clear separation between the heat rejected and heat source volumes [11]. This means that there is no opportunity for the occurrence of any early mixing of the hot and cold working fluid.

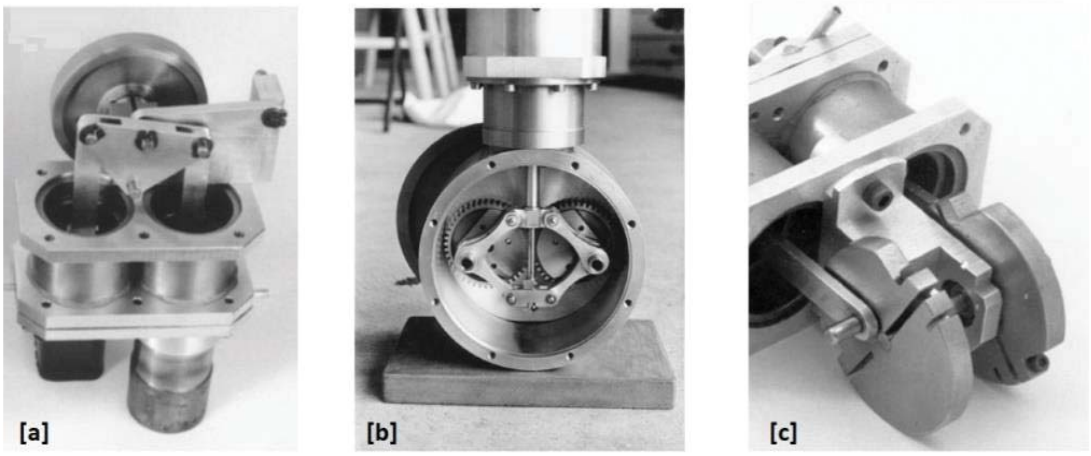


Figure 1.6,[a]: yoke drive mechanism, [b]: rhombic drive mechanism, [c]: crank drive mechanism [8]

1.2 V-type alpha Stirling engine

The two pistons of the alpha type Stirling engine are driven by crank, and the phase angle between these pistons decides the arrangement type of the engine as it can be seen on Figure 1.7. The engine with drive mechanism (Ross linkage) in Figure 1.7 (a) is defined as Dual – arrangement which has a phase angle of 180^0. Figure 1.7 (b) shows the engine with V-arrangement that has a phase angle of 90^0 is defined as V-type alpha Stirling engine. In this

work it was decided to choose the V-type alpha Stirling engine, because it offers a major advantage in terms of its stability and low vibration compare to the other type of arrangements. [8].

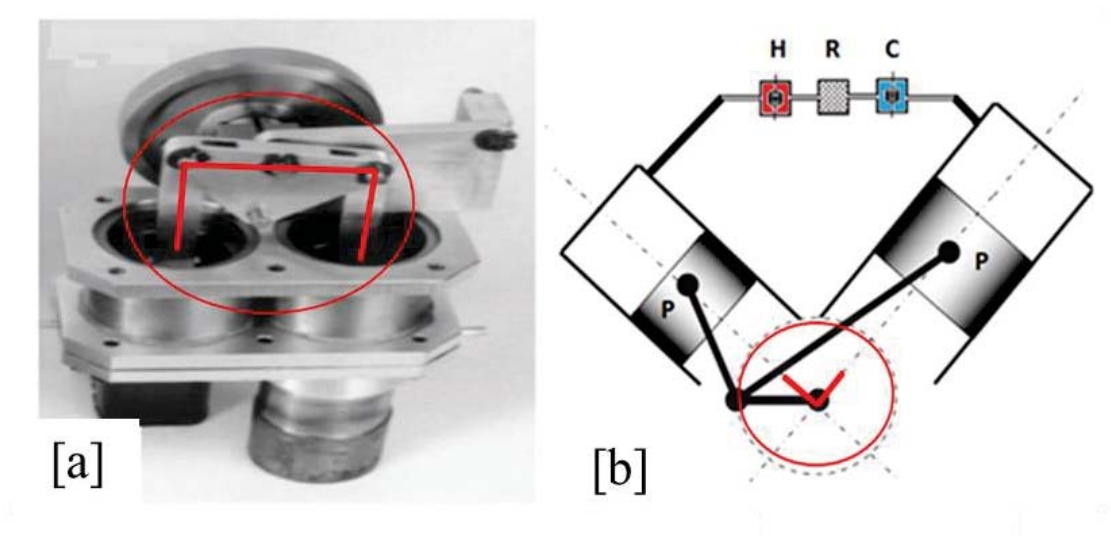


Figure 1.7 [a]:Dual -arrangement, [b]: V -arrangement

The V alpha-type Stirling engines, offer a major advantage in terms of their ability to separate the heat rejected and heat source volumes, thus no early mixing of the hot and cold working fluid. Despite these advantages, there has been no reported work on advanced modelling for such engines, particularly the 3D CFD modelling and the use of this modelling to improve the design parameters of the engine. Additionally, the approach of combining the thermodynamic modelling with the 3D CFD analysis for improving the performance of the V alpha-type Stirling engines was not reported in the open literature.

1.3 Research objectives

This study aims to improve the performance of V-type alpha Stirling engine through the following objectives:

- Develop a thermodynamic and CFD model for V-type alpha stirling engine.

- Develop new concept regenerator (Segmented Micro-channels) using advanced machining technologies (CNC) that can improve the engine performance through CFD modelling and experimental testing.
- Investigate the performance of a V-type alpha Stirling engine through parametric analysis including the effect of the segmented regenerator.
- Investigate through CFD modelling the development of V-type alpha Stirling engine from commercially available V type compressor.

1.4 Thesis outlines

This thesis is divided into seven chapters. Chapter (1) delivers a general introduction and overview about the research background and thesis objectives. Chapter (2) provides a comprehensive and detailed overview of previous theoretical and experimental work done on Stirling engines. Review of the previous studies on the development of parallel-geometry Stirling regenerators will be also included in this chapter.

Chapter (3) presents the development of detailed thermodynamic and full 3D CFD models for a V-type alpha Stirling engine using engine prototype and its experimental results from published work in the open literature. New approach combining the thermodynamic model with 3D CFD analysis is developed in this chapter to investigate the performance of the V-type alpha Stirling engine under various operating conditions and design parameters.

Chapter (4) introduces a new regenerator configuration for the V-type alpha Stirling engine; it is a parallel-geometry segmented regenerator with circular micro-channels structure each with hydraulic diameter of 1 mm. The regenerator is machined at the University of Birmingham using CNC machining technology and consisting of four parts, each part has 10 mm length with 40 mm diameter. The work involves 3D CFD modelling and experimental testing for three

regenerators: The Non-aligned micro-channels and Random fibre regenerators and the parallel-geometry Micro-channels regenerator. A detailed description of the test rig facility including measuring instruments and uncertainty analysis is also included in this chapter, with comparison and discussions of the experimental measurements.

Chapter (5) presents the development of efficient segmented micro-channel regenerator thorough CFD simulations that validated with the experimental measurements using unidirectional and oscillatory flows. The validated CFD model is used to carry out an investigation on the effect of increasing the number of segments on the regenerator effectiveness. Moreover, the effect of changing the channel diameter is also included in this chapter.

Chapter (6) investigates the routes to upgrade commercially available V-type compressor to develop V-type alpha type Stirling engine. The work involves the development of detailed CFD modelling and new concept for the cooler design, which improved the performance of the developed engine. Correlation of Nusselt number and friction factor for all segmented regenerators developed in chapter (5), are used as input porous media parameters in the CFD model for the V alpha-type Stirling engine developed in this chapter. The chapter presents a comprehensive comparison between all developed regenerator configurations and two commercial matrix regenerators, namely the Random fibre and the Screen woven on the engine performance.

Chapter (7) summarises the conclusions from this research and main suggestions for the future work.

CHAPTER 2

LITERATURE REVIEW

2.1 Introduction

This chapter provides a comprehensive overview of previous theoretical and experimental work carried out on Stirling engines, and it consists of three main sections. The first section reviews the all the analysis techniques used to describe the dynamics of the Stirling engines, including the advanced CFD modelling. The second section summarizes the reported work regarding the development of various V-type alpha Stirling engine prototypes. The third and last section of this chapter outlines the gap of knowledge on Stirling engine research work in the open literature

2.2 Stirling engine analysis techniques

The analysis of Stirling engine cycles are classified according to methods used to describe the engine models as shown in Figure 2.1, where the designation is suggested by [12]. The order of these models was proposed in accordance with their accuracy, complexity, and computational time needed to solve the model.

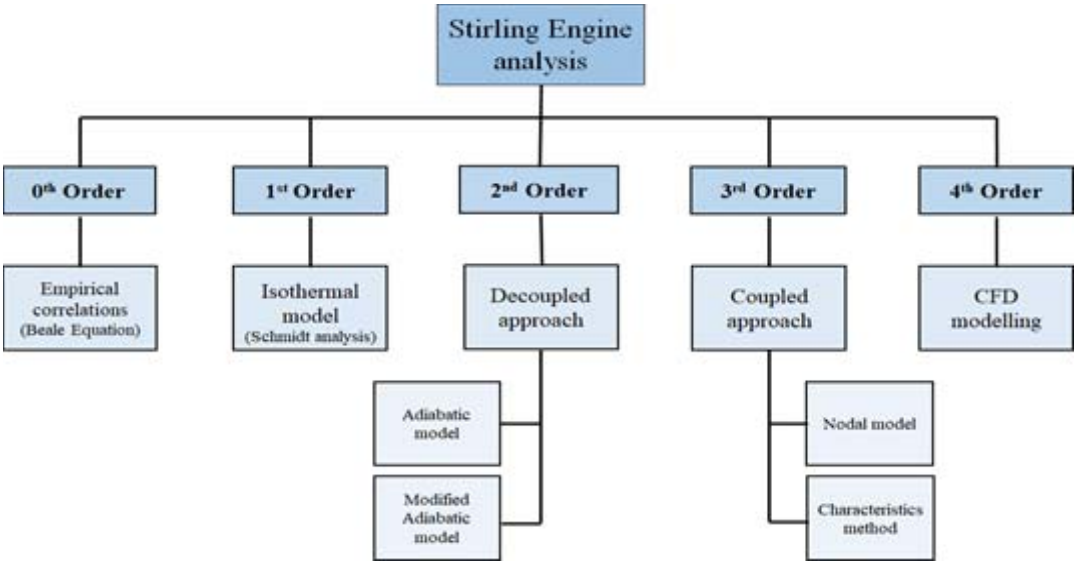


Figure 2.1 Different order techniques for Stirling engine

2.2.1 The zeroth-order analysis

In this model the engine power output W_0 in Watts, can be predicted by using an empirical formula proposed by [13], as follows:

$$W_0 = B_n . p_m . V_{SC} . f \qquad 2.1$$

The formula depends on the mean pressure p_m of the cycle in bar, the frequency f in Hz, the swept volume of the compression piston (power piston) in cm^3 and Beale number B_n. Beale et al [14] defined the Beale number B_n as a dimensionless parameter, and it is a function of the maximum heat (heat source) and minimum heat (heat of the sink temperature) as follows [14]:

$$B_n = 0.035 \frac{T_h - T_c}{T_h + T_c} \qquad 2.2$$

In general, Eq.(2.2) is valuable for the design of a new Stirling engine; it can give a reliable estimate for the new Stirling engine in terms of volume and performance. At high temperature,

the Beale number is often considered to be 0.015 [15]. The value of Beale number for low or medium temperature is considered to be between 0.008 to 0.002 [15].

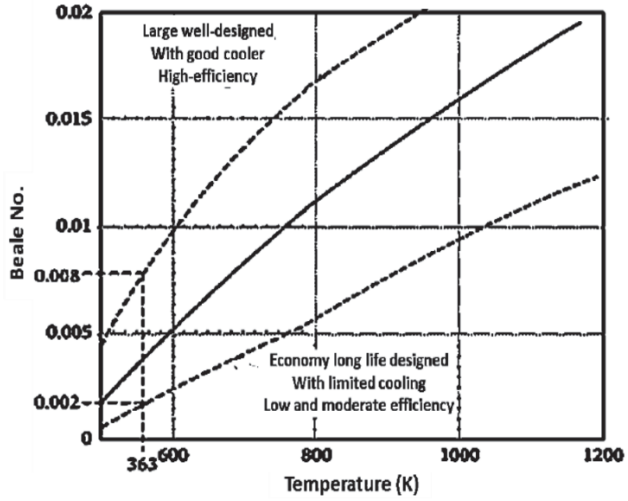


Figure 2.2 "Beale number for a range of heater temperature" [10]

West added some enhancements to the Beale formula by including the thermal irreversibility in both heat sources as in the following equation [16]:

$$B_n = 0.025 \frac{T_h - T_c}{T_h + T_c} \qquad 2.3$$

2.2.2 The first-order analysis (Schmidt analysis)

The first order method to predict engine power is known as Schmidt's analysis [17], and it is often called the isothermal analysis; it is an analytical approach based on isothermal working space and sinusoidal volume changes. The estimations of power output in respect to a certain engine size are adopted in this method [15]. All calculations in this method are based on algebraic equations of energy conservation and mass to evaluate the performance of the Stirling engines. The theory of Schmidt considering that the compression and expansion spaces are isothermal, it neglects all losses accrued due to the heat transfer and the internal parts

movements. The study by [18] concluded that the performance of Stirling engines using Schmidt analysis can be in general overestimated by 30%. On another hand it is considered that the isothermal analysis gives an initial indication of the power and performance of the engine.

Toda et al. [19] proposed an enhanced model by including the drive mechanism effectiveness to Schmidt analysis for a 10 kW LTD Gamma-type Stirling engine. The experimental results showed that the cycle shape and the pressure of the buffer have slight influence on the shaft power, while the measured affect results due to the mechanical effectiveness.

El-Ehwany et al. [20] studied the changing in the performance of an alpha-type Stirling engine by using elbow-bend heat exchangers as a cooler and heater. The dimensions of the elbow-bend heat exchangers were concluded from experimental tests performed in previous work by the author to evaluate eight heat exchangers. The results of the pressure drop and heat transfer observed from the experimental test on the engine were correlated and then inserted to a computer software to solve the cycle of the engine based on Schmidt analysis. The suggested engine showed 13% improvement in the performance of the engine compared to a similar engine in the literature at a high level of efficiency.

Combining the Schmidt analysis with CFD modelling was adopted by [21]. The study presented a Gamma-type Stirling engine where its heater works by burning agricultural waste such as Bagasse, Pruned Wood, Switch-grass, Poplar and Sawdust. Results showed that the engine can produce a wide range of power outputs depending on the type of heat source. The

study also suggested that the designed engine offers the potential to produce electricity for the countryside areas.

Kato et al. [22] utilized a CFD method to estimate the regenerator temperature and efficiency of a Gamma-type low-temperature differential Stirling engine. The two side temperatures of the regenerator were then used in the isothermal model analysis.

Senviboon et al. [23] performed a theoretical analysis using Schmidt analysis theory to examine the effect of various parameters on the shaft output power of an alpha-type Stirling engine. Different geometrical and operational parameters in this study were converted into dimensionless forms such as pistons movement equations, and mean pressure through the engine. The study concluded that the dead volume has a major influence on the engine performance.

Ipci and Karabulut [24] presented a dynamic analysis based on the first order for an alpha-type Stirling engine. The study used a Scotch yoke mechanism to drive the engine and the engine was divided into 15 volumes and the pressure was considered to be equal in all engine volumes. Motion equations were addressed to suit the crankshaft and the movement of the piston. The authors carried out a parametric study to investigate the optimum operating conditions for the engine. Results indicated that maximum power of 2057 W at 5.1 bar charge pressure and engine speed of 138 rad/s can be achieved.

Evaluating the effect of a beta-type Stirling engine regenerator on the engine performance based on Schmidt theory was adopted by [25]. The cylinder of the displacer was occupied with square wire sheets to be used as regenerator housing. The geometrical parameters were

investigated in terms of optimum dimensions. The model validated against experimental data from SCM81-engine. The power output from the proposed engine was 16% higher than that produced from SCM81-engine. The author compared his engine in another study [26] against the GPU3 engine which was operated without regenerator. He found that the designed engine not only can produce output power 20% higher than the GPU3 engine, but also his design reduced the dead volume of the engine.

The first-order analysis combined with the finite speed method in the study by [27]. The chosen engine in this study was Gamma configuration, which was heated using solar energy. Different losses were taken into consideration in each time step of the simulation solution. Results indicated that most losses in the engine were due to the gas leakage through the piston movement and the heat losses through the gab in the regenerator. The study proposed decreasing the clearance leakage with using filling material for the walls, cylinder and displacer can improve the performance of the engine.

The first-order technique can predict the performance of the engine in a short time; however, it only helps as an initial prospection.

2.2.3 The second-order analysis

Further development was made to the Schmidt's analysis by [28]. In this analysis, both the compression and expansion spaces considered adiabatic where the work involves an assessment and subtracting the power and heat losses from the analysis of the ideal cycle, it is often called the ideal adiabatic model. The engine is divided into five spaces: tow adiabatic spaces (compression and expansion) in addition to the three isothermal heat exchangers (cooler, heater and regenerator). In this approach, numerical integration is applied to solve the ordinary

differential equations of the energy and mass equations for each space. The second-order analysis then called the simple analysis when the temperature of the working fluid (gas) in both the heater and the cooler were calculated in accordance with the regenerator effectiveness. This means that the thermal losses such as the conduction losses and the pumping losses in all five spaces are taken into account and then the power of the engine will approach the actual real engine power. The second-order analysis: is fast and accurate enough to estimate the results when compared with Schmidt's analysis in terms of calculating the power and efficiency.

The most common experimental data in the open literature that was published by [12] based on GPU3. It is used as the most reliable source to validate different analyses for Stirling cycle. Many researchers improved the simple analysis by including different losses to the method of analysis such as adding the pumping losses, the shuttle losses and the random conduction heat transfer losses.

Developing a numerical code (Stirling Numerical Analysis Program) to analyse the cycle of Stirling engine based on the second order method was conducted by [29]. The code was introduced to evaluate the performance of Stirling engines by investigating the optimum design parameters of the engine. The commercial name of this code is "SNAP2002®".

A commercial code developed by [30] which was widely used in many studies in terms of evaluating the Stirling engine performance based on the second-order analysis, the code is called PROSA®. For example, 8 kW Amazon Stirling engine prototype, built by [31], used the PROSA® code to estimate the power output and it was 6.8% lower than Schmidt analysis. The study concluded that the PROSA® code is more accurate to simulate the engine performance.

Araoz et al. [32] developed a second-order model based on ideal adiabatic analysis, six parameters were investigated to improve the performance of the engine including porosity, phase angle, regenerator housing diameter and length, heater length and tubes diameter.

Timoumi et al. [33] and [34] conducted a numerical analysis for the (GPU-3) Stirling engine using a non-ideal adiabatic approach (quasi-steady flow) where the flow resistance, heat conduction losses, and gas behaviours were considered. The results are compared with experimental data and showed a 7.9-15% deviation. The study included an engine optimization module to reduce the pressure drop in the regenerator, and showed an enhancement in the engine performance by taking into account these losses.

Cheng et al. [35] studied the effect of the regenerator performance on the (300 W) Beta-type Stirling engine using various charge pressure and temperature ranges with two different working fluids (helium and air). They found that the optimal mesh gave 20% deviation compared with the experimental results. The model adopted in the study was based on the analysis of the non-ideal adiabatic approach.

Gheith et al. [36] presented a numerical and experimental investigation of the Stirling engine heater, a thermodynamic model based on the quasi-steady flow was presented for a Gamma type Stirling engine. The influence of several operating parameters (temperature of the heat and cold sources, charge pressure and rotation speed) on the heater were tested. The study concluded that the temperature of the heat sources and rotation speed have a major effect on the engine performance.

More recently, Ahmadi et al. [37] carried out an optimization of Stirling engine in which the performance of the engine changed with the changing of major parameters (such as high temperature, the effectiveness of the regenerator, frequency, piston movement and the volume ration). He developed a theoretical model for (GPU-3) Stirling engine and concluded his model can explore the optimum characteristics of such heat engines that receive energy from other heat sources.

Valenti et al. [38] conducted a numerical analysis on experimental results of a micro-cogeneration Stirling engine, the model applied a modified version (second-order model) of Berchowitz and Urieli approach [39] and they found the heat conduction losses and regenerator heat loss had a major effect on the engine performance. The results also concluded that using Nitrogen as a working fluid had strongly increased the engine performance.

Alfarawi et al. [40] developed a non-ideal adiabatic analysis, including the effect of the connecting pipe, an acceptable deviation between the model and experimental measurements of Gamma Stirling Engine (ST05 CNC). The validation was at different operating conditions to predict the shaft and indicated power. The influence of several operating and geometrical parameters (such as temperature difference, charge pressure, working fluid and phase angle) on the engine performance was also included in this study.

The simple analysis for (GPU-3) Stirling engine was implemented by [41], the method of analysis in this study was considered as an improved version of Berchowitz and Urieli approach [39]. Losses through the regenerator walls (due to the heat conduction) and pumping losses

were included and added to the rejected heat from the engine. The results were compared to experimental measurements and showed good accuracy prediction for the power output.

2.2.4 The third-order analysis

The third order analysis was developed in 1975 where Finkelstein carried out a nodal analysis of the Stirling engine using the equations of mass, momentum and energy conservation with nodes as elements, or cells [42]. This method forms the basis of many computer programs designed to simulate the Stirling engine.

Dyson et al. [43] published a summary of revision for some different methods to analyse the Stirling cycle. Some examples of codes in this publication were criticized based on the third-order method; in 1985, Gedeon established a code called 'GLIMPS' based on the third-order analysis, then 8 years later the enhanced version of 'GLIMPS' code was introduced with a feature of (friendly graphical user interface) and it was called 'Sage' code [44]. The first use of both 'GLIMPS' codes was in the NASA's labs. The 'H-FAST' code demonstrated by [45] was also based on the third method of analysis where the conservation, energy, momentum and mass equations were taken into account and solved in a simplified way.

Nepveu et al. [46] established a thermal model (using a nodal method) for analysing the alpha-type Stirling Engine (SOLO 161 Stirling). The engine was divided into 32 volumes and different parameters such as density, temperature and mass were evaluated. The results were compared to experimental measurements showing 21% deviation. The differential equation system is elucidated, and then calculated by an iteration method using the Matlab program.

Toghyani et al. [47] conducted a numerical analysis for optimizing the (GPU-3) Stirling engine performance using the third-order thermodynamic analysis. Two operational parameters (mean charge pressure and hot source temperature) and two geometrical parameters (engine speed and stroke) were optimized in terms of enhancing the engine performance and reducing the pressure drop. The results showed that the efficiency and power output can be enhanced by 5.7% and 600 w respectively, and that based on the use of Fuzzy decision.

Hoegel et al [48] used the third-order analysis to optimize a low-temperature difference (LTD) alpha-type Stirling engine using the range of (100 - 200) ^{0}C as a heat source. The effect of different parameters on the engine performance was evaluated in this study. The results concluded that for the (LTD) Stirling engine, the optimum engine speed is 1800 r.p.m. As for the phase angle, it was found that a 160 ^{0} is suitable for Stirling engine working with (LTD), while the 90^0 is compatible with the engine working with a high-temperature difference (HTD).

2.2.5 The forth-order analysis (CFD analysis)

The movement due to the expansion and compression of the working fluid is the key point for getting work or power from the Stirling engine. The heat transfer, compressible flow, oscillating, transient, unsteady, turbulent or laminar and unsteady are the core physics processes controlling any produced engine power. Applying these physics with a suitable geometry that describing the engine dimensions to commercial software that adopts the computational fluid dynamics (CFD) modelling is basically called the fourth-order analysis. The computational fluid dynamics (CFD) modelling of the thermal performance of the Stirling engine is an effective tool to improve its design, efficiency and power output. The main steps that usually involved in the CFD modelling of Stirling engines are: 1- Import or draw the engine

geometry to the software. 2- Apply the suitable physics of the case study to the appropriate boundaries and identifying the moving parts of the geometry. 3- Mesh the whole geometry using suitable size mesh. 4- Use the FVM (Finite Volume Method) or the FEM (Finite Element Method) to solve the partial differential equations (governing equation). 5- The last step is describing the results in terms of various output parameters variation with time.

On the other hand, this approach is quite complex and expensive in computational time, in order to simulate the whole engine. In this computational fluid dynamics modelling the thermal equilibrium usually adopted in the porous media analysis for modelling the regenerator. The hypothesis reported by [4] was considered as a poor statement in an oscillating flow environment due to the temperature difference between the solid matrix and the working fluid.

Several studies have reported the use of CFD modelling to investigate the performance of Stirling engines.

Mahkamov modelled axisymmetric engine geometry using the k-e turbulence model to study the performance of a solar powered Stirling engine. Results predicted from this approach were more accurate than those produced by the (lower-order) methods [49]. Mahkamov developed a 3D CFD model for a Biomass Stirling engine to identify the parameters that cause a reduction in power output [50]. The CFD results shown an accuracy of 18% compared to the experimental ones. In this study, some recommendations were suggested on how to achieve significant improvement in the engine performance.

The adoption of 3D CFD modelling was also used by [51] and [52] to investigate the effect of the flow through the regenerator of a twin-power-piston γ Stirling engine on the engine

performance. The study concluded that the matrix material and matrix wire diameter of the regenerator had a major effect on the effectiveness of the γ Stirling engine performance.

Salazar et al. [53] and Chen et al. [54] developed a comprehensive study on β and γ Stirling engines using an axisymmetric CFD model and 3D CFD modelling respectively to study the working cycle. Both studies help with understanding the basic process of the engine cycle and predict engine power by defining the heat input. Results showed the heat transfer rates were much higher than those gained by a second-order model.

Lia et al. [55] conducted a 3D CFD study on the performance of alpha-type using a Ross mechanism technique which converts the dual piston motion into rotational motion. In this study, the regenerator was investigated and filled with porous-sheet heat exchangers. The results concluded that the low flow friction happened in the regular shaped micro-channel type porous-sheets regenerator, and thus it has the highest impact on the performance of the engine.

Chen et al. [56] carried out a parametric study on the low-temperature-differential γ-type Stirling engine, 3D CFD modelling was developed to determine the best design parameters that would enhance the engine performance in terms of power output and efficiency.

Costa et al. [57] conducted a 3D CFD study on different regenerator parameters, under oscillating flow conditions, to simulate the fluid flow through a wound-woven wire matrix regenerator. The results of this study predicted the pressure drop occurring in the regenerator, and its effect on the heat transfer characteristics of the Stirling engine's regenerators.

Costa et al. [58] presented another CFD model on woven wire matrix for a Stirling regenerator in order to investigate the effect of changing the porosity and flow condition, this study emphasized that the regenerator acts as thermal storage and plays an important role in terms of enhancing the engine power.

Alfarawi et al. [59] carried out a parametric study on Gamma-type Stirling engine, a 2 D CFD model was created to investigate the effect of dead volume and phase angle aiming to improve the engine performance. The CFD model was validated against experimental measurements with 9% difference in calculating the indicated power. Results showed that by using a phase angle of 105^{0} instead of 90^{0}, the engine indicated power can be increased from 700 W to 750 W.

2.2.6 Acceptable maximum deviation

The following points are summarised the previous review in terms of maximum deviation:

- In studies [33] and [34], the maximum deviation in the results between the model prediction and experimental data was 7.9 and 15% .
- Cheng et al. [35] found that the optimal results gave 20% deviation compared with the experimental results.
- The model results by Nepveu et al. [46] were compared to experimental measurements showing 21% deviation
- The results predicted from the CFD by Mahkamov [50] shown an accuracy of 18% compared to the experimental ones.

Based on [46], the maximum deviation in the results of the modelling in this work is 21% and it is considered to be an acceptable.

2.3 Design of V-type alpha Stirling engine prototype

This section presents a review on V-type alpha Stirling engine prototypes and the potential of upgrading commercially available existing engines to develop V-type alpha type Stirling engine.

Karabulut et al. [60] designed, built and tested a V- type alpha Stirling engine prototype with 129 cc swept volume in order to investigate the optimum performance at different operating conditions. The pressure varied from 1 to 4 bars with a temperature range of 600 ^{0}C to 1100 ^{0}C. The regenerator porosity was 0.7, using Chrome-Nickel woven wire as regenerator mesh. The cooling system was water-jacket shrouded the cooler while the electrical furnace was used to heat the heater walls. The study concluded that as the pressure and temperature increases the power increases, however, more increase in the pressure caused leakage in the system. The engine produced maximum power of 65 W at 1100 ^{0} C and 2.5 bar.

Çınar et al. [61] carried out an experimental investigation on V- type alpha Stirling engine, they manufactured and tested an engine having 98 cc swept volume. The test carried out in order to evaluate some operating parameters such as pressure and temperature which varied ranging from (1 to 4 bars) and (800 to 1000 ^{0}C) respectively. An electrical heater was used for heating while water-jacket circulated around the cooler. The maximum power produced from the engine was 30.7 W at 1000 ^{0}C, 3 bar and engine speed of 437 r.p.m.

Podesser designed and constructed an alpha-type Stirling engine[62]. The selection of this type was considered as cost reasonable and most of its parts can be easily produced. The engine was used for electricity production in rural villages and to was heated using biomass furnace The

crank mechanism used in the Stirling engine was that of a series produced engine for a motor cycle. The bore diameter of the cylinder of the power piston 140 mm and the stroke 51mm, which means the swept piston volume, is 840 cm^3. The engine power reached up to 3.2 kW with a charge pressure of 33 bar at engine speed = 600 r.p.m which was acceptable compare to the swept volume of the engine (large scale).

Batmaz and Üstün manufactured a V-type alpha Stirling engine having two heaters and one cooler. They provided a theoretical analysis based on the second order approach to design the engine configurations. The maximum power provided from the engine was 118 W with the input heat at 950 ^{0}C and charge pressure = 1 bar.

Demir and Güngör carried out an experimental study on V-type alpha Stirling, where the engine was designed, manufactured and tested by the authors [64]. The engine performance was evaluated under different operating conditions, producing power output of 31W with a charge pressure of 1.5 bar at a temperature of 1050 ^{0}C.

Upgrading a four-stroke Diesel to develop V-type alpha Stirling was conducted by Yusof et al. [65]. The design was considered simple and low cost, since the major components were taken from an existing engine. The total swept volume 97 cc and the operating conditions for the developed engine were: air as a working fluid, hot temperature from 550 to 650^0 C, cold temperature of 30^0 C, charge pressure changed above 1 bar and the speed of the engine = 1200 r.p.m. The engine was heated using swirl burner, and maximum power achieved 25 W at 1.4 bar and 1200 r.p.m.

Reducing manufacturing cost and engineering times were adopted in the work by Shiferaw et al. [11]. They converted a V-type block air compressor into a V-type alpha type Stirling engine with total swept volume of 176.32 cc (See Figure 2.3). A propane burner was used as a source of heat with heating temperature reached up to 423.8 ^{0}C, while ice was used on the top of the cooler to cool down the engine temperature to 29.3°C. The maximum speed was 1150 r.p.m and the power output was about 62 W.



Figure 2.3 "Compressor used for pistons of the Stirling engine" [11]

2.4 Review of previous work on regenerators

The pressure drop through the regenerator and thermal losses have a major effect on the indicated power of the Stirling engine. The pressure drop in small-scale Stirling engines leads to about 11% reduction in the power output while about 1.5% reduction occurs due to the thermal losses [57]. This section discusses the work reported on the Stirling engine regenerators including the pressure drop and the heat transfer capacity. The work also includes the correlations that determine the friction factor and heat transfer coefficient in the Stirling engine regenerators.

Friction factor f in regenerators is function of the pressure drop and it is defined as follows:

$$f = \left(\frac{\Delta P}{\frac{1}{2}\rho {U_m}^2} \right) \frac{D_H}{L} \qquad 2.4$$

Where,

ΔP The pressure drop through the regenerator, D_H Cross section diameters, ρ Density, U_m mean velocity of the working fluid and L the regenerator length.

Regenerator effectiveness eff or regenerator efficiency is defined as:

The ratio of the quantity of heat actually taken up by regenerator matrix in each cycle to the quantity theoretically possible with an ideal regenerator

$$eff = \frac{Heat\ actually\ absorbed}{Heat\ theoretically\ possible\ to\ absorb} \qquad 2.5$$

The effectiveness of the regenerator in terms of temperature of the gas entering and leaving the regenerator and the temperature of the heater and cooler is [67] :

$$eff = \frac{(\mathbf{T}\boldsymbol{h_i}) - (\mathbf{T}\boldsymbol{c_i})\boldsymbol{in}}{(\mathbf{T}\boldsymbol{h_i}) - \boldsymbol{min}(\mathbf{T}\boldsymbol{c_i})} \qquad 2.6$$

Where; $\mathbf{T}\boldsymbol{h_i}$ is the maximum (inlet) temperature at the hot blow of the cycle (first half of the cycle), $(\mathbf{T}\boldsymbol{c_i})\boldsymbol{in}$ is the inlet temperature at the cold blow of the cycle (second half of the cycle) and $\boldsymbol{min}(\mathbf{T}\boldsymbol{c_i})$ is the minimum temperature during the cold blow of the cycle .

It is important to notice that the regenerator effectiveness, as it is defined, does not take the fluid friction and pressure drop into account.

A detailed investigation of various regenerator parameters was performed by Chen et al [51] for improving the Stirling engine performance. The woven-screen material was chosen to fill the regenerator housing. The diameter of the woven wire, with the accumulating arrangements and the material type, were investigated. In this study, to achieve an enhancement on the engine

performance between 10% - 20%, it was suggested to use copper material instead of stainless steel, this work found that the ideal filling factor is 0.00206. The study also concluded that the large pressure drop was due to choosing small wire diameter that led to reduction in the regenerator effectiveness.

Isshiki et al [68] used a small alpha-type Stirling engine driven by Yoke-Ross to test N-5 stainless steel wound wire-mesh and was found the performance of the engine improved up to 17%. Large beta-type Stirling engine (1.7 Litre swept volume) was also tested in this study, the type of regenerator was layered-plate with N-5 stainless steel wire mesh. In this test, the performance of the engine was improved by 36%. Furthermore, the study concluded that using low temperature difference of the layered-plate type regenerator produced higher power in comparison with the conventional wire-mesh.

An experimental test facility was designed in [69] using a 180° phase angle alpha-type Stirling engine approach to study the effect of the flow characteristics on the regenerator effectiveness. The hot blow was produced by passing the air via an electrical heater while the cold blow drove via an air conditioning system. The test section was filled with N-18 stainless steel and polyurethane foam. The oscillation in the temperature measurement between the two ends of the regenerator was used to calculate the regenerator effectiveness. It was found that the stainless steel mesh effectiveness, which has parallel layer to the fluid flow direction, was lower than the polyurethane foam, in contrast, the pressure drop was higher in the polyurethane foam than the stainless steel mesh.

A numerical study was conducted by [70] on the effect of changing the porosity and the mesh size of the regenerator on the pressure drop, heat transfer coefficient and regenerator effectiveness. The results were inserted into an alpha-type Stirling engine model with 180^0 phase angle. The study concluded increasing the length of regenerator leads to decreasing in pressure drop which the consequences a decreasing in break power of the engine. Pressure drop

in oscillatory flow is nearly doubles compare to pressure drop in steady one directional flow. Regenerator effectiveness increases with mesh size with expense of pressure drop.

An experimental investigation to find the best porosity for different regenerator matrix material was carried out by Gheith et al [71]. Aluminium, Monel 400, stainless steel and copper were tested in this study. Results initially showed that the optimum engine performance can be reached by using stainless steel with 85% as a regenerator matrix. They carried out a parametric study on five different porosities (0.75, 0.80, 0.85, 0.90 and 0.95) for the stainless steel matrix in order to reduce the pressure drop and increase the heat transfer coefficient. They found that the best engine performance can be achieved by using the stainless steel matrix regenerator with a porosity of 0.85.

Tanaka et al. [72] studied experimentally the heat transfer and flow characteristics in different regenerator matrixes such as sintered metal, sponge metal and stacked woven wire matrix. The flow was an oscillatory flow and pressure and temperature were measured at the hot and cold sides of the test sections flow (See Figure 2.4). The effect of the porosity was also included in this study in terms of changing the wire diameter. The study reported that the friction factor in the two directions flow was higher than that from one direction flow by 30%. Empirical correlations were developed from the study to estimate the pressure drop and Nusselt number for all regenerator matrixes, which were widely used by other authors.

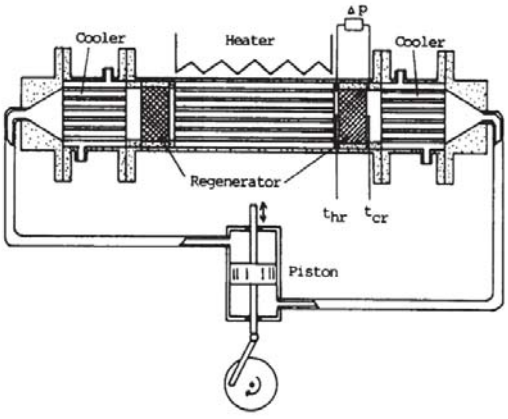


Figure 2.4 “Experimental apparatus” [72]

The empirical correlations for friction factor and Nusselt number for regenerator matrixes were also conducted by [73]. The research was supported by NASA and these correlations were used by many authors as a reference to validate their results. The samples of regenerator matrixes used were the woven wire mesh (screen and stacked) matrices in addition to the metal felt.

The following equation Eq. (2.7) is provided as an example to show how the friction factor correlations for the Woven Screens and Metal Felts matrices were estimated, while the Nusselt number correlations can be found in [73] .

$$f = \frac{a_1}{R_e} + a_2 {R_e}^{a_3} \qquad 2.7$$

Where,

R_e Reynolds number while "the estimated parameters (a1, a2, a3) appear in the following tables for the various matrices tested" [73]: (See Table 2.1 and Table 2.2)

Table 2.1 "Estimated parameters (a1, a2, a3) for Woven Screens" [73]

Woven Screens	200 mesh	100 mesh	80 mesh
a_1	129.3 ± 0.3	138.9 ± 0.5	120.1 ± 0.5
a_2	2.990 ± 0.038	2.567 ± 0.020	2.369 ± 0.020
a_3	-0.0758 ± 0.0019	-0.0816 ± 0.0010	-0.0836 ± 0.0010
R_{em} range	0.45 — 1700	0.88 — 5200	2.2 — 6100
V_a range	0.0052 — 3.0	0.026 — 17	0.042 — 21
δ/L range	0.028 — 2.2	0.087 — 1.2	0.079 — 0.95

± values are 90% confidence intervals

Table 2.2 "Estimated parameters (a1, a2, a3) for Metal Felts" [73]

Metal Felts	2.0 mil	1.5 mil (top)	1.5 mil (mid)
a_1	120.7 ± 0.5	214.1 ± 0.6	239.1 ± 0.7
a_2	3.730 ± 0.033	6.629 ± 0.068	8.295 ± 0.071
a_3	-0.0627 ± 0.0013	-0.0703 ± 0.0016	-0.0903 ± 0.0013
R_{em} range	0.83 — 2500	0.67 — 1500	0.36 — 1800
V_a range	0.015 — 5.2	0.012 — 3.7	0.005 — 5.6
δ/L range	0.19 — 2.6	0.19 — 2.4	0.15 — 2.6
	1 mil	0.5 mil	
a_1	213.8 ± 0.5	211.6 ± 0.7	
a_2	4.514 ± 0.041	4.217 ± 0.064	
a_3	-0.0705 ± 0.0014	-0.0651 ± 0.0024	
R_{em} range	0.21 — 1800	0.11 — 900	
V_a range	0.0056 — 5.3	0.0021 — 1.6	
δ/L range	0.043 — 1.3	0.102 — 2.2	

± values are 90% confidence intervals

Costa et al [74] and [6] conducted friction pressure drop and Nusselt number correlations respectively for a wound woven wire regenerator using 3D CFD modelling approach investigation with Reynolds number covering the laminar flow regime. The experimental published data by Tanaka et al. [72] and [73] were used to validate the CFD model as shown in Figure 2.5 and Figure 2.6 with an average deviation of 2.6%. Both studies concluded that the developed correlations from combining the CFD model with experimental can be used to predict the flow and heat transfer characterisations for the wound woven wire matrix.

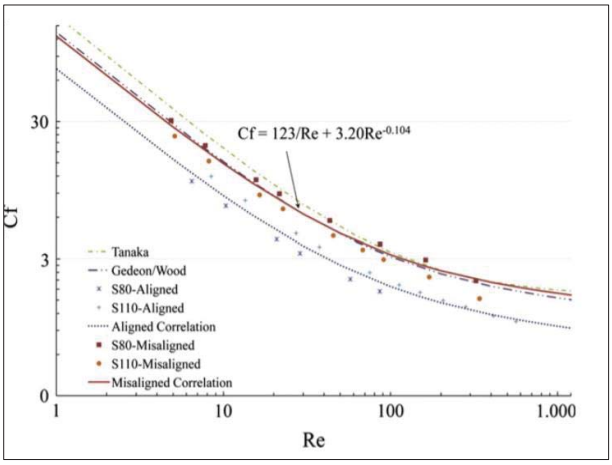


Figure 2.5 "Stacked woven wire matrices: friction factor vs. Reynolds number" [74]

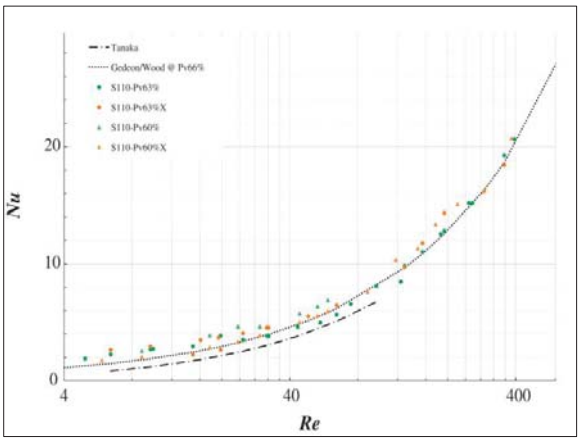


Figure 2.6 "Stacked woven wire matrices for 110 μm wire diameter: Nusselt number versus" Reynolds number [6]

A thin porous-sheet regenerator was developed by Takizawa et al [75] to enhance the performance of the Stirling engine, the porous-sheet has a rectangular cross-section shape to minimise the pressure drop. The developed regenerator was fitted to a Stirling engine type (NS03T), which was usually using the commercial screen wire-sheet type 200 M. A comparison was performed between using the developed regenerator and that with the commercial regenerator showing an enhancement by 15% on the engine performance with thin porous-sheet regenerator.

Caney et al [76] carried out experimental work on square mini-channel with (1 mm and 420 mm long) to investigate heat transfer and flow friction losses in the regenerator using Reynolds number ranged from 310 to 7780. They applied different ranges of heat fluxes in this experimental work and the temperature was measured along the channel walls, while it was difficult to measure the temperature inside the channel. The results showed that the pressure drop in this investigation behaved similarly to that from the conventional correlations.

A theoretical analysis conducted by Lia et al. [55] on a hexagonal-channels porous-sheet regenerator (each side = 4 mm with length = 73 mm) using CFD simulation to study the effect of flow and heat transfer in the regenerator on alpha-type Stirling engine. The results showed that the high performance of the model Stirling engine can be attributed to the low frictional loss and the excellent heat transfer characteristics, as well as the compact heat exchanger design that significantly reduces the dead volume. The flow friction happened in the regular shaped micro-channel type porous-sheets regenerator was low compared to that for the wire mesh, while the thermal effectiveness maintaining the same or higher in the regular shaped micro-channel. It can be concluded that the flow friction has the highest impact on the performance of the engine.

Alfarawi et al. [77] conducted an experimental and CFD study for three mini-channels (0.5, 1.0 and 1.5 mm) regenerators having an annuals gab to investigate flow friction and heat transfer. The test rig was built to study the unidirectional flow only, and the temperatures were measured at inlet, outlet and along the channel walls, while they were found a difficulty to measure the temperature inside the channel, also the pressure drop was recorded in this test. A 3D sector geometry was created for each configuration and imported to the developed CFD model. The authors compared their approach with the single-blow method approach in terms of results validation (See Table 2.3). Their results showed that the regenerator with 0.5 mm diameter had the highest heat transfer coefficient, but the pressure drop was highest. The study suggested that using segmentation will decrease the axial and radial conduction losses and the pressure drop.

Table 2.3 “Comparison between current testing technique and single-blow method” [77]

Condition	Transient testing technique	
	Current technique	Single-blow method
Inlet temperature	Arbitrary change	Step change
Fluid properties	Temperature dependent	Constant
Steady-state	Not required	Required
Thermal losses	Included (non-adiabatic walls, radial and axial conduction)	Non-adiabatic walls and axial conduction can be included
Numerical model	CFD (Conjugate heat transfer)	Analytical (Schumann-Hausen model)
Evaluation technique	Direct curve matching	Depends on NTU value but maximum slope method is recommended

The axial conduction losses in a parallel-wire type regenerator were studied by [78], these losses are common in tube bundles and parallel plates. In this investigation, the friction factor in the parallel-wire type regenerator was lower than that of the conventional wire-mesh regenerator and that leads to low-pressure drop, but on the other hand, the thermal performance of the parallel-wire was poor. The study suggested segmenting the wires in term of reducing the axial conduction losses. The study also mentioned the number of housing will increase duo to this segmentation which should be taken into consideration. The effect of segmentation clearly observed on the regenerator performance when the parallel wire geometry was segmented to 3 and then to 7 parts. The study concluded that the segmentation enhanced the regenerator performance and reduced the axial conduction losses.

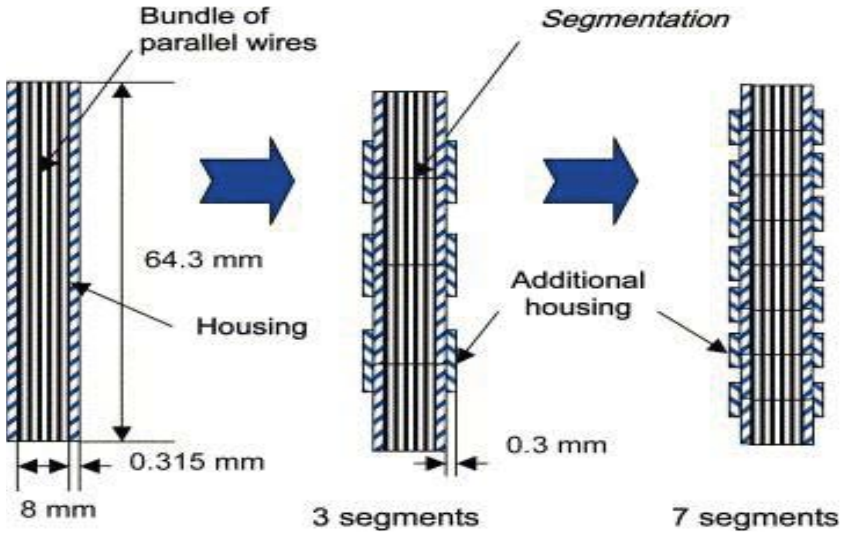


Figure 2.7 “Schematic diagram of the segmented parallel wire regenerator” [78]

The effect of segmentation was also reported in the study by Ibrahim et al [79] when they developed and analysed a segmented-foiled regenerator using the LiGA technique to fabricate the segmented regenerator which was considered as an expensive technique. The main aim of using the segmentation was to reduce both the pressure drop and the axial conduction losses. The results were considered to be close to the case of using an ideal parallel-plate regenerator.

Tao et al [80] carried out segmentation works in order to improve the regenerator heat transfer performance numerically and to study the pressure drop through the regenerator. Stainless steel metal mesh matrix with different porosities was used to fill the regenerator housing in this investigation. They designed multi-segments metal mesh regenerators and found that the segmentations have a direct impact on the axial heat conduction. The study concluded that the performance of the regenerator can be improved by increasing the number of regenerator segments.

2.5 Review summary and knowledge gap

The previous review can be summarised in the following points:

- The V alpha-type Stirling engines, offer a major advantage in terms of their ability to separate the heat rejected and heat source volumes, thus no early mixing of the hot and cold working fluid. Despite these advantages, there has been no reported work on advanced modelling for such engines, particularly the 3D CFD modelling and the use of this modelling to improve the design parameters of the engine. Additionally, the approach of combining the thermodynamic modelling with the 3D CFD analysis for improving the performance of the V alpha-type Stirling engines was not reported in the open literature.

- The experimental measurements combined with the CFD modelling for a segmented-micro channel regenerator (parallel-geometry regenerator) in oscillatory flow for V alpha-type Stirling engine has not been reported yet in literature. All previous studies [55], [76], [77] were on using the parallel-geometry and without including the effect of segmentations.

- Very limited work on the development of micro-channels regenerators and their impacts on heat transfer, pressure drop and engine performance.

- Finally, using CFD modelling approach to investigate the routes of upgrading commercially available existing engines to develop V-type alpha type Stirling engine has not been reported in the open literature.

CHAPTER 3

THERMODYNAMIC AND CFD MODELLING FOR V-TYPE ALPHA STIRLING ENGINE

Part of the work presented in this chapter has already been published in [83] as:

A. K. Almajri, S. Mahmoud, and R. Al-Dadah, "Modelling and parametric study of an efficient Alpha type Stirling engine performance based on 3D CFD analysis," *Energy Convers. Manag.*, vol. 145, 2017.

Almajri is the lead author, he has made the most significant contribution to the research including design, analysis and interpretation of data. He has written and edited a major part of the work, he also takes charge of getting approval from all the other authors and communicating with the journal.

Mahmoud and Al-Dadah fulfil the following criteria: Contribute to the conception, design, analysis and interpretation of data. Participate in drafting and help revising the manuscript for intellectual content. Approve of the version to be published.

3.1 Introduction

The alpha-type Stirling engine offers design simplicity compared to other types of Stirling engines in terms of clear separation between the heat source volume and that of the heat rejected one which avoids the possibility of early mixing between the hot and cold working fluid [11]. Modelling the engine performance is a very powerful tool that can be used to assess the effects of various engine parameters on its performance leading to improved designs with higher efficiencies and power outputs. A number of studies have been conducted to develop empirical

correlations for the estimation of engine power and efficiency [17], [81], [82] . Also, various studies were published using computational fluid dynamics (CFD) modelling to achieve more in depth analysis for engines performance and the effects of various parameters [49], [53], [56].

This chapter describes the thermodynamic and CFD modelling for a V alpha-type Stirling engine. Results from the developed models were compared to published experimental data [60] for validations. Figure 3.1 shows schematic and pictorial diagrams of the alpha type engine Stirling engine used in this study as reported by [60].

The engine consists of a crankcase with two pistons positioned at a phase angle of 90^0. The heater and cooler were placed on the top of the pistons, with a water jacket added around the cooler volume while a furnace was used to heat up the volume of the heater. The regenerator was placed between the two heat exchangers with connecting pipes. The regenerator was made of Chrome-Nickel woven wire of 100 μm wire diameter with 70% volumetric porosity. Table 3.1 lists the dimensions and specifications of this engine.

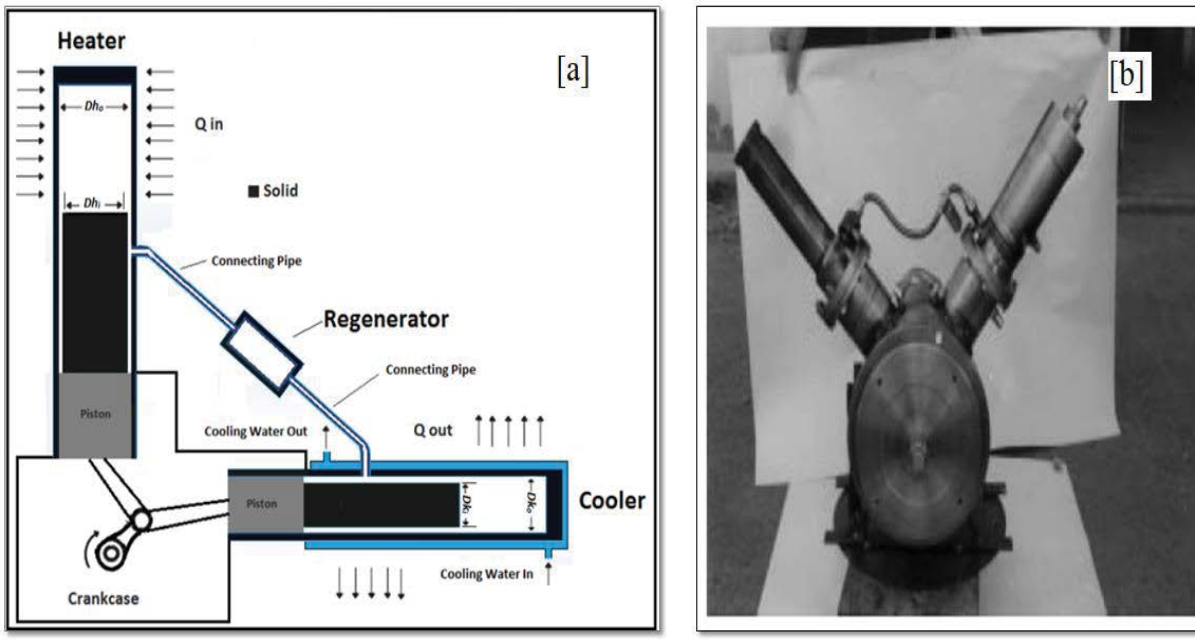


Figure 3.1: [a] Schematic diagram [b] Pictorial diagram taken from [60]

Table 3.1 Stirling engine specifications and operating conditions [60]

Parameter	**Value**
Engine type	Alpha α (V)
Cylinder bore	52.4 mm
Cylinder Stroke	60 mm
Swept volume	129.39 cm^3
Phase angle Working gas Air	90 ^{0}
Length of the connecting pipe	155 mm
Diameter of the connecting pipe	5 mm
Heater outer diameter	46 mm
Heater inner diameter	40 mm
Cooler outer diameter	32 mm
Cooler inner diameter	25 mm
Length of the heater	100 mm
Length of the cooler	120 mm
Total dead volume	108 cm^3
Max. engine speed	850 rpm
Cooling	Water
Working fluid	Air
Type of the cooler	water jacket
Type of the heater	Annulus
Type of the regenerator's matrix	woven wire
Wire diameter (Micron)	100 Chrome-Nickel
Porosity	70%
Inlet water temperature	20 (°C)
Hot source temperature	1100 (°C)
Charge pressure	1,2,2.5 (bar)

3.2 Thermodynamic analysis model

The engine thermodynamic model is divided into seven volumes: compression, cooler, connecting pipe, regenerator, connecting pipe, heater and expansion (c, k1, k2, r, h1, h2, e) respectively, as shown in Figure 3.2. The compression and expansion volumes are assumed adiabatic while the flow through the six interfaces between the volumes (ck1, k1k2, k2r, rh1, h1h2, h2e) is assumed to be Quasi-steady flow [82]. Energy is transferred through the interfaces of the cells by changing the enthalpy in terms of mass flow and the upstream temperature. Based on Berchowitz and Urieli approach [39], ordinary differential equations can be solved consecutively by giving initial arbitrary value and then integrated until reaching the steady state. The thermodynamic model was developed using Matlab software to investigate the initial Stirling engine performance. Figure 3.3 shows the flow chart for the Matlab's code of engine thermodynamic analysis. (The MATLAB code is included in Appendix B)

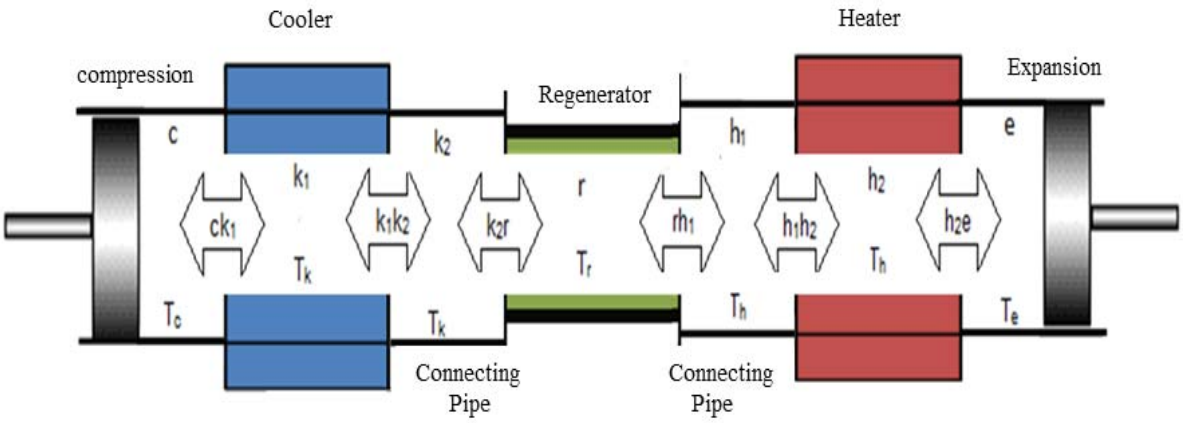


Figure 3.2 Schematic diagram of the adiabatic model with seven engine parts

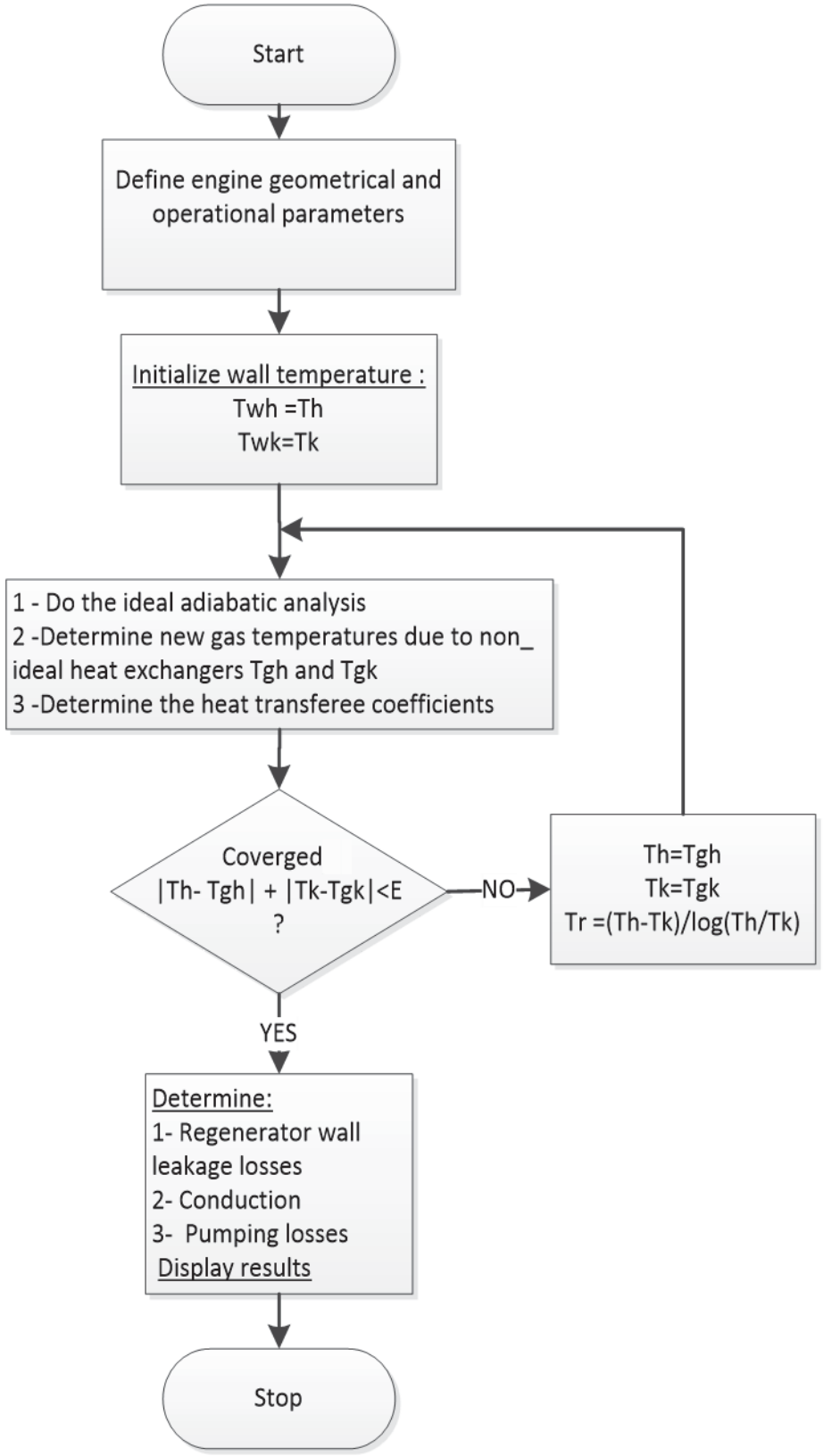


Figure 3.3 Flow chart for the Matlab code

The variation of compression and expansion volumes are estimated using compression and expansion swept volumes, V_{SC} and V_{SE}, described by Eq. (3.1 and 3.2):

$$Ve = CVE + \frac{V_{SE}}{2}[1 + cos(90 + \alpha)] \quad 3.1$$

$$Vc = CVC + \frac{V_{SC}}{2}[1 + cos(\alpha)] \quad 3.2$$

The pressure is considered to be uniform throughout the whole engine spaces and the working gas is an ideal gas.

$$p = mR/(\frac{V_c}{T_c} + \frac{V_{k1}}{T_k} + \frac{V_{k2}}{T_k} + \frac{V_r}{T_r} + \frac{V_{h1}}{T_h} + \frac{V_{h2}}{T_h} + \frac{V_e}{T_e}) \quad 3.3$$

The change in pressure is obtained from equation Eq. (3.4) as:

$$dp = -\left[\frac{\gamma p[(dV_c/T_{ck1}) + (dV_e/T_{h2e})]}{\frac{V_c}{T_{ck1}} + \gamma(\frac{V_{k1}}{T_k} + \frac{V_{k2}}{T_k} + \frac{V_r}{T_r} + \frac{V_{h1}}{T_h} + \frac{V_{h2}}{T_h}) + \frac{V_e}{T_{h2e}}}\right] \quad 3.4$$

The temperature is assumed to change linearly between the cold and hot sides of the regenerator as shown in Figure 3.4.

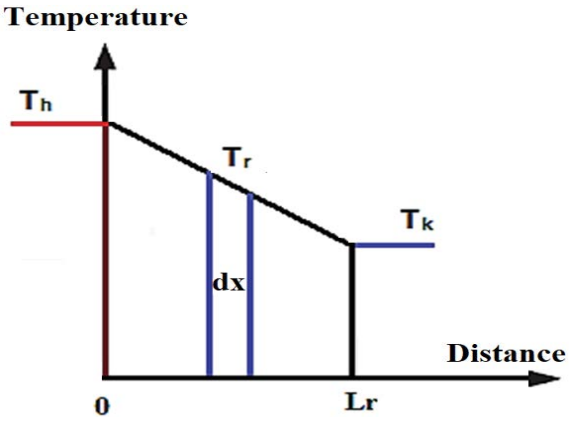


Figure 3.4 Linear temperature profile of regenerator

Hence, the regenerator temperature T_r can be calculated by:

$$T_r = (T_h - T_k)/ln(T_h/T_k) \quad 3.5$$

The change in mass through the heat exchangers can be determined from the equation of state as:

$$m_i = \frac{pV_i}{RT_i};\ i = h_1, h_2, r, k_1\ k_2 \quad 3.6$$

At the same time, the accumulation of mass in the expansion and compression parts can be defined as:

$$dm_e = (pdV_e + V_e dp/\gamma)/RT_{h2e} \quad 3.7$$

$$dm_c = (pdV_c + V_c dp/\gamma)/RT_{ck1} \quad 3.8$$

The direction of the flow can be stated as:

$$\text{if } \dot{m}_{he} > 0\ then\ T_{h2e} = T_h \text{ else } T_{h2e} = T_e \quad 3.9$$

$$\text{if } \dot{m}_{ck} > 0\ then\ T_{ck1} = T_c \text{ else } T_{ck1} = T_k \quad 3.10$$

The mass flow rate for each part's interfaces can be calculated as:

$$\dot{m}_{ck1} = -dm_c/dt \quad 3.11$$

$$\dot{m}_{ck1} = -dm_c/dt \quad 3.12$$

$$\dot{m}_{k2r} = -\dot{m}_{k1k2} - dm_{k2}/dt \quad 3.13$$

$$\dot{m}_{rh1} = -\dot{m}_{k2r} - dm_r/dt\, dm_{h1}/dt \quad 3.14$$

$$\dot{m}_{h1h2} = -\dot{m}_{rh1} - dm_{h1}/dt \quad 3.15$$

$$\dot{m}_{h2e} = -\dot{m}_{h1h2} - dm_{h2}/dt \quad 3.16$$

Cyclic temperature compression and expansion space are calculated in the differential form of using the state equation:

$$dT_i = T_i(dp/p + dV_i/V_i - dm_i/m_i);\ i = e, c \quad 3.17$$

By applying the first law of thermodynamics of heat transfer on the heat exchangers:

$$dQ_h = \frac{c_v V_{h2} dp}{R} - c_p(T_h \dot{m}_{rh1h2} - T_e \dot{m}_{h2e}) \quad 3.18$$

$$Q_r = \frac{c_v V_r dp}{R} - c_p(T_k \dot{m}_{k2r} - T_h \dot{m}_{rh1}) \quad 3.19$$

$$dQ_k = \frac{c_v V_{k1} dp}{R} - c_p(T_c \dot{m}_{ck1} - T_k \dot{m}_{k1k2}) \quad 3.20$$

Over the cycle:

The heat absorbed by the heater:

$$Q_h = \oint \delta Q_h \quad 3.21$$

The heat rejected from the cooler:

$$Q_k = \oint \delta Q_k \quad 3.22$$

The indicated work:

$$W_i = \oint p\, dV_e + \oint p\, dV_c \quad (3.23)$$

The engine's indicated power $\dot{W}_I$ can be determined in terms of engine speed (n) and the engine work indicated power:

$$\dot{W}_i = W_i\left(\frac{n}{60}\right) \quad (3.24)$$

The following equations show the calculations for the shaft power:

The actual heat rejected from the cooler:

$$Q_k = \frac{60}{n}(h_{k1}A_{k1} + h_{k2}A_{k2})(T_{wk} - T_k) + Q_{r,loss} \quad (3.25)$$

Thus, the actual heat absorbed by the heater:

$$Q_h = \frac{60}{n}(h_{h1}A_{h1} + h_{h2}A_{k2})(T_{wh} - T_h) - Q_{r,loss} \quad (3.26)$$

The heat loss in the regenerator (imperfect regenerator) can be calculated as:

$$Q_{r,loss} = (1-\varepsilon)\left(Q_{r,max} - Q_{r,min}\right) \quad (3.27)$$

3.2.1 Losses modelling

The effectiveness of the regenerator ε defined by Eq.(3.27) has a direct effect on the actual heat transfer to the regenerator and it can be calculated based on NTU as:

$$\varepsilon = NTU/(1+NTU) \quad 3.28$$

Where, NTU is function of Nusselt number, Nu based on [84].

$$NTU = 4Nu(lr/dr)/(RePr) \quad 3.29$$

[84] presented more details for the correlation of the friction-factor for woven matrix and its parameters (a1, a2, a3), these correlations are based on oscillatory flow.

$$Nu = 1 + b_1(RePr)^{b_2} \quad 3.30$$

$$f = \frac{a_1}{R_e} + a_2 {R_e}^{a_3} \quad 3.31$$

The heat losses in the regenerator due to internal conduction can be calculated from:

$$Q_{d,loss} = \frac{k_r A_r}{l_r}(T_h - T_k) \quad 3.32$$

The shuttle losses due to oscillatory motion of the piston can be calculated as:

$$Q_{sh,loss} = \frac{0.4 {Z_d}^2 k_d D_d}{J_d l_d}(T_e - T_c) \quad 3.33$$

The actual heat transferred to the cooler and the heater:

$$Q_{act,k} = Q_k + Q_{d,loss} + Q_{sh,loss} \quad 3.34$$

$$Q_{act,h} = Q_h + Q_{d,loss} + Q_{sh,loss} \quad 3.35$$

The work loss function in the pressure drop in all five parts can be obtained by:

$$W_{loss} = \oint \Delta p_i \, dV_e \tag{3.36}$$

Where, the pressure drop determines as [85]:

$$\Delta p_i = -2 f_r \mu u \left(\frac{V_i}{A_i {d_i}^2} \right); \; k_1, k_2, r, h_1, h_2 \tag{3.37}$$

The Reynolds friction factor (f_r) is a function of Darcy friction factors and Reynolds number:

$$f_r = \left(\frac{f_D}{4}\right) Re \tag{3.38}$$

Friction factor evaluated by [86] as function of Reynolds number as following:

If Re < 2000

$$f_D = \frac{64}{Re} \tag{3.39}$$

If 2000 < Re < 20000

$$f_D = 0.316 Re^{-0.25} \tag{3.40}$$

If Re >20000

$$f_D = 0.184 Re^{-0.2} \tag{3.41}$$

The forced work per cycle $\bar{W}$ (as in Figure 3.5) calculated as:

$$\bar{W} = \oint [(p - p_{ch}) \, dV] \tag{3.42}$$

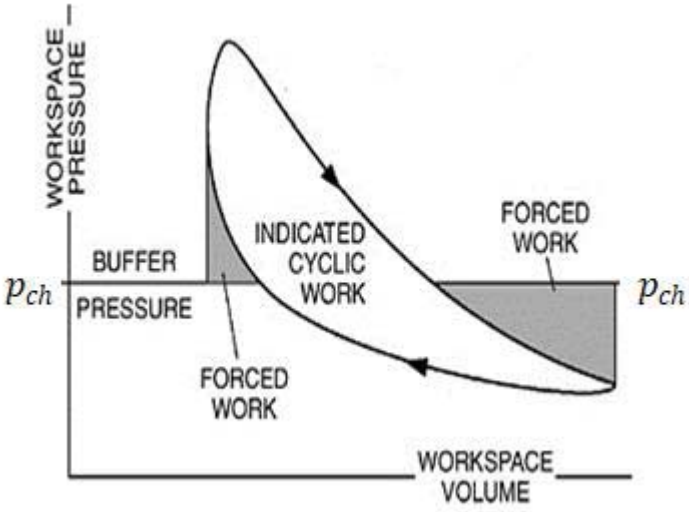


Figure 3.5 Forced work [87]

From Senft's theory [87], the indicated work and forced work used to calculate the shaft work of the engine as:

$$W_s = E(W_i - W_{loss}) - (1/E - E)\overline{W} \qquad 3.43$$

The value of the mechanism effectiveness E ranged between 0.7 t- 0.9. Using the engine experimental data with a trial and errors process, the value of the mechanism effectiveness E in Eq. (3.43) is decided to be 0.75.

The engine shaft power $\dot{W}_s$ can be calculated in terms of the engine speed and the work shaft power of the engine:

$$\dot{W}_s = W_s\left(\frac{n}{60}\right) \qquad 3.44$$

3.2.2 Thermodynamic model validation

Figure 3.6 compares the results from the thermodynamic model to the experimental in terms of shaft power at three different charge pressures 1, 2 and 2.5 bar and engine speed ranging from 100-800 RPM as reported by [60].

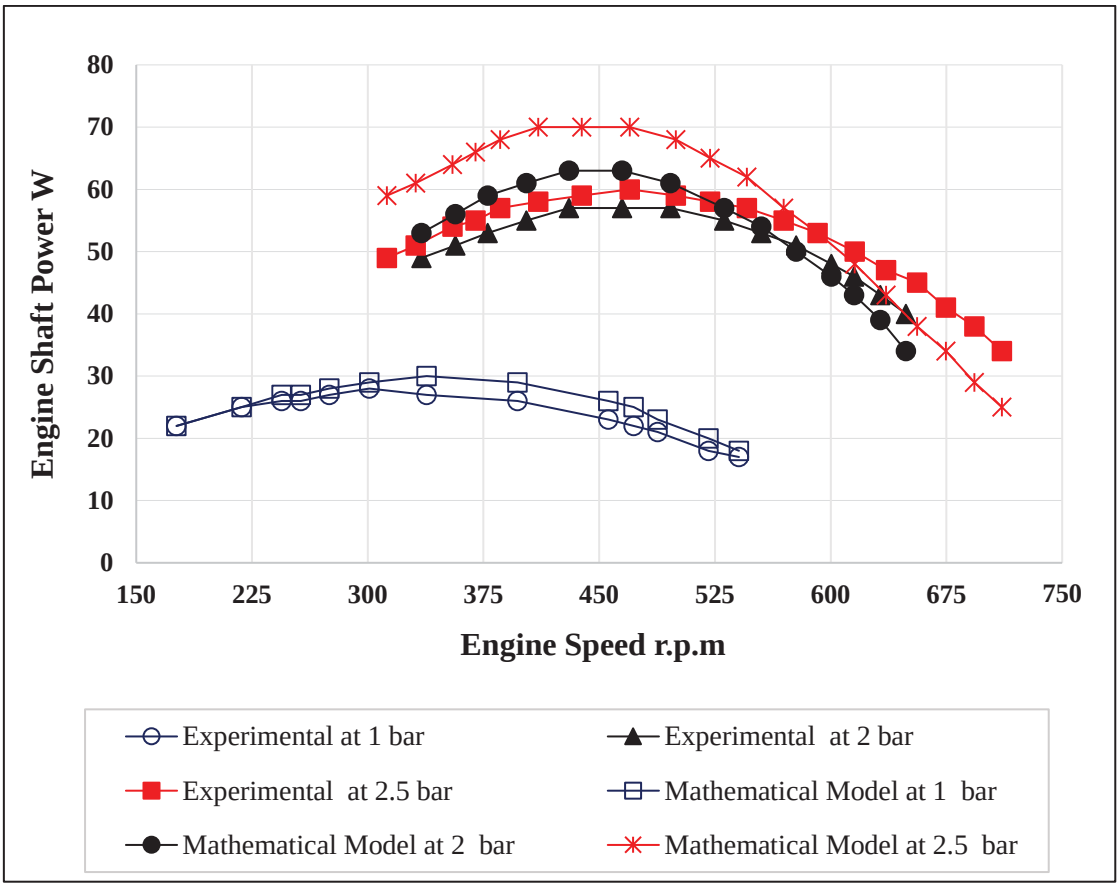


Figure 3.6 Comparison of shaft power between the mathematical model and experiment at fixed charge pressure and different engine speed

Results showed deviation values from 3.7% to 12 % at 1 bar, from 2% to 10% at 2 bar and from 3.5% to 18% at 2.5 bar. The maximum deviation of the model prediction is lower than that deviation from the open literature (See Chapter 2, Section 2.2.6). It is worth mentioning that the increased deviation at higher charging pressure is attributed to the leakage reported by the authors [60].

3.3 Engine CFD modelling

This section describes the developed CFD model that simulates the V alpha-type Stirling engine reported by Karabulut et al. [60]. Commercial comprehensive simulation software (Comsol multiphysics 5.3) was chosen to develop this CFD model. In the beginning, the modelling of porous media, moving meshing and the governing equations will be presented in the features of the Comsol setting. This including the approaches applied for the regenerator to be treated as porous media. Then applying boundary conditions, meshing methods and structure of solution will be discussed. Presenting the model validation against experimental data and a parametric study using the developed CFD model will also be presented.

3.3.1 Heat transfer in porous media

There are two common approaches in general used in porous media; the (LTE) local thermal equilibrium and the (LTNE) and local thermal non-equilibrium models. Their accuracy is depending on their field and its specification.

3.3.1.1 Local thermal equilibrium

This approach is used to model heat transfer in porous media when it is taken into account that the temperatures are equal in both the fluid and the solid. Only a single energy equation is used when endless heat transfer occurs between the fluid phase and the solid phase. The (LTE) approach treats the stable conduction issues with slow movement when the volumetric internal heating in both materials does not change [88]. However, in this approach where the local temperature difference between the solid and fluid phases is zero, this means the radial heat transfer is therefore negligent thus generates entropy.

The (LTE) approach was reported in many researches to model the Stirling regenerator. Experimental and numerical results by Schreiber [89] and Sage [90] respectively on a wire-

screen Stirling regenerator, concluded that there are variance between the solid phase and the working fluid phase. This demonstrates that the local thermal equilibrium is inconvenient in oscillating-flow medium and heat applications such as regenerators in Stirling engines.

The disregarding of enthalpy-flux losses in the regenerator is another shortcoming of this approach [91]. This demand that the capacity of the heat of solid is unlimited compared to the gas's ability to accurately evaluate.

The energy equation is subedited as:

$$(\rho C_p)_{eff}\frac{\partial T}{\partial t} + \rho C_p \boldsymbol{u}.\nabla T + (\nabla.\left(-k_{eff}\nabla T\right)) = Q \qquad 3.45$$

The effective thermal conductivity, k_{eff} can be calculated for an isotropic environment by three models; power law model, reciprocal average model and volume average model and they are explained in [92]. The effective heat capacity, $(\rho C_p)_{eff}$ calculated based on the volume fractions of the solid and the fluid.

3.3.1.2 Local thermal non-equilibrium

This approach is used to model heat transfer in porous media when it is taken into account that the temperatures are not equal in both fluid and the matrix of porous domain. The normal equations of heat transfer are used in this approach as a governing equations and they are needed to be multiplied by θ_p and $(1-\theta_p)$, and with an additional quantitative source factor to exchange the heat between the porous matrix and the fluid [92]

$$\theta_p \rho_s C_{ps}\frac{\partial T_s}{\partial t} + \nabla.(-\theta_p k_s \nabla T_s) = q_{sf}\left(T_f - T_s\right) + \theta_p Q_s \qquad 3.46$$

$$(1-\theta_p)\rho_f C_{pf}\frac{\partial T_f}{\partial t} + (1-\theta_p)\rho_f C_{pf}\boldsymbol{u}_f \nabla T_f + \nabla.(-(1-\theta_p)k_f \nabla T_f) = q_{sf}\left(T_s - T_f\right) + (1-\theta_p)Q_f \qquad 3.47$$

Where,

θ_p is the fraction of the solid volume.

ρ_s is the density of the solid (kg/m^3).

ρ_f is the density of the fluid (kg/m^3).

C_{ps} is the heat capacity of the solid at constant pressure (J/kg·K).

C_{pf} is the heat capacity of the fluid at constant pressure (J/kg·K).

k_s is the thermal conductivity of the solid (W/m·K).

k_f is the thermal conductivity of the fluid (W/m·K).

q_{sf} is the interstitial coefficient of convective heat transfer (W/m^3·K).

Q_s is the heat source of the solid (W/m^3).

Q_f is the heat source of the fluid (W/m^3).

$\mathbf{u}_f$ is vector of the fluid velocity (m/s)..

$\mathbf{u}_p$ the porous velocity (interstitial fluid velocity and it is taken from the porous domain of the CFD model) (m/s).[93].

The velocity of the fluid is calculated from θ_p the solid volume fraction and $\mathbf{u}_p$ the porous velocity (interstitial fluid velocity), and according to [94] , it comes from Brinkman equations or Darcy's law:

$$\boldsymbol{u}_f = \frac{\boldsymbol{u}_p}{1 - \theta_p} \qquad 3.48$$

By substitution Eq. (3.48) in Eq. (3.47) then the heat transfer equation in the fluid domain can be rewritten as:

$$(1-\theta_p)\rho_f C_{pf}\frac{\partial T_f}{\partial t}+\rho_f C_{pf}\boldsymbol{u}_p\nabla T_f+\nabla.(-(1-\theta_p)k_f\nabla T_f) = \mathrm{q}_{sf}(T_s-T_f)+(1-\theta_p)Q_f \quad 3.49$$

The two terms in Eq. (3.46) and Eq. (3.49), $\mathrm{q}_{sf}(T_f-T_s)$ and $\mathrm{q}_{sf}(T_s-T_f)$ respectively are called heat rates, and they can be released or received from one phase to another depending on the temperatures difference in the porous domain.

The interstitial convective heat transfer coefficient, q_{sf} can be determined from:

$$\mathrm{q}_{sf}=a_{sf}h_{sf} \quad 3.50$$

Where, a_{sf} is the specific surface area of the solid and h_{sf} is the heat transfer coefficient. The h_{sf} evaluation depends on the porous matrix type and configurations, and then a suitable correlation can be chosen from the point of view of its definitions.

3.3.2 Moving mesh

In the CFD simulation of moving meshes for the Stirling engine, it is necessary to use a combination of algorithms to imitate the domain deformation that occurs by the movement of the pistons due to the compression and expansion of the gas. Lagrangian and Euler formulations are known as classical algorithms, and they can be used to describe this motion[95] and [96]. The choice between them depends on the domain space, moving boundaries or spaces, speed and physics. For small movement or small displacement, and then the liquid is limited, Lagrangian approach can be adequate. The Eulerian can be used for a non-moving boundary in the flow model that does not have a free surface. This is because of the spatial points are changed with the time and creating high deformity when they follow the motion.

3.3.3 Governing equations and solution methodology

COMSOL-Multiphysics [93] software was used to develop the engine model and investigate the effects of various geometric parameters and operating conditions on its performance. The model is based on a realistic non-isothermal flow (NITF) which is suitable for the porous domain in the engine regenerator. In this model the geometries of the engine parts were created as a 3D CAD model using SolidWorks and then imported into COMSOL software. (Table 3.1 shows all of the dimensions required to draw the geometries of the engine parts). The engine operating conditions, charge pressure, regenerator properties and other constant parameters were inserted as a table and defined as parameters. Another table containing the engine variables like pistons displacements and velocities, compression and expansion volumes, phase angle and crank angle, total volume was also inserted. In the material and properties section the different domains for all parts of the engine were defined, with air as the working fluid, copper for the connecting pipes and steel for the other engine parts. Figure 3.7 shows a symmetric view of the solid and fluid domains of the engine model. The next step is adding physics to the geometry with time dependent equations selected and the boundary conditions defined.

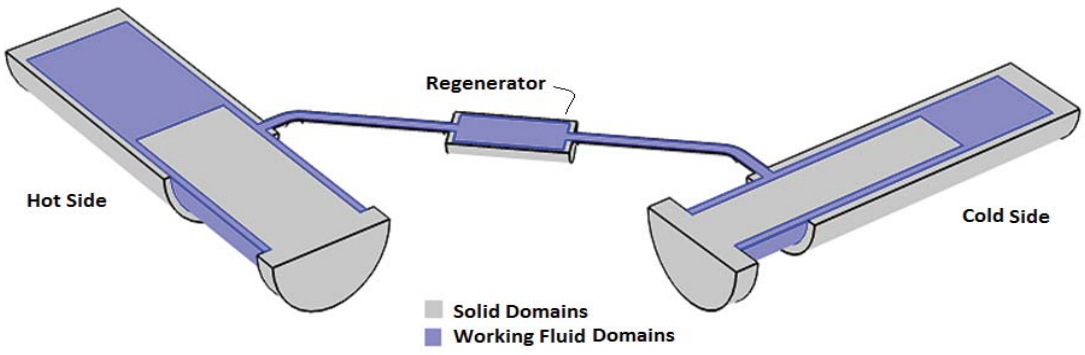


Figure 3.7 Symmetric view showing the solid and fluid domains of the engine

With Reynolds number less than 2000; compressible laminar flow was modelled using Naiver-Stokes, continuity and Brinkman Equations. The velocity equations were used to describe the moving walls, while fixed walls were set as no-slip boundary conditions.

The Naiver-Stokes equation relates the various terms corresponding to the inertial forces, pressure forces, viscous forces, and the external forces applied to the fluid [93] as shown in Eq.(3.51):

$$\rho\frac{\partial u}{\partial t}+\rho(u.\nabla)u=\nabla.\left[-pI+\mu(\nabla u+(\nabla u)^{T})-\frac{2}{3}\mu(u.\nabla)I\right] \tag{3.51}$$

The continuity equation is described as:

$$\rho\frac{\partial \rho}{\partial t}+\nabla.(\rho u)=0 \tag{3.52}$$

The regenerator was modelled as a porous medium, where the momentum equation is written to model the fluid flow in such medium, as shown in Eq.(3.53):

$$\begin{aligned}\frac{1}{\epsilon_p}\rho\frac{\partial u}{\partial t}+\frac{1}{\epsilon_p}\rho(u.\nabla)u\frac{1}{\epsilon_p}&\\ =\nabla.\left[-pI+\mu\frac{1}{\epsilon_p}(\nabla u+(\nabla u)^{T})-\frac{2}{3}\mu\frac{1}{\epsilon_p}(u.\nabla)I\right]&\\ -\left(\mu K^{-1}+\frac{\beta_F|u|}{\epsilon_P^2}\right)u&\end{aligned} \tag{3.53}$$

Where, Forchheimer drag coefficient β_F and the permeability, K can be evaluated by using the following one dimensional equation:

Darcy equation:

$$\frac{\nabla p}{L}=\frac{1}{2}\frac{f}{d_h}\rho u^2 \tag{3.54}$$

Darcy- Forchheimer:

$$\frac{\nabla p}{L} = \frac{\mu}{K}\, u + \beta_F\, u^2 \qquad 3.55$$

Geodon [84] also gives further details for the correlation of the friction-factor for woven matrix and its parameters (a1, a2, a3).

$$f = \frac{a_1}{R_e} + a_2 {R_e}^{a_3} \qquad 3.56$$

Where Reynolds number,

$$R_e = \frac{\rho u d_h}{\mu} \qquad 3.57$$

The hydraulic diameter, d_h of a woven matrix, in terms of wire diameter and porosity is determined by:

$$d_h = \frac{\epsilon_p}{1 - \epsilon_p} d_w \qquad 3.58$$

From the definition of Reynolds number, friction-factor, Eq. (3.54) and Eq. (3.55) it can be determined that:

$$K = \frac{2{d_h}^2}{a_1} \qquad 3.59$$

$$\beta_F = \frac{1}{2d_h}\, \rho\, (a_2 {R_e}^{a_3}) \qquad 3.60$$

In the convection heat transfer modelling process, the working fluid was considered as an ideal gas and the boundary conditions of the cooler and heater were selected. The 'Heat Transfer in Fluids' and the 'Heat Source' modules for both pistons were used to define the hot and cold

heat domains, while other domains were defined as 'thermal insulation'. Eq. (3.54 to 3.63) describe this heat conservation process:

$$\rho C_p \frac{\partial T}{\partial t} + \rho C_p u.\nabla T + \nabla.q = Q_p + Q_{vd} \quad 3.61$$

$$q = -k\nabla T \quad 3.62$$

$$\rho = \frac{p}{R_s T} \quad 3.63$$

Where Eq. (3.63) is the state equation of the ideal gas.

'Heat Transfer in Solids' module was used to model the heat transfer through walls and connecting pipes where Eq. (3.57) was previously used in this module as well.

The regenerator was modelled using the 'Heat Transfer in Porous Media' module, with all parameters and properties specified in tabular form, as shown in Eq. (3.54 to 3.70):

$$(\rho C_p)_{eff} \frac{\partial T}{\partial t} + \rho C_p u.\nabla T + \nabla.q = Q_p + Q_{vd} \quad 3.64$$

$$q = -k_{eff}\nabla T \quad 3.65$$

Where the mean effective thermal conductivity,

$$k_{eff} = \theta_p k_p + (1 - \theta_p)k + k_{disp} \quad 3.66$$

$$\theta_p = 1 - \epsilon_p \quad 3.67$$

Where,

The first term of the right-hand side of Eq. (3.57) is the work done by pressure changes.

$$Q_p = \alpha_p T\left(\frac{\partial p}{\partial t} + \nabla p\right) \quad 3.68$$

Where the coefficient of thermal expansion,

$$\alpha_p = -\frac{1}{\rho}\left(\frac{\partial p}{\partial t}\right)_p \quad 3.69$$

The second term of the right-hand side of Eq. (3.54) is the viscous dissipation in the fluid:

$$Q_{vd} = \tau : \nabla u \quad 3.70$$

The working gas inside the engine is Air where its density is calculated using the state equation Eq. 3.63 while its other thermal properties depend on the pressures and temperatures using in the CFD simulation. These properties are predefined in COMSOL-Multiphysics using piecewise polynomials covering the temperature variation in the range of 200 to 1600 K [93]. The dynamic viscosity of Air is defined by

$$\mu = -8.38278E^{-7} + (8.35717342E^{-8})T - (7.69429583E^{-11})T^2 + (4.6437266E^{-14})T^3 - (1.06585607E^{-17})T^4 \quad 3.71$$

The heat capacity of Air is defined by

$$C_p = 1047.63657 - (0.372589265)T + (9.45304214E^{-4})T^2 - (6.02409443E^{-7})T^3 + (1.2858961E^{-10})T^4 \quad 3.72$$

And finally, Air thermal conductivity is defined by

$$k = -0.00227583562 + (1.15480022E^{-4})T - (7.90252856E^{-8})T^2 + (0.11702505E^{-11})T^3 - (7.43864331E^{-15})T^4 \quad 3.73$$

3.3.4 Boundary conditions

The "moving mesh" physics was used to model the moving boundaries in this engine with parts displacement defined using Users Defined Function (UDF) interface. Eq. (3.74) and Eq. (3.75) gave the real motion for the expansion piston and compression piston respectively.

$$Ye = (\text{z0_m}/2) * (1 - \cos(theta)) \quad 3.74$$

$$Xc = (z0_d/2) * (1 - cos(theta - alpha)) - (z0_d/2) \quad 3.75$$

Where,

Ye Hot piston displacement (m)

Xc Cold piston displacement (m)

z0_m Hot piston stroke length (m)

z0_d Cold piston stroke length (m)

$theta$ Phase angle (^{o}) and $theta$ is the Crank angle (^{o})

All outer walls of the hot piston are moving wall except the vertical wall in y direction are sliding walls. The inner vertical walls of the cylinder holding the piston are freely moving following the prescribed motion of the piston. The cold piston walls are treated as moving wall for the boundary in physical contact with the piston in x direction and the other two walls (parallel to x direction) are freely moving following the prescribed motion of the piston. Free deformation is only activated for the compression and expansion spaces and has been avoided for other domains (regenerator, heater, cooler and piping's) for faster simulation running time. (See Figure 3.8).

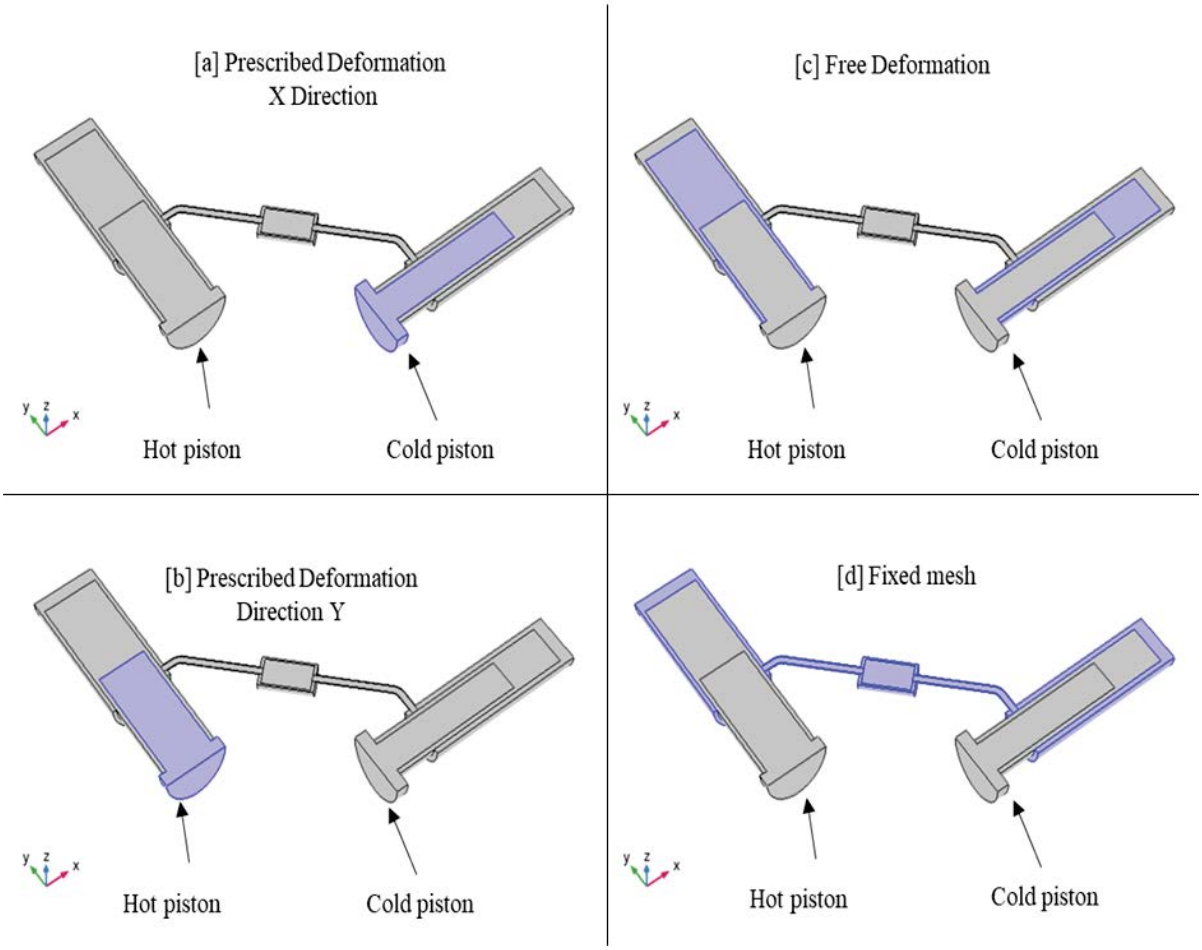


Figure 3.8 Symmetric view showing moving and fixed domains of the engine

The walls of the cooler and heater were treated as constant temperature while the other walls were considered as adiabatic. Figure 3.9 shows a symmetric view of the computational domains of the engine model. The unsteady time-dependent solution of the governing equations has been initialized with a stationary solution of heat transfer (no piston movement). As long as the temperature gradient established throughout the engine and the solution is a steady state, the computational time can be reduced.

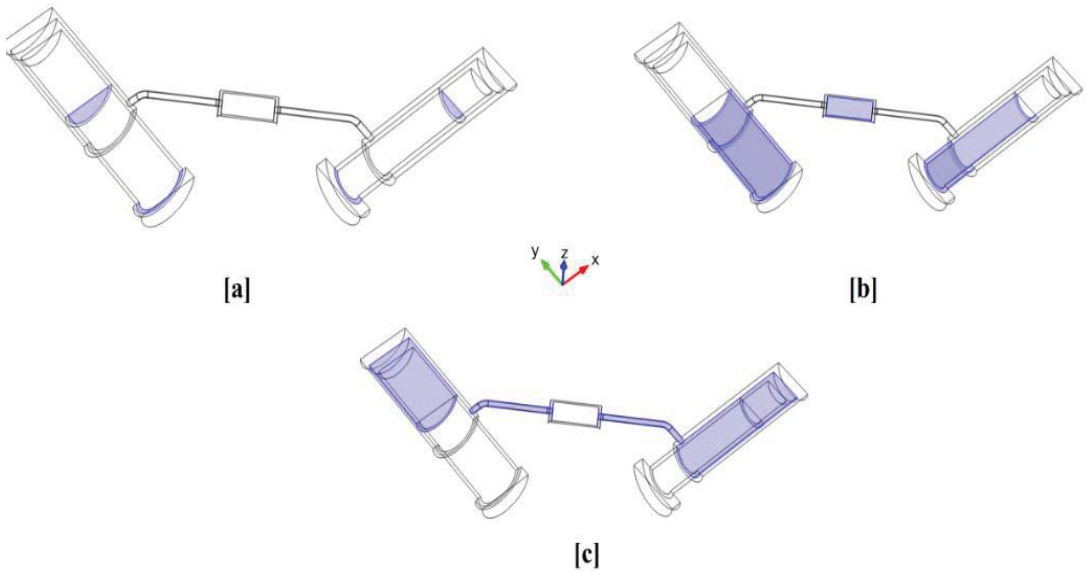


Figure 3.9 Symmetric view showing the computational domains of the engine

[a] Moving Walls, [b] Slip Walls and [c] No-slip Walls

3.3.5 Sequence of meshing and solver scheme

There are many types of meshing methods available in COMSOL-Multiphysics [93] such as coarse, normal, fine, finer and extra fine tetrahedral. The correct choice of the meshing method is essential to produce accurate modelling of the fluid behaviour. It should be taken into consideration that further refining of the computational mesh caused in the increase of the solving time and that sometimes it becomes unachievable. The geometry of the engine was meshed using tetrahedral elements to suit the engine's complex geometry. The sensitivity of such mesh was examined using coarse, normal, fine, finer and extra fine tetrahedral. The effect of mesh size on accuracy was studied using number of mesh elements ranging from (60310) to (2049753). The grid independence study is presented in Figure 3.10, where the indicated power for the Stirling engine expander versus the number of mesh elements indicating that results are not affected by the number of elements when using over (664712) elements, the difference in the simulation results between the coarse and fine mesh was 7% and between the fine and extra fine mesh was 1%. The other gain of using the finer mesh is the simulation time which is less

3 times that from the extra fine mesh. Figure 3.11 shows the fine tetrahedral elements used in modelling this engine with grid density of (216552) elements with average quality (0.75). The CFD model was set up with tolerance of 5e-4 and the time stepping is resolved by 50 times over the cycle. The run takes 1-2 days for each simulation (10 Cycle) using Intel® core™ CPU i7-4820K PC, with 3.7GHz processor and 48 RAM memory.

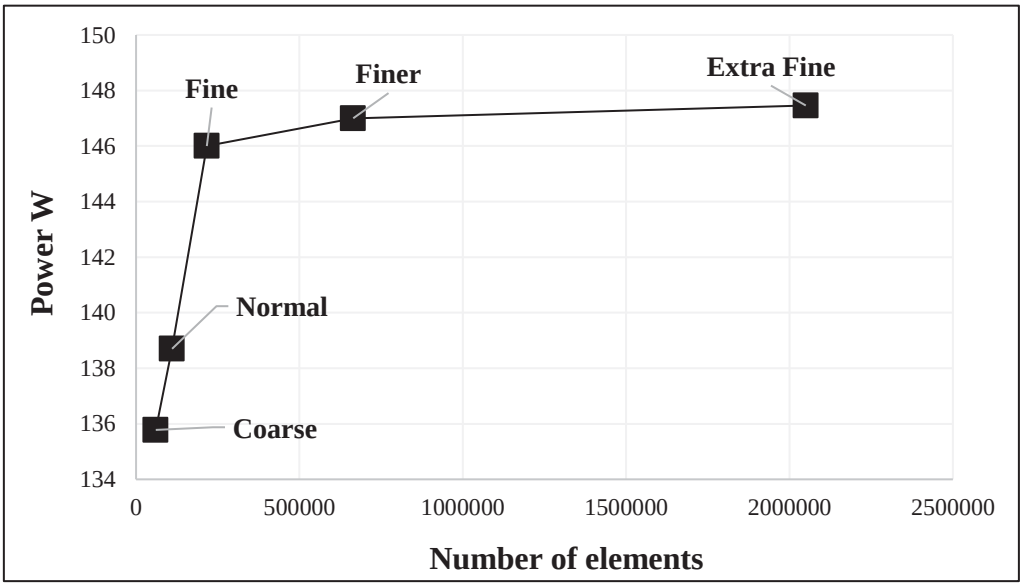


Figure 3.10 Grid independence Vs. Engine power

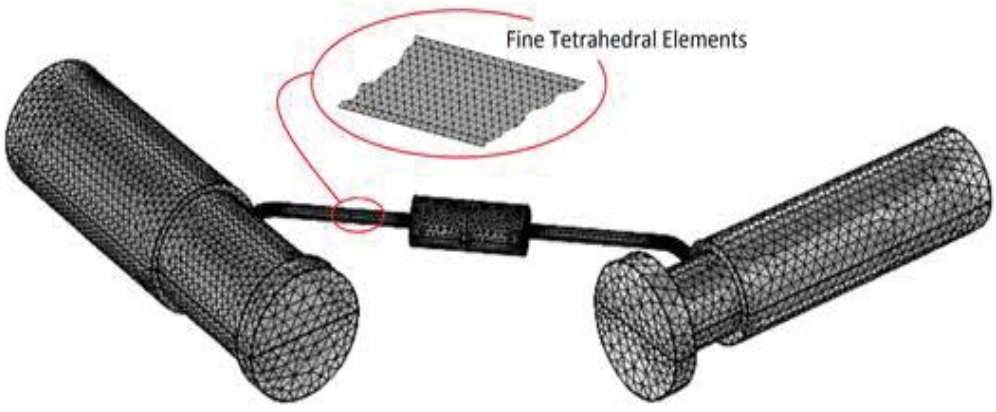


Figure 3.11 Engine model mesh distribution

Figure 3.12 shows the temperature contours at various sections in the heater domains where the temperature distribution in the middle slice is illustrated in the same figure. It is noticed that the

high gas temperature is near the solid domains, this is because the gas comes from the cooler to the heater with a low temperature, hence, the heat transfers from the solid domains (heater walls) to the working fluid. Figure 3.13 illustrates a symmetric view of the temperature contours at different crank angles during the engine's cycle. Figure 3.13 (a) presents the distribution of temperature inside the whole engine crank angle Theta equals 180^0. The cold piston is in its Bottom Dead Centre (BDC) position. The temperature inside the cooler varies from 300 to 700 ^{0}C, with higher values being observed near the cooler connecting pipe, as the working fluid comes from the hot space in the heater through the regenerator to the cooler. Figure 3.13 (b) shows the position of the hot piston in its Bottom Dead Centre (BDC) when Theta equal 360^0. The temperature inside the heater varies from 800 to 1100 ^{0}C. The working fluid transfers from the cold space in the cooler via the regenerator towards the hot space. The higher temperature values are observed near the heater connecting pipe. Figure 3.14 shows the pressure gradient through the spaces of the whole engine. There is a little difference in the gas pressure between the connecting pipes and the regenerator, and it can be concluded that the gas transfers inside the engine occurs with a low-pressure drop.

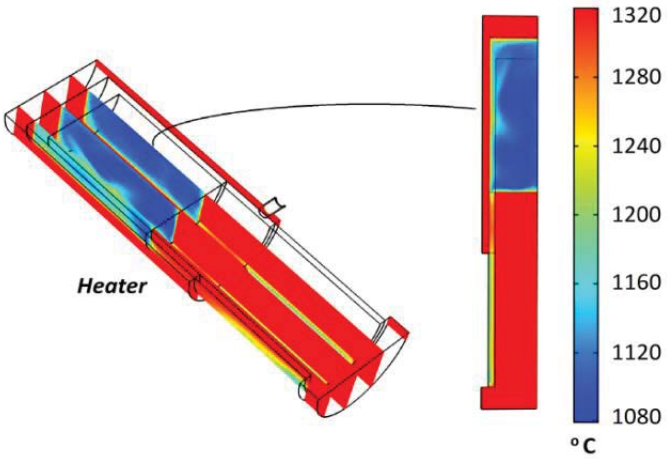


Figure 3.12 Temperature contours at various sections in the heater domains during the cycle at (t= 0.48s)

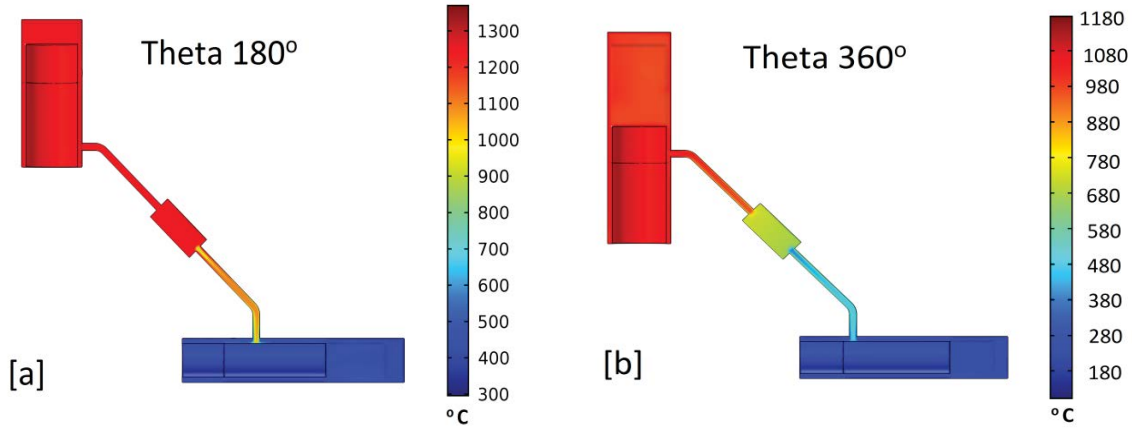


Figure 3.13 CFD results of Stirling engine of the temperature contours (^{0}C) at different [Theta] crank angels (^{o}) at ([a] t= 0.46s and [b] t= 0.48s)

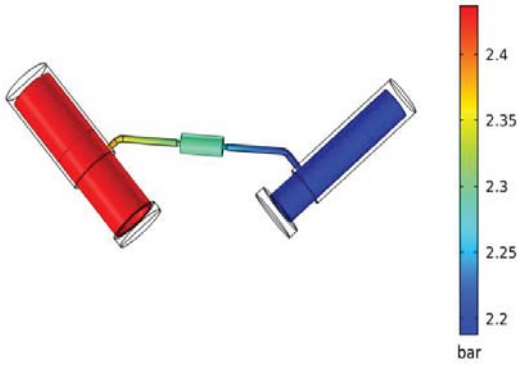


Figure 3.14 Pressure contours of the whole engine during the cycle at (t= 0.48s)

Figure 3.15 shows the variation of total expansion (hot cylinder/side) and compression (cold cylinder/side) space volumes versus the crank angle over the engine cycle. The minimum value of the total volume is 57.49 cm^3 and occurs at crank angle = 226.8^0, and the maximum value of the total volume is 240.38 cm^3 occurring at crank angle = 46.8^0. Figure 3.16 illustrates the variation of the pressure versus volume in the compression and expansion spaces (PV diagram). This figure shows that the net-work output for this operating condition is 15.78 J (146 W), which is calculated as the summation of the positive expansion and negative compression work [59], as shown in Eq. (3.76):

$$\dot{W} = \left[\oint p dV.\, dt\right]_{Exp} - \left[\oint p dV.\, dt\right]_{Comp} \qquad 3.76$$

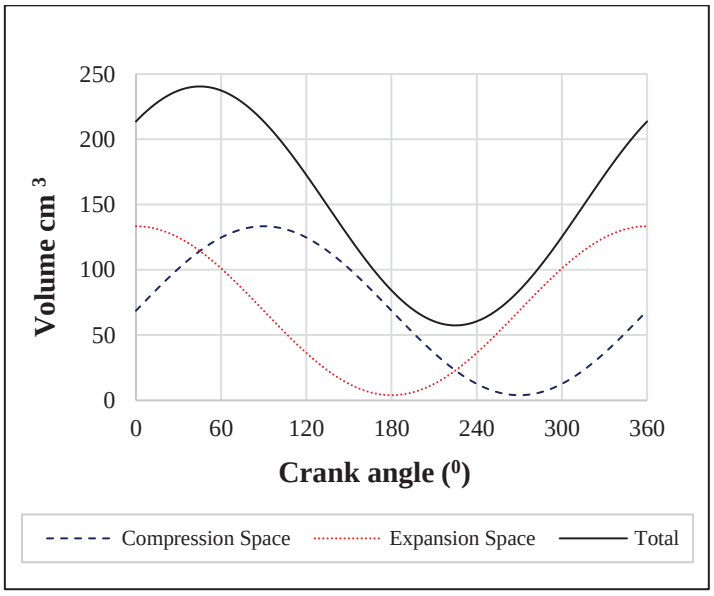


Figure 3.15 Variation of total, compression and expansion volumes versus crank angle within an engine cycle at 555 r.p.m

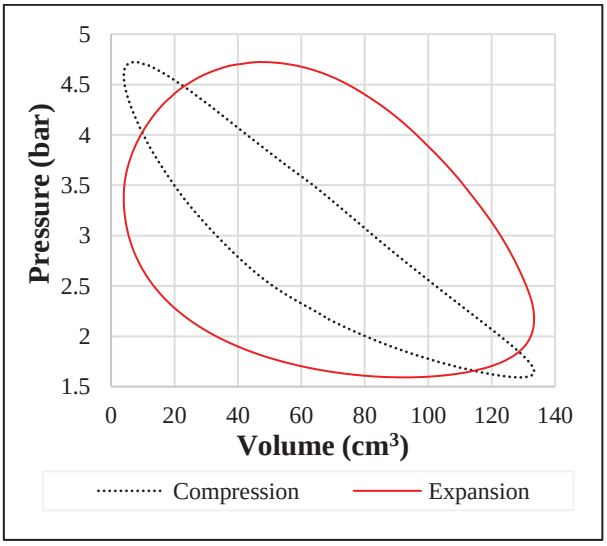


Figure 3.16 PV diagrams for compression and expansion volumes within an engine cycle at 555 r.p.m

3.3.6 Model Validation

Figure 3.17 compares the CFD results to the thermodynamic model results in terms of the indicated power at three different charge pressures of 1, 2 and 2.5 bars at engine speed ranging from 150-650 RPM. Results showed deviation values from 4% to 10 % at 1 bar, from 10% to 12.5% at 2 bar and from 8% to 13.5% at 2.5 bar. The maximum deviation of the model prediction lower than that deviation from the open literature (See Chapter 2, Section 2.2.6).

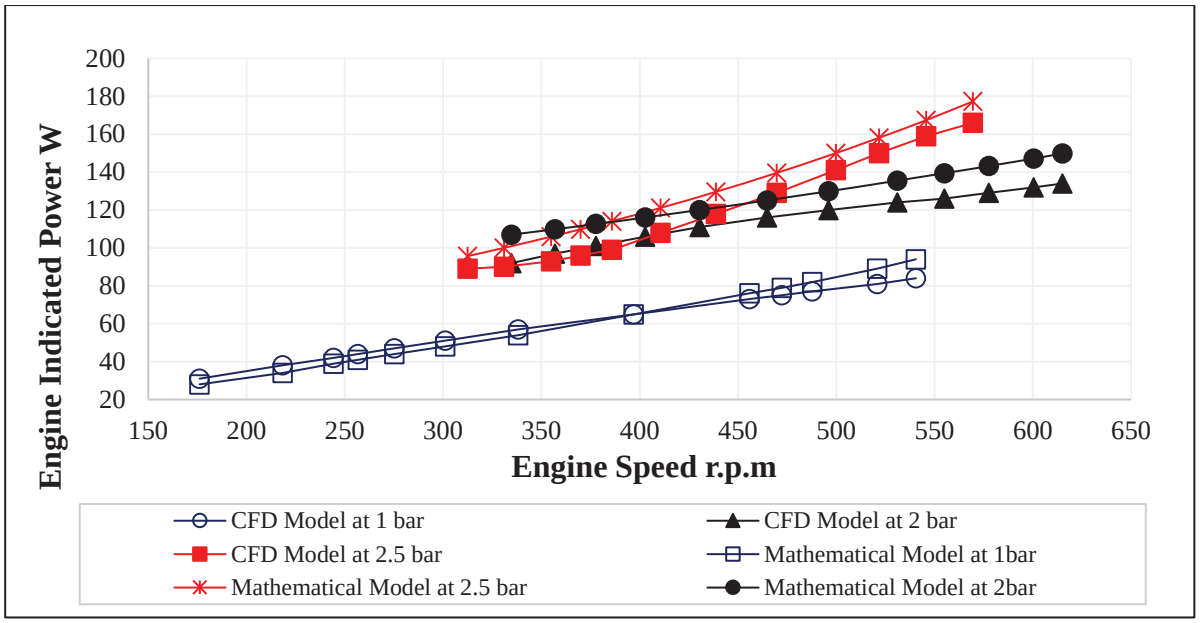


Figure 3.17 Comparison of indicated power between the mathematical model and CFD model at fixed charge pressure and different engine speed

It is worth mentioning that the reasons of comparing the CFD results to the thermodynamic model are:

- The mathematical model can predict both powers: (1) the shaft power which already has been successfully validated to the experimental (see Section 3.2.2) and (2) the indicated power.
- The CFD model can only predict the indicated power.
- The only experimental data available from the published work by [60] that used in this investigation is the shaft power and there is no indicated power available.

3.4 Parametric study using the developed CFD model

The validated CFD model has been used to investigate the effects of operating conditions and geometrical parameters on the engine performance, in terms of power output using the operating conditions and geometrical parameters listed in Table 3.1.

3.4.1 Effect of Cold Temperature

The effect of using low cooling temperature ranging from -20 to 20 ^{0}C on the indicated power of the engine was investigated. Figure 3.18 depicts the variation of power output against cooling temperature at various hot source temperatures of 600, 800 and 1100 ^{0}C. It is clear from this figure that the indicated power increases almost linearly as the cold side temperature decreases with power output of 162 W and can be achieved at -20 ^{0}C compared to 146 W at 20 ^{0}C. Figure 3.18 also shows the variation of power output against temperature difference (Th and Tc) in the hot and cold ends. This emphasises the study conducted by Chen et al. [56], where they demonstrated that the power output increases as the temperature difference between the cold and hot side increases.

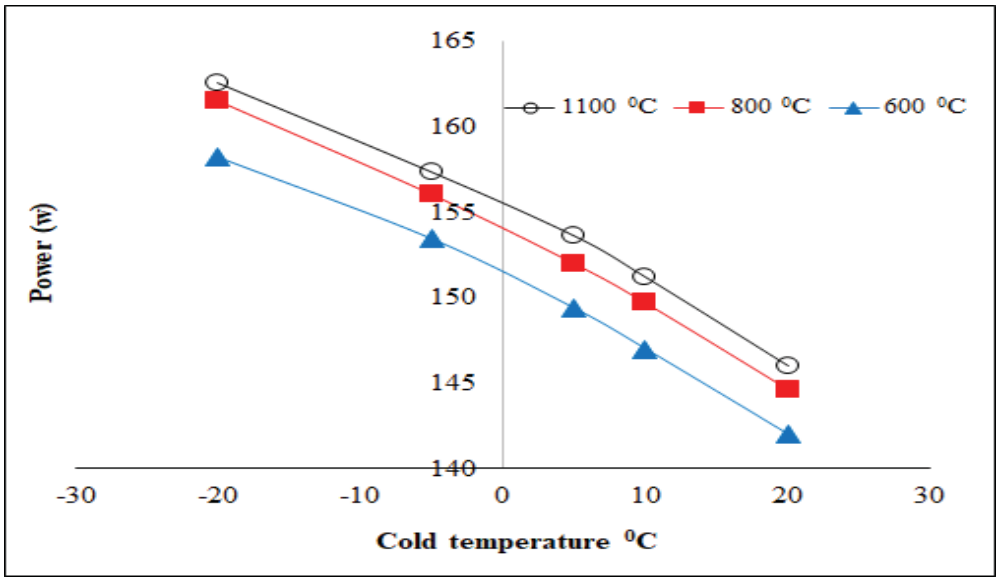


Figure 3.18 Cold temperatures Vs. Power at different hot temperatures (^{0}C)

3.4.2 Effect of Charge Pressure

Figure 3.19 illustrates the variation of the indicated power with the charge pressure at different hot source temperatures of 600, 800 and 1100 ^{0}C. It can be seen that the indicated power increases almost linearly as the charging pressure increases. This can be attributed to the assumption of the working fluid which is treated as an ideal gas, and hence, the pressure acting in accordance with the ideal gas law.

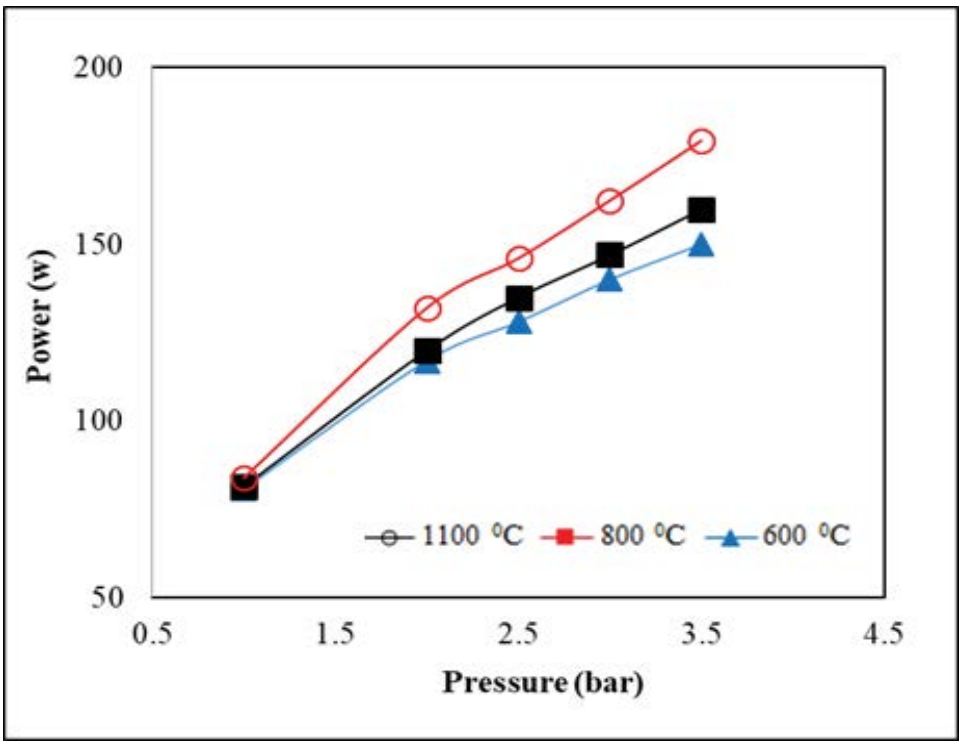


Figure 3.19 Effect of Charge Pressure on the engine performance at different hot temperature (^{0}C)

3.4.3 Effect of Matrix Wire Diameter

The engine is fitted with a woven wire matrix regenerator using wire diameter of 100 µm. In this work, the effect of three different wire diameters (shown in Table 3.2) on the engine indicated power was investigated.

Table 3.2 Matrix woven wire diameter

Number	Wire diameter, μm	Material
1	100	Chrome -Nickel
2	125	
3	155	
4	200	

Figure 3.20 shows the effects of matrix wire diameter on the engine's indicted power output at various hot side temperatures of 600, 800 and 1100 ^{0}C. It can be seen that at 1100 ^{0}C wire number (4) outperforms other wire diameters with indicated power reaching 155W compared to, 146, 147 W, and 150 W respectively. This higher performance of wire number (4) can be attributed to the higher surface area which leads to a better heat transfer rate. Andersen et al. [97] concluded that a matrix with a thicker wire could increase the power output.

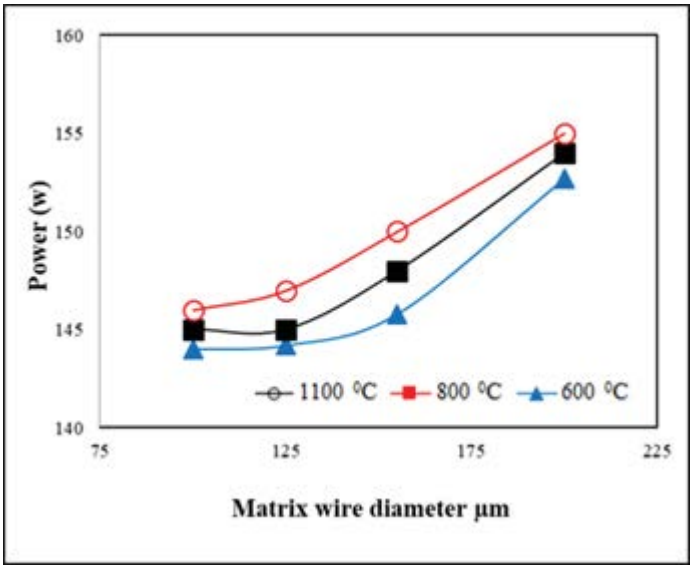


Figure 3.20 Effect of regenerator matrix on engine performance at different hot temperature (^{0}C)

3.4.4 Effect of Porosity

Figure 3.21 shows that the power output increases as porosity increases up to 80% and reaching 147.11 W, this is due to the decrease in the conduction loss as porosity increases [71], [98]. However, further increases in the porosity led to a reduction in the power output due to decreasing the contact surface of the regenerator matrix and the working flow.

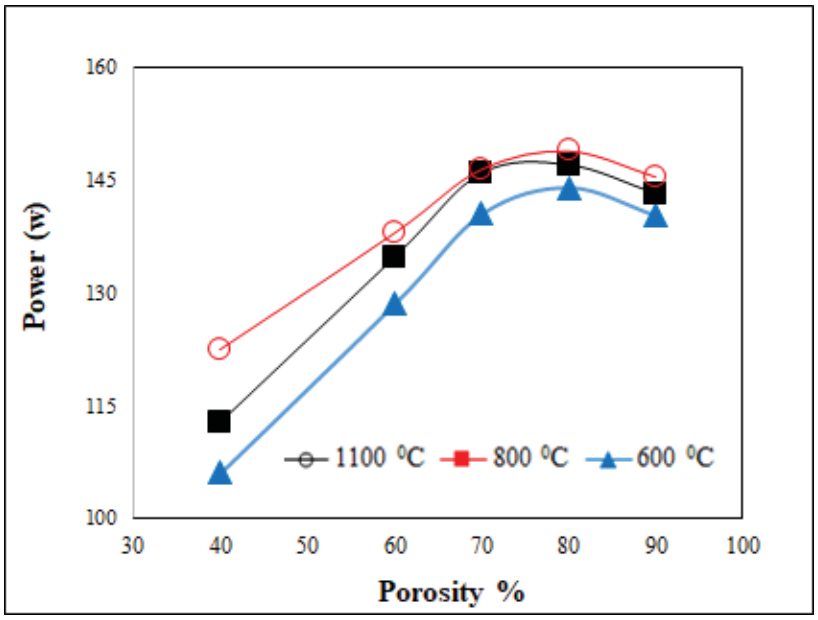


Figure 3.21 Effect of Porosity on engine performance at different hot temperature

3.4.5 Effect of Geometrical Parameters

The developed CFD model was applied to obtain the effects of geometrical parameters on the engine power output. The selected geometric parameters are illustrated in Figure 3.22.

Figure 3.23 shows the effect of changing the inner/outer diameters and the length of the heating / cooling volumes on the engine power output . Figure 3.23 (a) shows that engine power output increases as the Cooler inner diameter Dk_i increases at heater inner diameter of Dh_i = 36, 44 and 46 mm . Figure 3.23 (b) shows that engine power output increases as the heater inner diameter Dh_i at cooler inner diameter increases at Dk_i = 21, 25 and 29 mm. Both outer diameters and lengths were fixed at (the original engine dimensions) Dh_o=46 mm, the heater

length = 100 mm, Dk_o = 32 mm and the cooler length =120 mm . The difference between the outer diameter and the inner diameter is called the annular gap and is the area where the working fluid flows. Hence, as this gap reduces the dead volume reduces and the power output increases. The effects of increasing the annular gap of heat exchangers as a dead volume on the power output can also be seen in Figure 3.23 (c) and Figure 3.23 (d). The power output decreases as the outer diameter increases while fixing the inner diameters and heater/cooler length at (the original engine dimensions) Dh_i=40 mm, the heater length = 100 mm, Dk_i =25 mm and the cooler length =120 mm. Figure 3.23 (e) shows that the power output increases with increasing the heater and cooler lengths (using Dh_o=46 mm, Dk_o = 32 mm, Dh_i=40 mm and Dk_i =25 mm (the original engine dimensions)) until it reaches a maximum, at around 140 mm, then the power output stays constant due to the pressure drop along the heat exchangers.

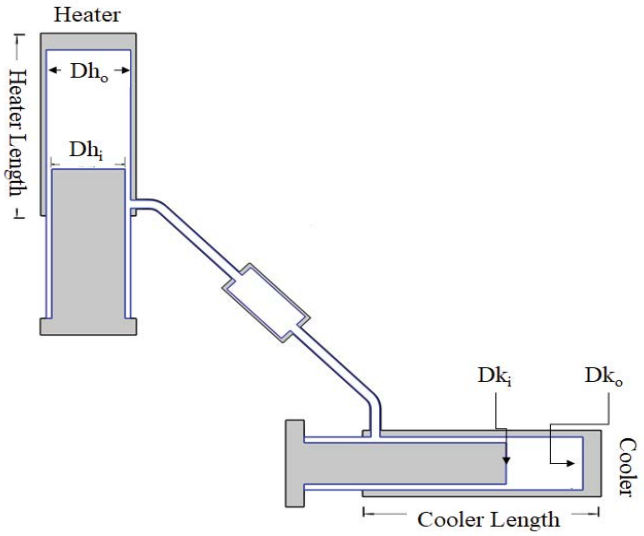


Figure 3.22 The selected geometric parameters [82][83]

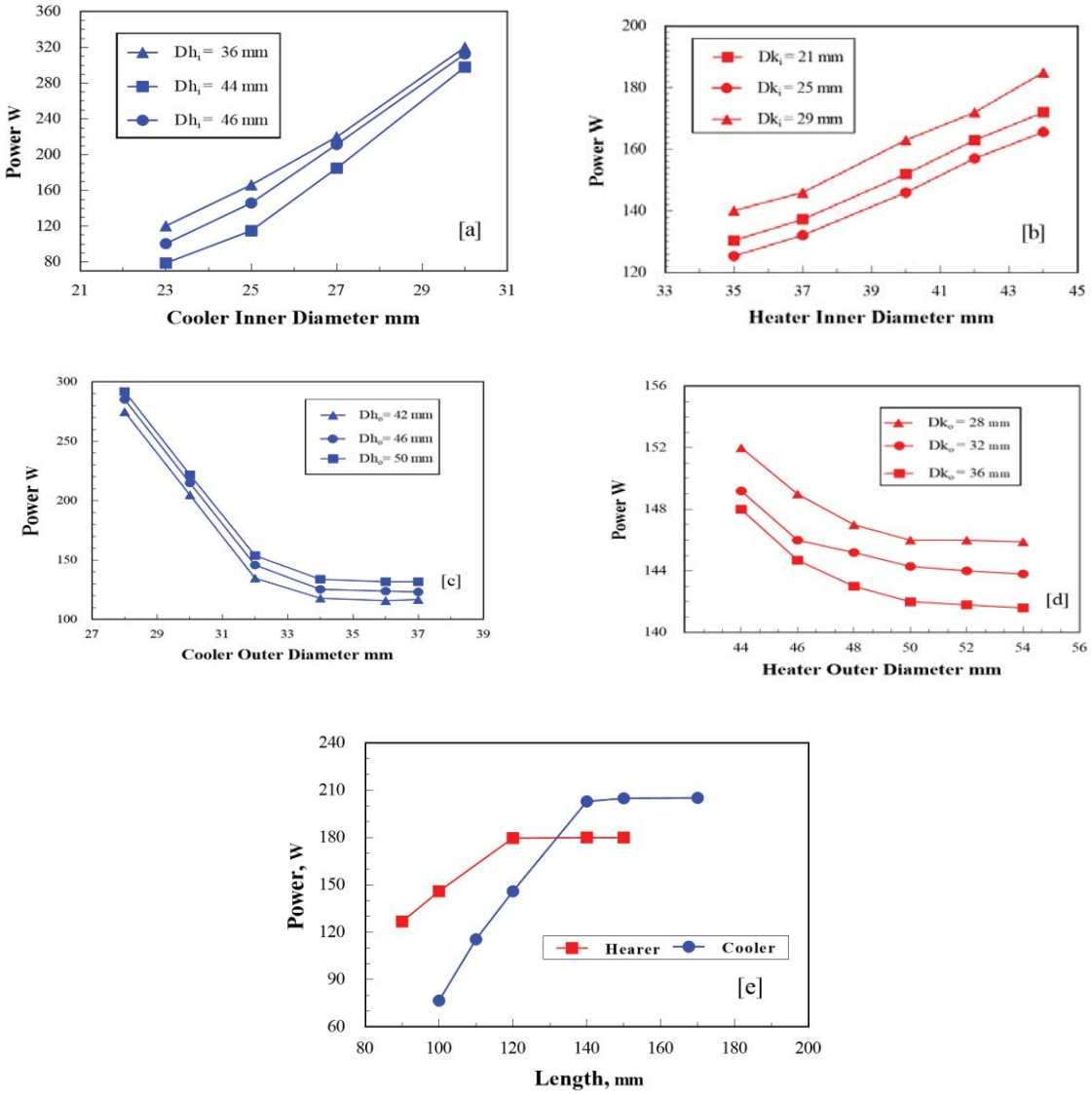


Figure 3.23 Effect of geometrical parameters on the engine performance:

[a] Dk_i vs. Power, [b] Dh_i vs. Power, [c] Dk_o vs. Power, [d] Dh_o vs. Power and [e] Heater and Cooler Length vs. Power.

3.4.6 Comparison between the original and the new Stirling engine

The engine CFD model was run with the ~~best~~ good design parameters and operating conditions, that obtained from the parametric study in previous sections, (Listed in Table 3.3) showing nearly 65% (from 146 W to 240 W) enhancements in the performance of the new design compared to the original one. It should be taken into account that the reason of chosen these design parameters due to the piston dimensions and manufacture restrictions, for example the results would be better if the difference between the outer and inner diameter was 1mm (as at

inner of 30mm outer of 32mm) but from the manufacturing point view it can be quite difficult to manufacture a particularly thin cooler/heater without any advanced machining tools. In addition to some of the layers which is resulting from metal erosion due to thermal stresses during the engine cycle, these cracks will block the thin gap, and then cause an explosion or engine failure.

Table 3.3 New Stirling Engine design parameters and operating conditions

Parameter	Value of the original engine	Value of the new engine
Engine type	Alpha α (V)	Alpha α (V)
Cylinder bore	52.4 mm	52.4 mm
Cylinder Stroke	60 mm	60 mm
Phase angle Working gas Air	90^{0}	90^{0}
Length of the connecting pipe	155 mm	155 mm
Diameter of the connecting pipe	5 mm	5 mm
Heater outer diameter	46 mm	44 mm
Heater inner diameter	40 mm	41 mm
Cooler outer diameter	32 mm	30 mm
Cooler inner diameter	25 mm	27 mm
Length of the heater	100 mm	120 mm
Length of the cooler	120 mm	140 mm
Max. engine speed	555 rpm	555 rpm
Cooling	Water	Water
Working fluid	Air	Air
Type of the cooler	water jacket	water jacket
Type of the heater	Annulus	Annulus
Type of the regenerator's matrix	woven wire	woven wire
Wire diameter (Micron)	200 Chrome-Nickel	200 Chrome-Nickel
Porosity	70%	80%
Inlet water temperature	-20 (°C)	-20 (°C)
Hot source temperature	1100 (°C)	1100 (°C)
Charge pressure	2.5 (bar)	3.5 (bar)

3.5 Conclusion

This chapter presents the development of a thermodynamic and complete 3D CFD models for a V alpha-type Stirling engine using the engine prototype and its experimental results published by Karabulut et al. [60]. New approach combining the thermodynamic model with 3D CFD analysis was developed to investigate the performance of a V-alpha Type Stirling engine under various operating conditions and design parameters such as, regenerator porosity, charge pressure, matrix wire diameter, dead volume and hot/cold ends temperatures on the engine performance in terms of power output, through predicting the PV diagram of the engine. Results showed that power output increased by 180W when the charge pressure was increased from 1 to 3.5 bar. As for the regenerator, maximum power output 155 W was achieved by increasing matrix wire diameter 200 μm. This study concluded that as the cold end temperature decreases, the power output increases reaching 162 W at -20 ^{0}C compared to 146 W at 20 ^{0}C, indicating the potential of using low temperature cooling to enhance the engine power output. Also, it was shown that the design of the heater and cooler affect the performance of the engine where the power output increased to 200 W by increasing the heater and cooler lengths to maximum value of 140mm. The power output of V alpha-type Stirling engine increased by up to 65% (from 146 W to 240 W) when the best new design parameters and operating conditions were applied. This work highlights the potential of using 3D CFD modelling to improve the performance of V alpha-type Stirling engine through identifying the best design parameters and operating conditions.

CHAPTER 4

REGENERATOR DEVELOPMENT, CFD MODELLING AND TESTING

Part of the work presented in this chapter has already been published in [83] as:

A. K. Almajri, S. Mahmoud, and R. Al-Dadah, "Modelling and parametric study of an efficient Alpha type Stirling engine performance based on 3D CFD analysis," *Energy Convers. Manag.*, vol. 145, 2017.

Almajri is the lead author, he has made the most significant contribution to the research including design, analysis and interpretation of data. He has written and edited a major part of the work, he also takes charge of getting approval from all the other authors and communicating with the journal.

Mahmoud and Al-Dadah fulfil the following criteria: Contribute to the conception, design, analysis and interpretation of data. Participate in drafting and help revising the manuscript for intellectual content. Approve of the version to be published.

4.1 Introduction

This chapter introduces a new regenerator configuration for the V alpha-type Stirling engine; it is a parallel-geometry segmented regenerator with circular micro-channels structure. The work involved 3D CFD modelling and experimental testing for the developed heat exchanger. The new micro-channels regenerator was designed, manufactured and tested using unidirectional and oscillatory flows test rig. The measured surface and flow temperatures and pressure drops at various operating conditions were compared to those from the CFD modelling

giving good agreement values. Experimental measurements were carried out for the Non-aligned micro-channels and Random fibre regenerators and results were compared to those of the parallel-geometry Micro-channels regenerator. Results showed that the pressure drop in the parallel-geometry micro-channels regenerator was lower than those for the Random fibre regenerator (conventional regenerator) indicating its potential to improve the performance of the Stirling engine.

4.2 Parallel-Geometry Regenerators

The regenerator is a heat exchanger, which is placed between two heat exchangers: the cooler and the heater. It works by absorbing the heat from the working fluid while it is passing from the heater to the cooler and restores it back to the working fluid whilst it is going in the opposite direction. Consequently, it can reduce the heat losses leading to increasing the performance of the Stirling engine.

Woven and fibre wire meshes regenerators are the most commonly used regenerators in Stirling engines due to their unpretentiousness and thermal performance. Parallel-geometry with regular shaped passages regenerators can offer the potential for enhancing the performance of the Stirling engine due to their ability to reduce the pressure drop across the regenerator and controlling the axial heat transfer process [99].

In this context, a micro channel regenerator can be fabricated to fill the regenerator housing with regular shape channels and in parallel direction to the flow. Flow separation in the parallel-geometry regenerators can be controlled to minimize frictional losses and pressure drops leading to improved engine performance, which is the main advantage of using the Parallel-Geometry Regenerators. On the other hand, the continuity of solid material in the parallel-geometry regenerators is the main disadvantage which causing large axial conduction losses. An attempt was reported in literature to overcome the axial conduction losses by using

segmentation as for example the experimental study by [79] for a segmented-involute-foil regenerator which found an enhancement in the regenerator performance by using segmentations. The effect of segmentation can be also found in the study by [78] when parallel wire geometry was segmented to 3 and then to 7 parts in order to enhance the regenerator performance. The study concluded that the segmentation enhanced the regenerator performance and can reduce the axial conduction losses.

A real Stirling engine or test rig based on either unidirectional flow or oscillatory flow are often used to evaluate the performance of any new proposed regenerator. However, recently, the regenerator evaluation can be achieved via CFD modelling for the whole engine and that will save time by reducing the experimental work and give more ability to adjust or make any design changing [79], [57] and [100].

4.3 Micro-Channel Regenerator

Figure 4.1 shows three configurations for the micro-channel regenerator used with circular-shaped channels, each with hydraulic diameter of 1 mm. The solid matrix was machined using CNC machining technology and consisting of four parts, each part has 10 mm length with 40 mm diameter. The regenerator material was Steel AISI 4340, with main proprieties are listed in Table 4.1. The reason of chosen Steel AISI 4340 because it was the only materials that available in the workshop during the time of machining the solid matrix.

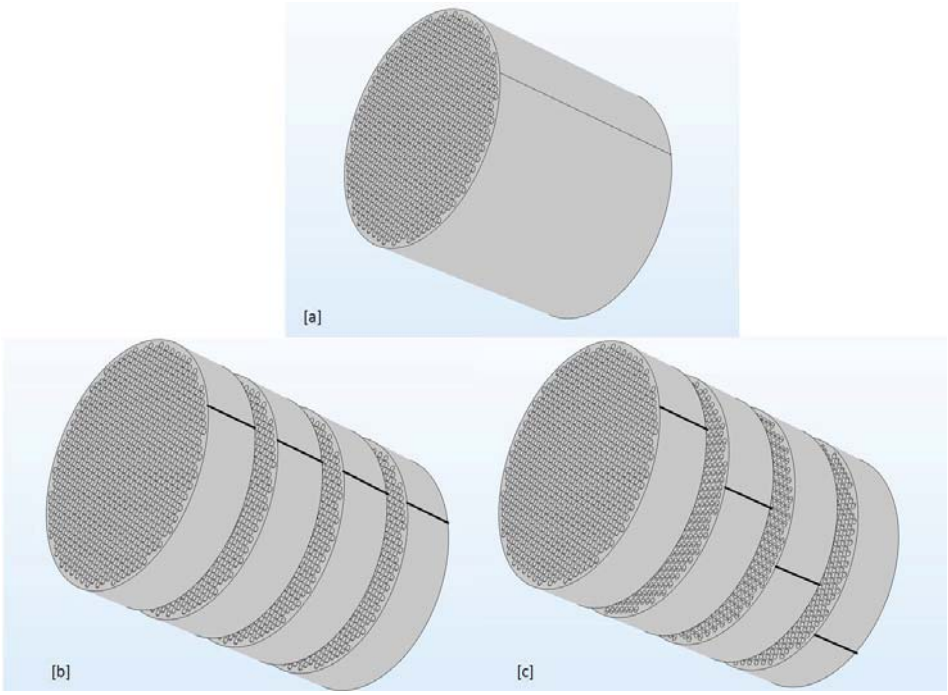


Figure 4.1 [a]Non-segmented micro-channel regenerator

[b] Exploded view: Aligned segmented- regenerator and [c] Exploded view: Non-aligned segmented -regenerator

Table 4.1 Summary of the main proprieties of the selected regenerator material

Property	Value
k	44.5 (W/m. K)
C_P	475 (J/kg. K)
ρ	7850 (kg/m3)

Figure 4.2 shows the distance ($\boldsymbol{\delta}$) between the micro channels which needs to be evaluated to keep the thermal penetration depth minimum, thus allows the heat to disperse through the matrix [101], it is a function of the engine speed (frequency f).

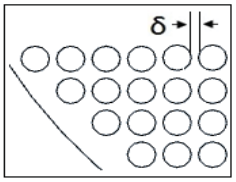


Figure 4.2 Distance between channels of regenerator

The engine speed was considered to range from 400 to 1000 rpm, and Eq. (4.1) calculates the thermal penetration depth (δ) [100], [101]. Figure 4.3 shows different values of the thermal penetration depth versus the engine speed.

$$\delta = \sqrt{(k/\pi f \rho C_P)} \quad 4.1$$

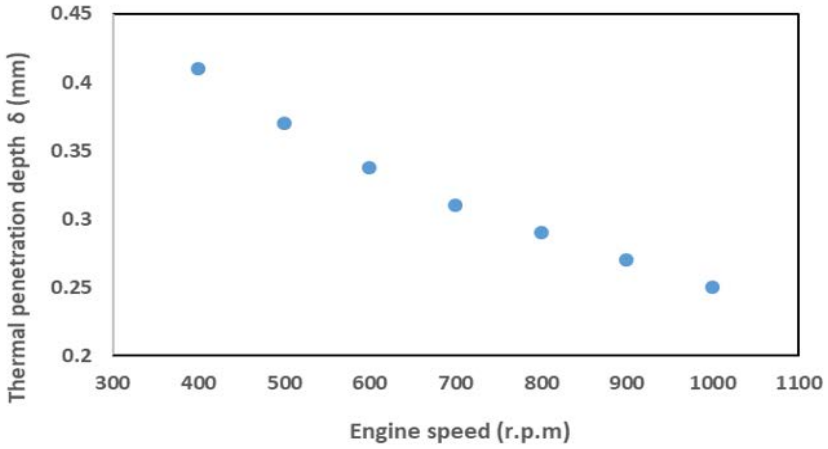


Figure 4.3 Thermal penetration depth vs. engine speed [100]

The thermal penetration depth for the proposed regenerator was chosen to be 0.25mm, leading to porosity value of 46.8% and 749 micro channels.

4.4 Regenerator Three-Dimensional CFD Modelling

Commercial comprehensive simulation software (COMSOL multiphysics 5.3a) was used to develop a CFD model for three-dimensional micro channel regenerator. In the beginning, the modelling of flow type, heat transfer and the governing equations are presented in the features of the COMSOL setting. Then applying boundary conditions, meshing methods and structure of solution will be discussed. Presenting the model validation against experimental data for the pressure drop and the temperature measurement will be also included in the next section.

The geometry of the developed regenerator was divided into 8 sectors including the housing, with each 3D sector was created as a CAD models using SolidWorks and then imported to COMSOL 5.3a software. The operating parameters, charge pressure, inlet (hot side) and outlet

(cold side) temperatures, frequency and mass flow rate were inserted as a table and defined as Parameters.

In the material and properties section, the three domains were defined with air as the working fluid passing the channels and steel for the solid domains. Figure 4.4 shows the view of the 3D sector with the solid and fluid domains.

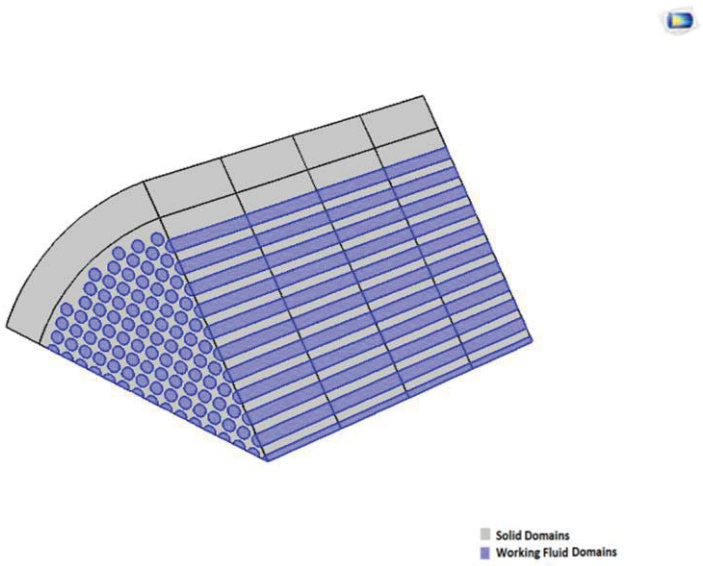


Figure 4.4 3D sector view showing the solid and fluid Domains of the regenerator

The next step is adding physics to the geometry with time dependent equations selected and the boundary conditions defined.

With range of flow rate of (3, 5, 7 and 9 SLPS) Reynolds number is less than 2000; compressible laminar flow was modelled using Naiver-Stokes and continuity Equations.

Where Reynolds number is defined as:

$$R_e = \frac{\rho u d_h}{\mu} \qquad 4.2$$

The Naiver-Stokes equation relates the various terms corresponding to the inertial forces, pressure forces, viscous forces, and the external forces applied to the fluid, as:

$$\rho\frac{\partial u}{\partial t}+\rho(u.\nabla)u=\nabla.\left[-pI+\mu(\nabla u+(\nabla u)^{T})-\frac{2}{3}\mu(u.\nabla)I\right] \quad 4.3$$

The continuity equation is described as:

$$\frac{\partial \rho}{\partial t}+\rho\nabla.(\boldsymbol{u})\ =\ 0 \quad 4.4$$

4.4.1 Boundary conditions and solver scheme

The inlet boundary conditions for the pressure and temperature were specified and inserted similar to the expected experimental data at the hot side of the test section. The inlet velocity equation was calculated as:

$$v_{max}=\ \pi.f.V_q\ /A_f \quad 4.5$$

The charge pressure was decided to be the reference pressure while the ambient temperature was chosen to be the reference temperature. The inlet and outlet boundaries were treated as constant temperature while the remaining walls were set as no-slip adiabatic boundary conditions[82].

In the convection heat transfer modelling process, the working fluid was considered as an ideal gas and the boundary conditions of the whole channels were selected. The `Heat Transfer in Fluids` and the 'Heat Source' modules were used to define the hot and cold heat boundaries, while the remaining walls were set as `no-slip` and `adiabatic` boundary conditions [82].

The following Equations describe this heat conservation process [82]:

$$\rho C_p\frac{\partial T}{\partial t}\ +\rho C_p u.\nabla T+\nabla.q=Q_{vd}+Q_p \quad 4.6$$

$$q=\ -k\nabla T \quad 4.7$$

$$\rho = \frac{p_A}{R_s T} \qquad 4.8$$

Where Eq. (4.8) is the state equation of the ideal gas.

`Heat Transfer in Solids' module was used to model the heat transfer through solid domain as following:

$$\rho C_p \frac{\partial T}{\partial t} + \rho C_p u.\nabla T + \nabla.q = Q_p + Q_{vd} \qquad 4.9$$

Where, the first term of the right-hand side of Eq. (4.6) and Eq. (4.9) is the work done by pressure changes.

$$Q_p = \alpha_p T\left(\frac{\partial p}{\partial t} + \nabla p\right) \qquad 4.10$$

Where the coefficient of thermal expansion can be calculated as:

$$\alpha_p = -\frac{1}{\rho}\left(\frac{\partial p}{\partial t}\right)_p \qquad 4.11$$

The second term of the right-hand side of Eq. (*4.9*) and Eq. (4.12) is the viscous dissipation in the fluid:

$$Q_{vd} = \tau : \nabla u \qquad 4.12$$

The working gas inside the engine is Air where its density is calculated using the state equation Eq. (4.8) while its other thermal properties depend on the pressures and temperatures using in the CFD simulation. These properties are predefined in COMSOL-Multiphysics using piecewise polynomials covering the temperature variation in the range of 200 to 1600 K [93].

The dynamic viscosity of Air is defined by

$$\mu = -8.38278E^{-7} + (8.35717342E^{-8})T - (7.69429583E^{-11})T^2 + (4.6437266E^{-14})T^3 - (1.06585607E^{-17})T^4 \quad 4.13$$

The heat capacity of Air is defined by

$$C_p = 1047.63657 - (0.372589265)T + (9.45304214E^{-4})T^2 - (6.02409443E^{-7})T^3 + (1.2858961E^{-10})T^4 \quad 4.14$$

And finally, Air thermal conductivity is defined by

$$k = -0.00227583562 + (1.15480022E^{-4})T - (7.90252856E^{-8})T^2 + (0.11702505E^{-11})T^3 - (7.43864331E^{-15})T^4 \quad 4.15$$

Figure 4.5 shows the 3D sector view of the computational domains of the regenerator model.

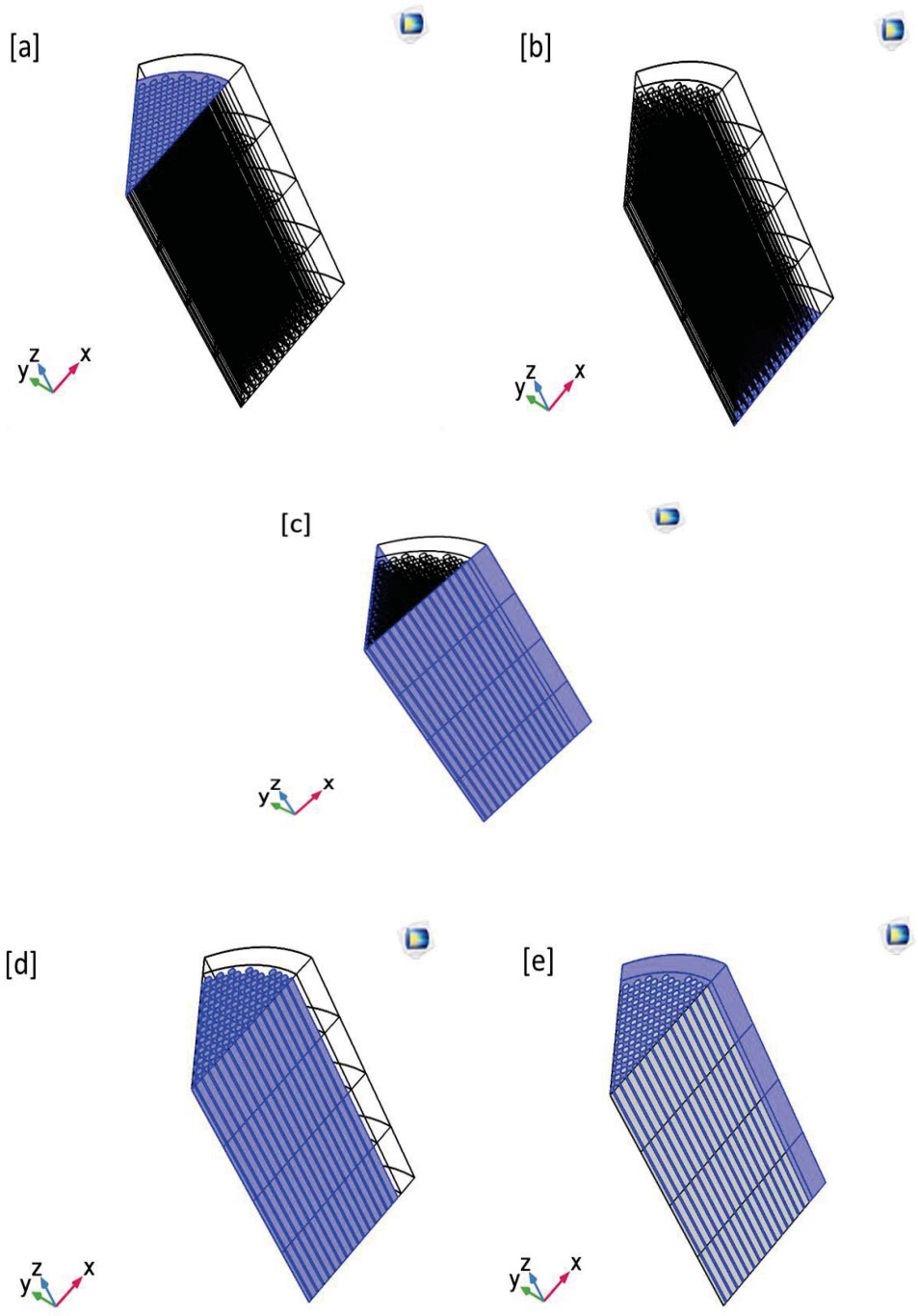


Figure 4.5 3D Sector view showing the computational domains Regenerator

[a]: Outlet Walls, [b]: Inlet Walls, [c]: Symmetry Walls

[d]: Air domains and [e]: Solid domains (matrix and housing)

The unsteady time-dependent solution of the governing equations has been initialized with a stationary solution of heat transfer. As long as the temperature gradient established throughout the whole regenerator and the solution is a steady state, the computational time can be reduced.

The inlet faces of the regenerator geometry were meshed using Free Triangular elements and then the swept feature was used to sweep these elements over the length of the regenerator. The sensitivity of such mesh was examined using coarse, normal, fine, finer and extra fine tetrahedral. The grid independence study is presented in Table 4.2, which summarises the details of each meshing sequence and the obtained solution of Nusselt number. The difference in the simulation results between the finer and extra fine mesh was 1.24% while the difference in the simulation solving time 10 hours. In order to minimise the solving time, and as it can be seen in Figure 4.6, the finer tetrahedral elements used in modelling this engine with grid density of (304872) elements with average quality (0.7983). The CFD model was set up with relative iteration convergence tolerance of 1e-4. The larger tolerance values produce inaccurate results since convergence tolerance applies to each step, and then error accumulates over a series of iterations when tolerance is not sufficiently tight. The time stepping is resolved by 20 times over the cycle in this model. The run takes up to one day for each simulation using a PC with specification of run at speed 3.7 GHz with 48 RAM memory, Intel® core™ CPU i7-4820K.

Table 4.2 Grid independence and CFD results

Mesh sequence	No of elements	Mesh quality	Solving time (hours)	Growth rate	Nu
Coarse	43128	0.6448	15	1.334	6.0135
Normal	81216	0.7234	18	1.327	5.9344
Fine	225816	0.7477	21	1.259	5.79
Finer	304872	0.8319	22	1.219	5.7505907
Extra-fine	462528	0.8714	32	1.179	5.6998165

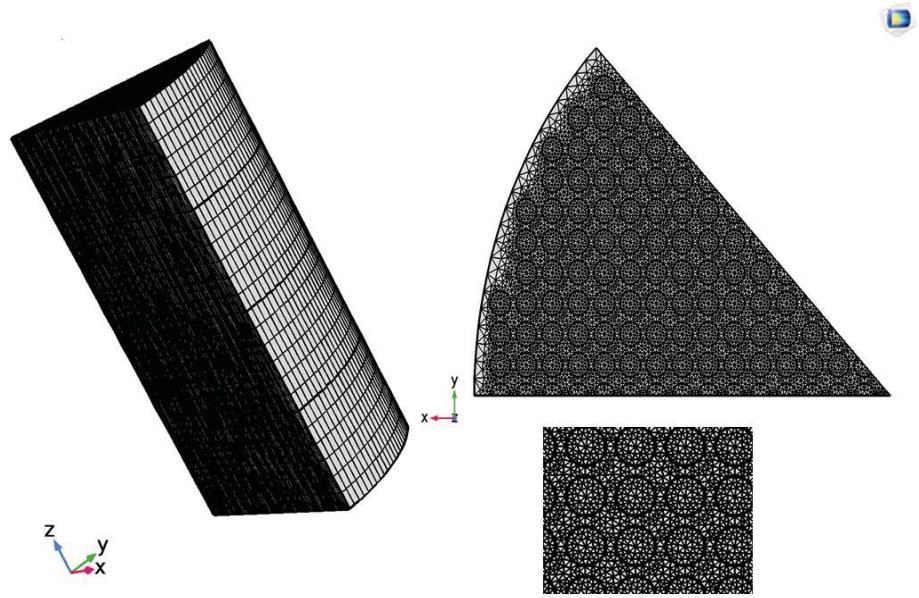


Figure 4.6. Regenerator model mesh distribution

Since the pressure drop is known from this simulation, then the porous media parameters Forchheimer drag coefficient β_F and Permeability K can be obtained from the following Eq. (4.16):

$$\frac{\nabla p}{L} = \frac{\mu}{K} u + \beta_F u^2 \qquad 4.16$$

Forchheimer drag coefficient β_F , Permeability K and porosity will be used later in the CFD model of V alpha-type Stirling engine in terms of evaluation of the engine performance with the developed regenerator. Figure 4.7 illustrates the temperature contours for the main four inlet faces of the 4-segmented regenerators in one directional flow with 10 mm distance between each face. In Figure 4.7 (a) the maximum temperature is around 90 ^{0}C, while the minimum temperature in Figure 4.7 (d) at the beginning of the fourth face is around 85.5 ^{0}C and both after 360 s.

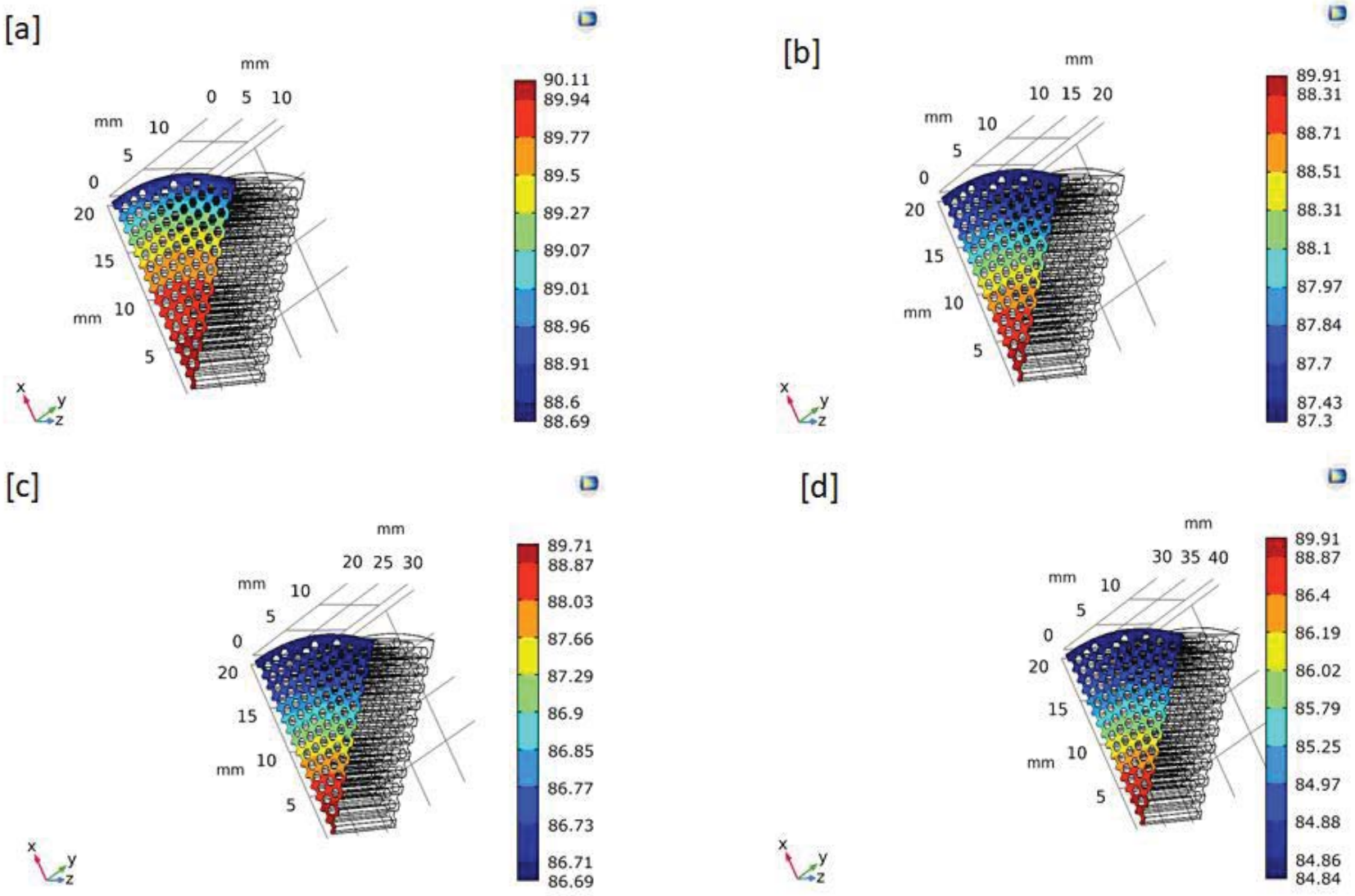


Figure 4.7 Temperature faces contours (^{0}C) for the 4-segmented regenerator at time of 360 s and one direction flow

4.4.1.1 Nusselt number calculation method

Study by reference [100] was chosen in order to validate the values of Nusselt number obtained from the CFD model. The study by was conducted on an experimental and numerical study using an annuals min-channels regenerator with one directional flow.

The Nusselt number *Nu* is defined as:

$$Nu = \frac{h\, D_h}{k_f} \tag{4.17}$$

The calculation of the heat transfer coefficient was based on the heat flux and the average temperature of both the bulk fluid and the interfaces wall as:

$$h = \frac{\mathbf{q}''_{-net}}{T_b - T_w} \tag{4.18}$$

Where,

$\mathbf{q}''_{-net}$ the net heat flux and can be evaluated from the CFD model as,

$$\mathbf{q}''_{-net} = k_f \left[\left(\frac{\partial T}{\partial r}\right)_{wall}\right]_x \tag{4.19}$$

The total heat flux $\mathbf{q}''_{-tot}$ can be determined from equation 6.16,

$$\mathbf{q}''_{-tot} = \dot{m} C_p \Delta T / A_s \tag{4.20}$$

Where;

ΔT is the air temperature difference between two ends, while A_s is internal surface area of the regenerator. The effect of the forced convection in the unidirectional flow can be seen in Figure 4.8, which illustrates the results of the total heat flux against the flow rate. The heat flux increases as the flow rate increases and that follows the basic concepts of heat transfer.

Figure 4.9 shows the comparison between the Nusselt numbers CFD predicted values and the correlated ones indicating good agreement with maximum deviation value of 10.5%.

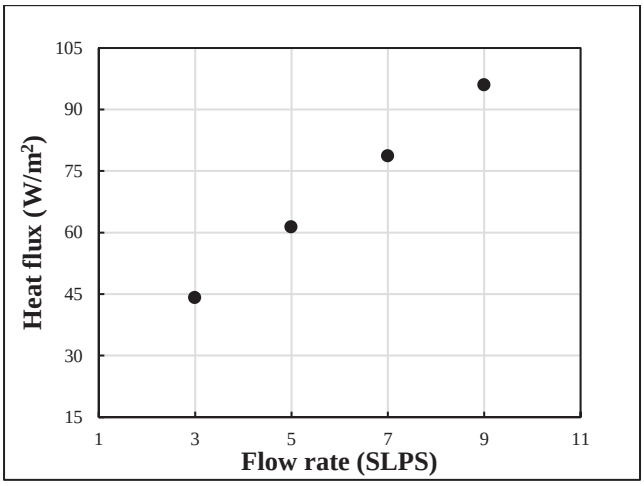


Figure 4.8 Heat flux Vs. flow rates

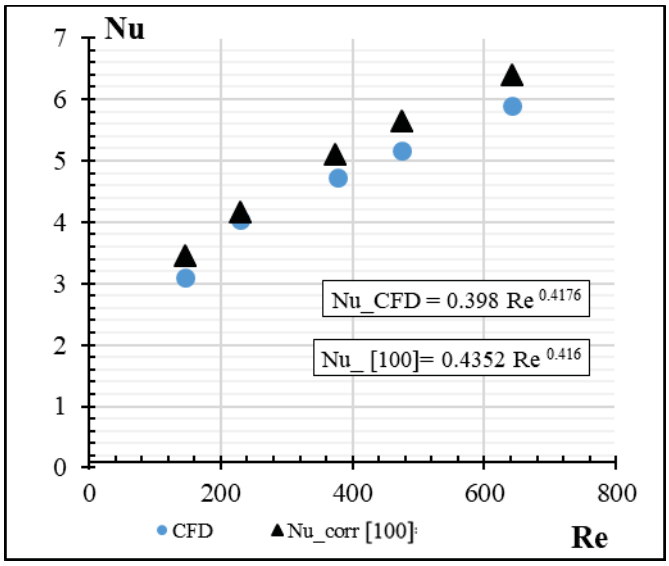


Figure 4.9 Validation of Nusselt number

The friction factor is calculated from the mean air velocity and pressure drop as:

$$f = \left(\frac{\Delta P}{\frac{1}{2}\rho {U_m}^2} \right) \frac{D_H}{L} \qquad 4.21$$

4.4.2 Regenerator Test Facility Layout

In this section, a detailed description of the developed micro channel regenerator heat exchanger test rig components and measuring devices is presented. This experimental work aims to validate the developed CFD modelling, evaluate and compare the developed micro channel regenerator with a conventional regenerator heat exchanger made of random fibre in terms of pressure drop and temperature difference between the hot and cold side.

Figure 4.10 shows the CAD drawing for the segmented micro-channel regenerator heat exchanger consisting of four parts, 10 mm length each and overall diameter of 40 mm. The four micro-channel parts were assembled and fitted in four housings with two conical adaptors (10 mm to 40 mm), the whole assembly is labelled as the test section. (The engineering drawings in Appendix C)

Figure 4.11 shows the segmented micro-channel regenerator heat exchanger with each micro hole havimg a hydraulic diameter of 1 mm. This was machined using advanced CNC machining facilities at the University of Birmingham. Two thin metal wire (each has diameter of 0.5 mm) were inserted into two of the matrix micro holes in order to aligned the four parts (segments) of the solid matrix.

Figure 4.12 shows a schematic diagram of the experimental regenerator test facility. The test rig contains four solenoid valves to ensure flow in directions, two pressure transducers, three heaters, one flow meter and eight thermocouples distributed along, before and after the test section. Figure 4.13 shows a pictorial presentation of the fully assembled experimental test facility for the micro channel regenerator, which was built in the thermo-fluid laboratory at the University of Birmingham.

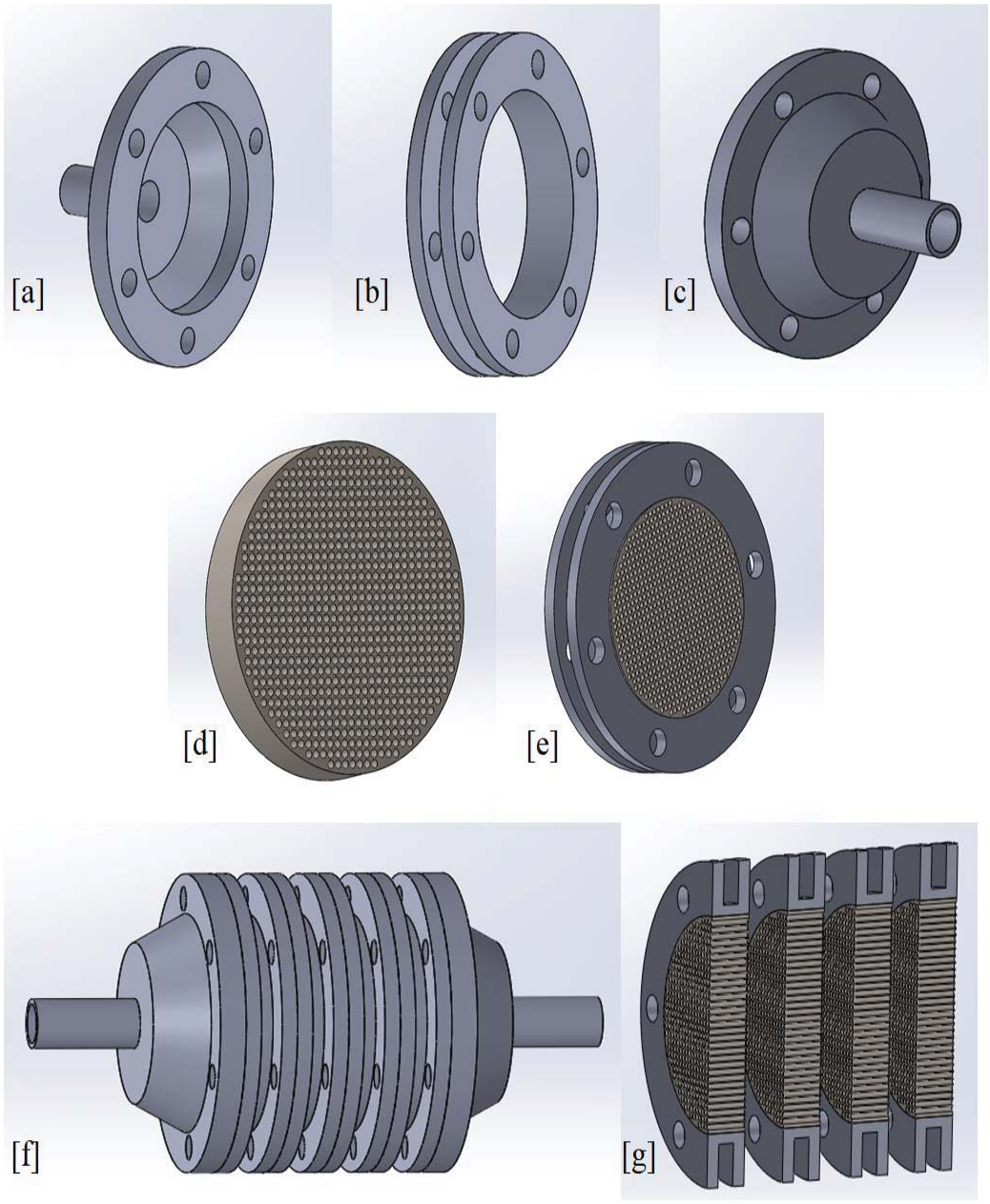


Figure 4.10 CAD drawing of the test section:

[a] conical adaptor (hot side), [b] housing, [c] conical adaptor (cold side), [d]&[e] one micro-channel regenerative heat exchanger & its housing, [f] whole test section, [g]symmetric & exploded view of the 4micro-channels and their housings



Figure 4.11: [a] Exploded view of the micro-channels regenerative heat exchanger and their housing ,[b] Micro-channels heat exchanger and [c] Random fibre regenerative heat exchanger

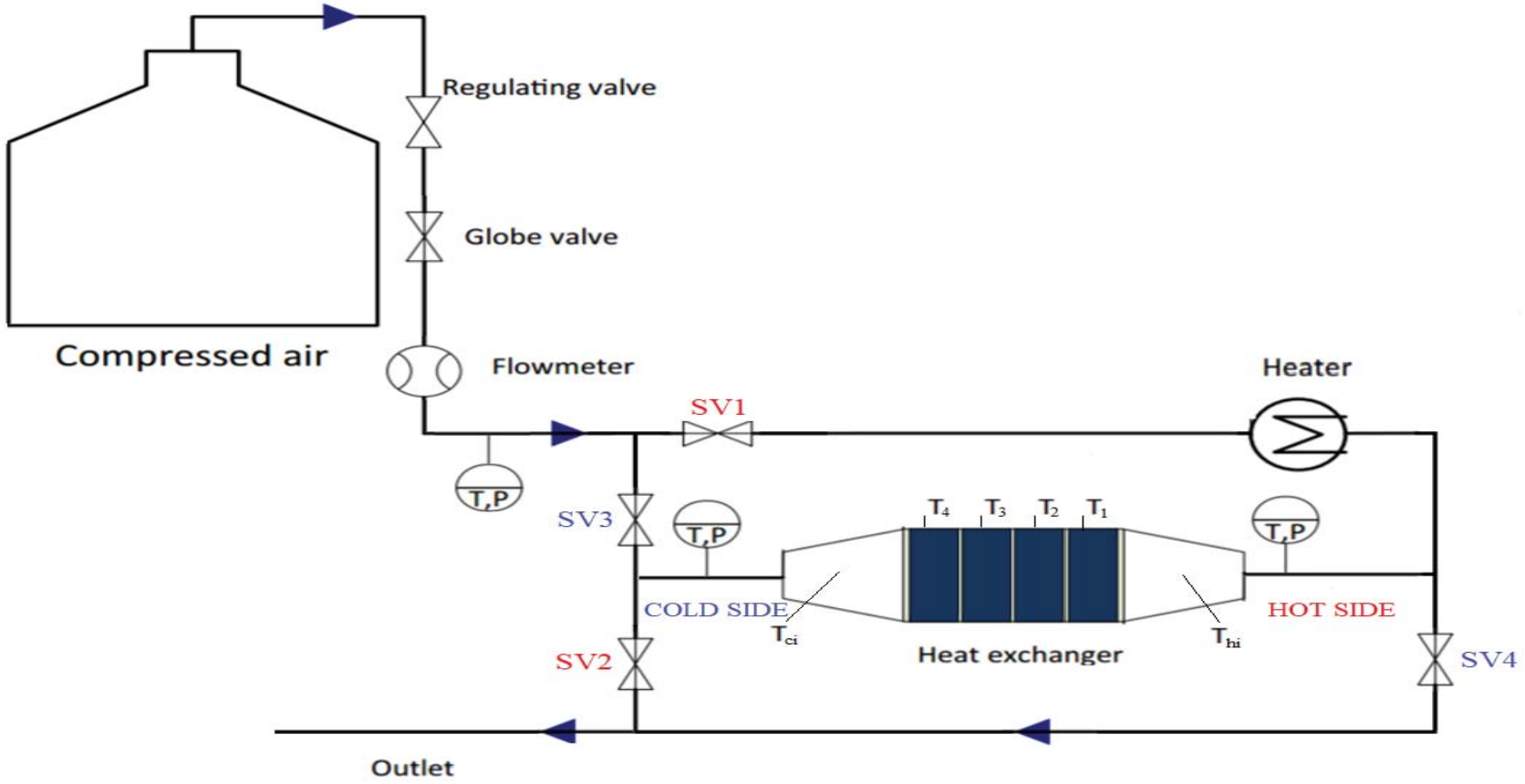


Figure 4.12 schematic of the Regenerator test rig

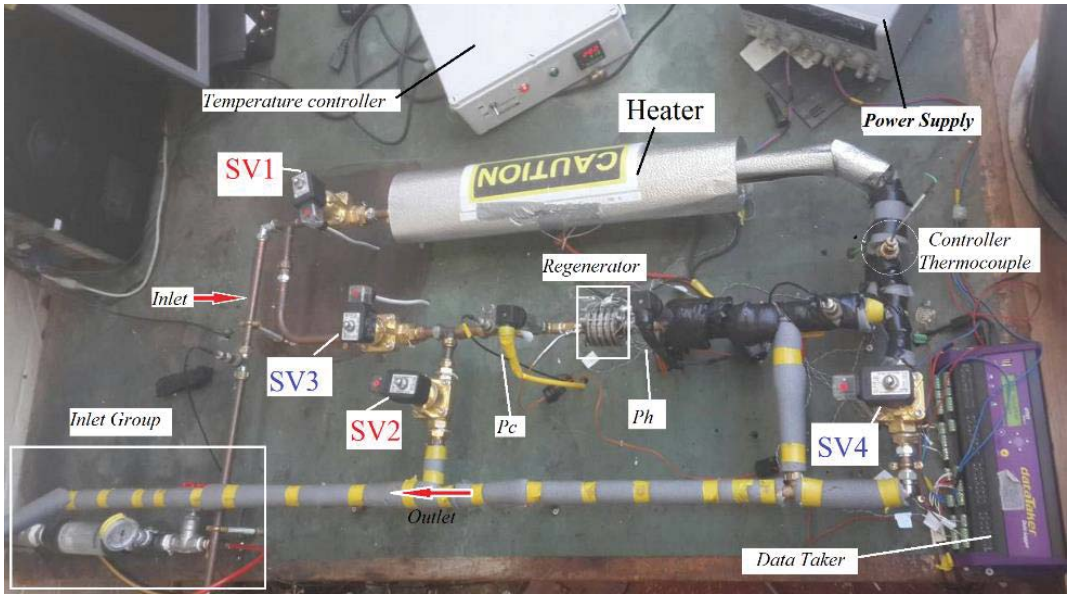


Figure 4.13 Pictorial figure of the whole regenerator test rig

4.5 Instruments and Measuring Devices

4.5.1 Flow meter

Compressed air was used to run this system through copper pipes (15 mm diameter) with a flow meter that measures the inlet airflow rate. Figure 4.14 shows the Omega FLMG-10050A flow meter used in this experiment; it has capacity up to 23 SPLS.



Figure 4.14 Omega FLMG-10050AL

4.5.2 Heater

The air is heated using three electrical rope heaters (OMEGALUX®), each heater is wrapped around the copper pipe just before entering to the test section from the heating side (See Figure 4.15). Each rope heater provides about 0.16 W/mm (as a linear wattage scale) and has a diameter of 5 mm and 3 m length.

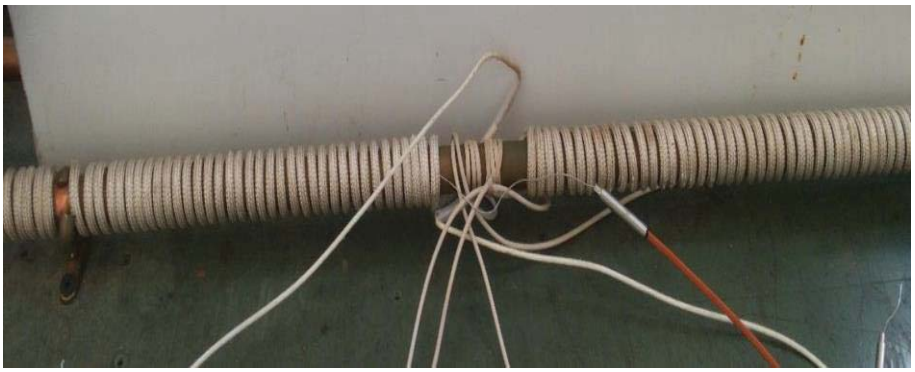


Figure 4.15 Electric heater wraps around inlet line

4.5.3 Electrical control box

Figure 4.16 (a) shows the temperature controller box (Inkbird Dual Digital PID with 25A SSR Solid State Relay) which controls the temperatures of the heaters. The PID controller as shown in Figure 4.16 (b) is connected with K- Type thermocouple as a sensor probe, which fitted inside the copper pipe to measure the temperature up to the specified value.

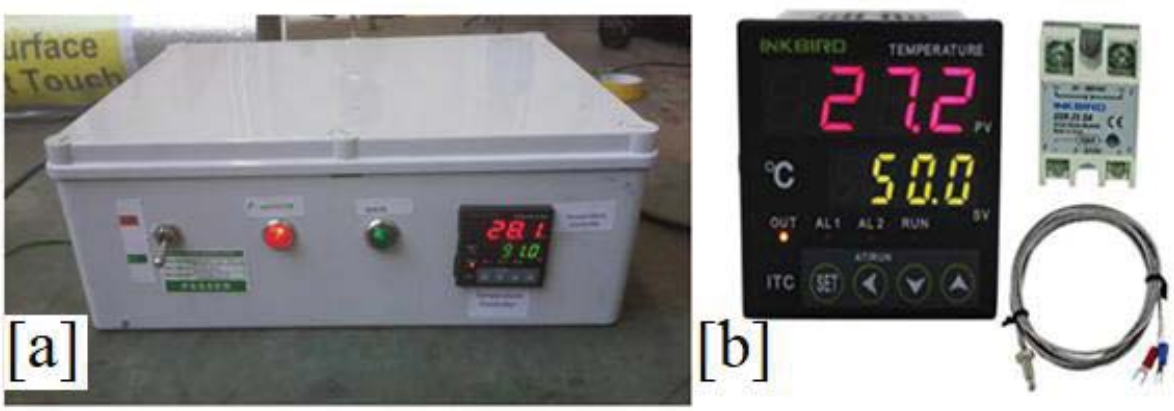


Figure 4.16 [a]Temperature Control box, [b] Inkbird Dual Digital PID with 25A SSR Solid State Relay and K Sensor probe" [102]

4.5.4 Flow control valves

The test rig designed to study two types of flow: unidirectional (single-blow) flow and two-directional (oscillatory) flow, with the air passes through the regenerator (test section) via four solenoid valves (SV1, SV2, SV3 and SV4), (See Figure 4.13), as:

For the unidirectional flow:

- Line SV1/SV2 is opened and line SV3/SV4 is closed.

For the oscillating flow:

- Case of heating blow: line SV1/SV2 is opened and line SV3/SV4 is closed.
- Case of cooling blow: line SV3/SV4 is opened and line SV1/SV2 is closed.

Figure 4.17 shows the on/off solenoid valves used in the test rig; it is made by 'Steam' type (SAH HH). It is designed to withstand temperature up to 180 ^{0}C, which is suitable to cover the target temperature ranges in the experiment.

'Labview' software was used to control the four solenoid valves via a control board. The control board, as in Figure 4.18 , made by 'National instruments' company, model number NI 6008. A screen shot in Figure 4.19 shows the user "Labview" interface where the half-cycle time, the number of cycles, the cold, and hot blow are shown. The solenoid valve electric circuit is opened or closed by a relay as it receives either 0 or 5 volts signal from the control board, these signals are driven by the 'Labview' software as shown in Figure 4.20.



Figure 4.17 Solenoid valve, 'Steam- SAH HH'



Figure 4.18 control board by National Instruments, 'NI 6008'

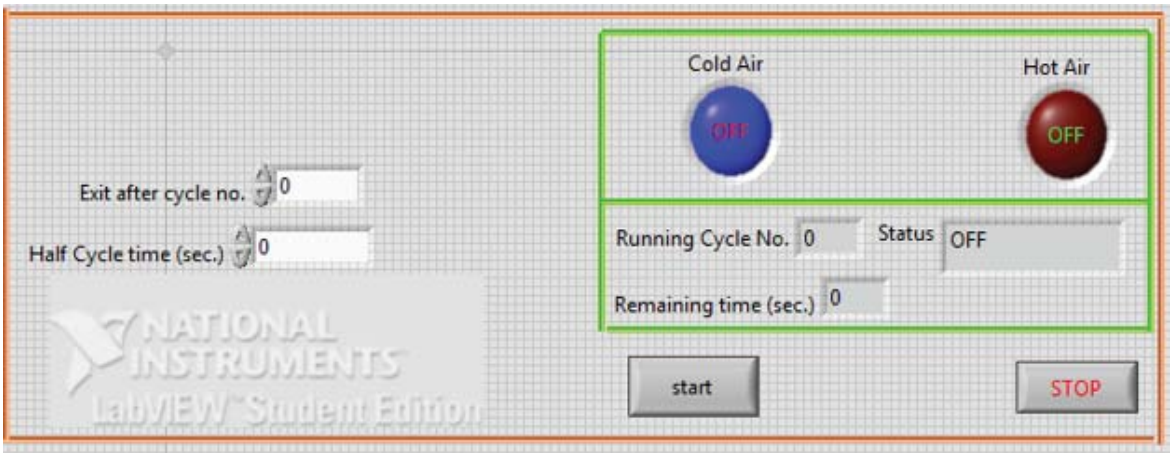


Figure 4.19 'Labview' software user interface

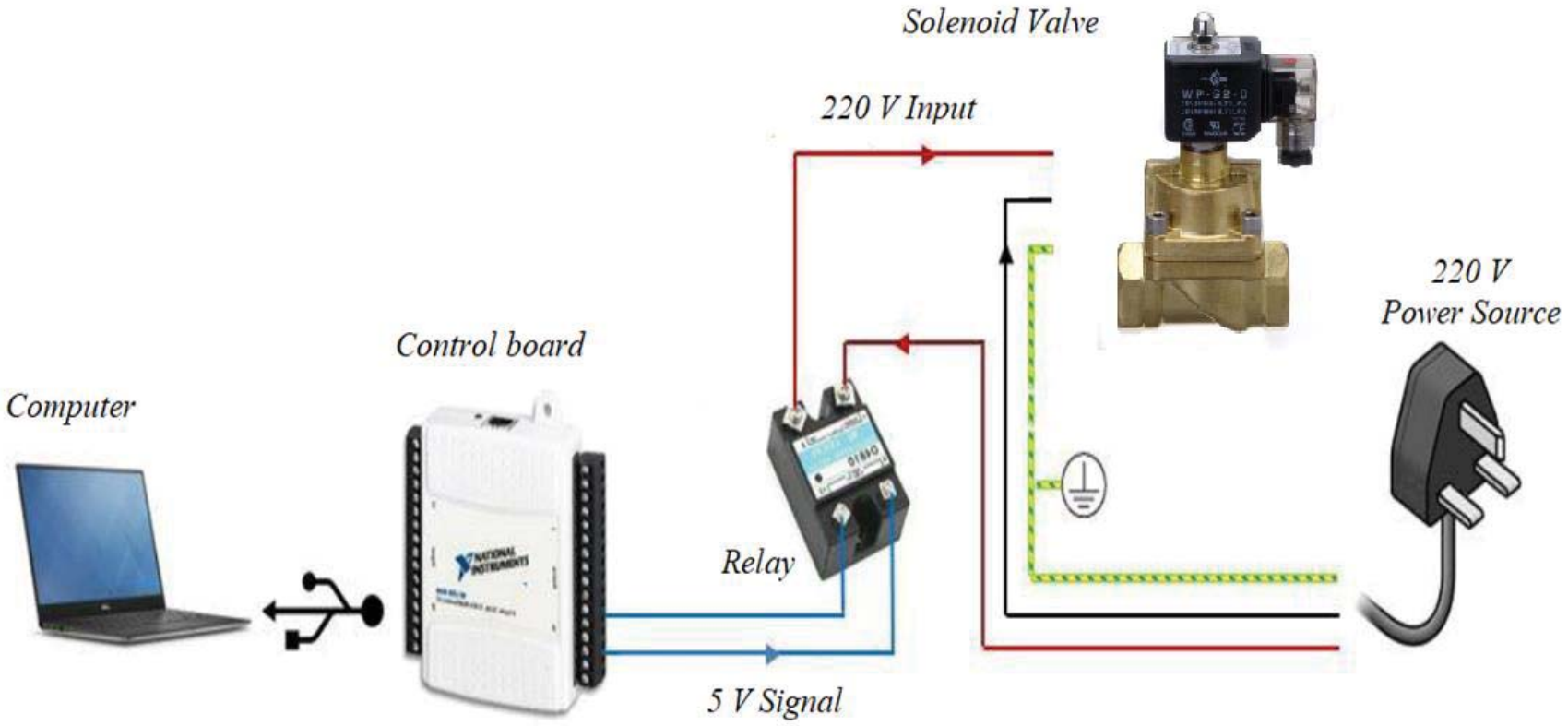


Figure 4.20 The control of solenoid valves electric circuit

4.5.5 Thermocouples

Three Platinum RTD probes were used in the test rig, each one has 6 mm diameter and 100mm length (See Figure 4.21), two of them were measuring the inlet (hot side) and outlet (cold side) flow temperatures of the test section and they are labelled **Th** and **Tc**. The third RTD probe is for measuring the inlet temperature $\mathbf{T_{in}}$ to the whole system and it is located at the main pipe just before the flow entering to SV1 or SV3.



Figure 4.21 RTD sensors

Four surface thermocouples T-type ($\mathbf{T_1}$, $\mathbf{T_2}$, $\mathbf{T_3}$ and $\mathbf{T_4}$) were distributed along the regenerator-housing surface with 10 mm distance between each one as shown in Figure 4.22.

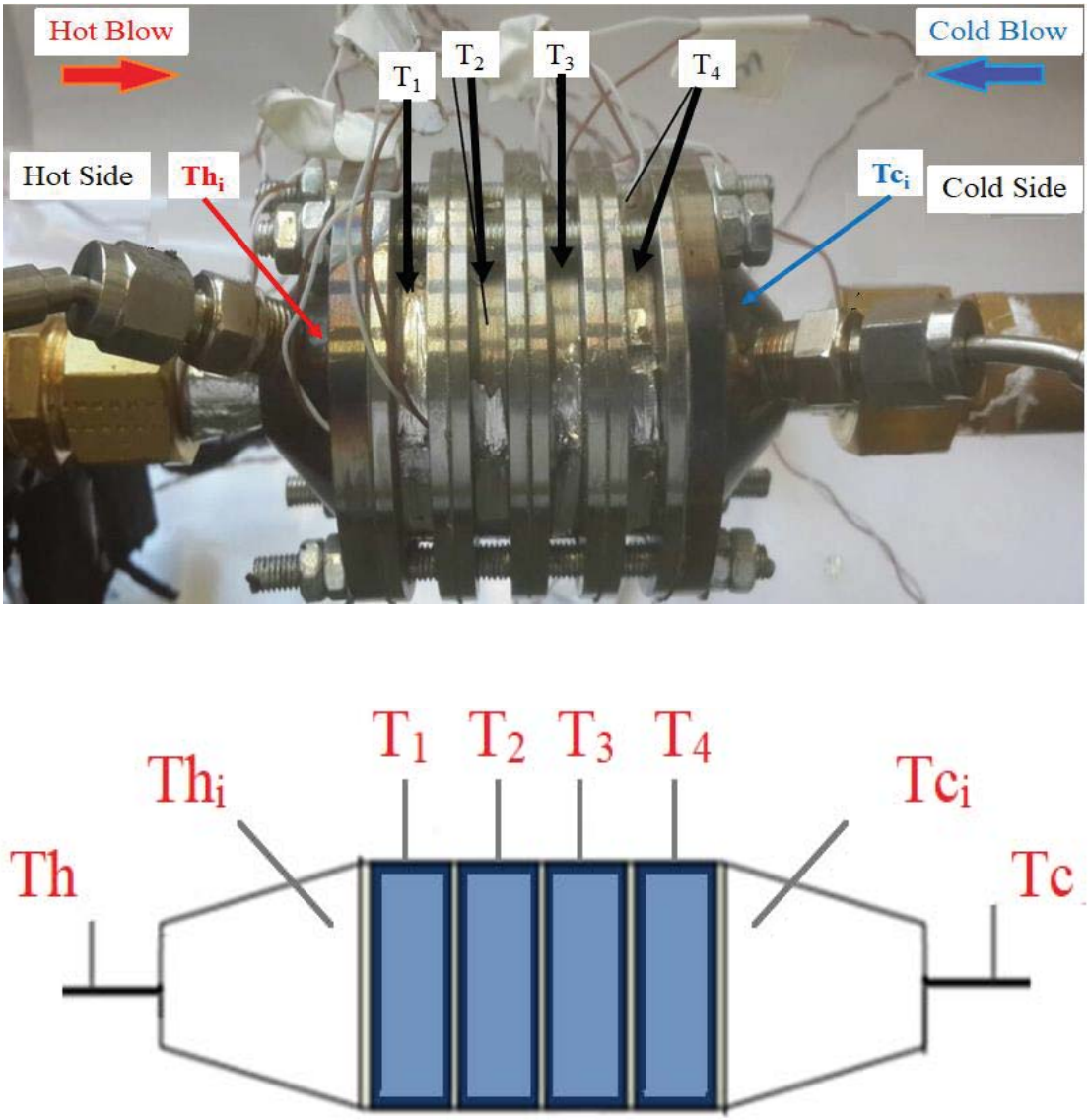


Figure 4.22 Positions of thermocouples at the inlet, outlet and on the surface of the test section

Two temperature probes T-type of (**Th_i** and **Tc_i**) can be seen in Figure 4.22, each one has 3 mm diameter with 0.1 °C accuracy, and they are respectively located at inlet and outlet of regenerator (both are inserted in the conical adaptor and measuring the flow temperature).

4.5.6 Pressure transducers

A constant recording and measuring of the pressure during each test was applied in the test rig by using two pressure transducers. One is measuring the pressure at the hot side while the other measuring the pressure at the cold side (See Figure 4.23). Both pressure transducers can work between 0 to 10bar range, with accuracy of ±0.2%, and they are made by Omega Engineering Ltd. They have current output value from 4 to 20 mA, with 100 ohms' resistance was used to convert the pressure transducers current to voltage signals to match the input requirements for the data taker. Figure 4.24 shows the pressure transducers wiring diagram and the DC power supply that was used in the test rig.



Figure 4.23 Pressure transducers at the cold side of the test section

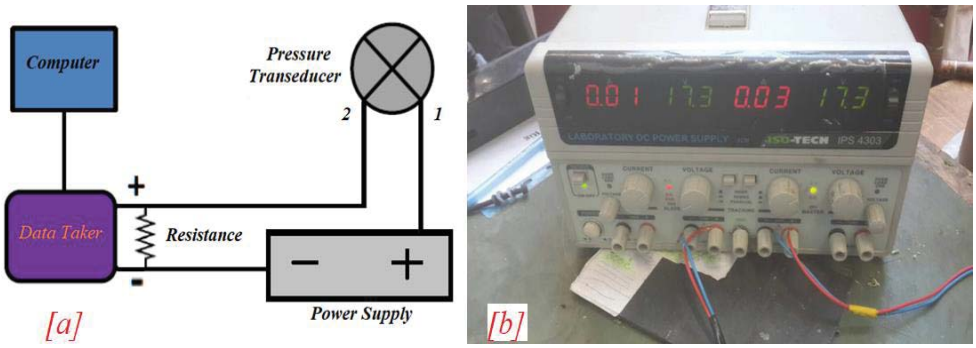


Figure 4.24 [a] Pressure transducer electrical wiring diagram [b] the DC power supply

4.5.7 Data taker

Figure 4.25 shows the Data Taker DT85, which was used to log the temperature and pressure readings from the thermocouples and pressure transducers, the logged data was saved each 1 second to a computer.



Figure 4.25 Data taker

4.6 Devices Calibration:

To ensure that the data evaluation for the regenerator fluid flow and heat transfer characteristics are accurate, all thermocouples and pressure transducers were calibrated. This task was achieved by comparing a standard measurement against the measured data.

4.6.1 Thermocouple calibration

The thermocouples and the pressure transducers were calibrated before fitted to the test rig in term of achieving accurate results at different conditions. An alcohol thermometer was used against the all thermocouples, including the one that connected with the Temperature Control box, they are all put together in a beaker which was filled with water after they were connected with the DataTaker. The beaker was heated using an electrical heater; the whole group can be seen in Figure 4.26. The Data Taker was recording all the changes in the thermocouple

temperature with the time. Figure 4.27 shows a sample of the thermocouple calibration chart for T_1 while for the other thermocouples can be found in Appendix D.

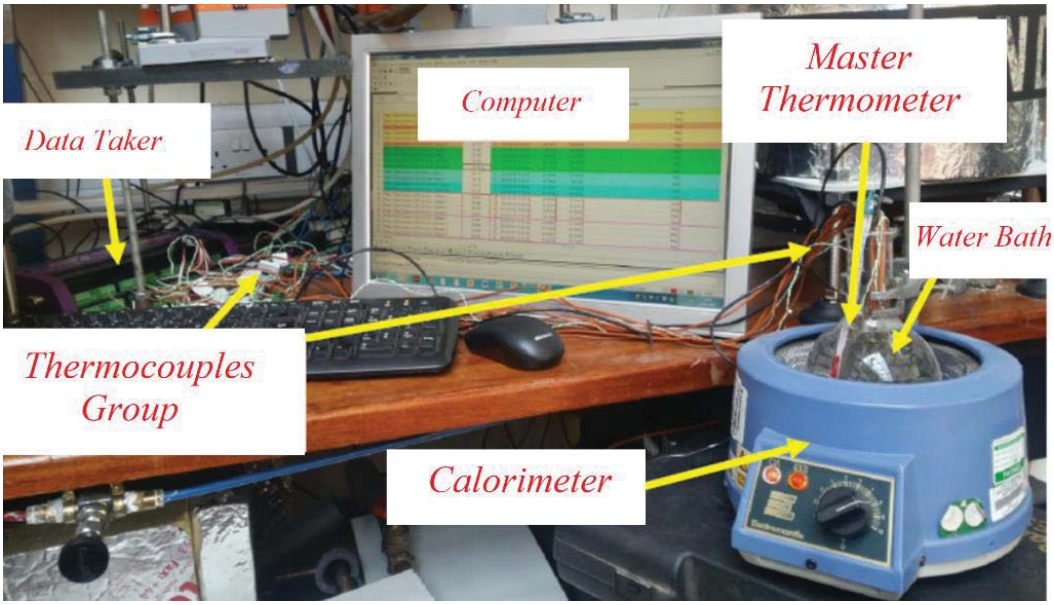


Figure 4.26 Thermocouples calibration

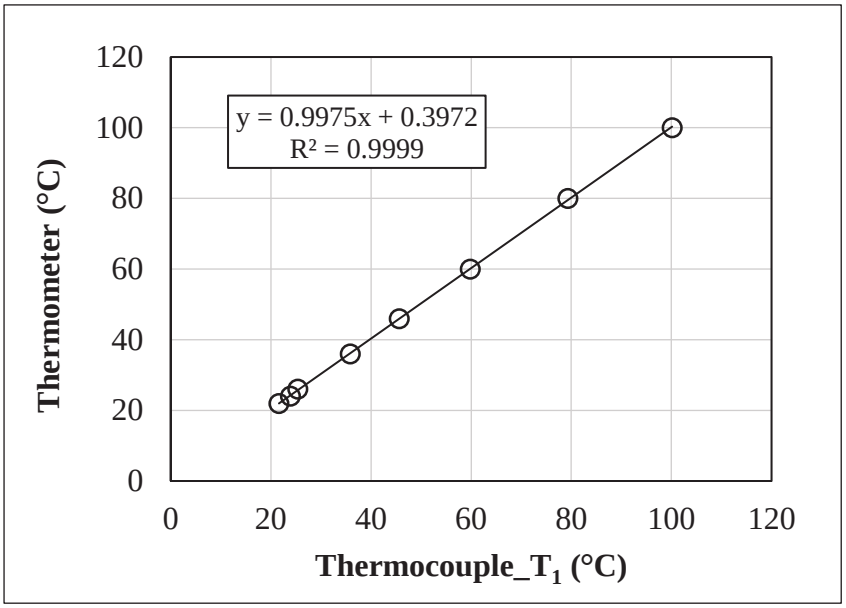


Figure 4.27 Thermocouple calibration chart for T1

4.6.2 Pressure transducers calibration

For the calibration of the pressure transducers, a standard pressure gauge was used against each pressure transducer reading, as seen in Figure 4.28. Similar to the thermocouples calibration, both pressure transducers were connected to the Data Taker which was recording all the changes in pressure transducer readings with the time (See Figure 4.29). The other pressure transducer procedure can be found in Appendix D

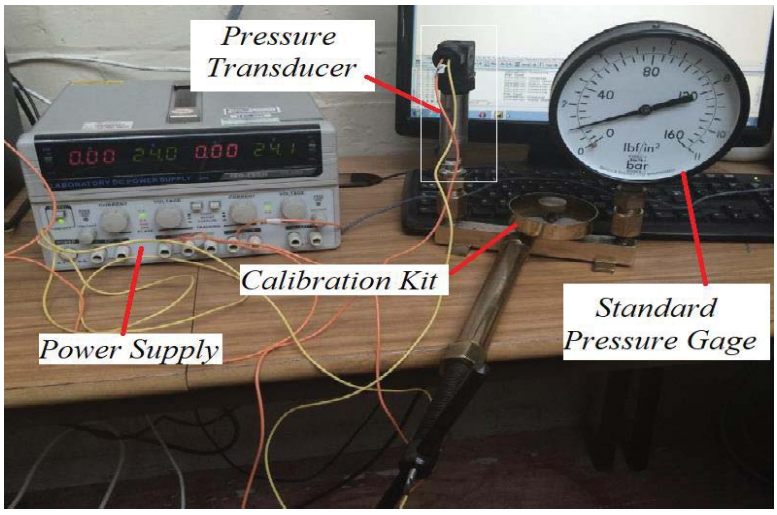


Figure 4.28 Pressure transducers calibration

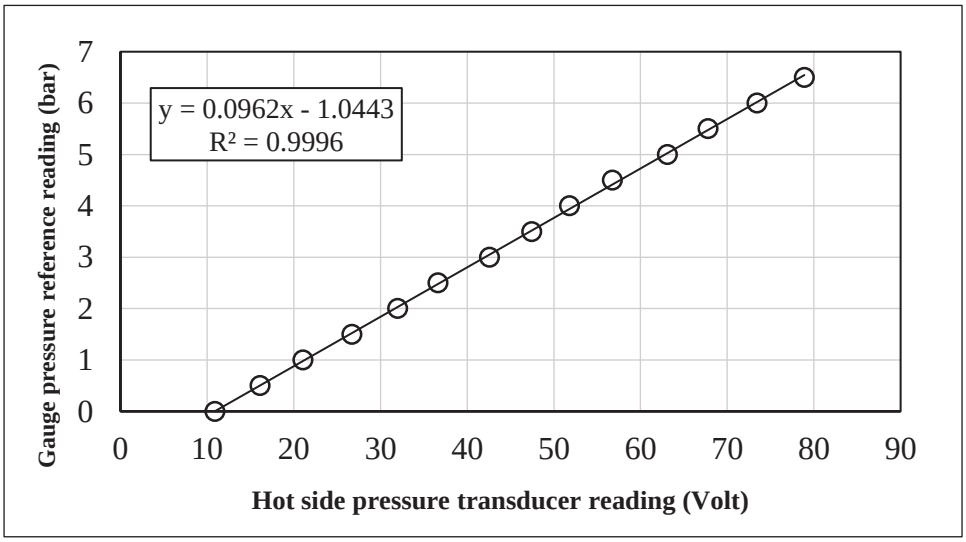


Figure 4.29 Pressure transducer calibration chart

4.7 Measurement Accuracy

As introduced previously, for achieving accurate measurements, all pressure transducers and thermocouples (T-type and RTD) were calibrated. The systematic (Z_{sys}) (bias) error and the random (Z_{random}) (Precision) error which is known as the overall uncertainty (deviation) combined using the standard mean square approach as[103]:

$$Z_{Overall} = \pm\sqrt{Z_{Sys}^2 + Z_{random}^2} \qquad 4.22$$

The systematic error, which related to a several number of fixed error measuring device (N), can be corrected as:

$$Z_{Sys} = \sqrt{\sum_{i=1}^{N} Z_{i,Sys}^2} \qquad 4.23$$

The naturally statistical error called the "random error" can be calculated by using standard mean deviation with a 95% confidence interval as:

$$Z_{random} = t_N - 1{,}95\%\dot{O}s \qquad 4.24$$

Where:

t: is the coefficient of standard distribution

$\dot{O}s$: is the mean deviation and it determined as[103]:

$$\dot{O}s = \frac{1}{\sqrt{N}}\sqrt{\frac{\sum_{i=1}^{N}(X_i - \bar{X})^2}{N-1}} \qquad 4.25$$

Where: X_i: Standard device reading, and the curve fit value is $\bar{X}$

All thermocouple and pressure transducers uncertainties are listed in Table 4.3 and Table 4.4 respectively.

Table 4.3 Summary of thermocouple calibration and uncertainties

Item Name	Thermocouple	Curve Fit Formula	R2	Uncertainty (^{0} C)
T-Type	Th_i	0.9961×T+0.3272	0.9999	±0.3
	T_1	0.9975×T + 0.3972	0.9999	±0.354
	T_2	0.9963×T + 0.2944	0.9999	±0.314
	T_3	0.9978×T + 0.3046	0.9999	±0.32
	T_4	0.9979×T + 0.0739	0.9999	±0.309
	Tc_i	0.9976×T+0.3512	0.9999	±0.3
RTD	Th	0.9961×T + 0.2254	0.9999	±0.42
	T_{in}	0.9874×T+1.0529	0.9999	±0.71
	Tc	0.9972×T + 0.2417	0.9999	±0.715

Table 4.4 Summary of pressure transducers calibration and uncertainties

PRESSURE TRANSDUCER	CURVE FIT FORMULA	R2	UNCERTAINTY (mbar)
Ph (Hot Side)	0.0962 × volt - 1.0443	0.9996	±0.84
Pc (Cold Side)	0.0957 × volt - 1.042	1	±0.81

4.8 Test Procedure

The test rig was developed to study the pressure drop and heat transfer characterises in Stirling engine regenerator and then to validate the CFD model of the proposed micro-channel regenerator. The test rig was designed to test two different regenerators under two different flow configurations: the unidirectional flow and the oscillating flow. The regenerator was tested for range of flow rates and inlet temperatures (SLPS = 3, 5 and 7) and (70 and 90 ^{0}C) respectively, with the recording of inlet and outlet pressure drops and temperatures.

The heater was switched on, and the flow was directed to the exhaust before entering to the test section, for around 10 min to ensure that the inlet temperature reaching the desired target of (70 or 90 ^{0}C) and then the flow was ready to be directed to the test section.

The four solenoid valves (See Figure 4.12 and Figure 4.13) (SV1, SV2, SV3 and SV4) were then operated to simulate an appropriate chosen rotational speed (r.p.m = 3, 6 or 30) using the 'Labview' software by entering the half-cycle time. The number of cycles also required to be inserted to the 'Labview' software interface to control the test running time (12 min for each run). The results of the fluid flow characteristics and heat transfer colorations of the regenerator matrixes are described in the next chapter.

4.9 Experimental Results

This section presents the experimental results for three regenerators: The Micro-channels, Random fibre and Non-aligned micro-channels in the one and two directions flow.

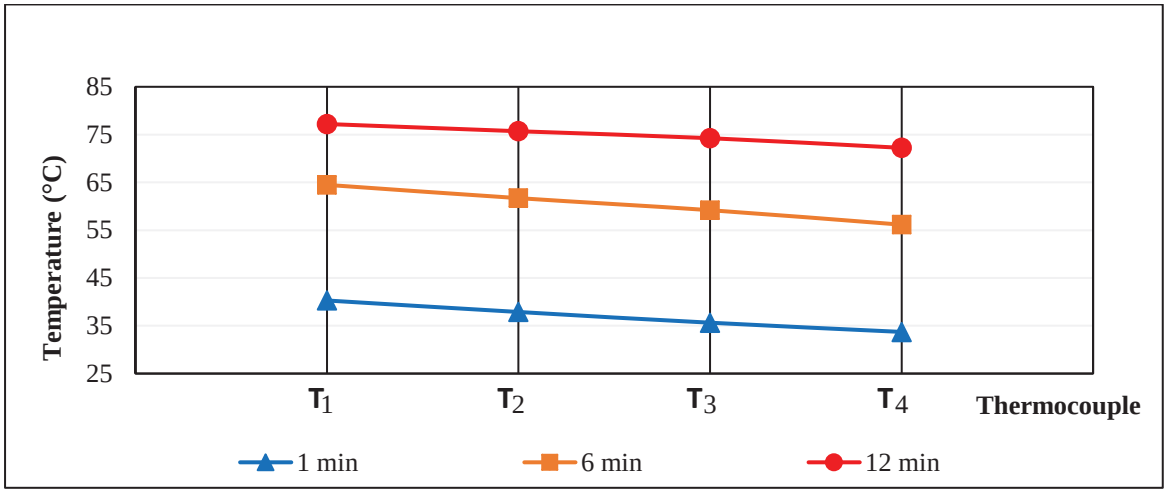
4.9.1 Results of one direction flow

The following results are based on the unidirectional flow test measurements of the inlet, outlet, housing surface temperatures and pressure losses.

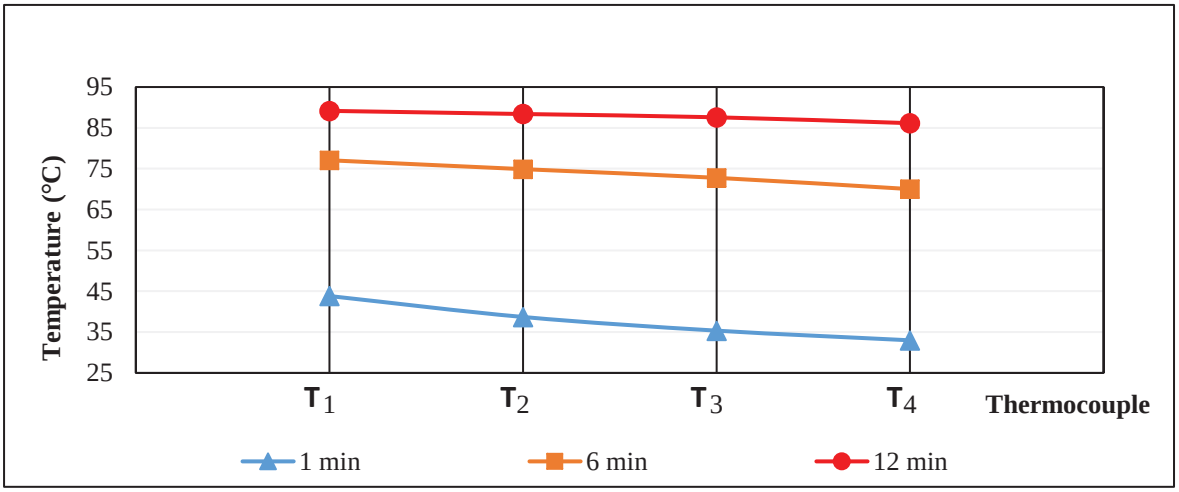
4.9.1.1 Surface temperature profile

The surface temperature distribution of the regenerator housing for the three regenerators Micro-channels, Random fibre and Non-aligned micro-channels at 3 different recording times (1, 6 and 12 minutes) with flow rate of SPLS=3 and SPLS=5 are shown in Figure 4.30 and Figure 4.31 respectively, with inlet fluid temperature was kept at 90^0 C for both cases. The surface temperatures measurement positions are presented in Figure 4.22 from Section 4.5.5.

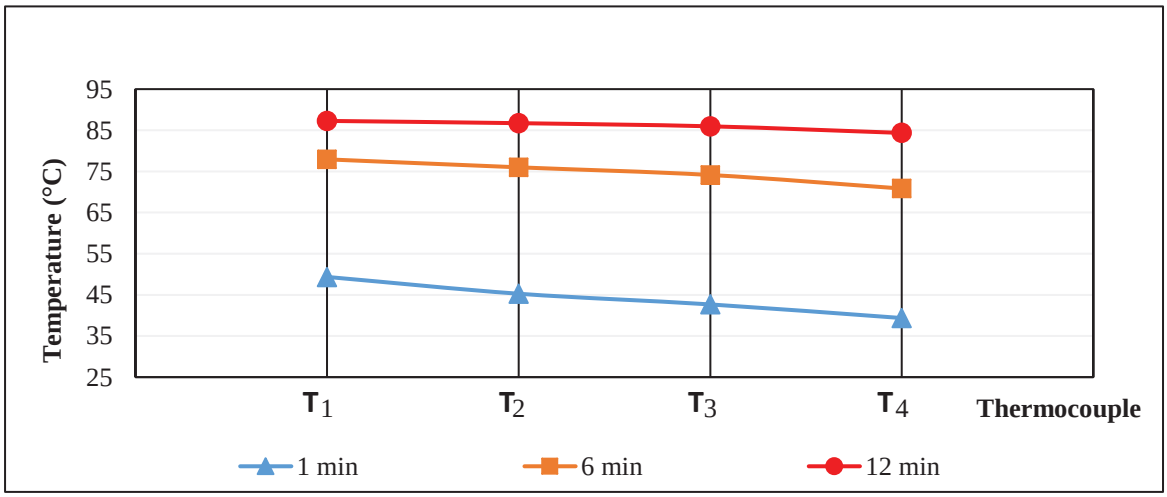
Figure 4.30 (b) and Figure 4.31 (b) show the Non-aligned micro-channels matrix surface temperatures, with the highest surface temperature value and it nearly equals to the inlet air temperature of 90 ^{0}C at flow rate of SPLS=5. The reasons can be related to the fact that the Non-aligned micro-channels matrix has the average pressure drop compared to the other (random and aligned micro-channels), and the other reason due to the high Reynolds number in the non-aligned channels leading to increased surface heat transfer coefficients.



[a] : (Random fibre matrix)

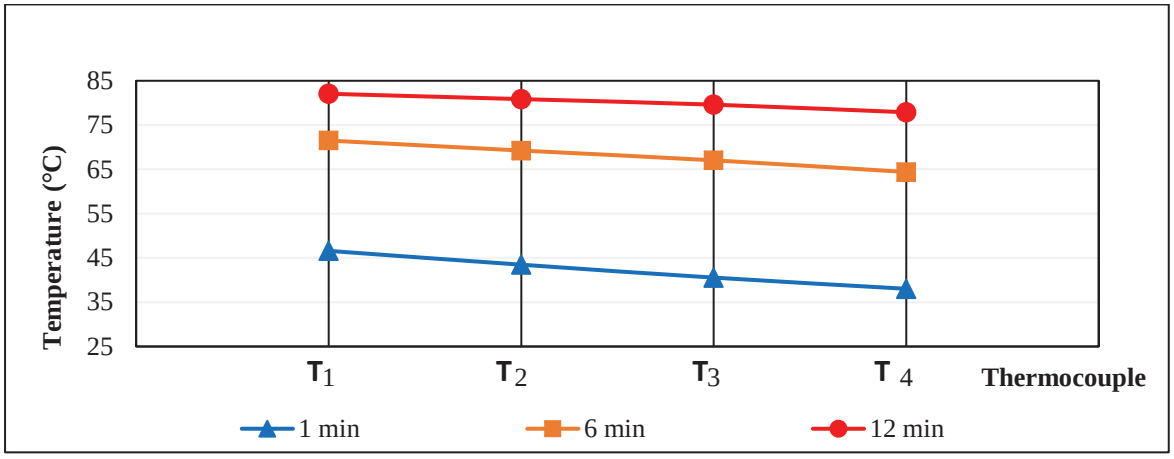


[b] : (Non-aligned micro-channels matrix)

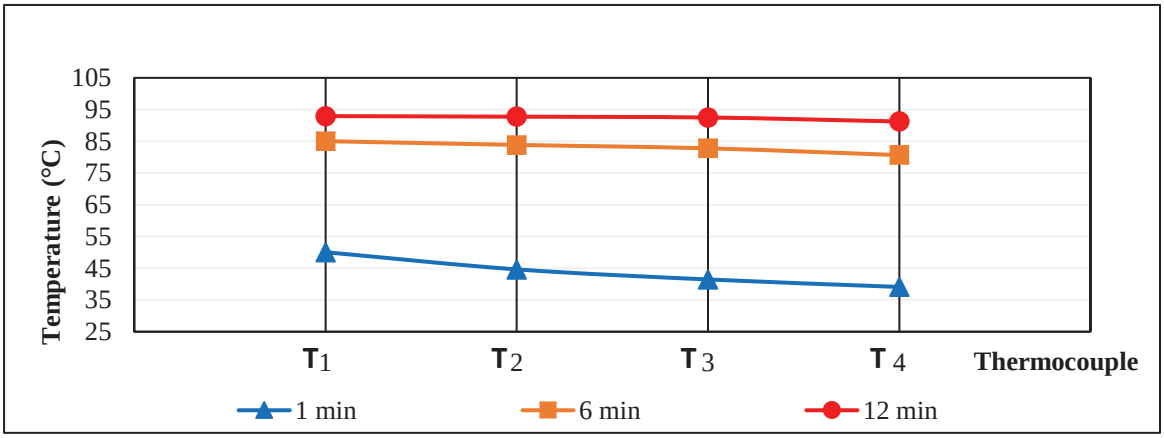


[c] : (Micro-channels matrix)

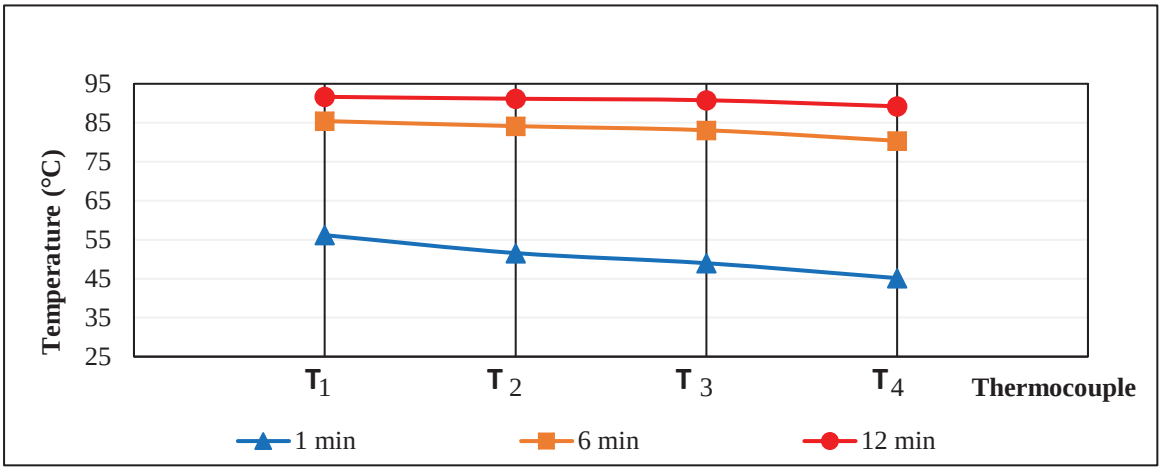
Figure 4.30 Surface temperature vs. Time (Th= 90 °C & SLPS=3)



[a] : (Random fibre matrix)



[b]: (Non-aligned micro-channels matrix)



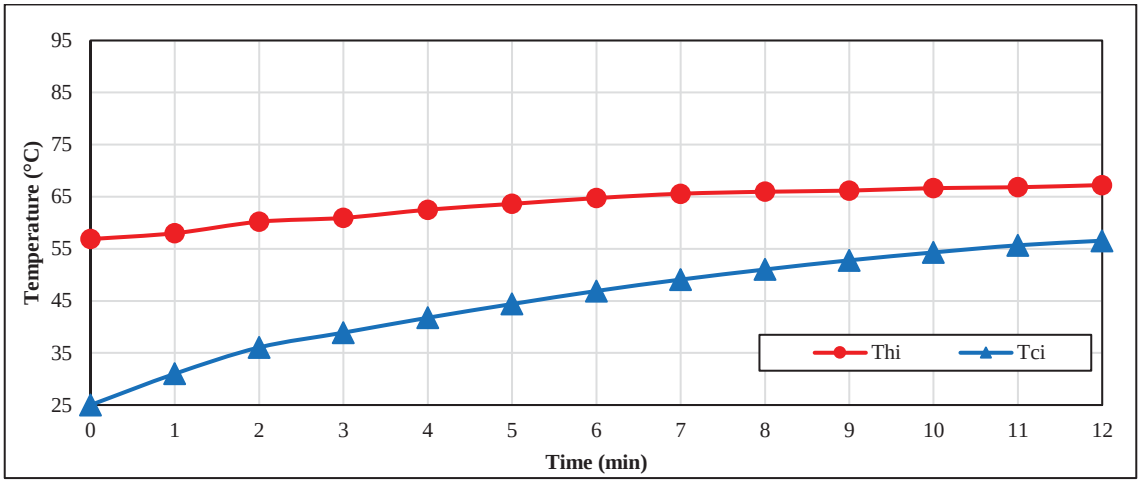
[c]: (Micro-channels matrix)

Figure 4.31 Surface temperature vs. Time (Th= 90 °C & SLPS=5)

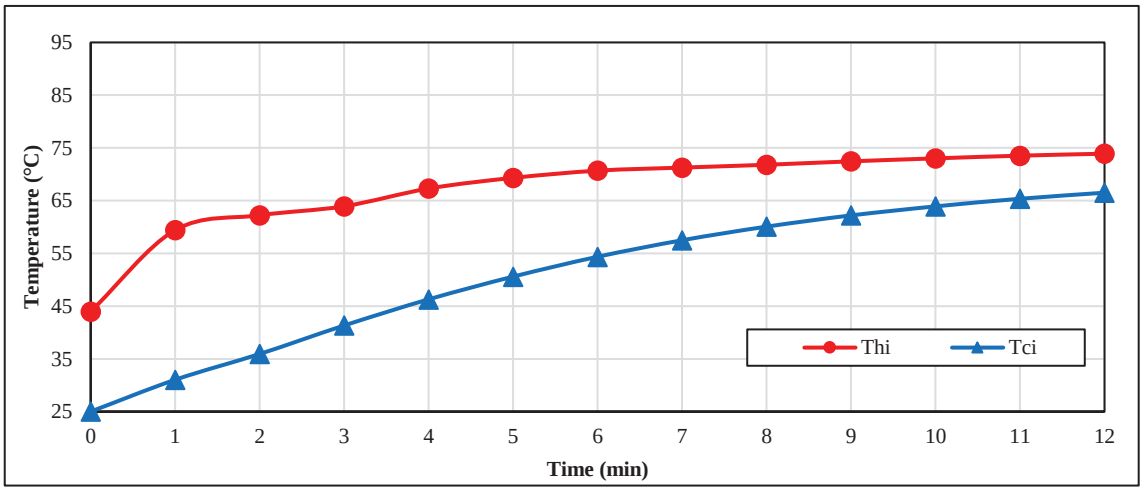
4.9.1.2 Inlet and outlet temperature difference

Figure 4.32 and Figure 4.33 show samples of inlet and outlet temperature profiles at main inlet temperatures of 70 ^{0}C & 90 ^{0}C, flow rate SPLS=3, and recording time of 0 to 12 min. Figure 4.34 shows the inlet temperature profile with an inlet temperature of 90 ^{0}C and flow rate SPLS=5, and recording time from 0 to 12 min. It is clear from these figures that similar trend in temperature increase with time is demonstrated with all regenerators which conform to the principles of the heat transfer.

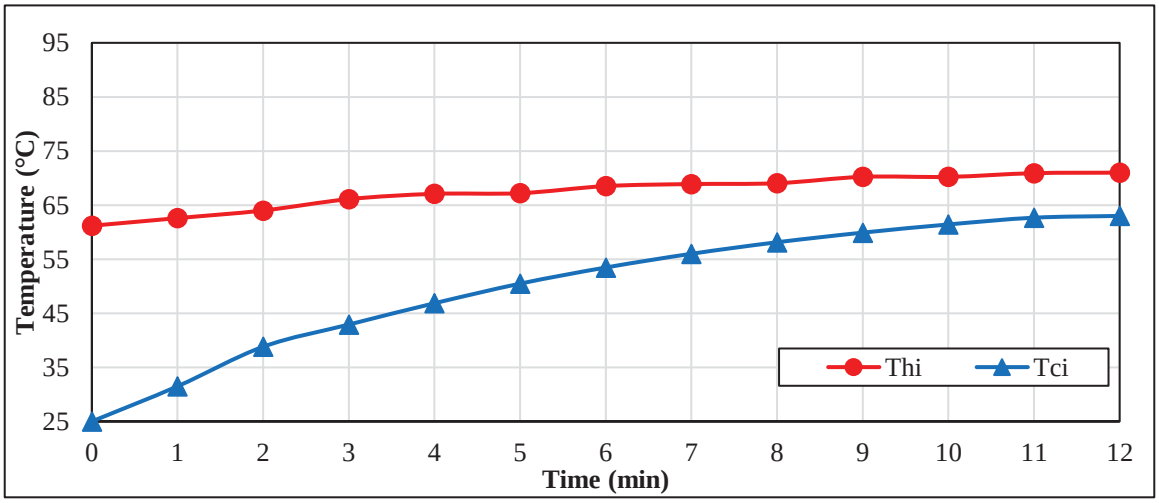
Figure 4.35 (a) and Figure 4.35 (b) showing the effect of changing the flow rate on the temperature difference between inlet and outlet temperature for the three regenerators: Micro-channels, Random fibre and Non-aligned micro-channels. The inlet temperature changed from 70 ^{0}C to 90 ^{0}C while the values of the flow rates are (3, 5, 7 at SPLS=9). Both figures showing a decreasing temperature trend with the increasing of the flow rate for the three matrixes. The Micro-channels matrix has the lowest temperature difference of 5.1 ^{0}C while the Random fibre matrix has the highest temperature difference of 7.9 ^{0}C at inlet temperature of 90 ^{0}C with similar trend at inlet temperature of 70 ^{0}C. The higher temperature difference across the regenerator will lead to better overall engine performance from the thermal point view since it allows for more efficient heat transfer between the working fluid and the regenerator matrix, but it may lead to higher pressure losses across the regenerator.



[a]: (Random fibre matrix)

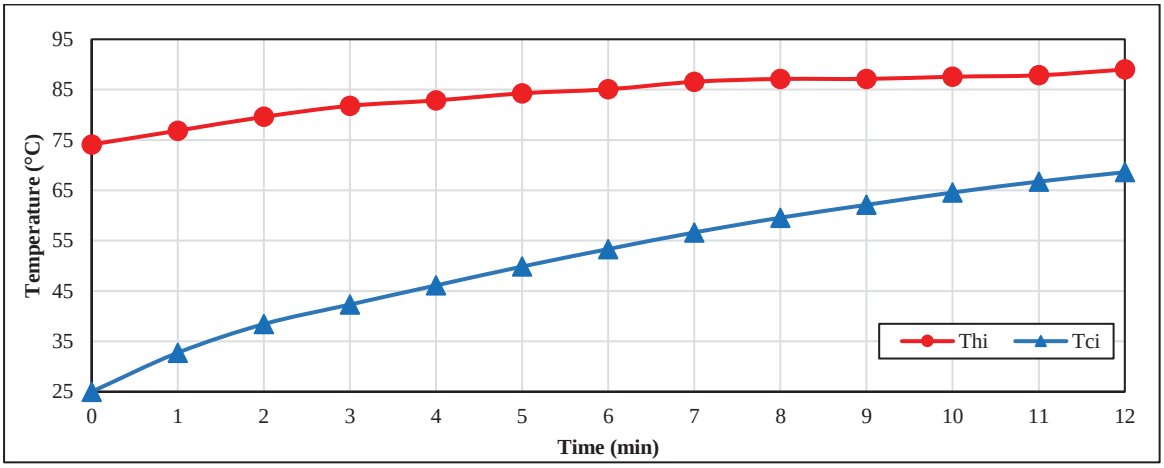


[b] : (Non-aligned micro-channels matrix)

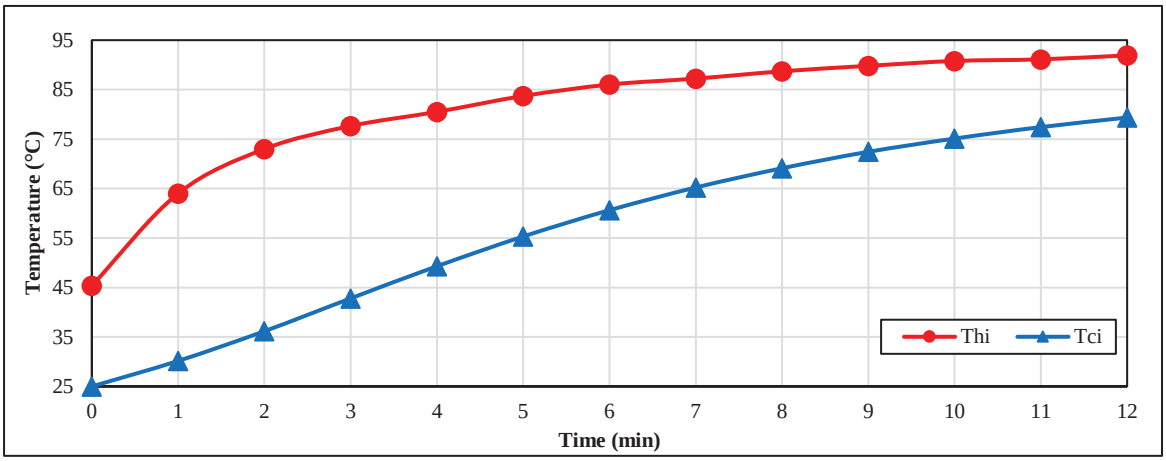


[c] : (Micro-channels matrix)

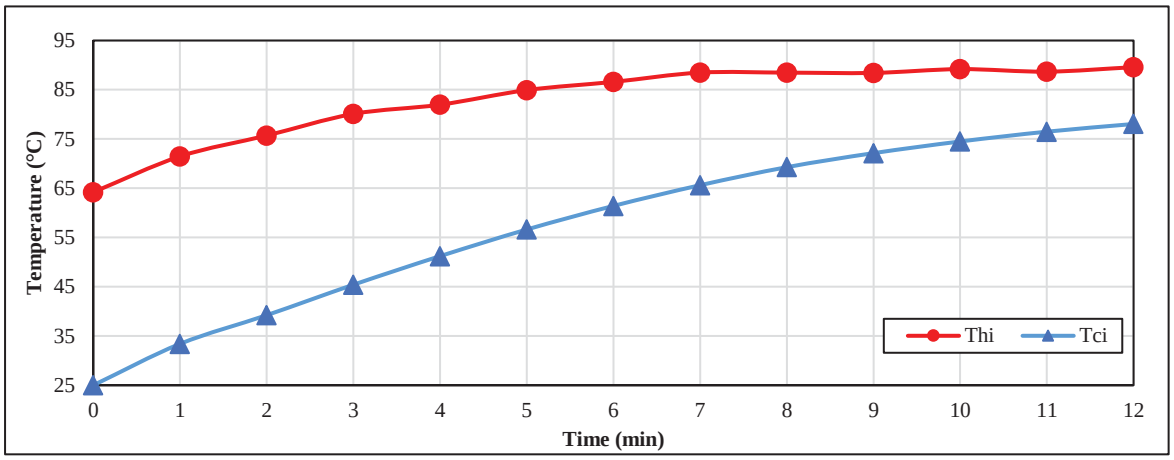
Figure 4.32 Inlet and outlet Temperature vs. Time (Th = 70 ^{0}C & SLPS=3)



[a]: (Random fibre matrix)

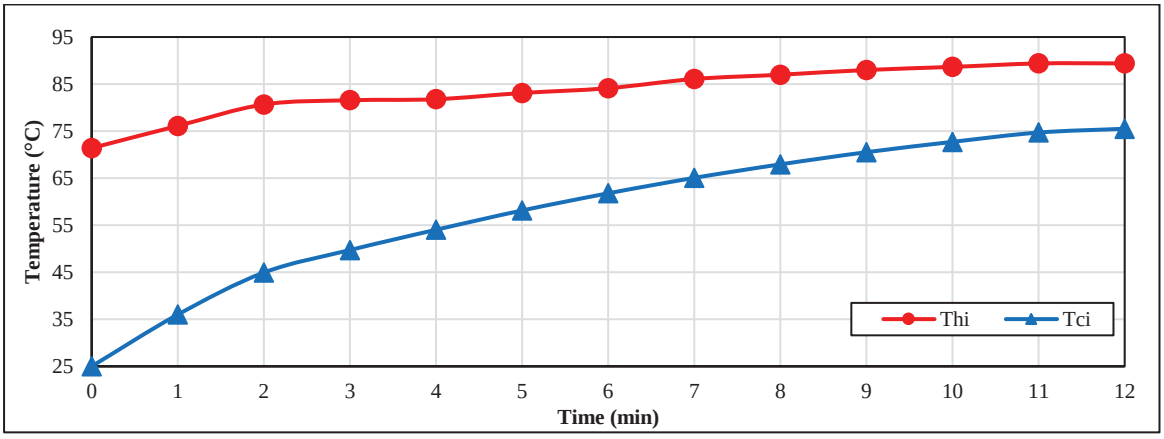


[b]: (Non-aligned micro-channels matrix)

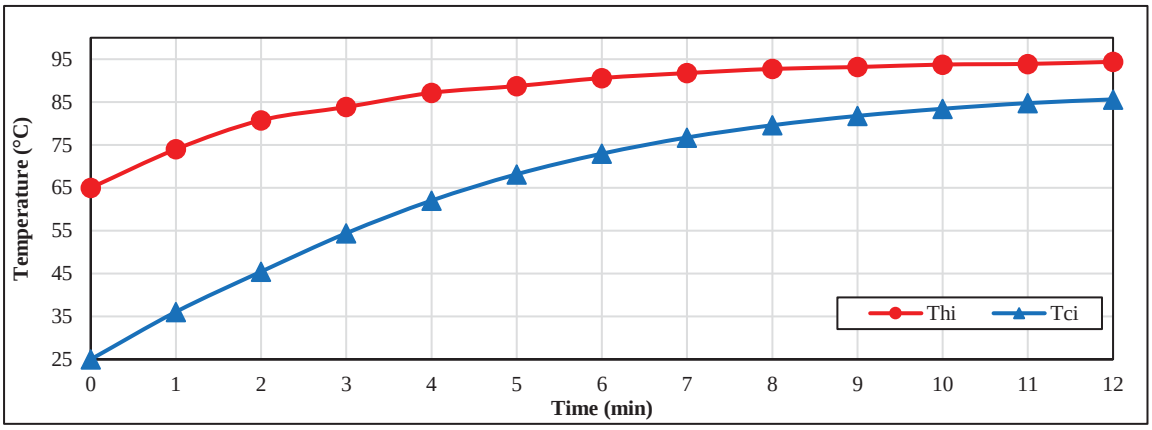


[c]: (Micro-channels matrix)

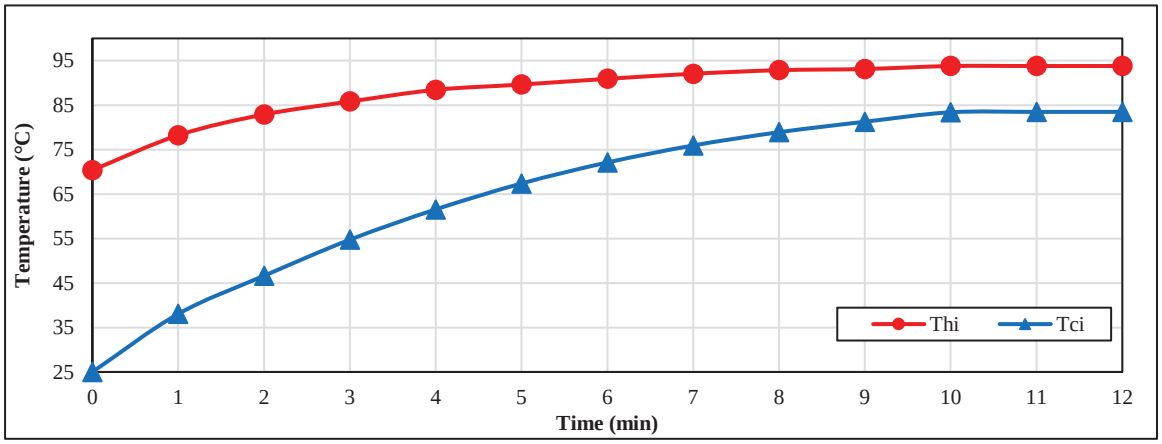
Figure 4.33 Inlet and outlet Temperature vs. Time (Th = 90 ^{0}C & SLPS=3)



[a]: (Random fibre matrix)

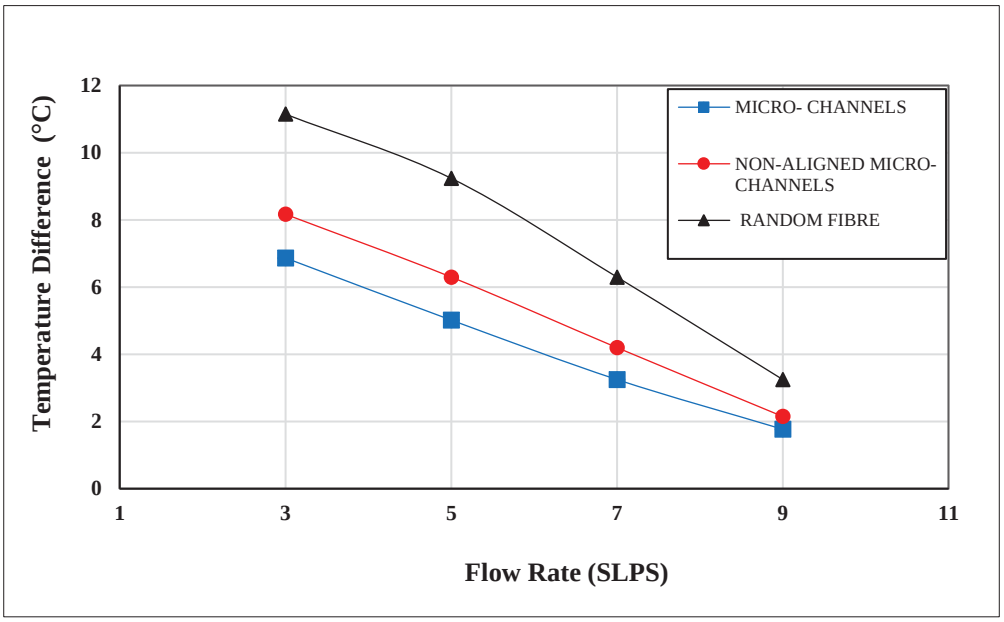


[b]: (Non-aligned micro-channels matrix)

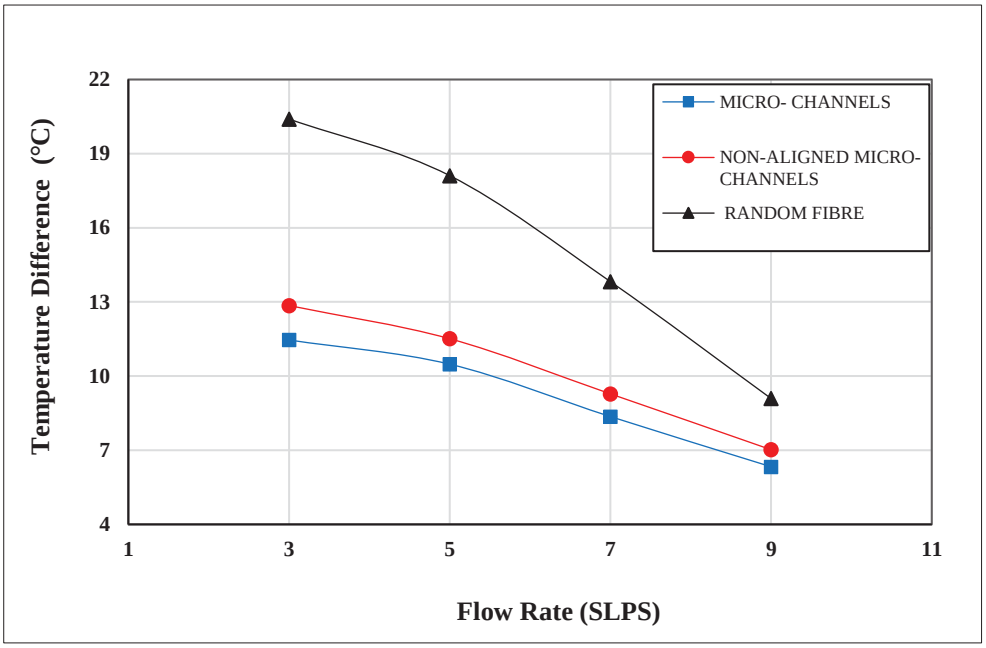


[c]: (Micro-channels matrix)

Figure 4.34 Inlet and outlet Temperature vs. Time (Th = 90 ^{0}C & SLPS=5)



[a]: at (Th= 90 ^{0}C)



[b]: at (Th= 70 °C)

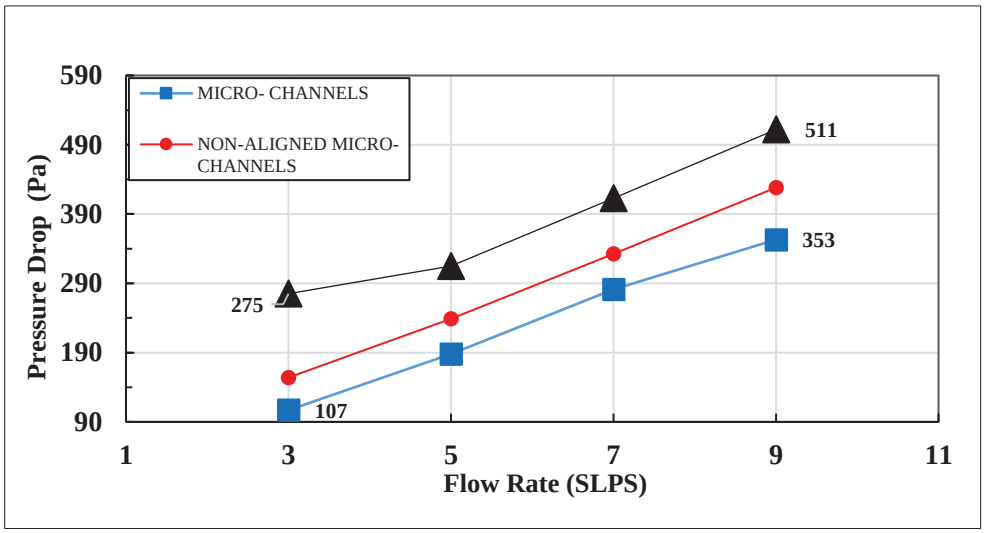
Figure 4.35 Temperature Difference (ΔT) vs. Flow rate

4.9.1.3 Pressure drop

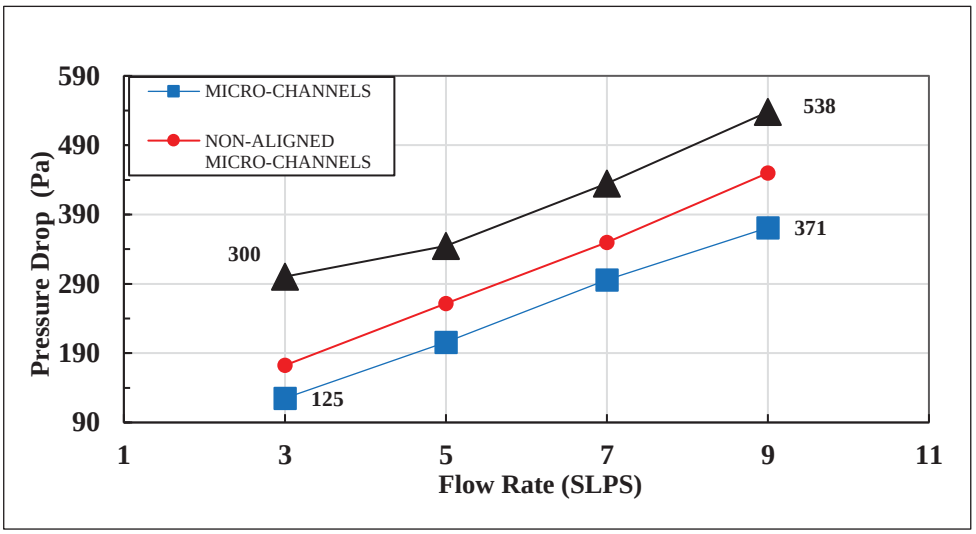
The effect of the regenerator pressure drop (which is function of the friction flow (See Section 2.4 and Eq.4.27)) has high impact on the Stirling engine performance. In the Parallel-geometry regenerators with regular shaped passages, the regenerators can offer the potential for enhancing the performance of the Stirling engine due to their ability to reduce the pressure drop between inlets and outlets and controlling the axial heat transfer process [98]. The pressure drop across the regenerators in small-scale Stirling engines leads to about 11% reduction in the power output while about 1.5% reduction occurs due to the thermal losses [57]. It was also found by [55] that the pressure drop has the highest impact on the performance of the Stirling engine. Figure 4.36 (a) and Figure 4.36 (b) showing the effect of changing the flow rate on the pressure drop for the three regenerators: Micro-channels, Random fibre and Non-aligned micro-channels. The inlet temperature changed from 70 ^{0}C to 90 ^{0}C while the values of the flow rates are (3, 5, 7 and SPLS=9). Both figures showing an increase in the pressure drop with increasing the flow rate for the three matrixes. The Random fibre has the highest pressure drop trend compared with the other two matrixes while the Micro-channels matrix has the lowest pressure drop trend. For example, the pressure drop varies in the Random fibre from 300 to 538 Pa as the flow rate increases from SLPS=3 to SLPS=9 at inlet temperature of 90 ^{0}C. For the Micro -channels matrix the pressure drop varies from 125 to 371 Pa, while for the Non-aligned micro-channels matrix the pressure drop varies from 172 to 450 Pa for flow rate from SLPS=3 to SLPS=9 at inlet temperature of 90 ^{0}C. It can be concluded that the use of high flow rate is conducive to increase the pressure drop. Furthermore, the pressure drop is affected by changing of the inlet temperature when the increase in the inlet temperature led to more increase in the pressure drop. Samples of the experimental measurements showing the effect of inlet temperatures (70 ^{0}C and 90 ^{0}C) on the inlet and outlet pressures with flow rate SPLS=5

can be seen in Figure 4.37 and Figure 4.38 respectively. The inlet and outlet pressure recording between 710 and 720 sec.

It can be concluded from Figure 4.36, Figure 4.37 and Figure 4.38 that the pressure drop across the regular shaped micro-channel type regenerator was lower compared to that for the Random fibre and Non-aligned micro-channels matrix. This lower regenerator pressure drop will lead to high performance for the Stirling engine due to lower frictional loss [55].

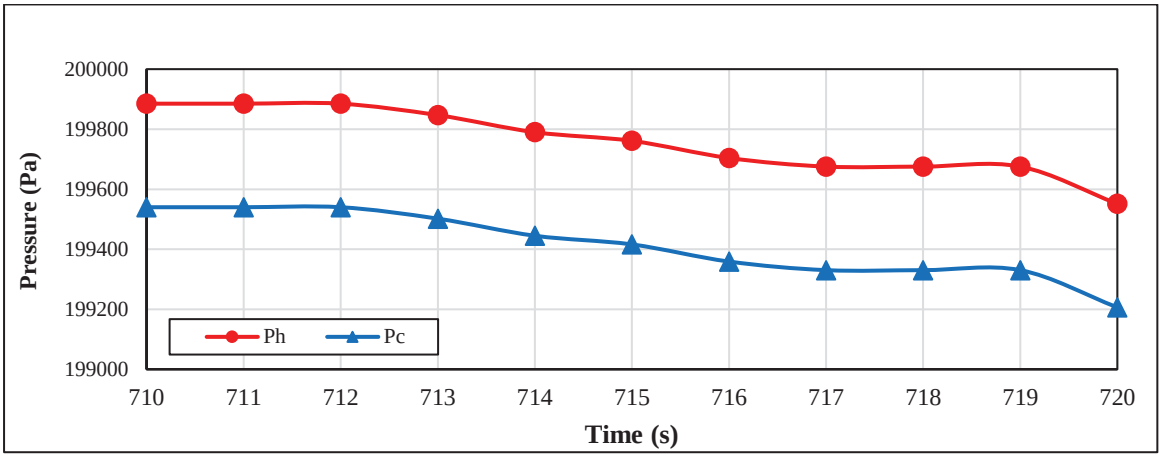


[a]: at (Th= 70 °C)

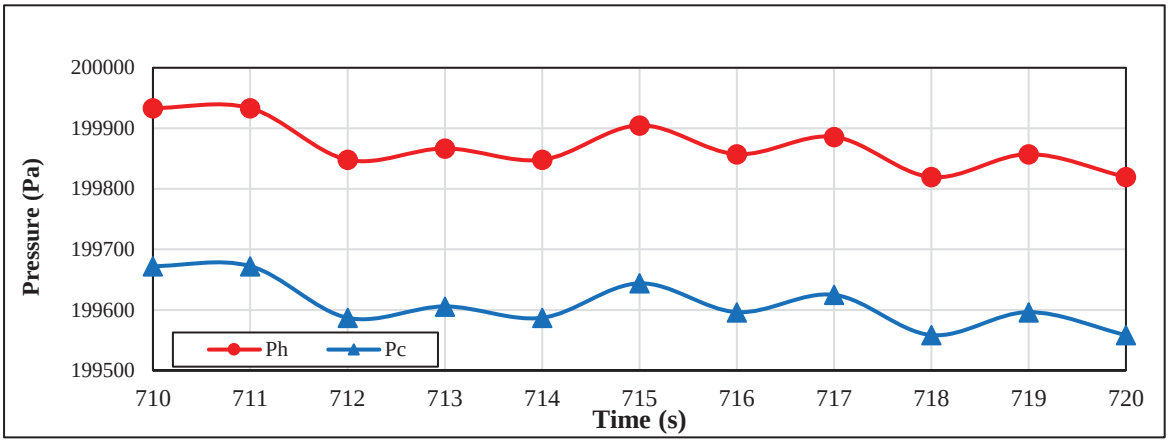


[b]: at (Th= 90 °C)

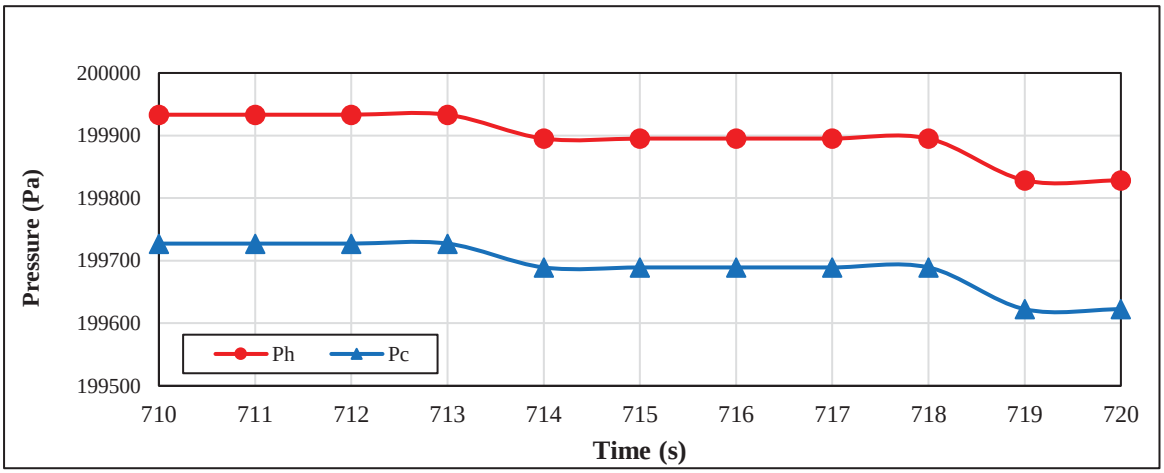
Figure 4.36 Pressure Drop (ΔP) vs. Flow rate



[a]: (Random fibre matrix)

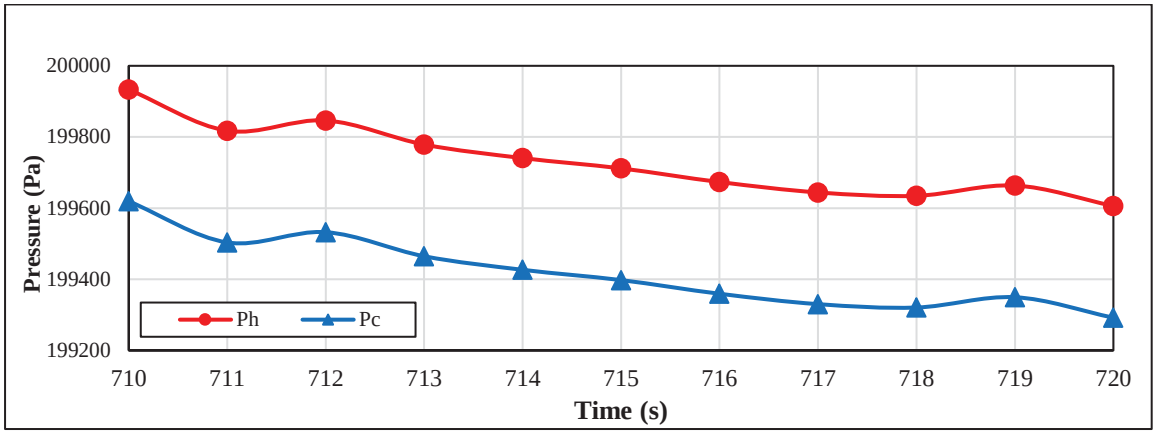


[b]: (Non-aligned micro-channels matrix)

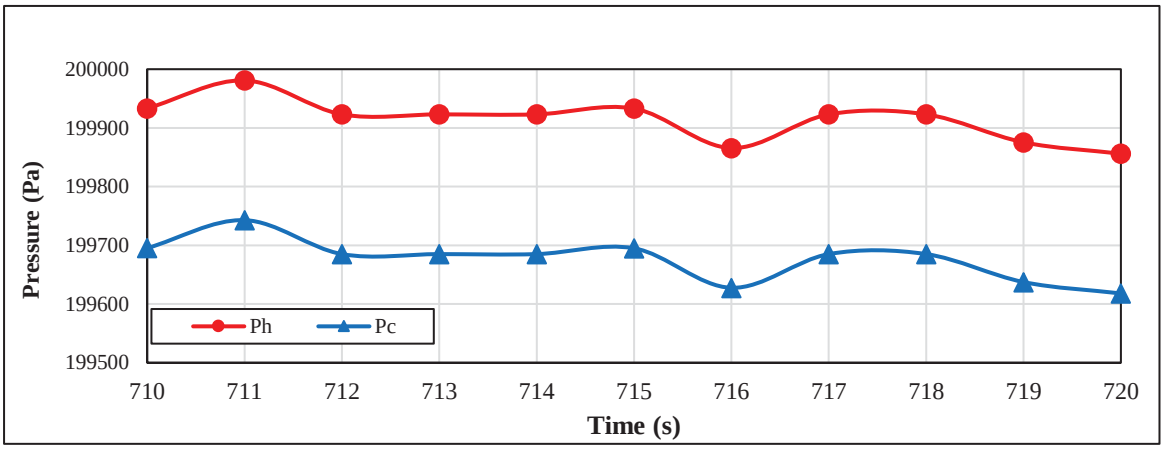


[c] : (Micro-channels matrix)

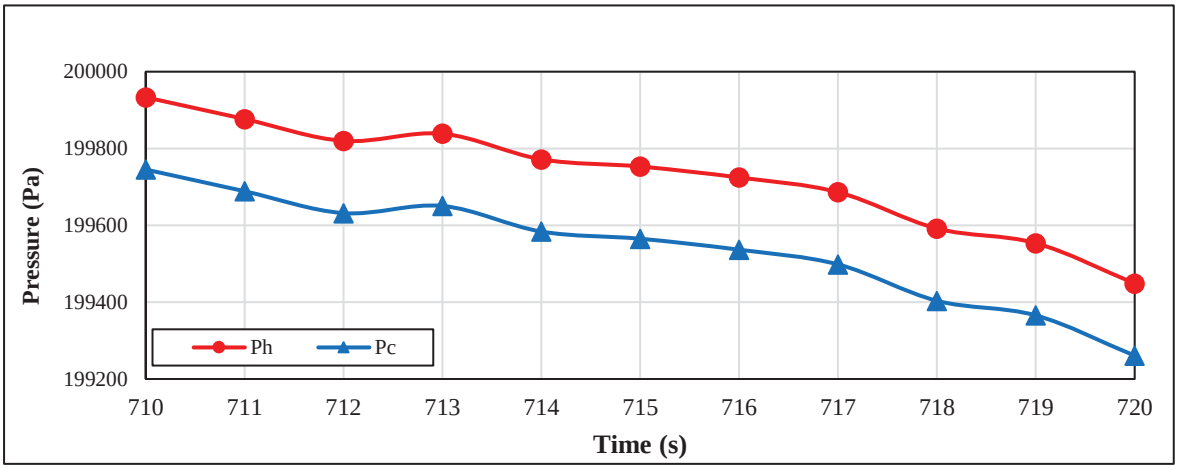
Figure 4.37 The inlet and outlet pressure vs. Time (Th = 70 ^{0}C & SLPS=5)



[a] : (Random fibre matrix)



[b]: (Non-aligned micro-channels matrix)



[c]: (Micro-channels matrix)

Figure 4.38 The inlet and outlet pressure vs. Time (Th = 90 ^{0}C & SLPS=5)

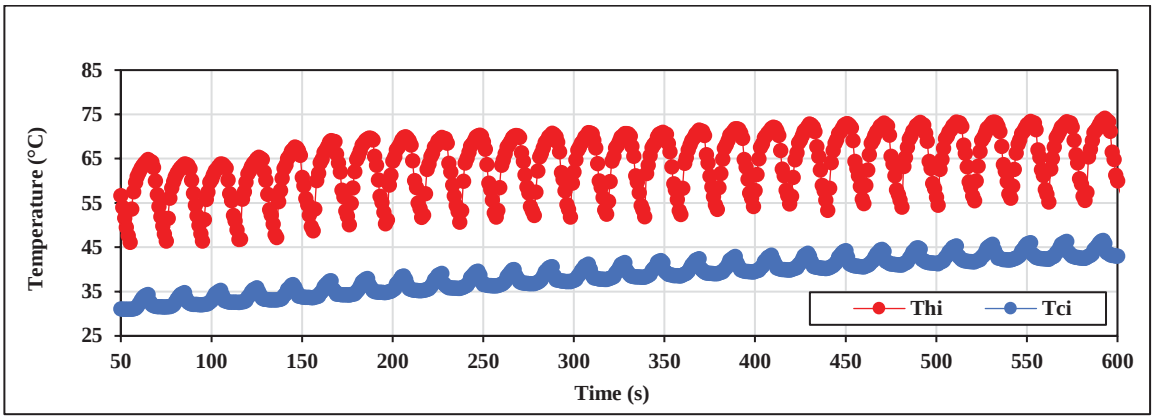
4.9.2 Results of two direction flow

4.9.2.1 Inlet and outlet temperature difference

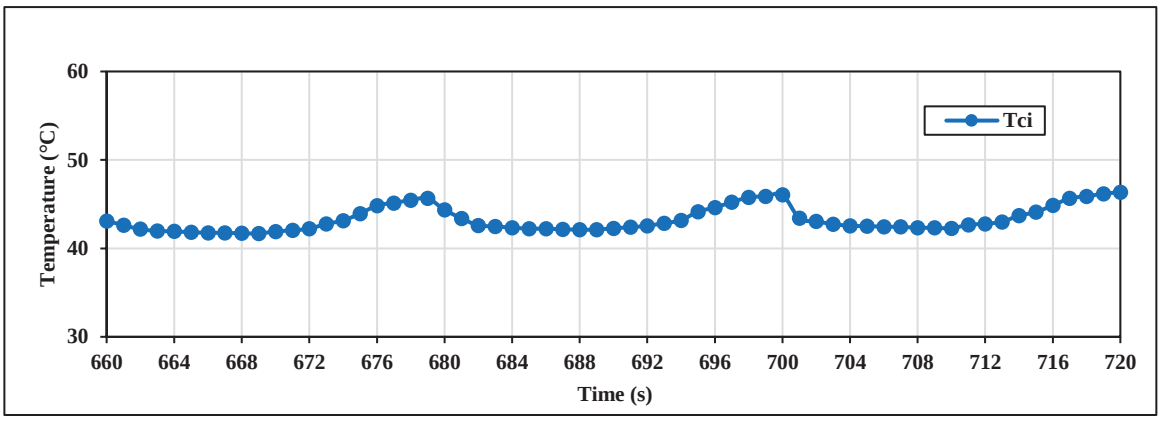
Figure 4.39 to Figure 4.45 show examples of the experimental measurements for inlet (**Thi**) and outlet (**Tci**) temperatures for the two directions flow during different test run times for the three regenerators: Micro-channels, Random fibre and Non-aligned micro-channels. The fluctuations in all graphs highlight the regenerator function as (the regenerator acts as a heat reservoir when hot gas passes through the regenerator, it absorbs heat and therefore the temperature of the gas drops through the regenerator. In reverse flow while cold gas passes through the regenerator the gas absorbs heat from the regenerator and its temperature increases as it goes through the regenerator). It should be observed that (**Thi)** has high fluctuation amplitude in the micro-channels regenerator matrix compared to the other two regenerator matrixes as in the case in Figure 4.45.

Figure 4.46 (a) and (b) show example measurements for the influence of changing valve frequency on the temperature difference between inlet (hot side) and outlet (cold side) for the three regenerators: Micro-channels, Random fibre and Non-aligned micro-channels. The inlet temperature (heater temperature) at 70 ^{0}C and 90 ^{0}C and the value of the flow rates (SLPS =5) while the valve speed varies from r.p.m=3 to 30. In all cases, the temperature difference (ΔT) in the random fibre matrix and non-aligned micro-channels matrix increases as the valve frequency increases while the temperature difference (ΔT) in the micro-channels matrix decreases as the valve speed increases. This can be related to the increase in the pressure drop between the two sides of the regenerator as the valve frequency increases. For example, in Figure 4.46 (a) (Th= 90 °C), temperature difference (ΔT) increased from 25 to 44 ^{0}C in the random fibre matrix and from 31 to 39 ^{0}C in the non-aligned micro-channels matrix while it decreased from 34.7 to 30.3 ^{0}C in the micro-channels matrix. In Figure 4.46 (b) (Th= 70 ^{0}C), temperature difference (ΔT) increased from 14.5 to 34 ^{0}C in the random fibre matrix and from

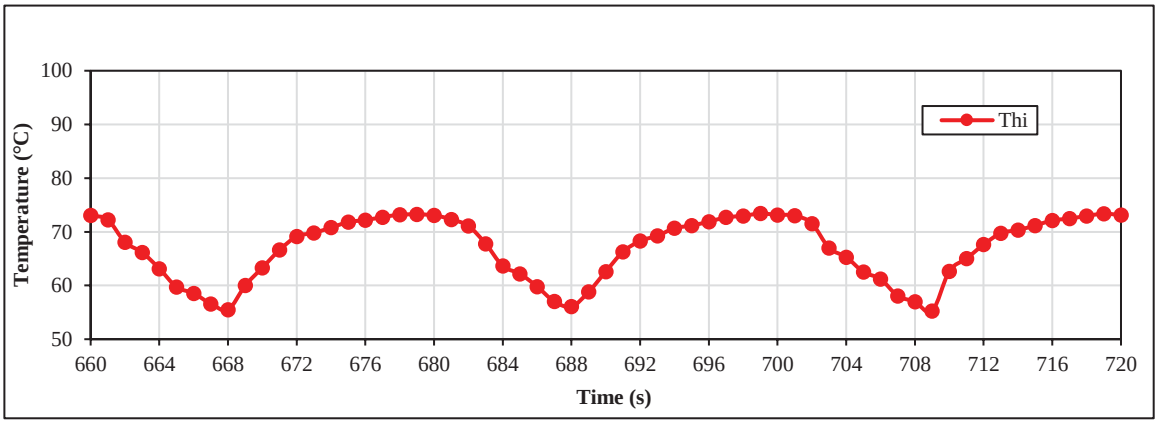
19 to 31 ^{0}C in the non-aligned micro-channels matrix while it decreased from 24.7 to 20 ^{0}C in the micro-channels matrix.



[a]: (Th_i and Tc_i) vs. Time

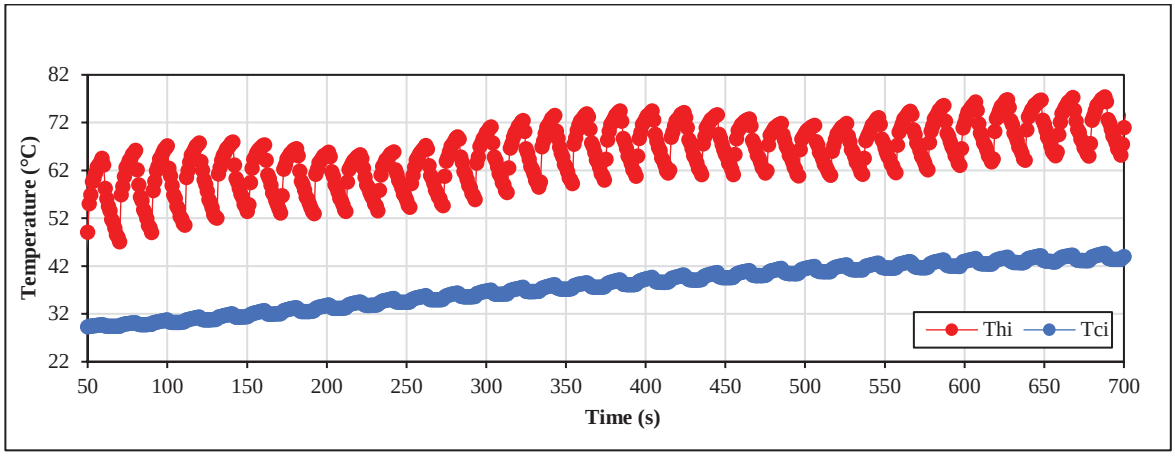


[b]: Tc_i vs. Time

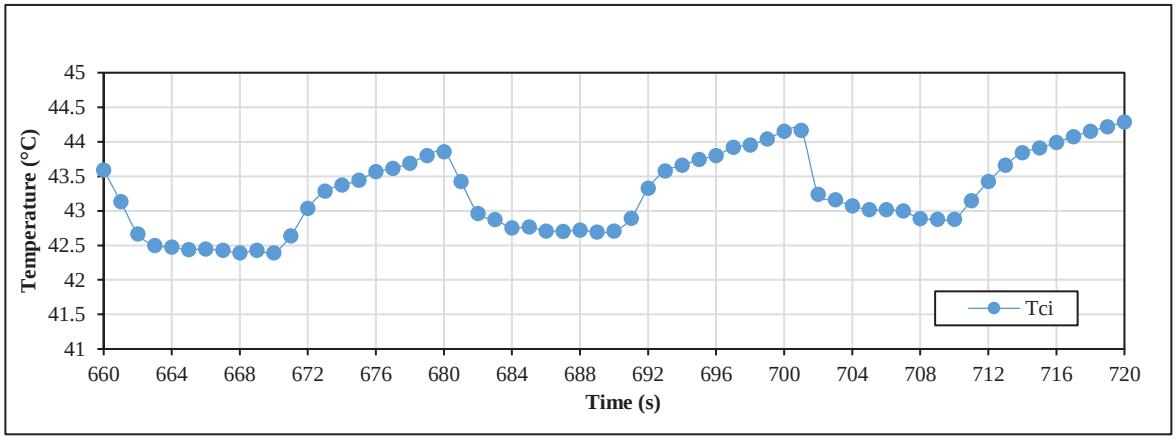


[c]: Th_i vs. Time

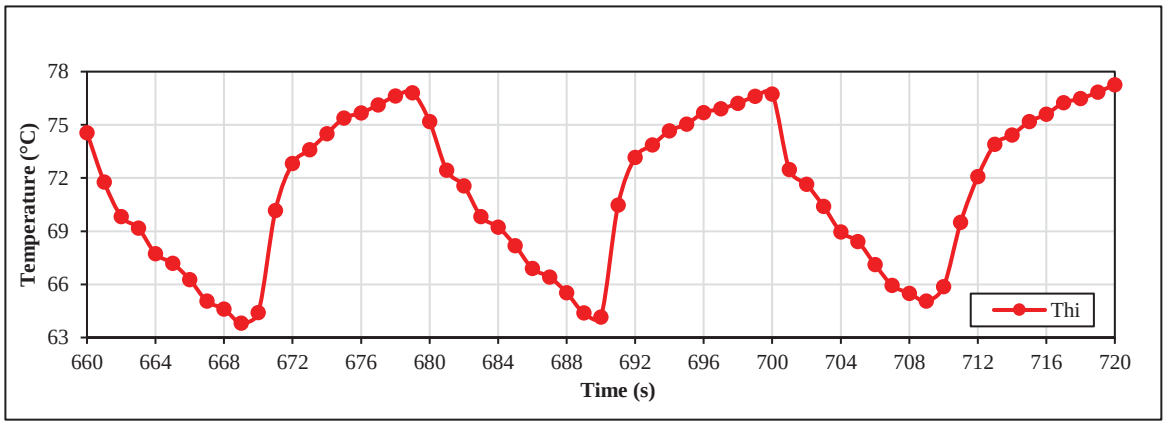
Figure 4.39 Example of Temperature (Th_i and Tc_i) vs. Time at (90 ^{0}C, SLPS=3& r.p.m=3) (Random fibre matrix)



[a]: (Th_i and Tc_i) vs. Time

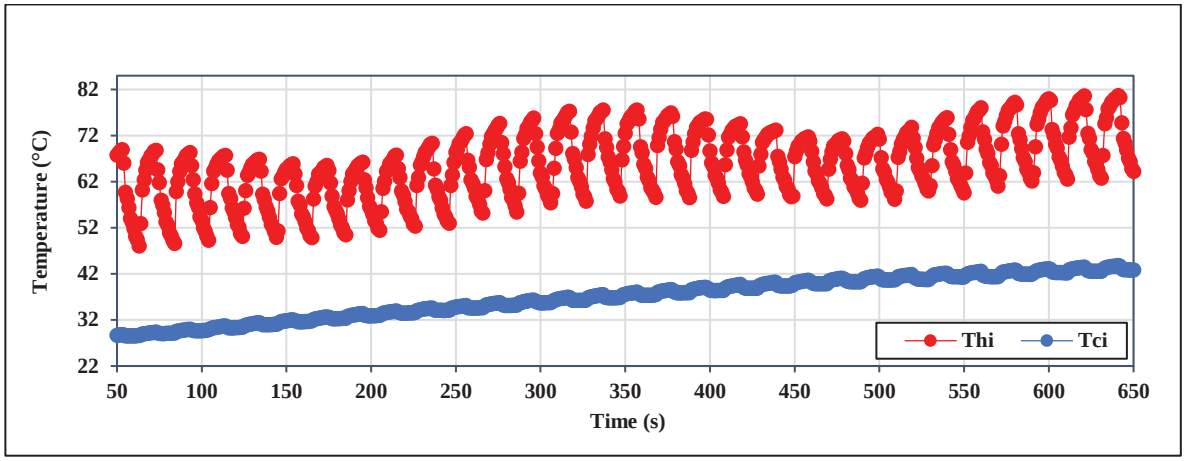


[b]: Tc_i vs. Time

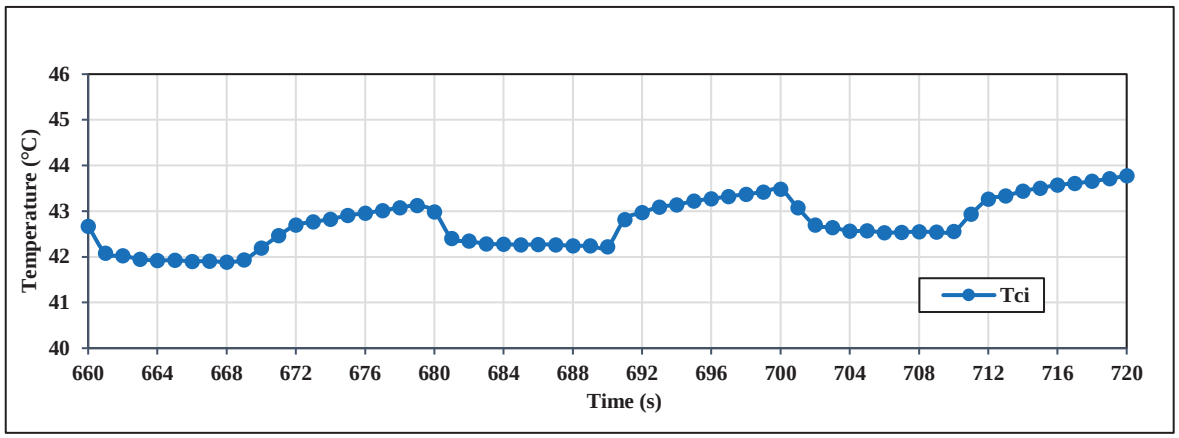


[c]: Th_i vs. Time

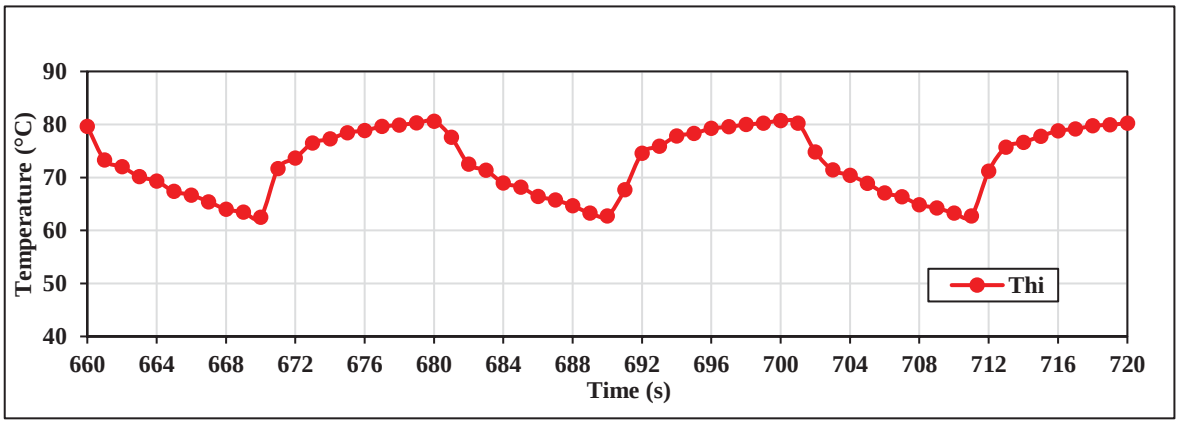
Figure 4.40 Example of Temperature (Th_i and Tc_i) vs. Time at (90 ^{0}C, SLPS=3& r.p.m=3) (Non-aligned Micro-channels matrix)



[a]: (Th_i and Tc_i) vs. Time

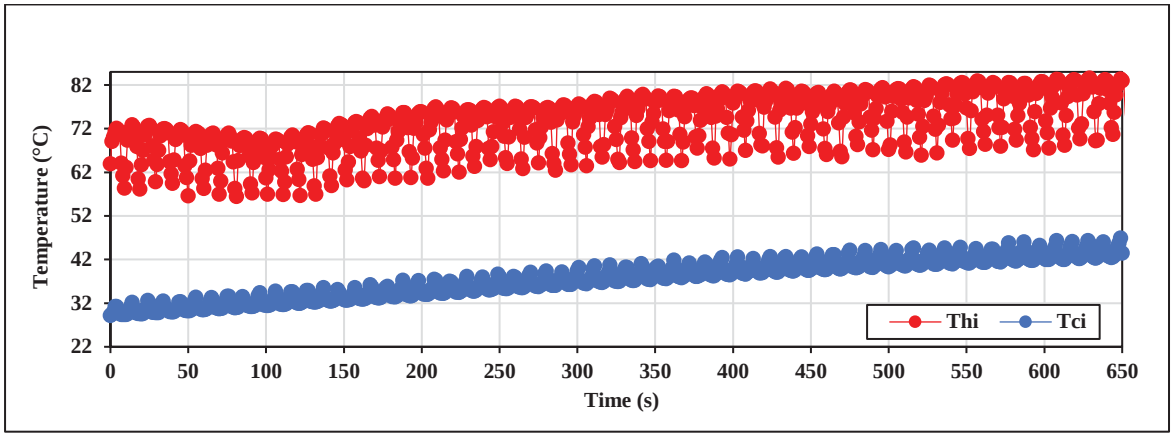


[b]: Tc_i vs. Time

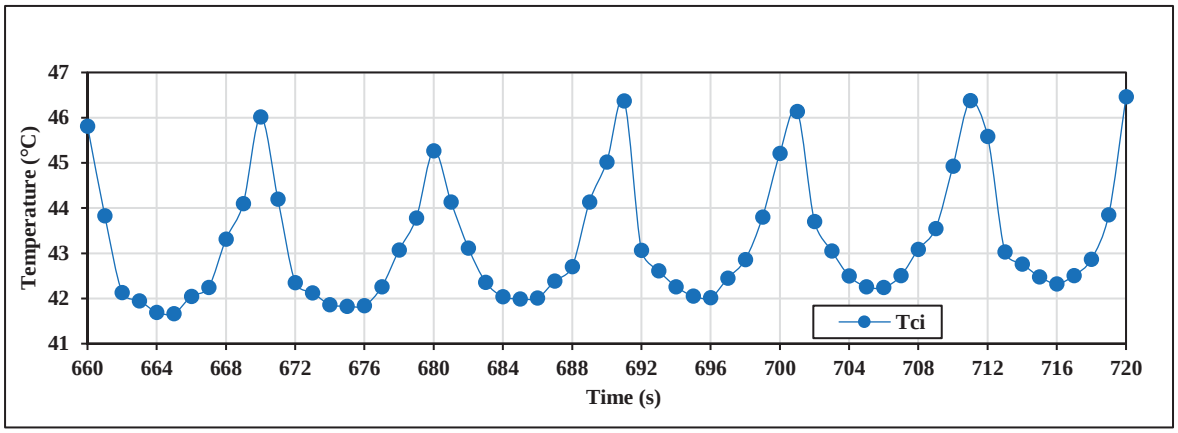


[c]: Th_i vs. Time

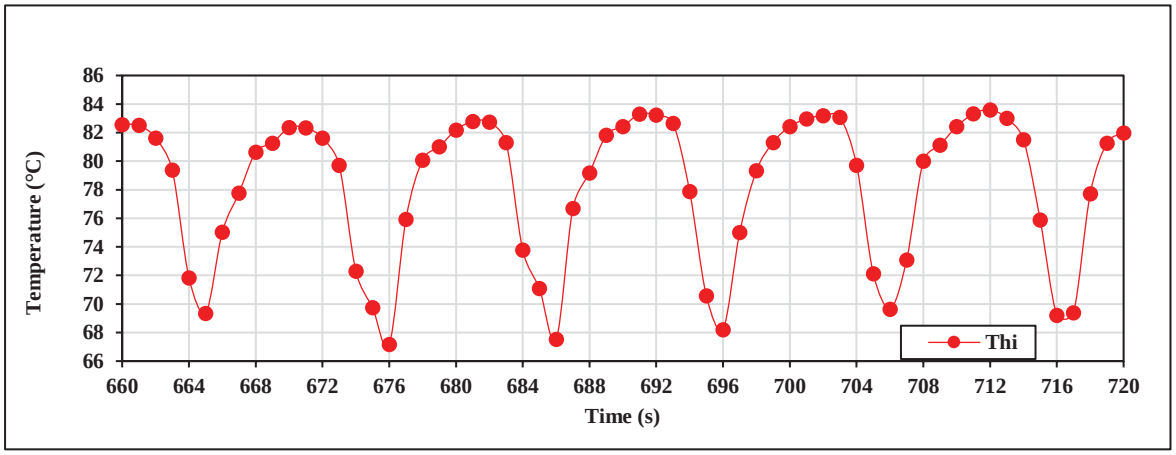
Figure 4.41 Example of Temperature (Th_i and Tc_i) vs. Time at (90 ^{0}C, SLPS=3& r.p.m=3) (Micro-channels matrix)



[a]: (Th_i and Tc_i) vs. Time

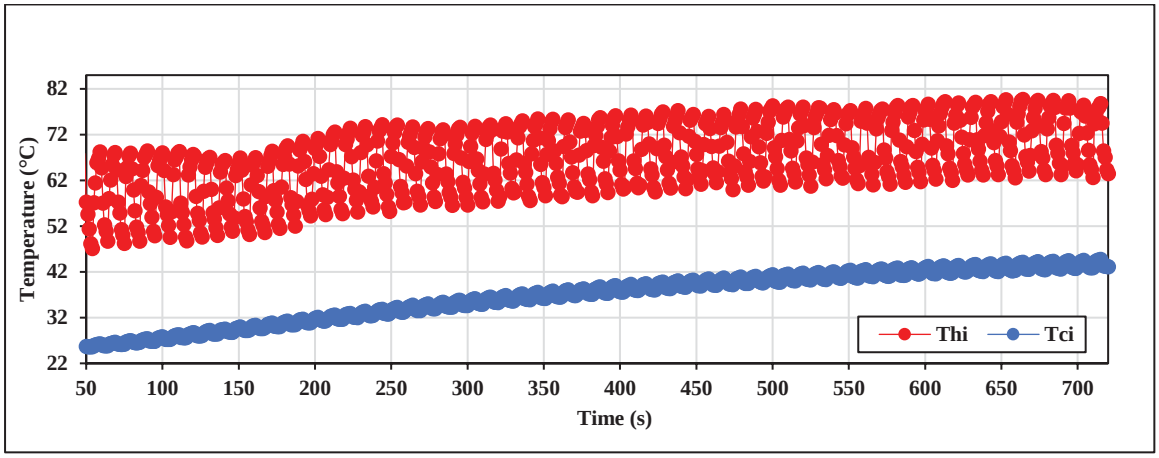


[b]: Tc_i vs. Time

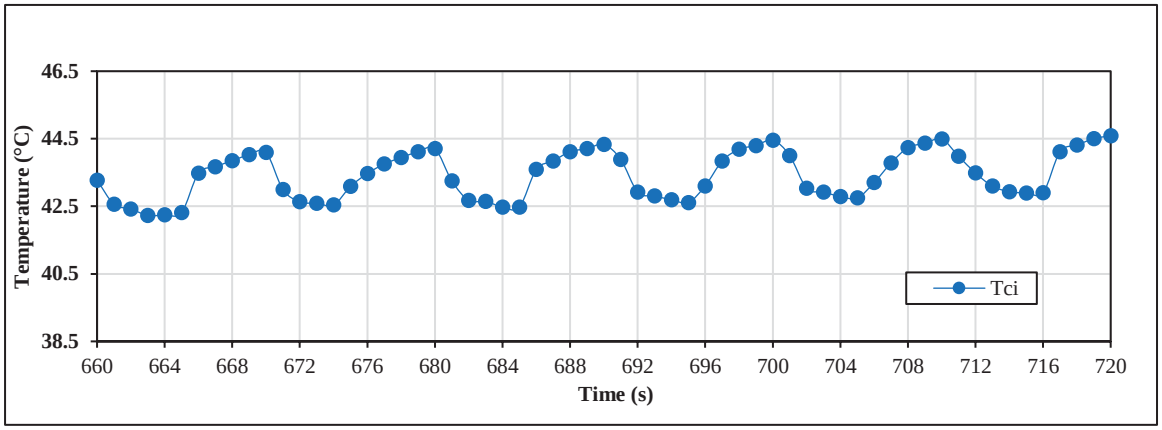


[c]: Th_i vs. Time

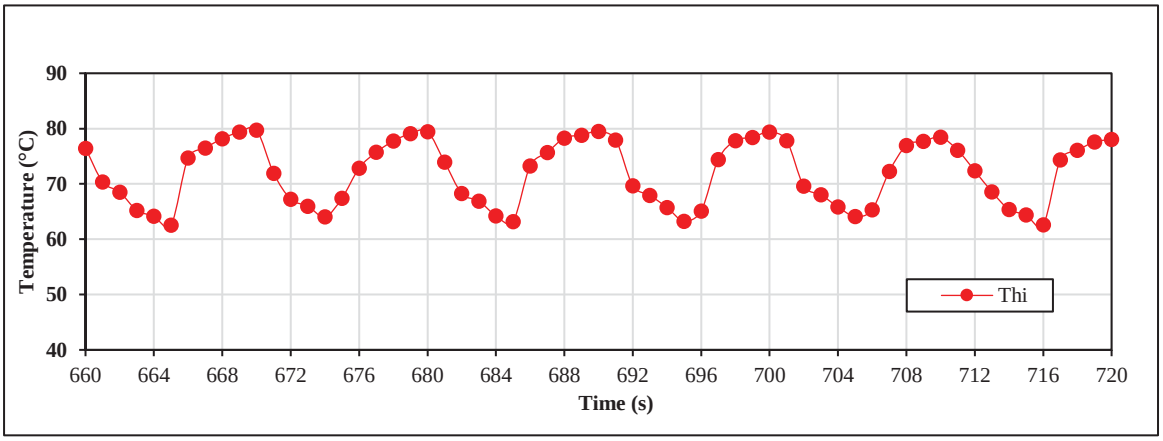
Figure 4.42 Example of Temperature (Th_i and Tc_i) vs. Time at (90 ^{0}C, SLPS=5& r.p.m=6) (Random fibre matrix)



[a]: Example of Temperature (Th_i and Tc_i) vs. Time

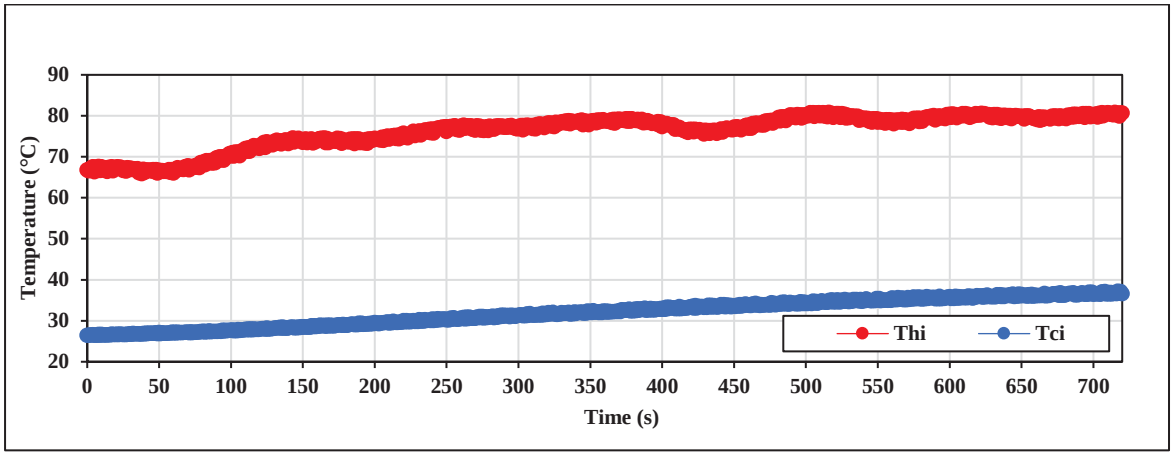


[b]: Tc_i vs. Time

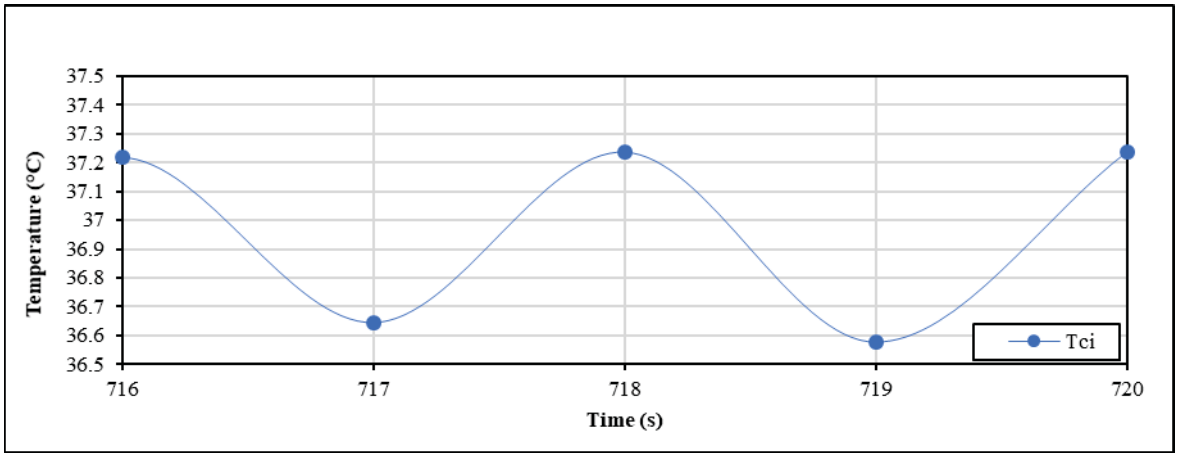


[c]: Th_i vs. Time

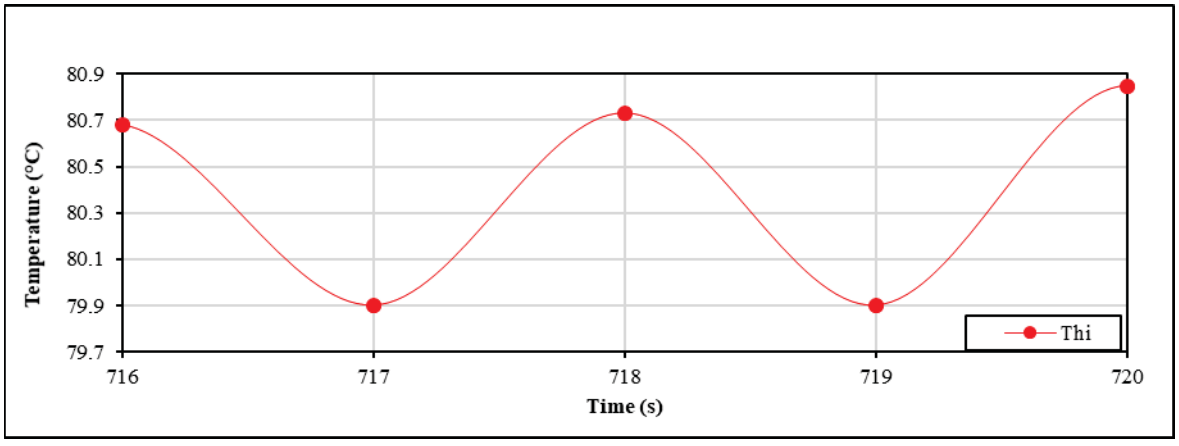
Figure 4.43 Example of Temperature (Th_i and Tc_i) vs. Time at (90 ^{0}C, SLPS=5& r.p.m=6) (Micro-channels matrix)



[a]: (Th_i and Tc_i) vs. Time

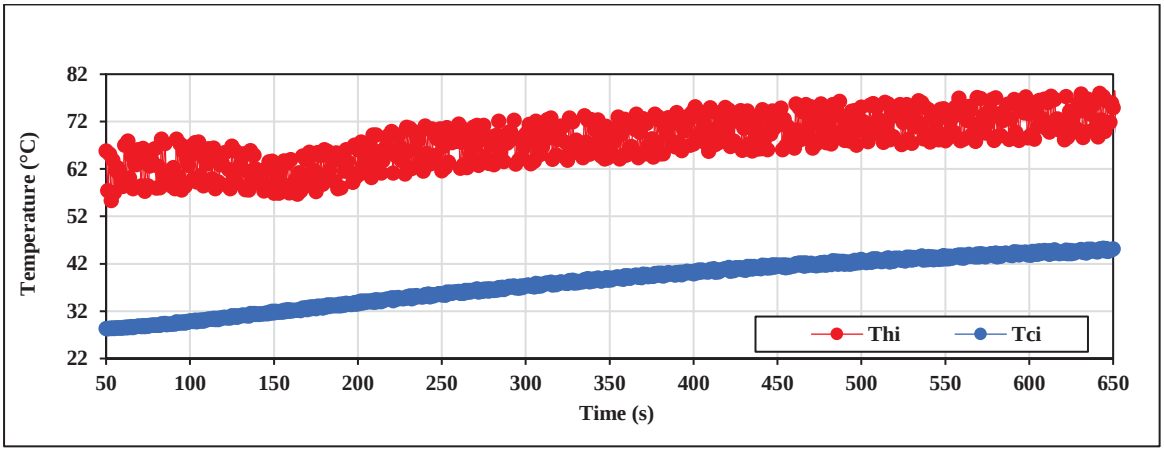


[b]: Th_i vs. Time

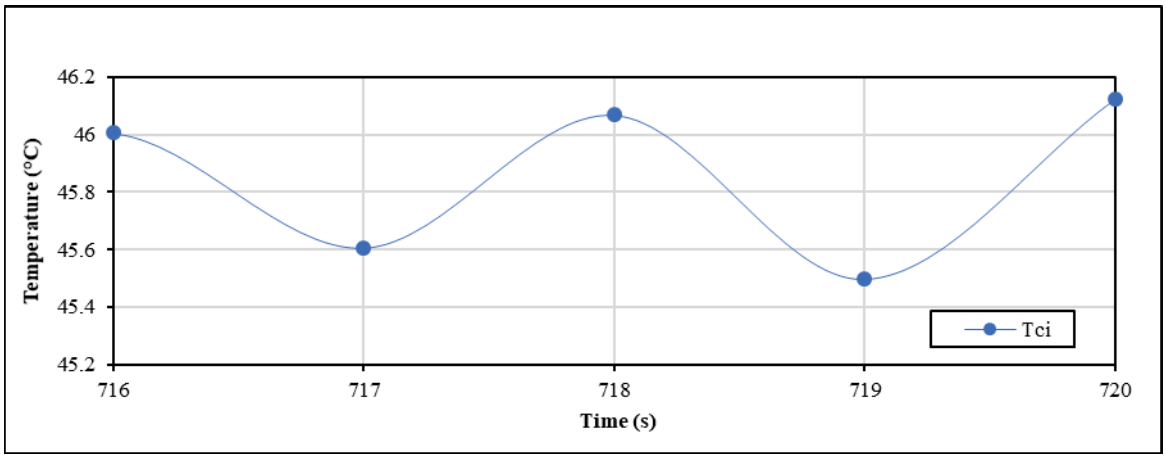


[c]: Tc_i vs. Time

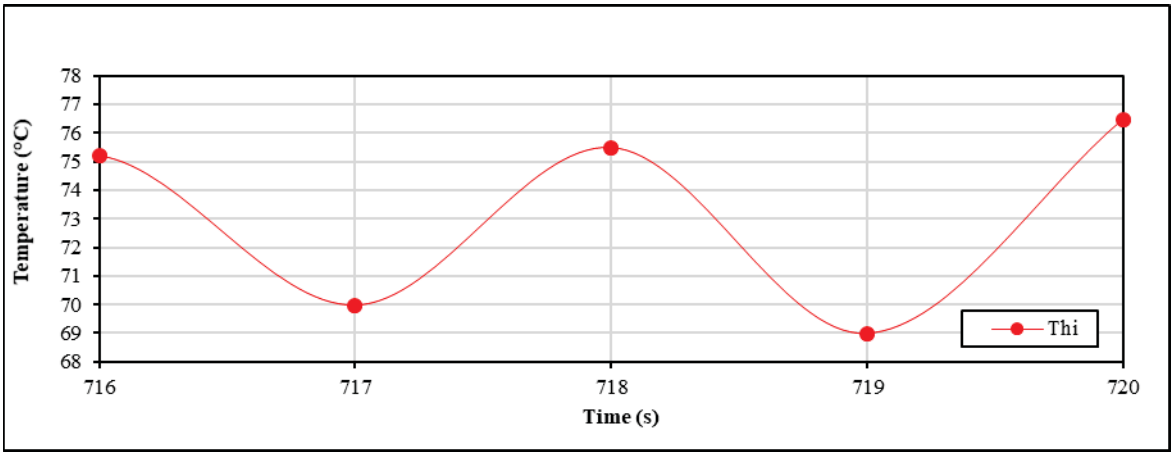
Figure 4.44 Example of Temperature (Th_i and Tc_i) vs. Time at (90 ^{0}C, SLPS=5& r.p.m=30) (Random fibre matrix)



[a]: (Th_i and Tc_i) vs. Time

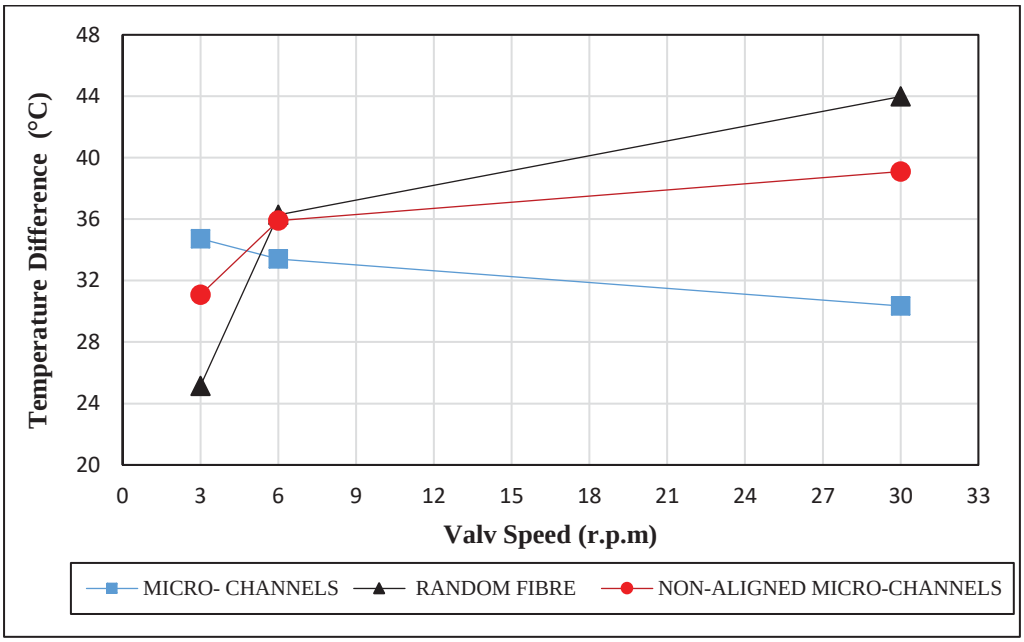


[b]: Tc_i vs. Time

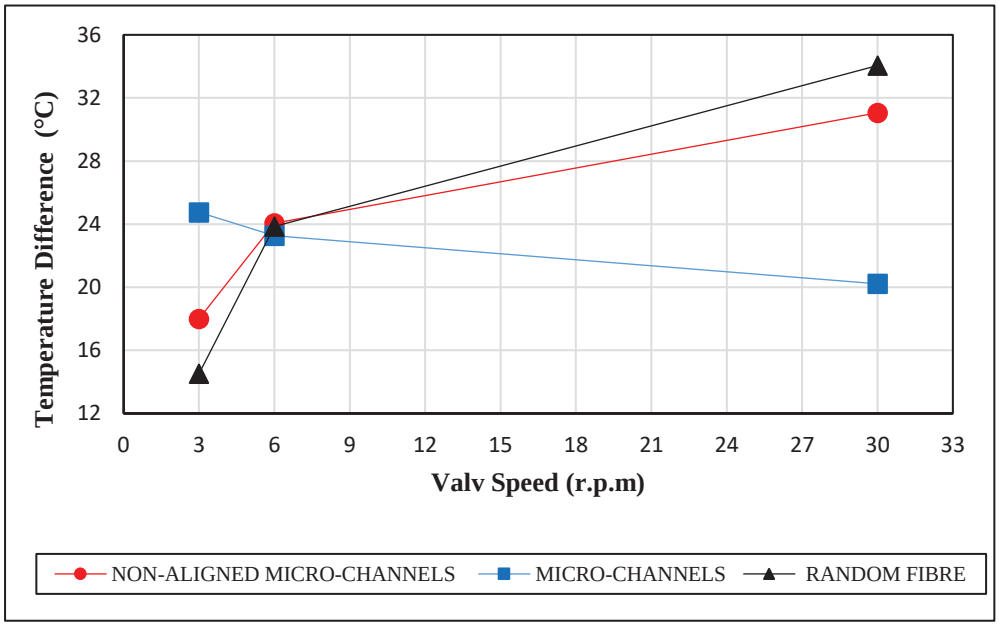


[c]: Th_i vs. Time

Figure 4.45 Example of Temperature (Th_i and Tc_i) vs. Time at a (90 ^{0}C, SLPS=5& r.p.m=30) (micro-channels matrix)



[a]: at (Th= 90 ^{0}C)



[b]: at (Th= 70 °C)

Figure 4.46 Temperature Difference (ΔT) vs. r.p.m with SLPS=5

In order to evaluate the performance of the micro-channels and random fibre regenerators based on the $\mathbf{Th_i}$ and $\mathbf{Tc_i}$ temperature measurements during one cycle , the effectiveness parameter is used for each configuration using the following equation [67] :

$$eff = \frac{(\mathbf{Th_i}) - (\mathbf{Tc_i})\boldsymbol{in}}{(\mathbf{Th_i}) - \boldsymbol{min}(\mathbf{Tc_i})} \qquad 4.26$$

Where; $\mathbf{Th_i}$ is the maximum (inlet) temperature at the hot blow of the cycle (first half of the cycle), $(\mathbf{Tc_i})\boldsymbol{in}$ is the inlet temperature at the cold blow of the cycle (second half of the cycle) and $\boldsymbol{min}(\mathbf{Tc_i})$ is the minimum temperature during the cold blow of the cycle .

Results are given in Table 4.5 and Table 4.6 for the tests with various regenerators (micro-channels and random fibre) at r.p.m = 3, 6 and 30 with flow rates SLPS= 3, 5, 7 and 9. The heater is kept at a constant temperature (90 ^{0}C) and temperature of the cooler around 23 ^{0}C. The effectiveness decreases with increasing the flow rate. For example, at r.p.m = 3 with flow rate SLPS=3, 5, 7 and 9, respectively, for the random fibre matrix the effectiveness = 0.963, 0.923, 0.908 and 0.89, and for the micro-channels matrix, the effectiveness = 0.975, 0.971, 0.969 and 0.952. Similarly, at r.p.m = 30 the effectiveness in the random fibre matrix = 0.986, 0.985, 0.983 and 0.979, and in the micro-channels matrix = 0.964, 0.961, 0.957 and 0.938.

Furthermore, Table 4.5 and Table 4.6 compare the effect of changing the valve frequency (directly related to the closing speed in r.p.m) on the effectiveness for the various regenerators (micro-channels and random fibre). In all results while the valve frequency was changed from r.p.m=3 to 30. It can be seen that the effectiveness in the random fibre regenerator increases as the speed increases while the effectiveness in the micro-channels regenerator decreases as the speed increases. This may be due to the effect of convection force and the contacting surface

area on both matrixes, where the contacting surface area in the random fibre regenerator is higher than the micro-channels regenerator and then it can adsorb more heat.

Table 4.5 Effectiveness of the Random fibre regenerator at different r.p.m and flow rates:

Random Fibre		r.p.m		
		3	**6**	**30**
Flow Rate	**3**	0.963	0.9644	0.986
	5	0.9233	0.931	0.985
	7	0.908	0.911	0.983
	9	0.89	0.907	0.979

Table 4.6 Effectiveness of the micro-channels regenerator at different r.p.m and flow rates:

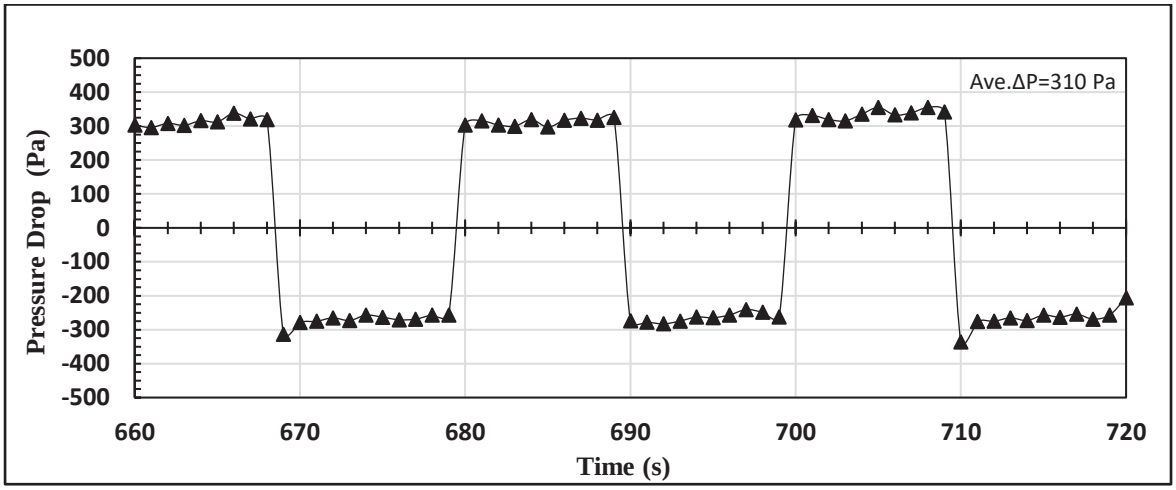
Micro-Channels		r.p.m		
		3	**6**	**30**
Flow Rate	**3**	0.975	0.972	0.964
	5	0.971	0.969	0.961
	7	0.969	0.9613	0.957
	9	0.952	0.948	0.938

4.9.2.2 Pressure drop

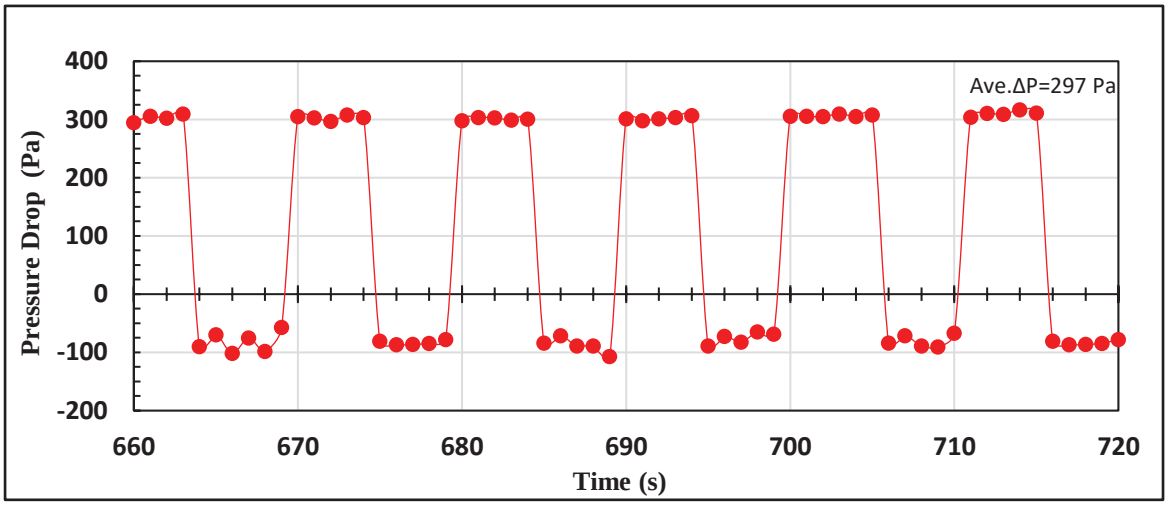
Figure 4.47 (a), (b) and (c) show various examples of the pressure drop for the three regenerators Micro-channels, Random fibre and Non-aligned micro-channels with inlet temperature 90 ^{0}C. It is clear that the fluctuation in pressure values are due to the oscillating nature of the flow, and it differs in each figure according the change of the valve frequency (r.p.m= 3, 6 and 30). Figure 4.47 (a) has the lowest pressure drop fluctuation with a valve frequency of 3 r.p.m, while Figure 4.47 (c) has the highest pressure drop fluctuation as the valve frequency increases up to 30 r.p.m at the same period of test timing.

In all experimental measurements, the pressure drop in the cold blow was higher than the pressure drop in the hot blow due to the decrease in the air density during the cooling processes which results in increasing the Reynolds number [57].

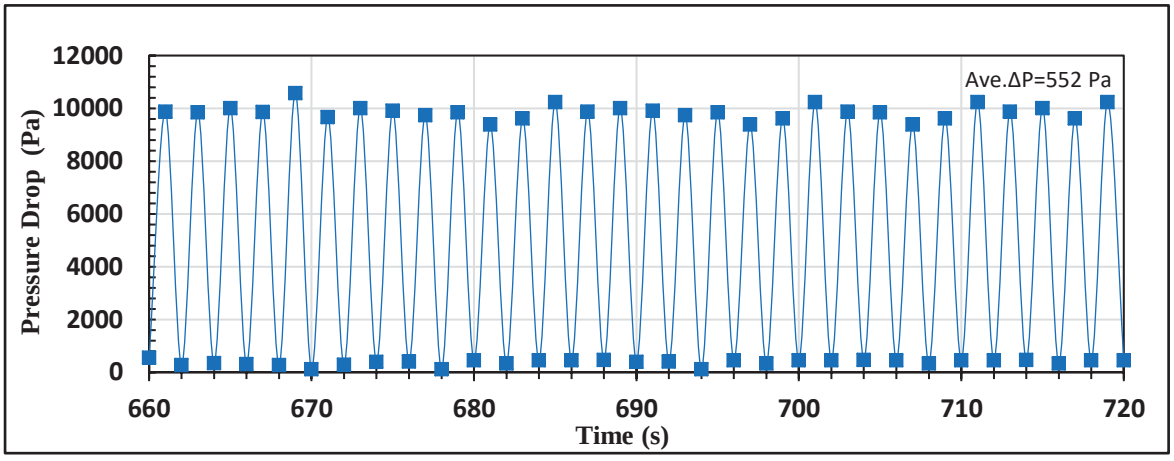
Figure 4.48 to Figure 4.50 show the variation of the pressure drop and the flow rate with the changing the valve frequency and the inlet temperature for three regenerators micro-channels, Random fibre and Non-aligned micro-channels. In Figure 4.48 (a) and (b), for the inlet temperature of 90 ^{0}C and 70 ^{0}C and r.p.m=3, as the flow rate increases, the pressure drop increases. For example, at a flow rate SLPS=7 and r.p.m=3, inlet temperatures of 90 ^{0}C and 70 ^{0}C, the pressure drops are: for the Random fibre 467 and 454 Pa, for the Non-aligned micro-channels 382 and 368 and for the Micro-channels 328 and 324 Pa. This result is compatible with the forced convection trend shown in figures Figure 4.49 and Figure 4.50.



[a]: (Random fibre matrix) at (r.p.m=3& SLPS=3)

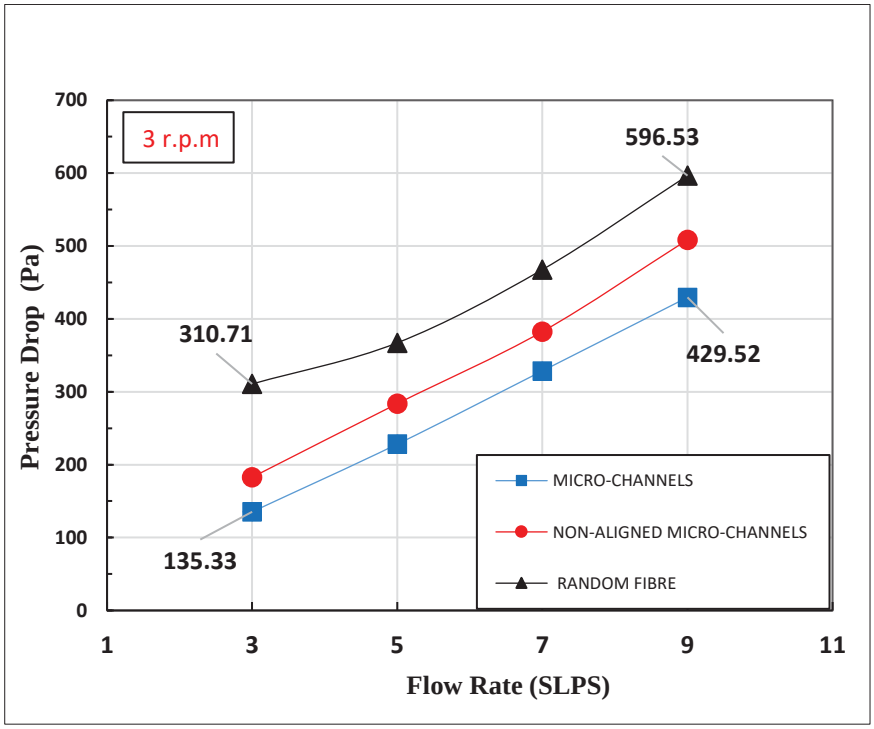


[b]: (Non-aligned micro-channels matrix) at (r.p.m=6& SLPS=5)

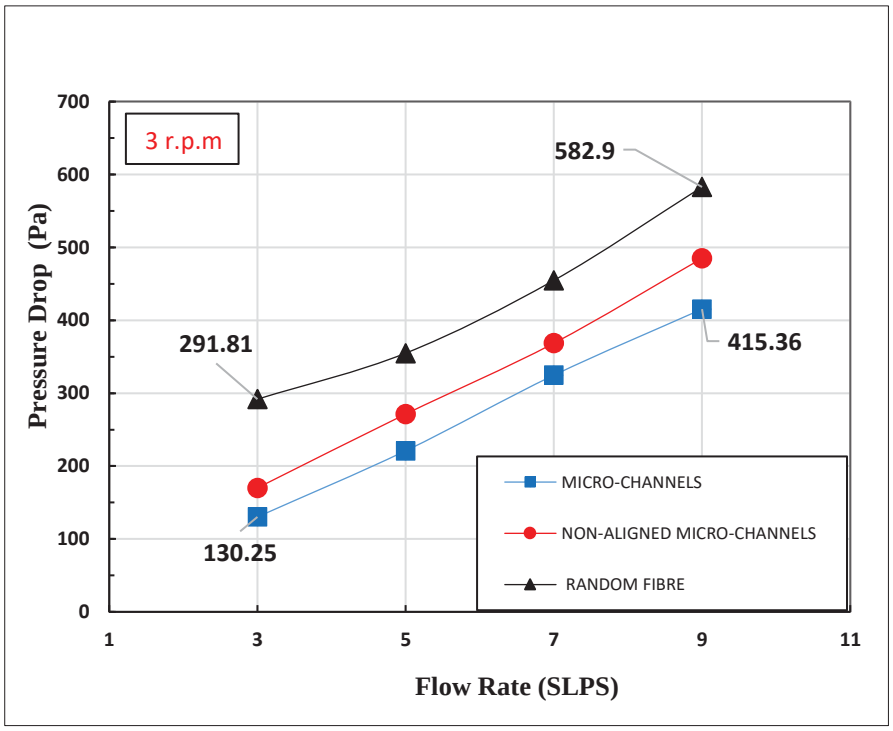


[c]: (Micro-channels matrix) at (r.p.m=30& SLPS=9)

Figure 4.47 Example of Pressure drop vs. Time in the oscillating flow

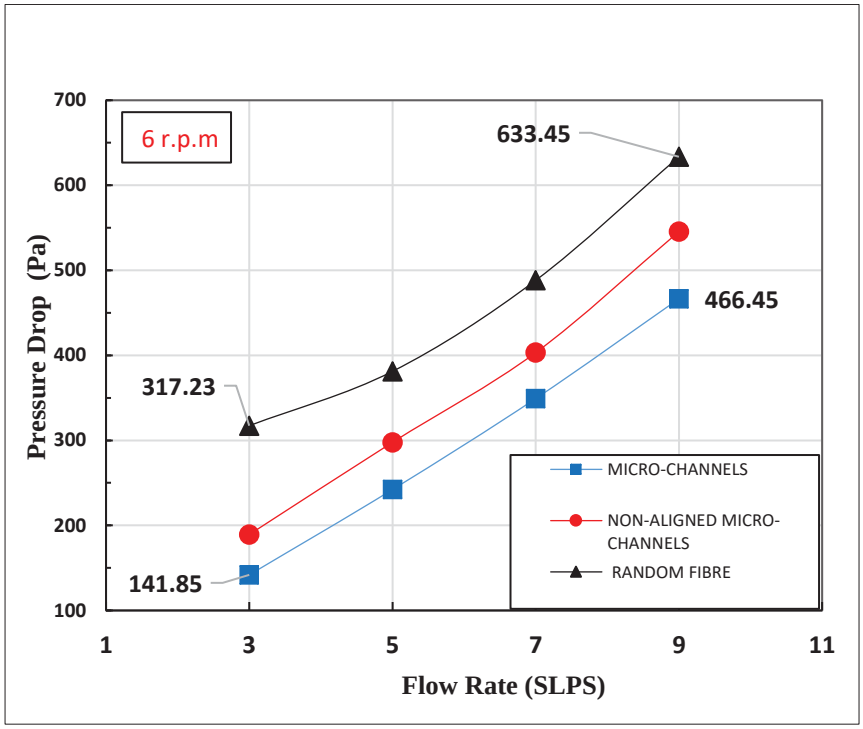


[a]: at (Th= 90 ^{0}C)

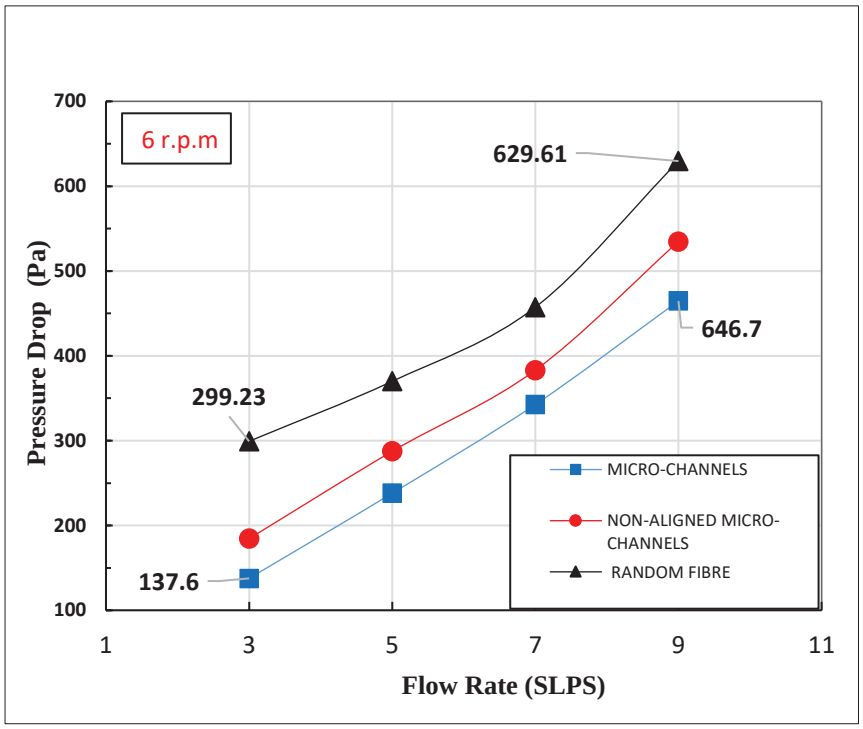


[b]: at (Th= 70 ^{0}C)

Figure 4.48 Pressure Drop (ΔP) vs. Flow rate with (r.p.m=3)

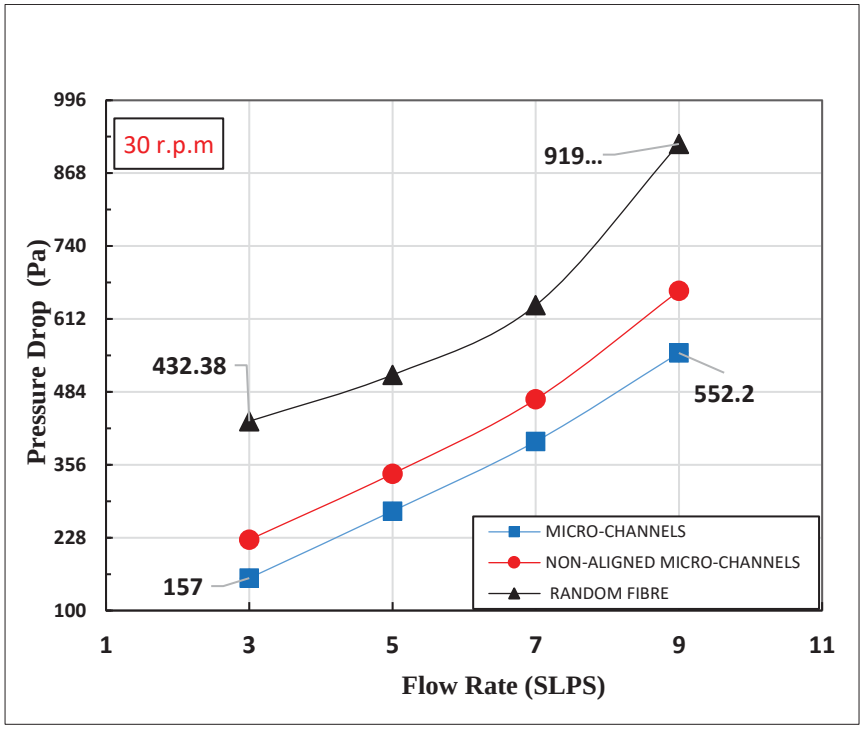


[a]: at (Th= 90 ^{0}C)

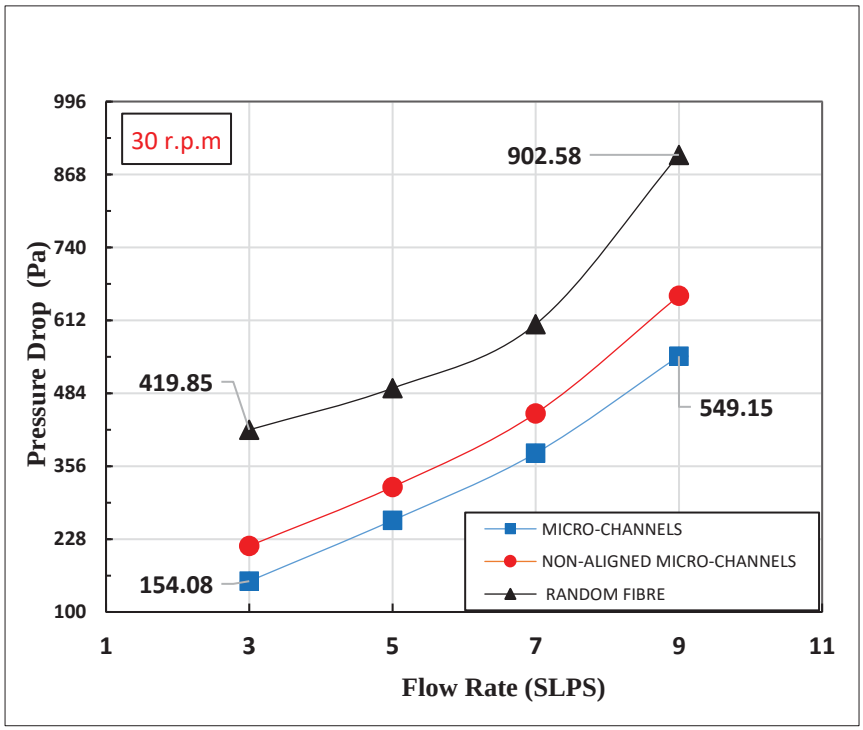


[b]: at (Th= 70 ^{0}C)

Figure 4.49 Pressure Drop (ΔP) vs. Flow rate with (r.p.m=6)



[a]: at (Th= 90 ^{0}C)



[b]: at (Th= 70 ^{0}C)

Figure 4.50 Pressure Drop (ΔP) vs. Flow rate with (r.p.m=30)

In all previous figures (Figure 4.48 to Figure 4.50) the Random fibre matrix has the highest average pressure drop, while the Micro-channels matrix has the lowest average pressure drop. For examples, in Figure 4.50 (a), at r.p.m=30 and SLPS=9 the average pressure drop 919 and 552 Pa for the Random fibre matrix and the Micro-channels matrix respectively. This is due to the flow separation which is high in the Random fibre matrix and not significant in the micro-channels [100]. This is good result since it confirms that the Micro-channels regenerator produces the lowest pressure drop during the oscillatory flow compared to the Random fibre and the Non-aligned micro-channels regenerators, which will also have the potential to improve the performance of the Stirling engine [55].

Figure 4.51 (a) to (d) compare the effect of changing the valve frequency (directly related to the closing speed in r.p.m) on the pressure drop for the three regenerators in both types of the flow: the unidirectional and the oscillatory flow. The inlet temperature in this comparison was Th= 90 °C in all figures while the flow rate was changed from SLPS=3 to 9. It can be seen that the pressure drop in the oscillatory flow case is very high compared to the case of one directional flow as the speed increases [104]. The pressure drop in the oscillatory flow was more than triple compared to the pressure drop in the unidirectional flow. For example, in Figure 4.51 (a) at flow rate SLPS=3 and flow conditions r.p.m = 0, 3, 6 and 30, respectively, for the micro-channels matrix, the pressure drop reads 125, 135, 142 and 157 Pa, and for the random fibre matrix the pressure drop rate reads 300, 310, 317 and 432 Pa. Similarly, in Figure 4.51 (d) with flow rate SLPS=9 the pressure drop in the micro-channels matrix reads 371, 429.5, 466 and 552 Pa, and in the random fibre matrix reads 538, 596.5, 633 and 919 Pa. It is observed that the pressure drop in the random fibre matrix in the unidirectional flow is almost double that of the unidirectional flow and that was concluded also in the study by [104]. From all data presented in this section, it is clear that the pressure drop in the micro-channels

regenerator is lower than that of the conventional regenerator (namely random fibre regenerator) indicating its potential to improve the performance of the Stirling engine.

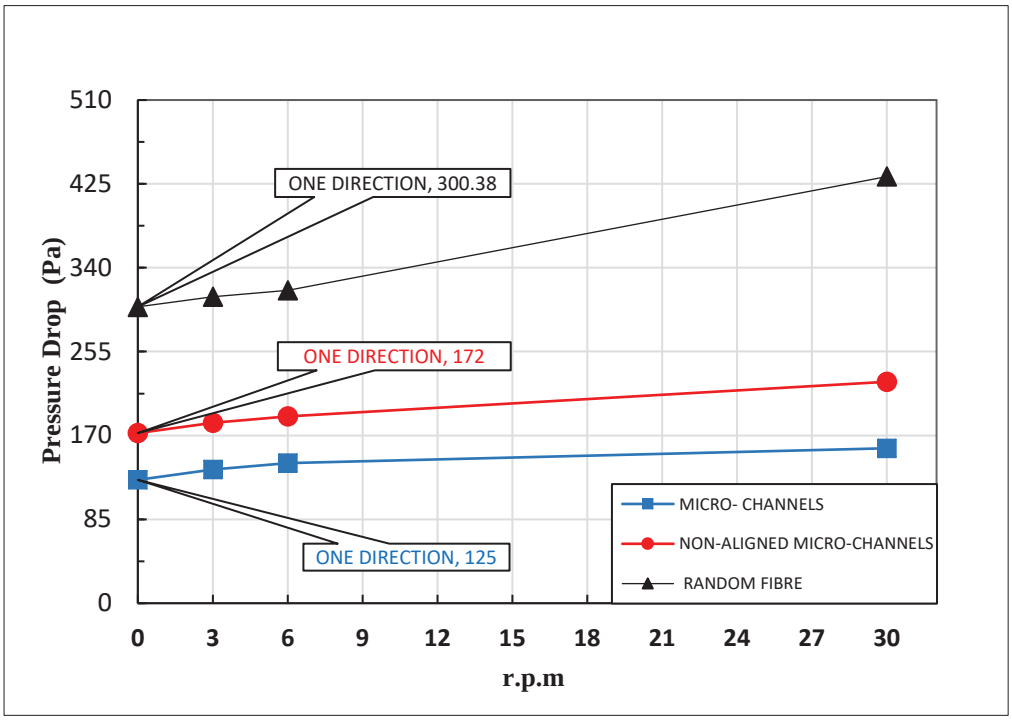


Figure 4.51 [a]: Pressure Drop (ΔP) vs. r.p.m at (SLPS=3 & Th= 90 ^{0}C)

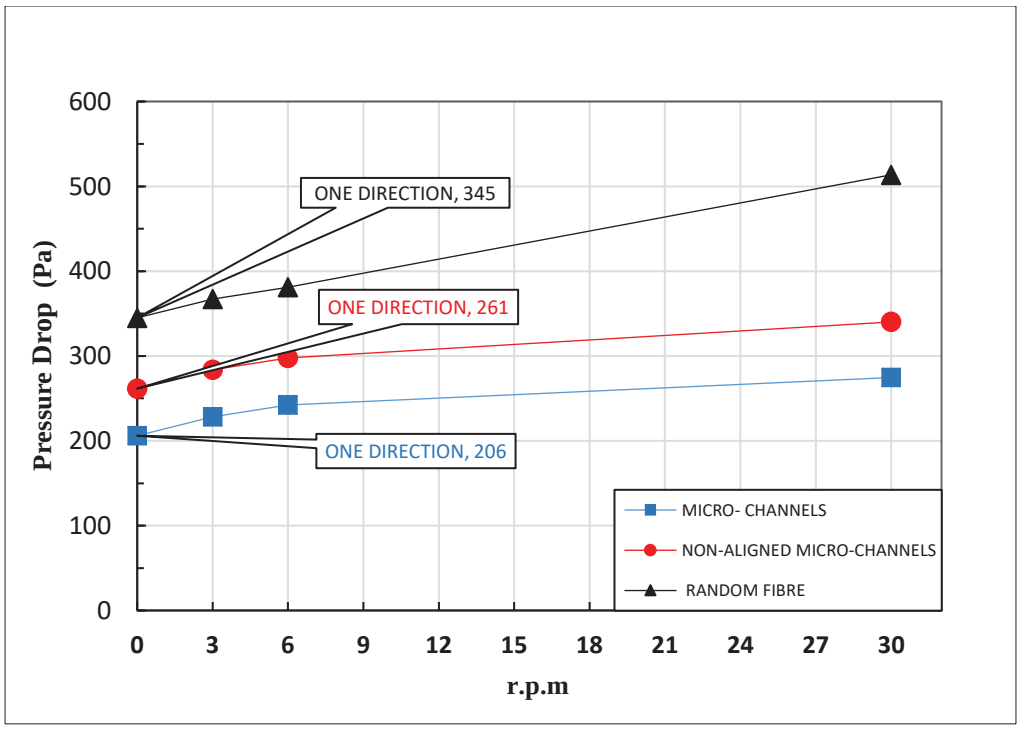


Figure 4.51 [b]: Pressure Drop (ΔP) vs. r.p.m at (SLPS=5 & Th= 90 ^{0}C)

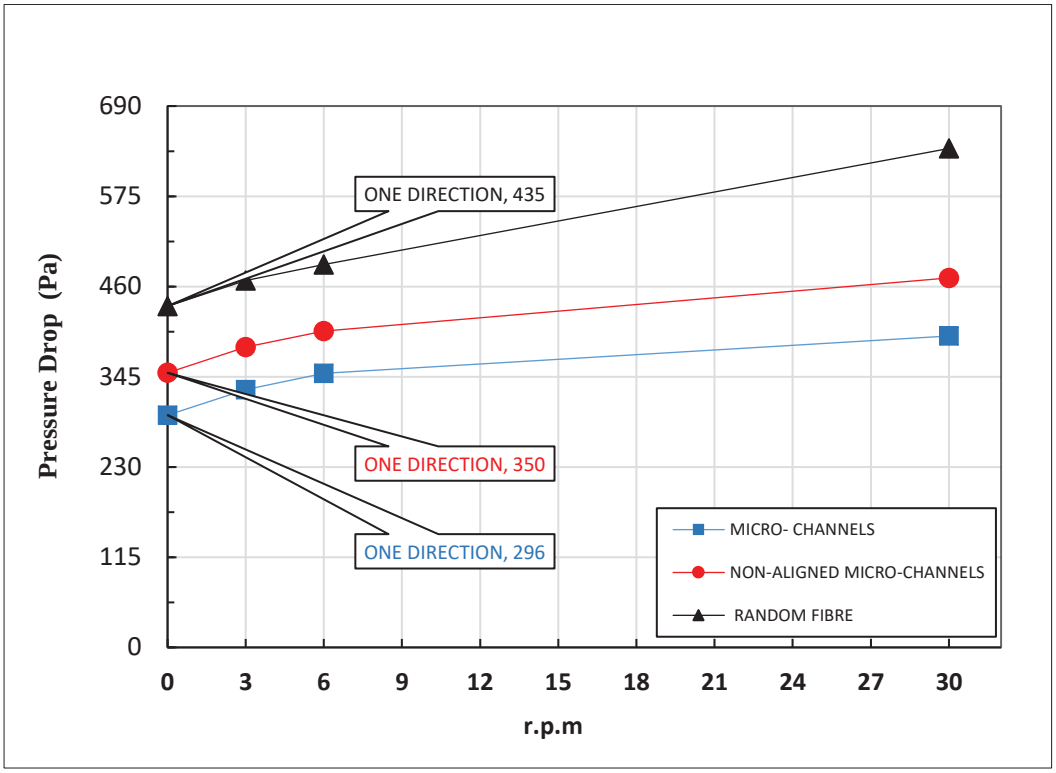


Figure 4.51 [c]: Pressure Drop (ΔP) vs. r.p.m at (SLPS=7 & Th= 90 ^{0}C)

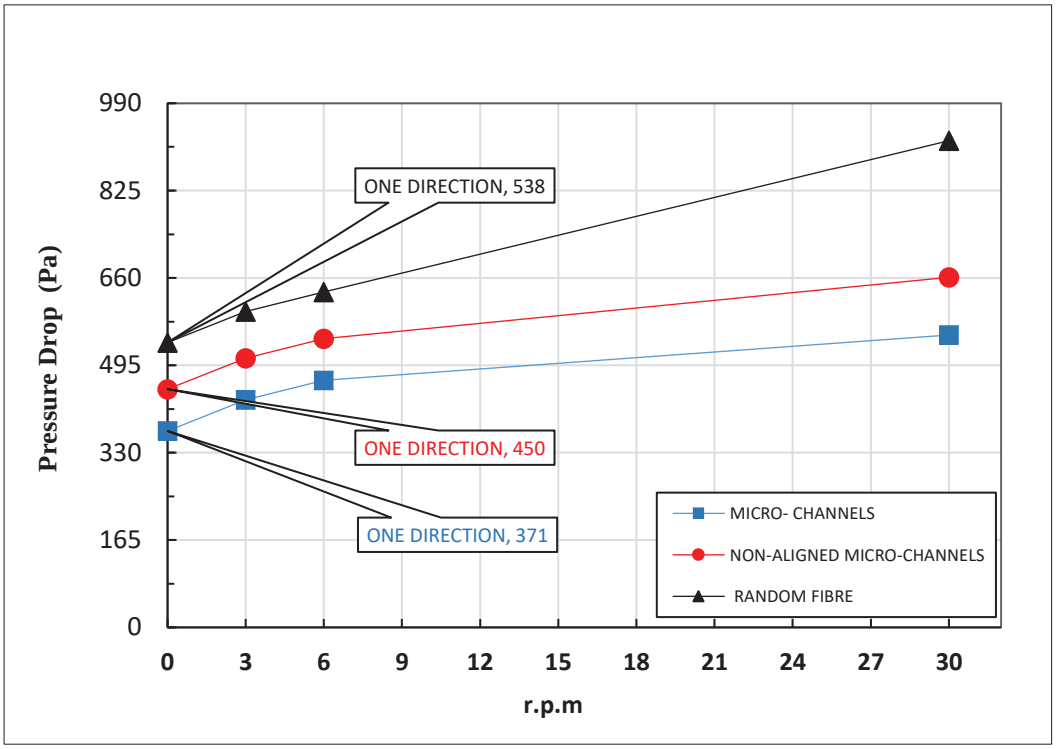


Figure 4.51 [d]: Pressure Drop (ΔP) vs. r.p.m at (SLPS=9 & Th= 90 ^{0}C)

Figure 4.51 Pressure Drop (ΔP) vs. r.p.m at different flow rate (Th=90 ^{0}C)

4.10 Conclusion

A new parallel-geometry segmented regenerator with circular micro-channels structure was manufactured and developed at the University of Birmingham with its CFD model. Experimental measurements were conducted by using a test rig which designed in order to compare three regenerators: The Non-aligned micro-channels and Random fibre regenerators and the parallel-geometry Micro-channels regenerator.

From the experimental results that shown in this chapter, it was found that the Random Fibre regenerator performed better than the other two-segmented regenerator in terms of thermal effectiveness regenerator did. However, in the other hand, the pressure drop in the Random Fibre regenerator was higher than the other segmented regenerators, and that can be more observed in terms of friction factor correlations.

A comparison between flow friction correlations for the segmented micro-channel regenerator and two conventional regenerators: Screen woven and Random fibre woven matrixes using their available correlation from the open literature. The flow friction correlations for the Screen woven and Random fibre woven matrixes were taken from Geodon [84]. It found that the friction factor in the micro-channels matrix is smaller more than five times of the other conventional matrixes (See Table 4.7); that was also conducted by [78]. This comparison by using the friction factor can be considered as pressure drop comparison where the friction factor can be defined to be a function of the pressure drop (See Eq.4.27).

$$f = \left(\frac{\Delta P}{\frac{1}{2}\rho {U_m}^2} \right) \frac{D_H}{L} \qquad 4.27$$

The pressure drop through the regenerator and thermal losses have a major effect on the indicated power of the Stirling engine. The pressure drop in small-scale Stirling engines leads to about 11% reduction in the power output while about 1.5% reduction occurs due to the thermal losses [57].

It should be noteworthy that the friction factor for the developed regenerator (micro-channels matrix) is close to Darcy friction factor for the laminar flow. This pointed to that the use of classical friction correction for micro-channels can be applied in this investigated choice. (See Table 4.7).

The validation of the developed regenerator will be presented in the next chapter with some suggestions in terms of enhancing the new developed regenerator.

Table 4.7 Darcy friction factor comparison for the regenerator matrixes: Micro-channels, Screen woven and Random fibre at different Reynolds numbers

	Friction factor			
Re	**Darcy**	**Micro-Channels**	**Screen woven**	**Random fibre**
567.8	0.112716	0.166088	2.45668257	3.345892559
946	0.067653	0.103247	2.251581412	3.153745759
1324	0.048338	0.075511	2.140599185	3.045836068
1703	0.037581	0.060521	2.066706316	2.972226765

CHAPTER 5

DEVELOPMENT OF EFFICIENT SEGMENTED MICRO-CHANNELS REGENERATORS

5.1 Introduction

This chapter presents the development of efficient segmented micro-channel regenerator thorough CFD simulations that been validated with experimental measurements. The temperature, pressure and flow rate were the various parameters measured during the experimental tests; as shown in the previous chapter. The validation of the developed regenerator CFD modelling will be presented in tow sections, the first section for the unidirectional flow model, and the second one for the oscillatory flow model. The third section will be devoted for the effect of increasing the number of segmentation on the regenerator effectiveness. The effect of changing the micro channel diameter on the performance of the best segmented regenerator will be presented in the fourth section. This chapter will conclude with developing correlations for Nusselt number and friction factor that gained from the CFD model based on the oscillatory flow results. These correlations will be inserted as porous media parameters (Forchheimer drag coefficient β_F and Permeability K) to the CFD model of the V-type alpha Stirling engine developed in the next chapter (6) in terms of evaluation the engine performance.

5.2 Experimental and CFD comparison for unidirectional flow

This section presents the comparison between the CFD results and the experimental measurements as shown in Figure 4.22 for the inlet, outlet, housing surface temperatures and pressure losses for the micro channel regenerator with 1mm channel diameter in one directional flow. Figure 5.1 shows the geometry for the micro-channel regenerator CFD model including the front and back cones, the regenerator housing and the micro-channels four sections. Figure 5.2 shows the CFD temperature contours for the micro-channel regenerator at 3SPLS flow rate case and run duration of 360s with the flow going from the hot side to the cold side. Figure 5.2 (a) shows the temperature contours for the whole micro-channel assembly, while Figure 5.2 (b) to (e) shows the temperature contours for the micro-channels sections, and Figure 5.2 (f) to (h) shows the temperature contours for regenerator housing, hot and cold cones.

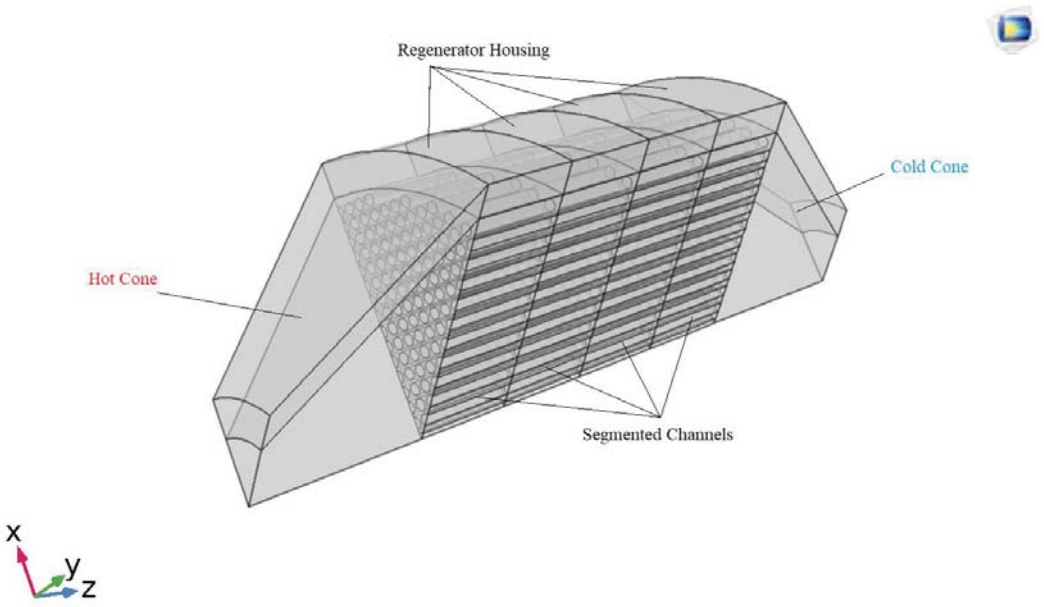


Figure 5.1Micro-channel regenerator geometry for the CFD model

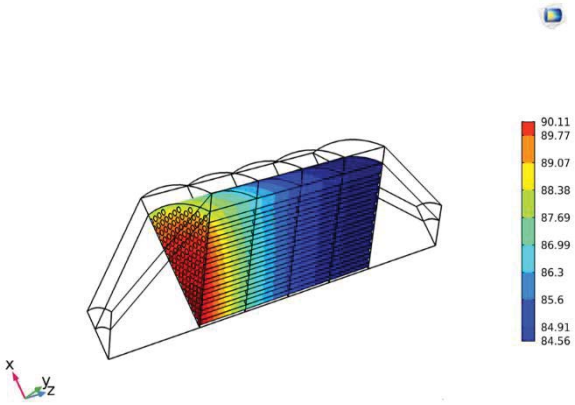


Figure 5.2: [a] Temperature contours (^{0}C) for the micro-channels assembly

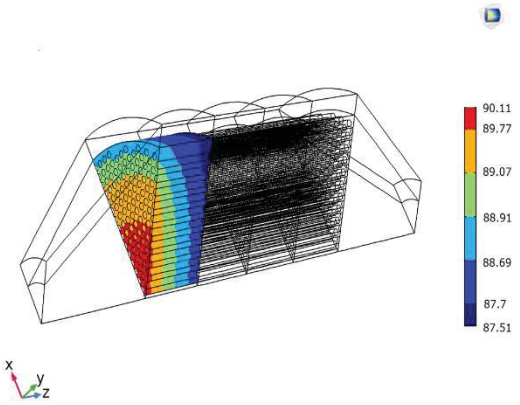


Figure 5.2: [b] Temperature contours (^{0}C) for the micro-channels sections 1

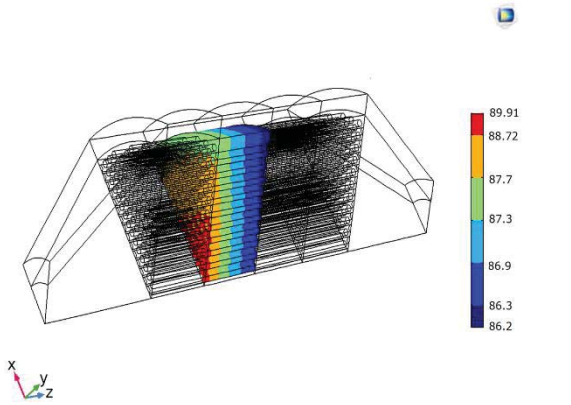


Figure 5.2: [c] Temperature contours (^{0}C) for the micro-channels sections 2

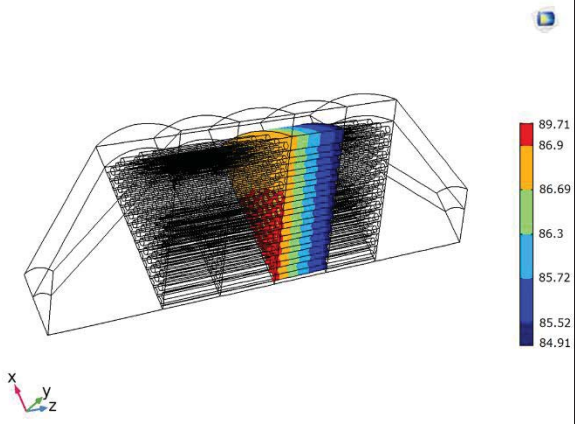


Figure 5.2: [d] Temperature contours (^{0}C) for the micro-channels sections 3

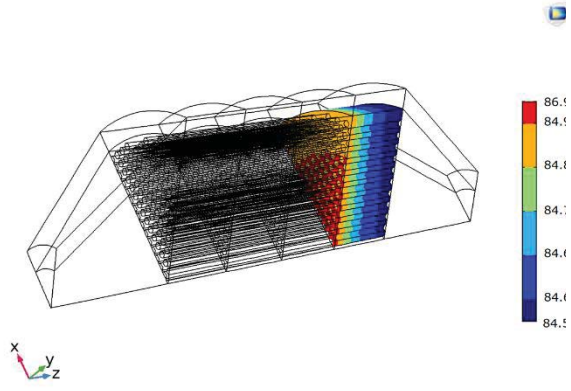


Figure 5.2: [e] Temperature contours (^{0}C) for the micro-channels sections 4

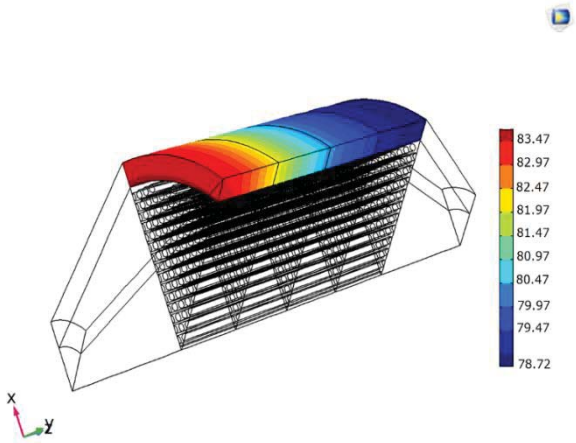


Figure 5.2:[f] Temperature contours (^{0}C) for regenerator housing

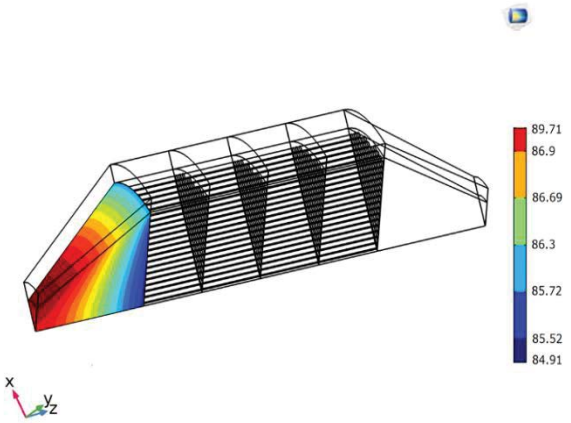


Figure 5.2:[g] Temperature contours (^{0}C) for hot cone

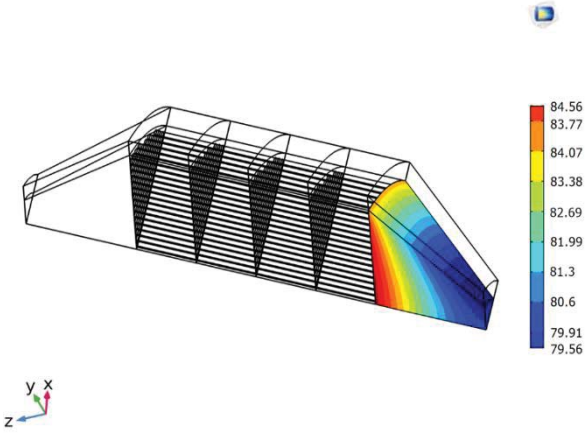


Figure 5.2: [h] Temperature contours (^{0}C) for cold cone

Figure 5.2: [a] to [h] Micro-channel regenerator temperature contours at t=360 s and SLPS=3

Figure 5.3 compares the surface temperatures T_1, T_2, T_3 and T_4 (as shown in Figure 4.22) CFD time variation with their experimentally measured ones for SLPS = 3 and 5 respectively.

Figure 5.3 (a) presents the CFD simulation for surface temperaturT_1 with experimentally measured values for SLPS = 3 and 5. Maximum deviations between CFD and experimental are 18.3% and 18.8% for SLPS = 3 and 5 respectively.

Figure 5.3 (b) shows the surface temperature T_2 CFD values compared with experimentally measured ones with maximum deviations of 13.2% and 18.8% for SLPS = 3 and 5 respectively.

Figure 5.3 (c) shows the surface temperaturT_3 CFD values compared with experimentally measured ones with maximum deviations of 9.21% and 15.6% for SLPS = 3 and 5 respectively.

Figure 5.3 (d) shows the surface temperaturT_4 CFD values compared with experimentally measured ones with maximum deviations of 7.4% and 14.76% for SLPS = 3 and 5 respectively.

Figure 5.4 compares the CFD and experimental time variation for the (Tc_i) temperature, which is the air outlet temperature from the micro-channel regenerator from outlet cone side (as shown in Figure 4.22). The comparison at inlet hot air temperature Th= 70 ^{0}C and 90 ^{0}C with flow rates of SLPS = 3 and 5 respectively.

Results showed that maximum deviations between CFD simulation results and the experimental measurements varied between 3.1% and 10.56%.

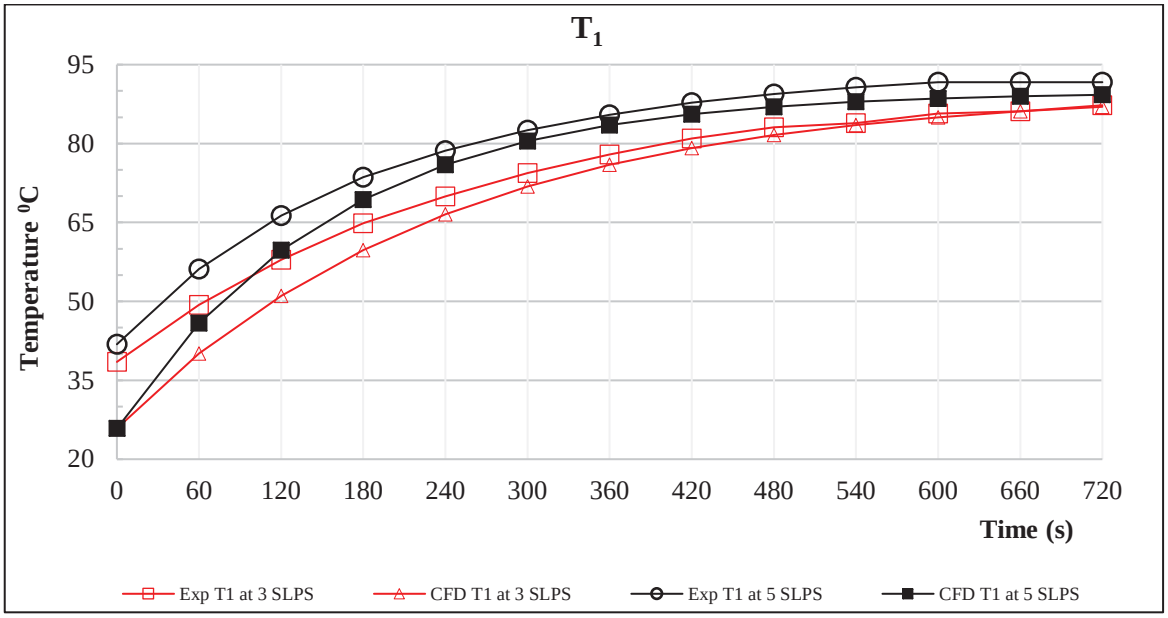


Figure 5.3: [a] Surface temperature T_1 CFD values compared with experimentally measured for SLPS = 3 and 5

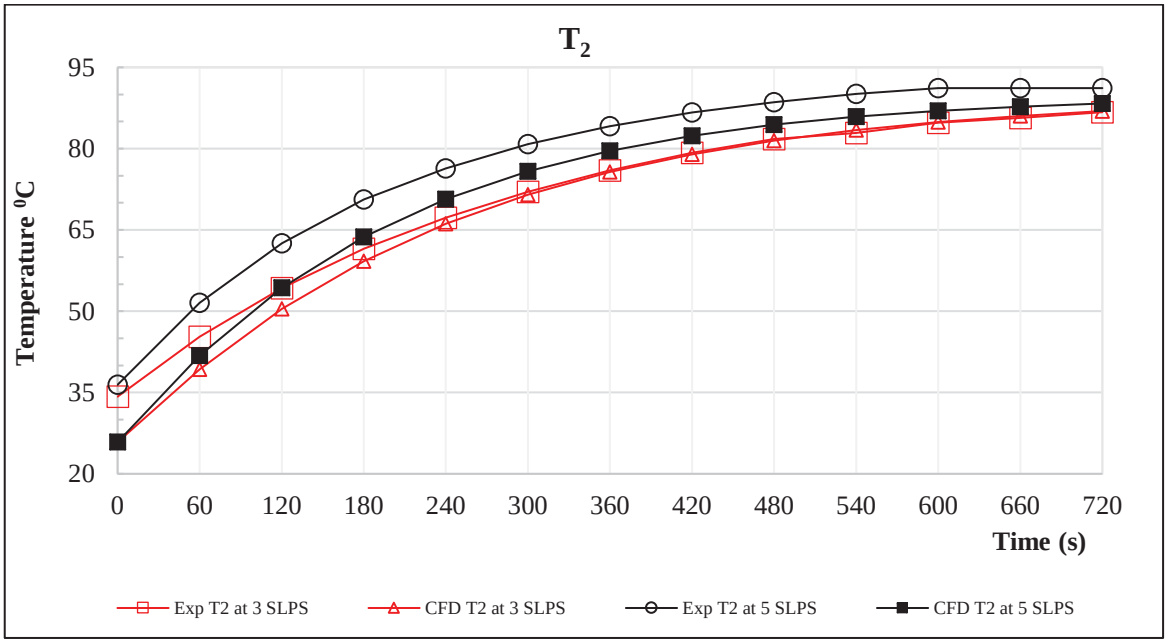


Figure 5.3: [b] Surface temperature T_2 CFD values compared with experimentally measured for SLPS = 3 and 5

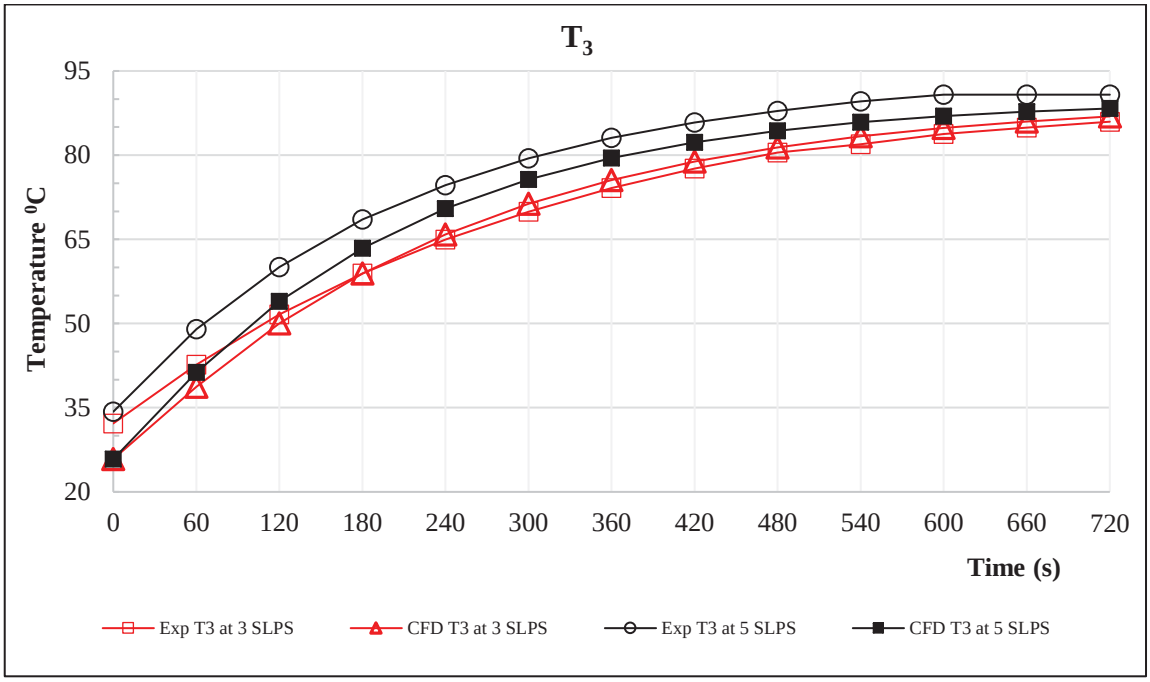


Figure 5.3: [c] Surface temperature T_3 CFD values compared with experimentally measured for SLPS = 3 and 5

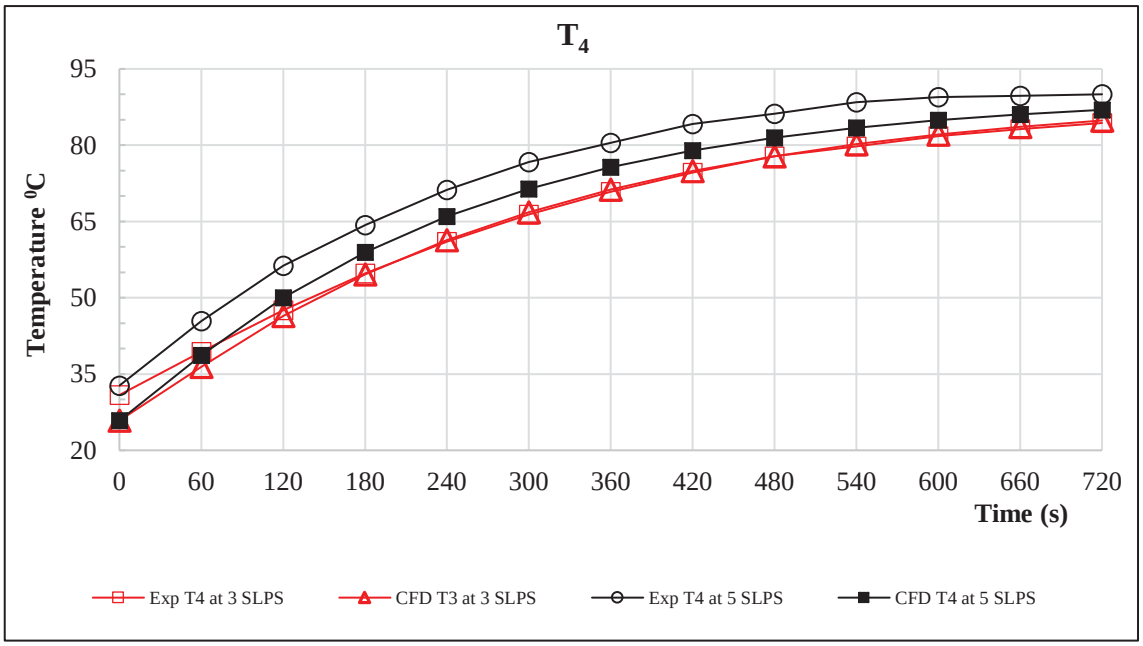


Figure 5.3: [d] Surface temperature T_4 CFD values compared with experimentally measured for SLPS = 3 and 5

Figure 5.3 [a]to[d] Surface temperature CFD values compared with experimentally measured for SLPS = 3 and 5.

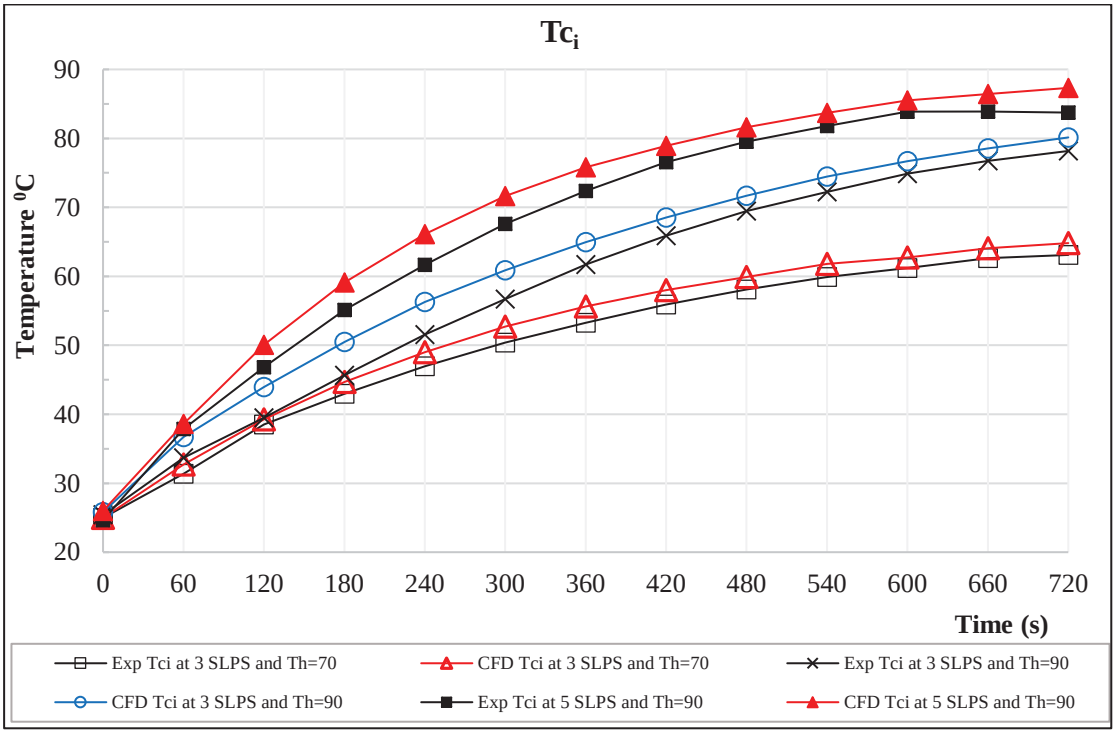


Figure 5.4 CFD and experimental time variation for the (Tc$_i$) temperature at Th= 90 with SLPS=3 and 5.

Figure 5.5 compares results from the experiment to the CFD modelling in terms of pressure drop and the inlet fluid velocity. It can be seen that; as the inlet velocity increases the pressure drop increases and the relation is almost varying linearly. The maximum deviation value is 10.6%.

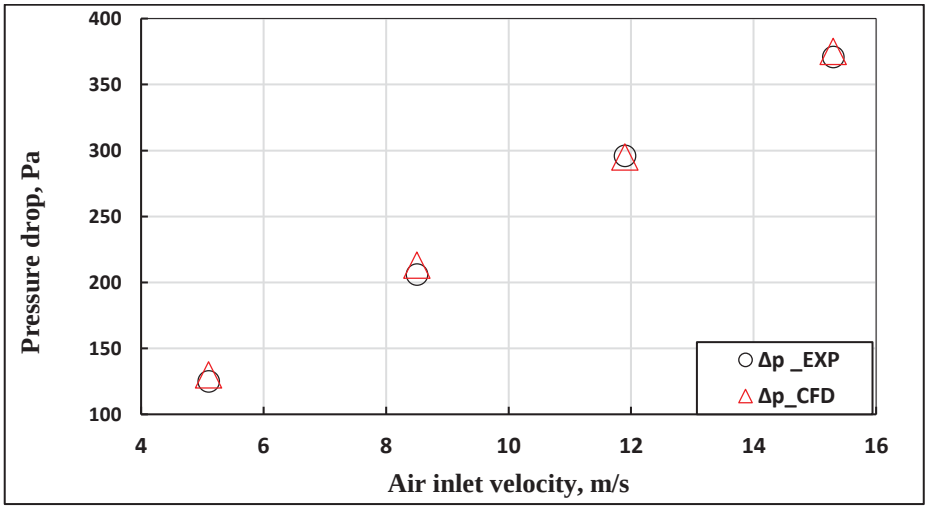


Figure 5.5 comparison of pressure drop across the micro-channels regenerator between experiment and CFD

5.3 Experimental and CFD comparison for two directional flows

This section presents the comparison between the CFD results and the experimental measurements at r.p.m = 30 for the inlet, outlet, surface temperatures and pressure losses for the micro channel regenerator with 1mm channel diameter in two a directional flow. Figure 5.6 (a) shows the surface temperature contours at the cold blow, at the end of the cycle 359, with SPLS=3 and r.p.m=30, while Figure 5.6 (b) shows the surface temperature contours at the hot blow, at the beginning of the cycle 360.

In the case of the cold blow the maximum temperature is 59.6 ^{0}C and the minimum is 54.7 ^{0}C. In the case of the hot blow the maximum temperature is 60.5 ^{0}C and the minimum is 55 ^{0}C. Figure 5.7 compare the surface temperature measurements (T_1, T_2, T_3 and T_4) from experimental measurements and CFD modelling. The deviations of the CFD predictions from experimental data for the surface temperature measurements were in the range of ±4% to ±18%.

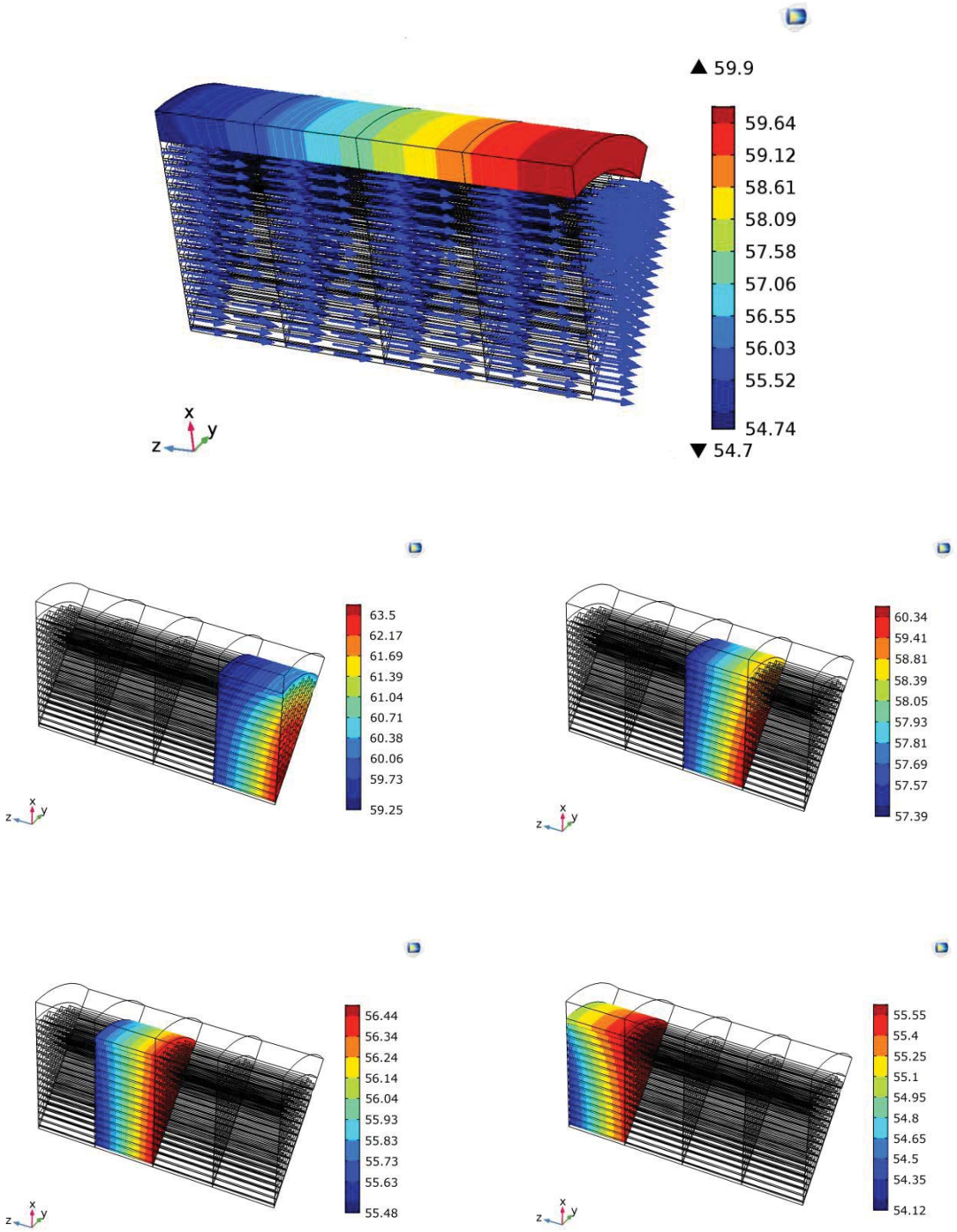


Figure5.6 [a]: Temperature contours (^{0}C) (Cold blow)

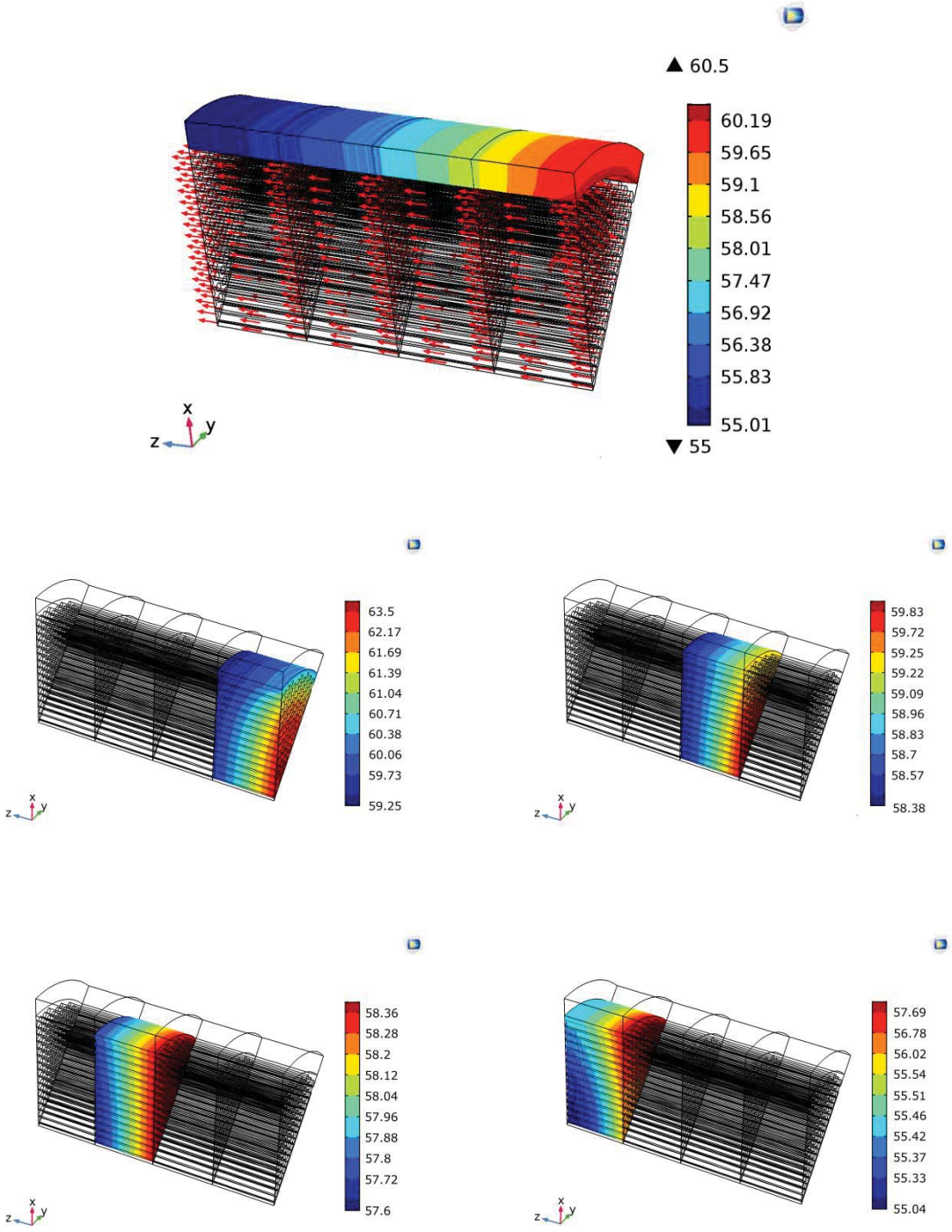


Figure5.6 [b]: Temperature contours (^{0}C) (Hot blow)

Figure 5.6 Regenerator temperature contours (^{0}C) at (t=720s, SLPS=3& r.p.m=30)

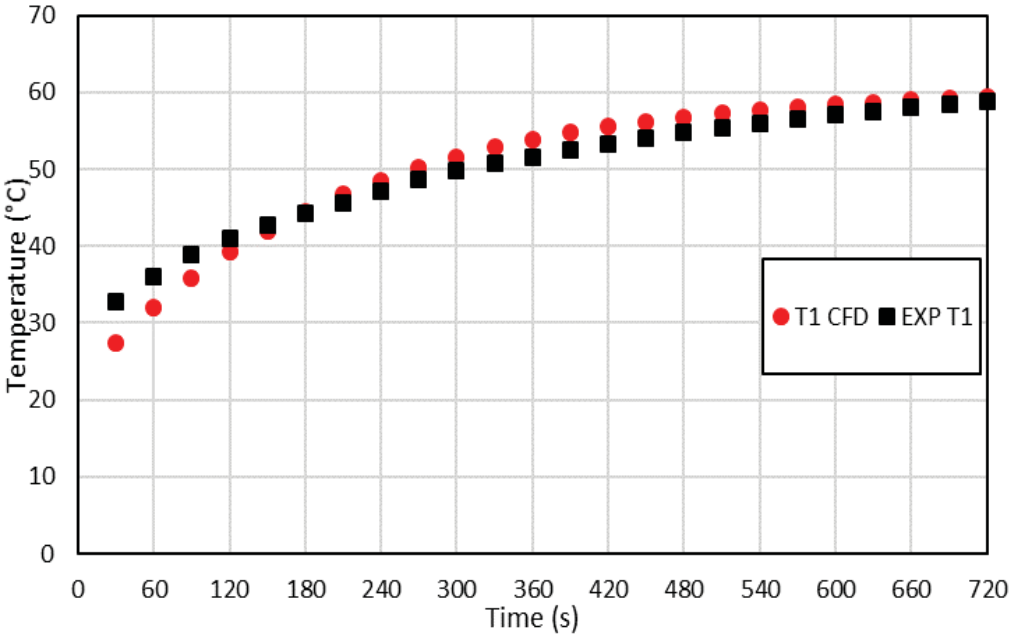


Figure 5.7 [a]: (T_1)

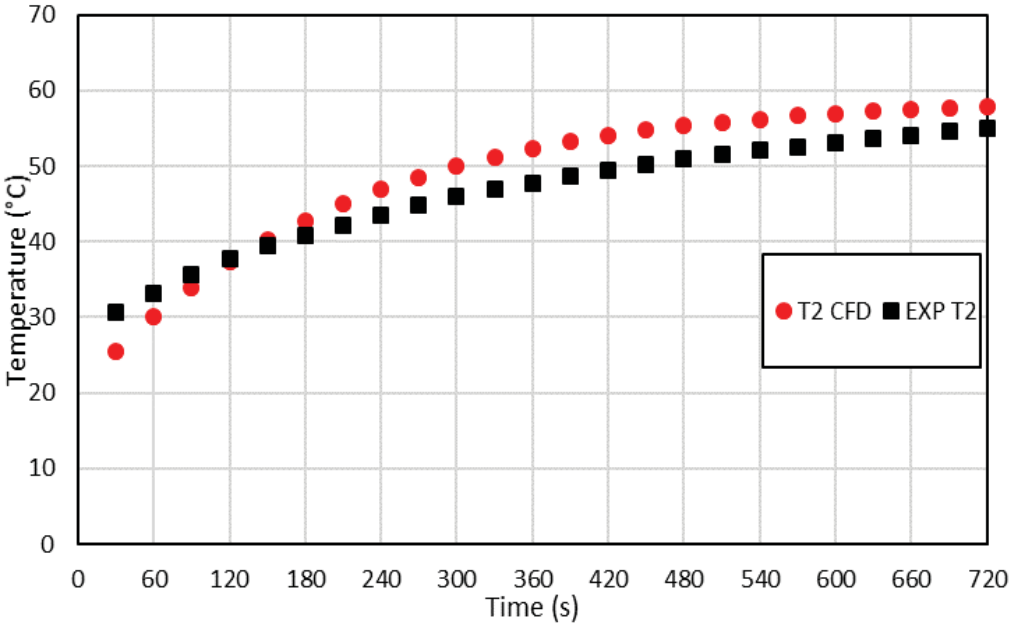


Figure 5.7 [b]: (T_2)

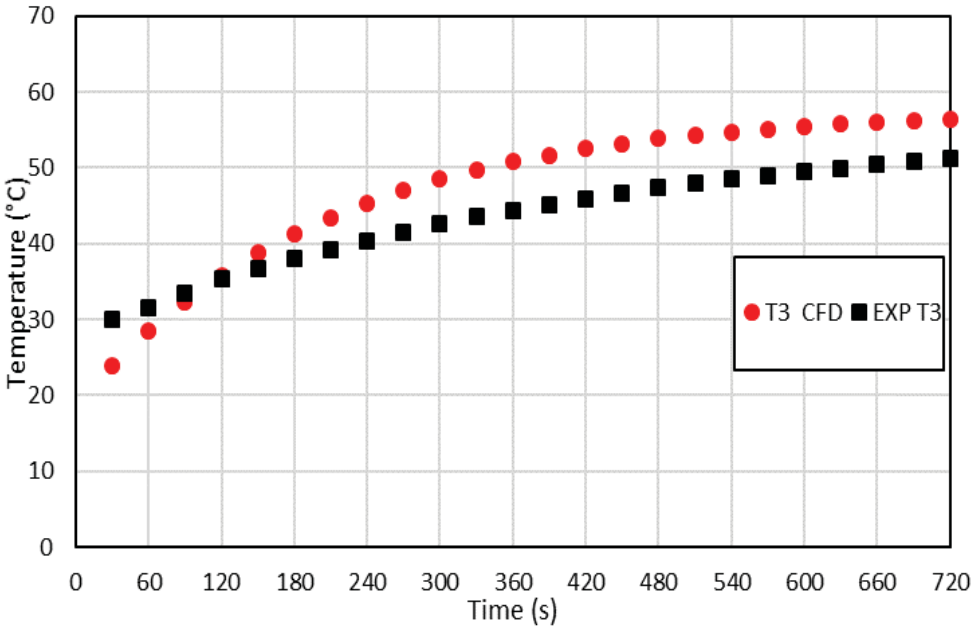


Figure 5.7 [c]: (T_3)

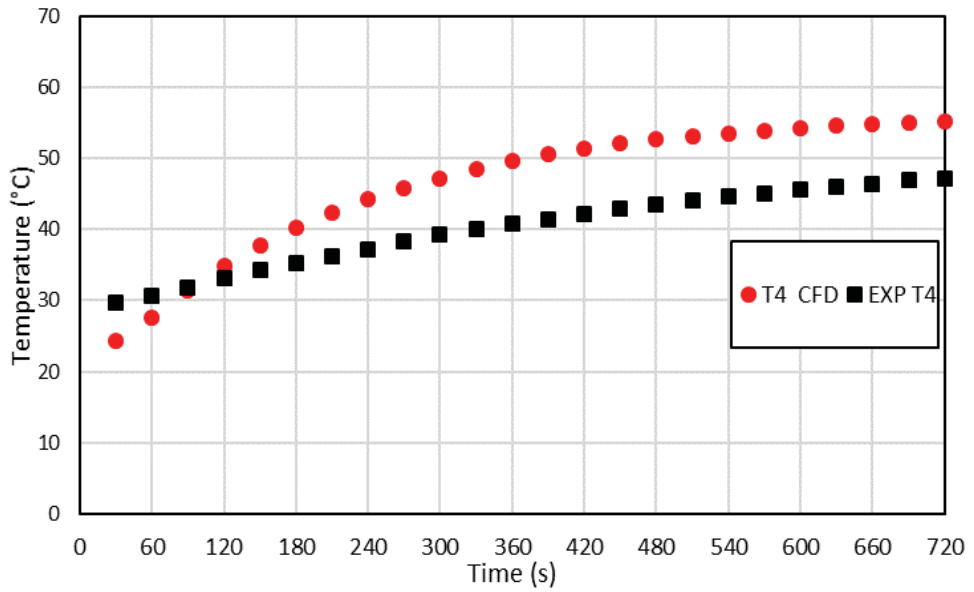


Figure 5.7 [d]: (T_4)

Figure 5.7 Comparison of surface temperature from CFD simulations and experiments for two directional flow at SLPS=3 & r.p.m=30.

Figure 5.8 and Figure 5.9 compare the samples of the CFD predicted inlet and outlet temperatures (**Th_i** &**Tc_i**) with the experimental measurements (during cycles 359 and 360) at operating conditions r.p.m=30 and flow rates of **SLPS=3** and **SLPS=5** respectively.

Maximum deviations between CFD and experimental with flow rate SLPS = 3 are 6.03% and 6.41% for **Th_i** and **Tc_i** respectively. The maximum deviations with flow rate SLPS = 3 between CFD and experimental are 5.54% and 6.03% for **Th_i** and **Tc_i** respectively

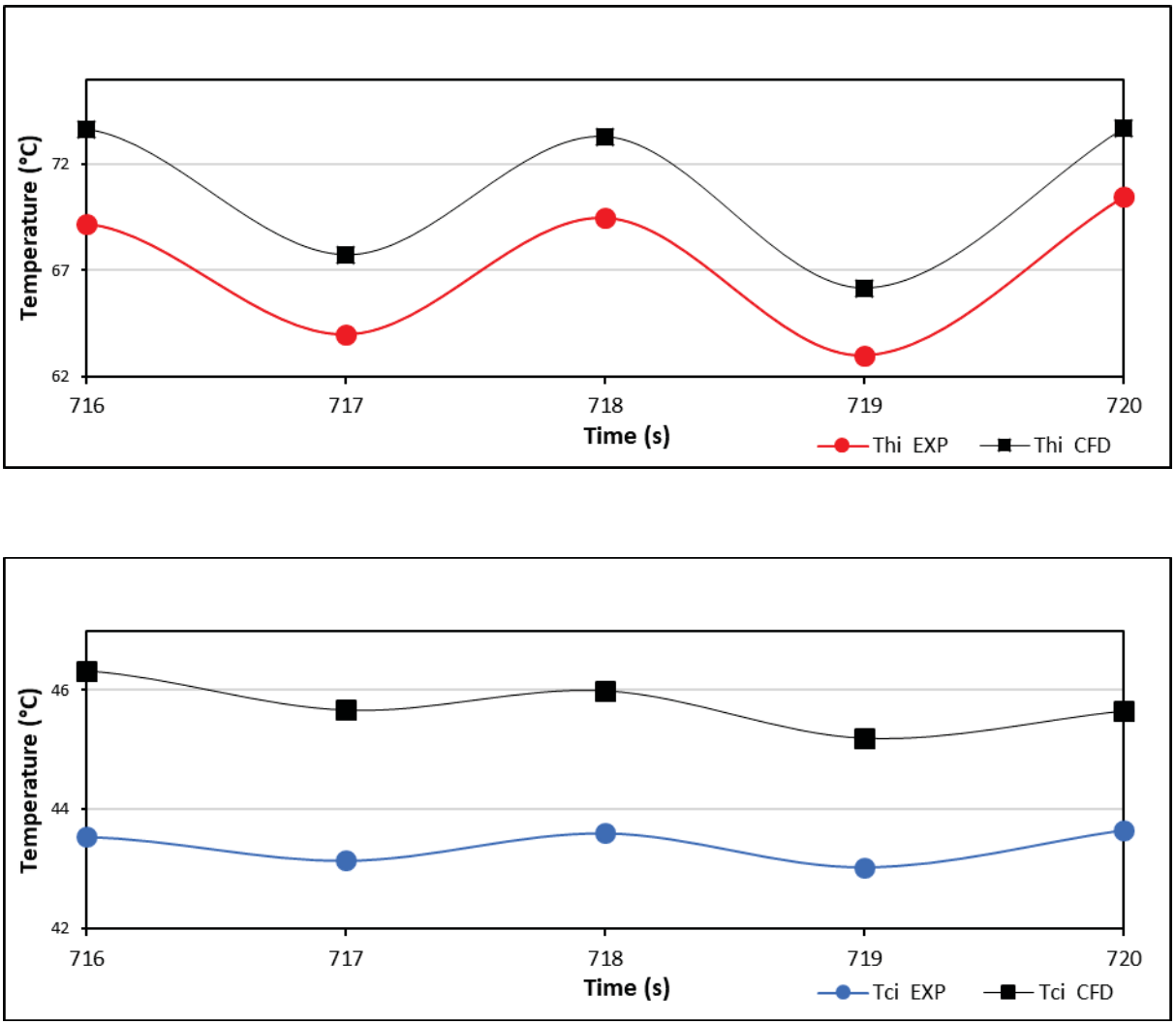
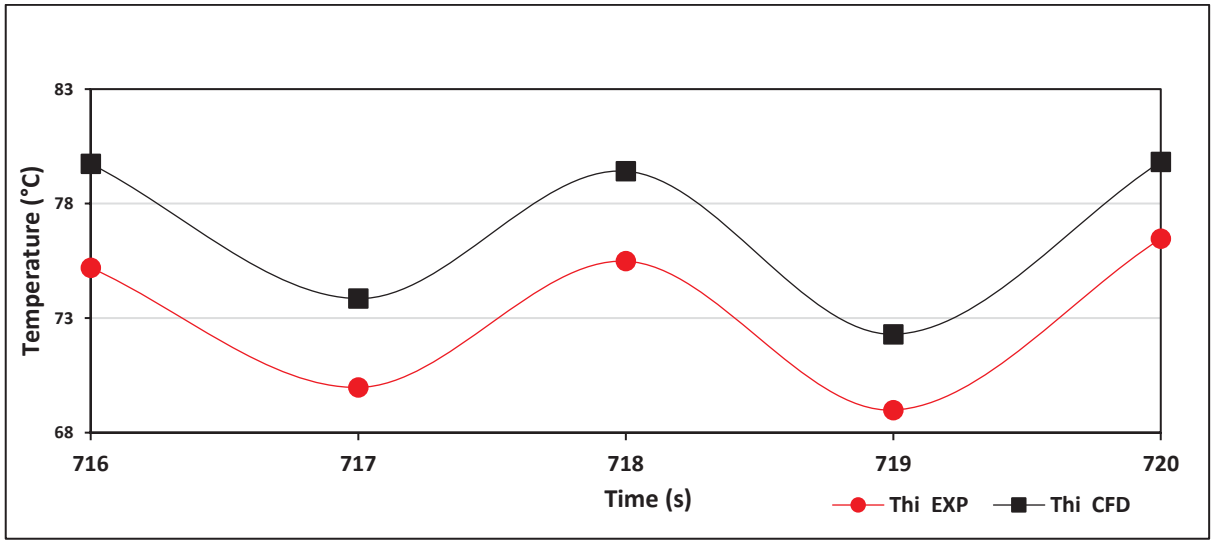


Figure 5.8 Comparison of inlet and outlet temperatures (Th_i &Tc_i) from CFD simulations and experiments for two directional flow at SLPS=3 & r.p.m=30 (cycle 359 & 360)



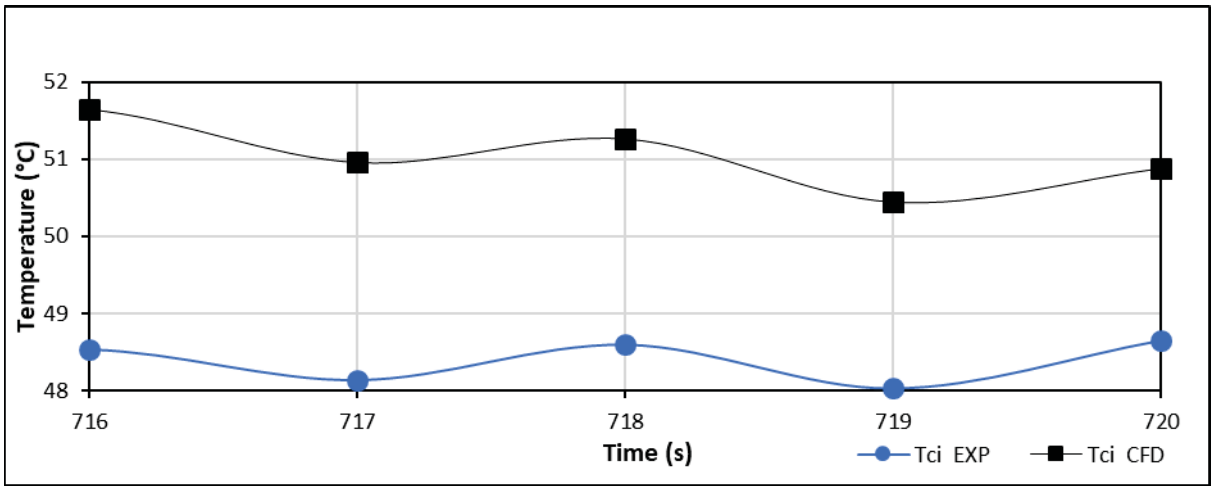


Figure 5.9 Comparison of inlet and outlet temperatures (Th_i &Tc_i) from CFD simulations and experiments for two directional flow at SLPS=5 & r.p.m=30 (cycle 359 & 360)

Figure 5.10 compares results from the experimental measurements to the CFD modelling in terms of pressure drop and the inlet fluid velocity. It is clear that as the inlet velocity increases the pressure drop increases and the relation is almost varying linearly. The deviation value is decreasing from 16.36 to 8.5% with increasing of the inlet velocity.

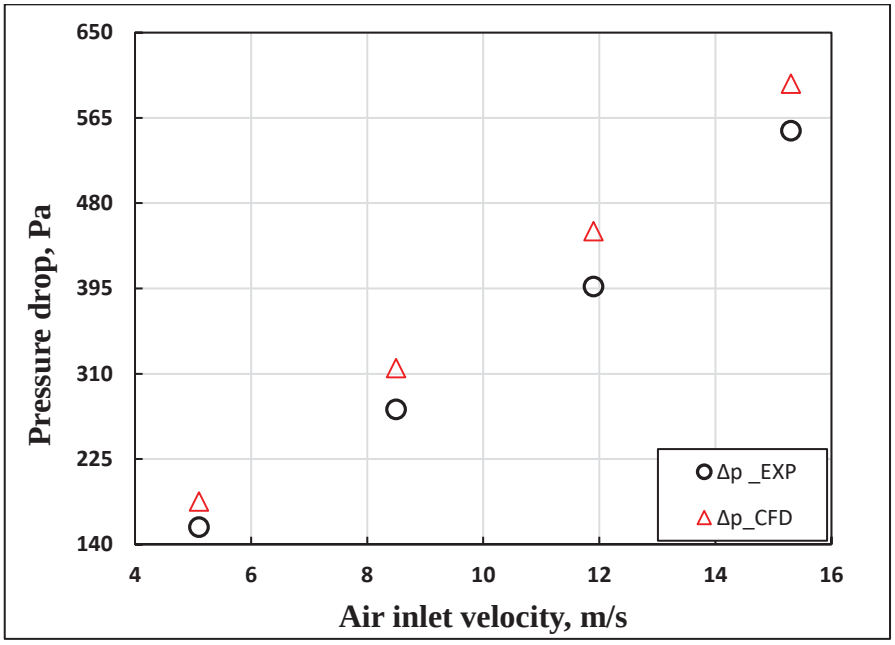


Figure 5.10 Pressure drop across the regenerator channels:

Experimental versus CFD results at r.p.m=30

Figure 5.11 shows the relationship between the friction factor and Reynolds number, with the friction factor calculated using (Eq.(4.21) form chapter (4)):

$$f = \left(\frac{\Delta P}{\frac{1}{2}\rho U_m{}^2} \right) \frac{D_H}{L} \qquad 5.1$$

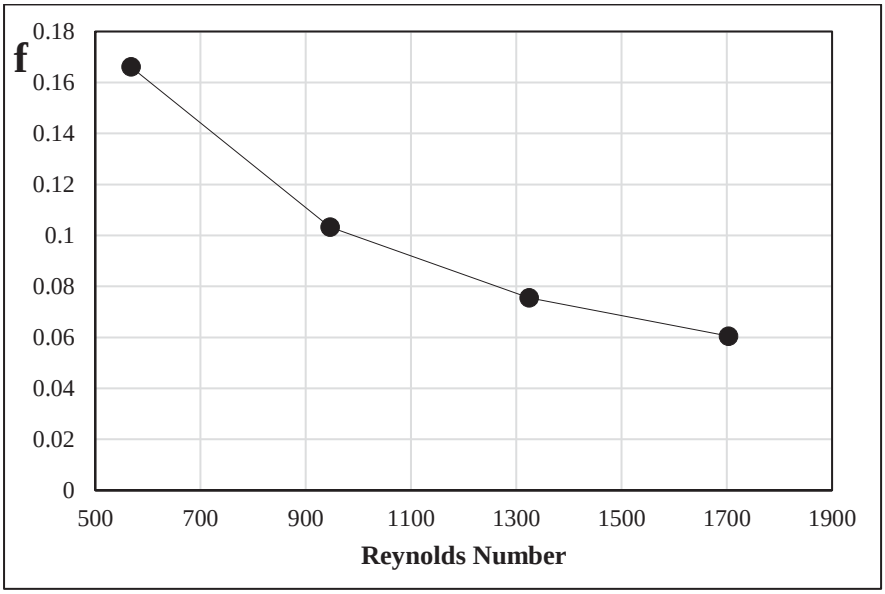


Figure 5.11 Friction factor versus Reynolds number for the micro-channels regenerator

The friction-factor correlation for the developed micro-channels regenerator is:

$$f = a_1 Re + a_2 \quad 5.2$$

Where,

$$a_1 = -9 \times 10^{-5} \quad 5.3$$

$$a_2 = 0.2047 \quad 5.4$$

The Forchheimer drag coefficient β_F and the permeability, K can be evaluated by using the following one-dimensional Darcy- Forchheimer equation:

$$\frac{\nabla p}{L} = \frac{\mu}{K} u + \beta_F u^2 \quad 5.5$$

Equation Eq.(5.5) (Darcy equation) can be re-written as:

$$\frac{\nabla p}{L} = \frac{1}{2}\frac{f}{d_h} \rho u^2 \quad 5.6$$

From the definition of Reynolds number, friction-factor, Eq. (5.5) and Eq. (5.6) , it can be determined that:

$$K = \frac{2{d_h}^2}{a_1 Re^2} \qquad 5.7$$

$$\beta_F = \frac{1}{2d_h}\,\rho\,(a_2) \qquad 5.8$$

Figure 5.12 shows the link between the average Reynolds number and Nusselt number. The trend is showing a linear behaviour. The calculation of the heat transfer coefficient was based on the heat flux and the average temperature of both the bulk fluid and the interfaces wall. An empirical equation for this relationship between the average Reynolds number and Nusselt number is shown on the legend of the figure.

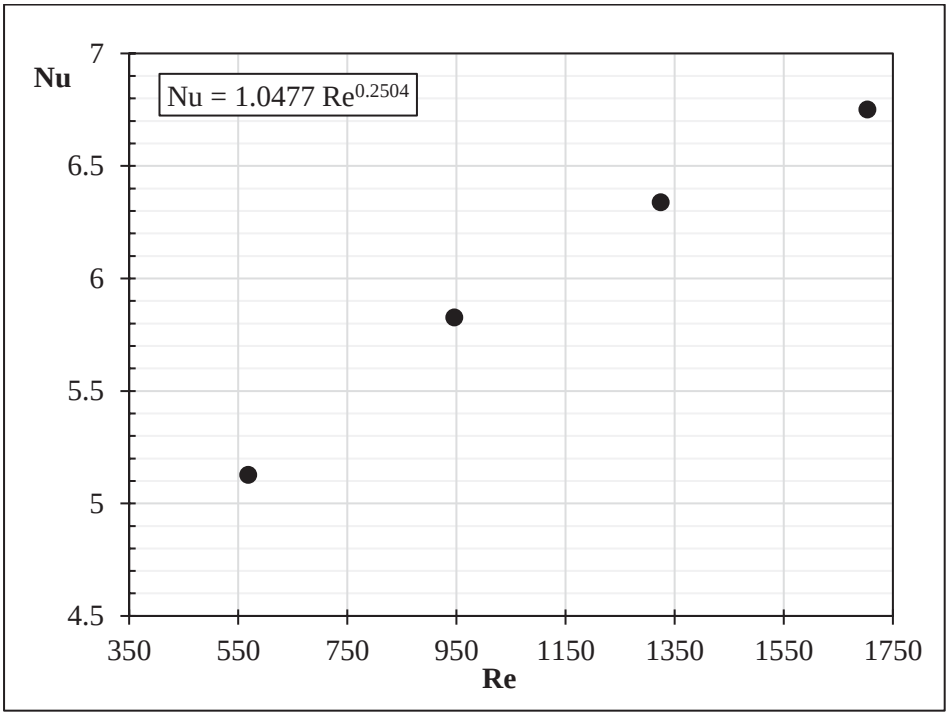


Figure 5.12 Reynolds number versus average Nusselt number for the micro-channels regenerator.

5.4 Regenerator segmentation

Increasing the number of segments for the micro-channels regenerator can alleviate the axial conduction losses due to interruption of the solid continuity [78] . In the previous chapter (4) it found that the pressure drop in the micro-channels matrix is smaller more than five times of the other two conventional matrixes namely: Screen woven and Random fibre woven. However, the micro-channels matrix regenerator performed worse than the other two regenerator in terms of thermal effectiveness regenerator. The CFD model for the oscillatory flow was used to investigate the effect of increasing the segmentation number on the performance of the micro-channels regenerator in terms of calculate the thermal effectiveness through the regenerator. Figure 5.13 shows the modelled configurations for the micro-channels regenerator with non-segmented, 4, 8, 16 and 32segments.

Figures from Figure 5.14 to 5.18 show the temperature contours at the interfaces between the solid and the air for the regenerator configurations shown in Figure 5.13 using flow rate SLPS=3, run test time of 12 minutes, open/close valve speed at r.p.m= 30 and T_h = 90 ^{0}C. It is clear from these figures that the temperature contours profile increases with the number of segmentations. The 32-segmented regenerator has the maximum temperature profile (See Figure 5.17) while the non- segmented regenerator is the lowest (See Figure 5.14). The average increasing in the interfaces temperature between the 4-segmented and the 16-segmented is about 2 ^{0}C. Although, Figure 5.15 shows a low increase in temperature profile (about 0.97 ^{0}C) for the 8-segmented compared to the 4-segmented regenerator , it is still possible to consider a temperature change between the 4-segmented and the 8-segmented (See Figure 5.14 and Figure 5.15). The 16-segmented and 32-segmented regenerators have shown maximum temperature changes where it has increased to 64.14 and 66.76 ^{0}C respectively.



Figure 5.13[a]:non-segmented

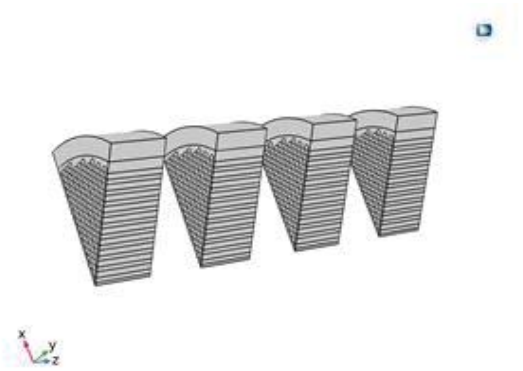


Figure 5.13 [b]:4-segmented

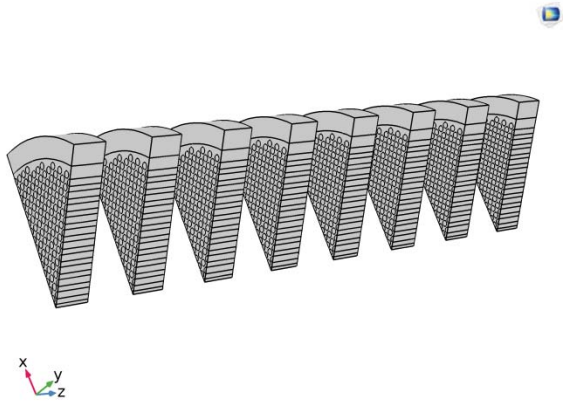


Figure 5.13 [c]:8-segmented

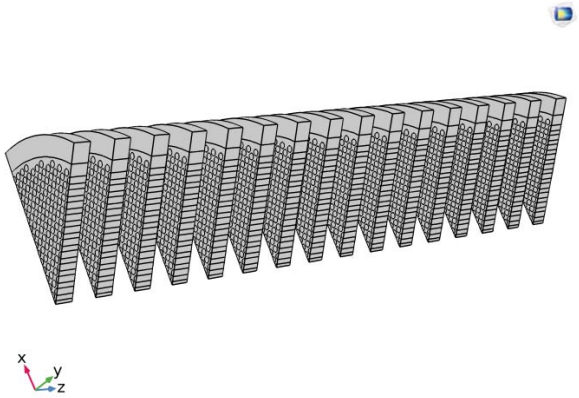


Figure 5.13 [d]:16-segmented

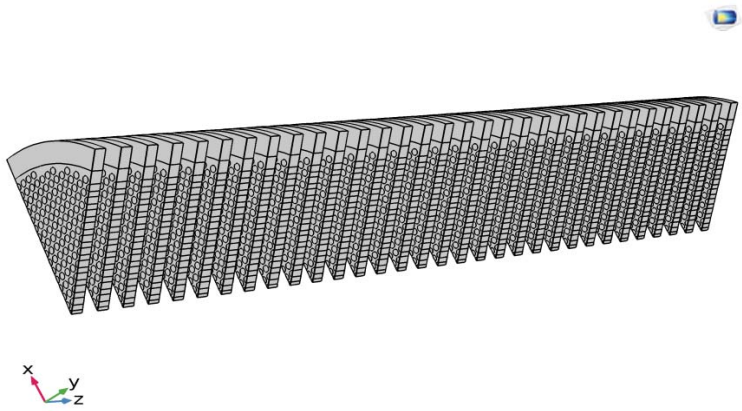


Figure 5.13 [e]:32-segmented

Figure 5.13 Exploded view for the different micro- channels regenerator

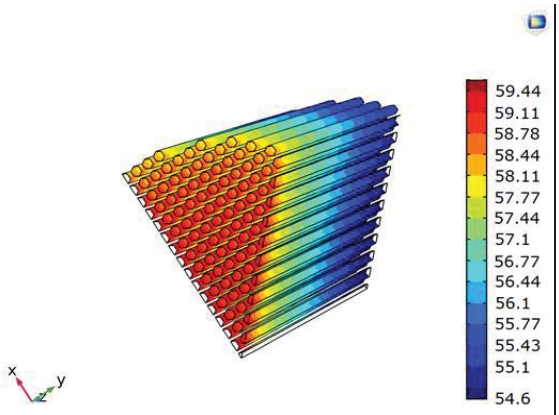


Figure 5.14 Interfaces temperature contours (^{0}C) for the non-segmented regenerator

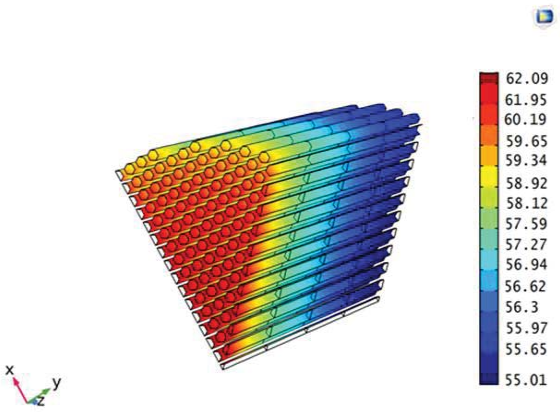


Figure 5.15 Interfaces temperature contours (^{0}C) for the 4-segmented regenerator

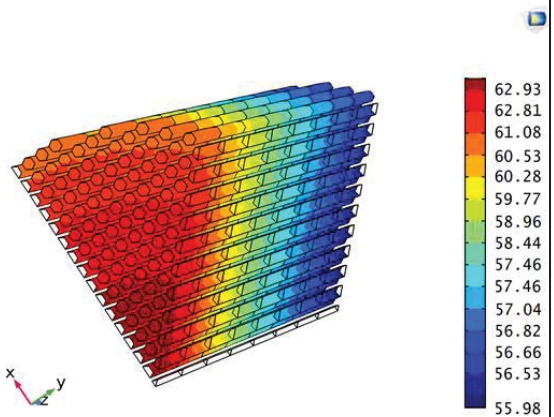


Figure 5.16 Interfaces temperature contours (^{0}C) for the 8-segmented regenerator

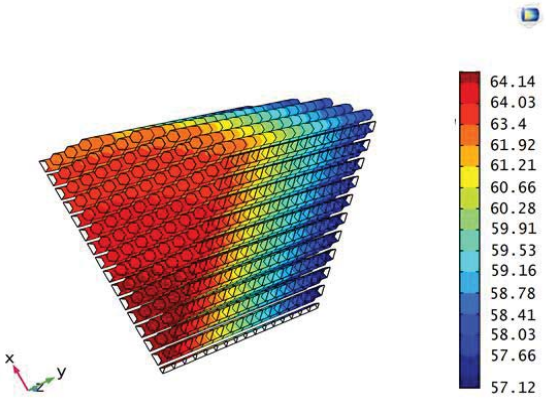


Figure 5.17 Interfaces temperature contours (^{0}C) for the 16-segmented regenerator

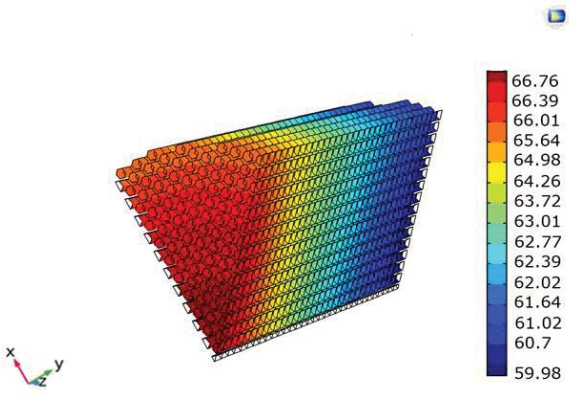


Figure 5.18 Interfaces temperature contours (^{0}C) for the 32-segmented regenerator

Figure 5.19 shows the position of three different lines (centre, middle and top) where axial temperature distribution from the CFD simulation are measured, while Figure 5.20 shows the axial temperature variations along these lines for the various segmentations.

The 32-segmented regenerator has the maximum temperature profile while the non-segmented regenerator is the lowest. For example, in Figure 5.20, in the first 5 mm and at the centre line, the axial temperature of the regenerator raised around 6.7 ^{0}C between the non-segmented and the 32-segmented. After 2.5 mm and at the top line, for the non-segmented and the 32-segmented the axial temperature of the regenerator raised from 57.4 ^{0}C to 64.38 ^{0}C respectively.

The increasing in the axial temperature still occurs at the end of the regenerator (40mm), for example at the middle of the geometry the axial temperature profile increased from around 54.7 ^{0}C with the non-segmented to 60.82 ^{0}C with the 32-segmented.

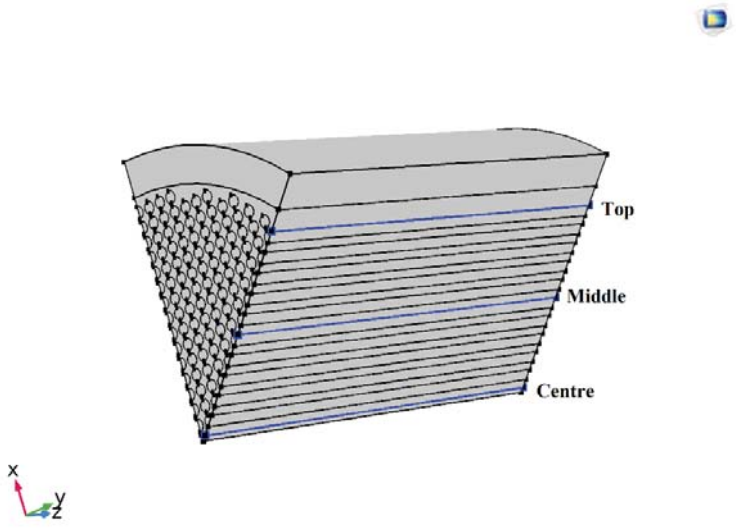
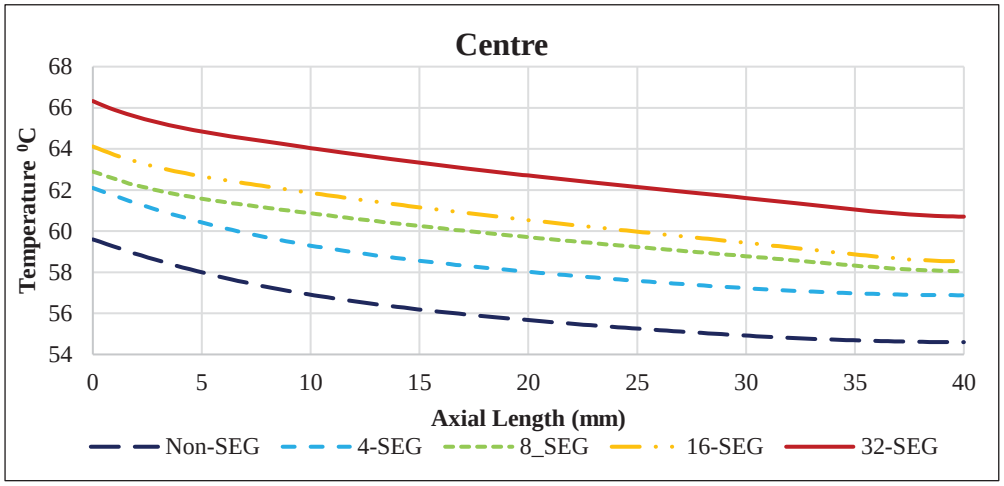
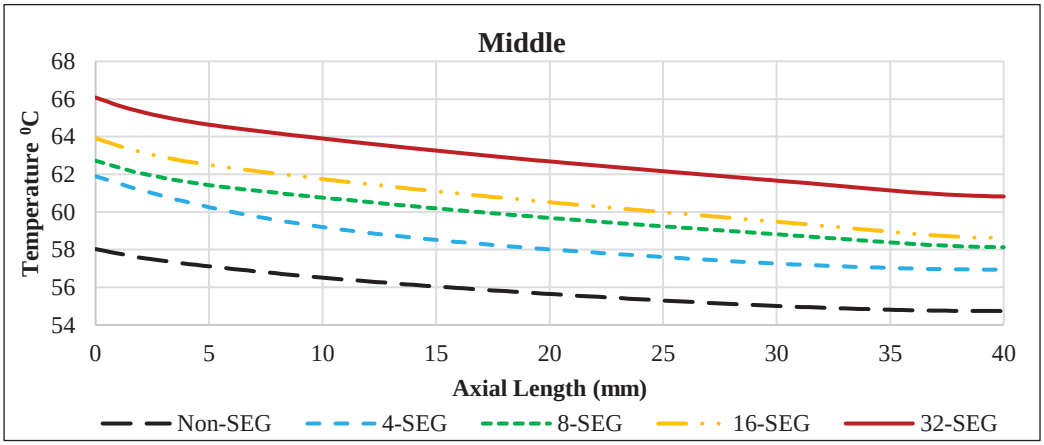


Figure 5.19 Positions of the axial temperature measurement (centre, middle and top)





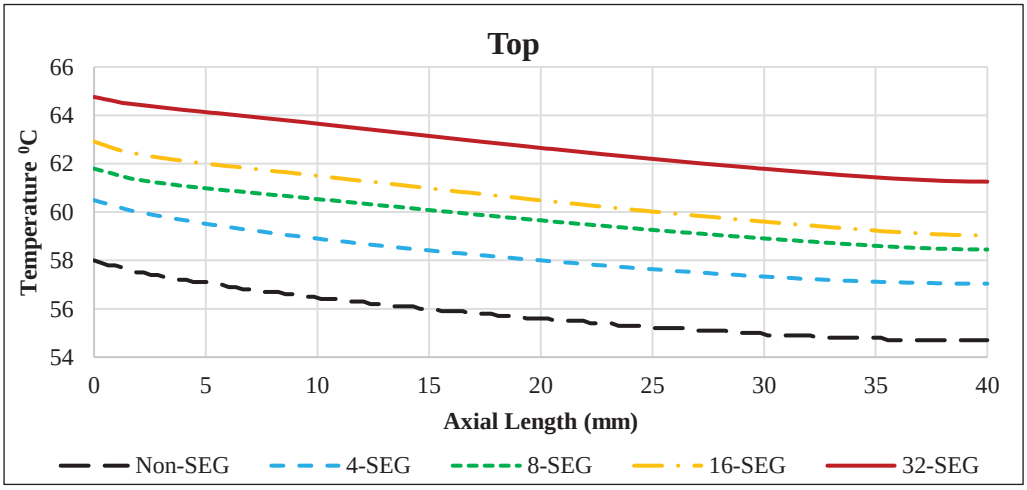


Figure 5.20 Axial temperature for the micro-channels regenerator

Figure 5.21 shows the clear effect of the segmentations where the temperature profile of the air inlet ($\mathbf{Th_i}$) and outlet ($\mathbf{Tc_i}$) temperature for the non- segmented-regenerator and the four segmented-regenerators matrixes are shown. For the hot side of the regenerator, the temperature ($\mathbf{Th_i}$) increases from 73.68 ^{0}C in the 4-segmented regenerator to 74.88 ^{0}C, 77.08 ^{0}C and 79 ^{0}C in the 8-segmented regenerator 16-segmented regenerator and 32-segmented regenerator respectively, while it is only 69.8 ^{0}C for the non-segmented regenerator. For the cold side of the regenerator, the temperature ($\mathbf{Tc_i}$) decreases from 45.65 ^{0}C in from 45.65 ^{0}C in the 4-segmented regenerator to 44.75 ^{0}C, 38.65 ^{0}C and 37 ^{0}C in the 8-segmented regenerator 16-segmented regenerator and 32-segmented regenerator respectively, while it is almost 47.8 ^{0}C for the non-segmented regenerator. The impact of segmentation (which can be defined as the non-continuity of solid material) is more obvious on the cold side of the regenerator where the air temperature is decreased by 7 ^{0}C on the cold side, while on the hot side, the air temperature increased only 3.5 ^{0}C.

In order to compare the performance of the segmented-regenerator, the effectiveness parameter, calculated by using (Eq. (4.26) form chapter (4)) , and it is used for each configuration:

$$eff = \frac{(\mathbf{Th_i}) - (\mathbf{Tc_i})\boldsymbol{in}}{(\mathbf{Th_i}) - \boldsymbol{min}(\mathbf{Tc_i})} \qquad 5.9$$

Where; $\mathbf{Th_i}$ is the maximum (inlet) temperature at the hot blow of the cycle (first half of the cycle), $(\mathbf{Tc_i})\boldsymbol{in}$ is the inlet temperature at the cold blow of the cycle (second half of the cycle) and $\boldsymbol{min}(\mathbf{Tc_i})$ is the minimum temperature during the cold blow of the cycle .

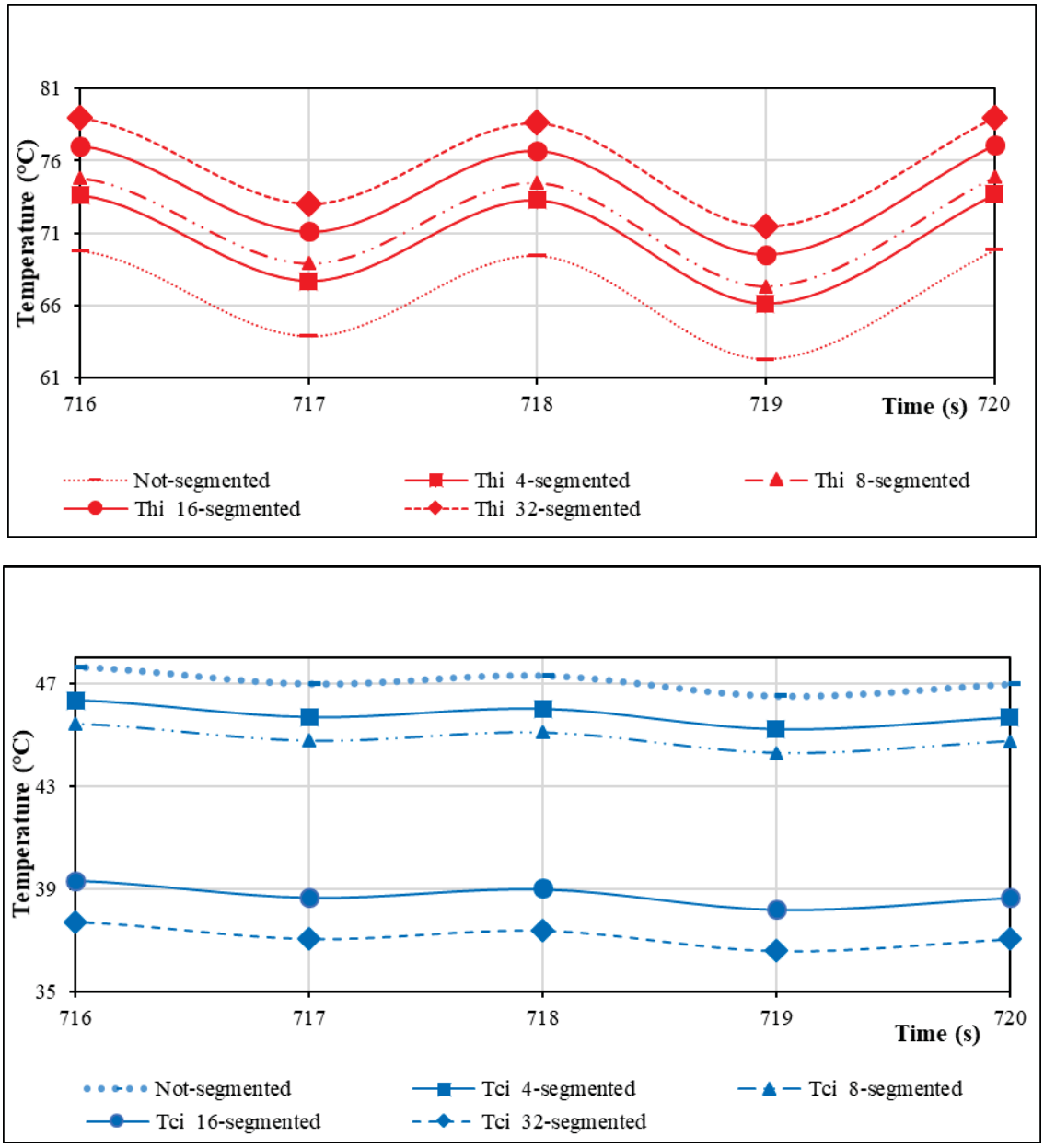


Figure 5.21 Comparison of inlet and outlet temperatures (Th_i &Tc_i) from CFD simulations for the segmented-regenerator with experiments at SLPS=3 & r.p.m=30 (cycle 359 & 360)

The calculated effectiveness (eff) for the non-segmented and the segmented parallel channels regenerator 4, 8, 16 and 32 are 0.965, 0.972, 0.973, 0.979 and 0.981 respectively. In real engine, the 32-segmented regenerator is superior to the other segmented-regenerators in terms of reducing the amount of heat supplied from the heater and the amount of heat rejected from the cooler. In addition, the effectiveness of the 32-segmented micro- channels matrix (0.981) is comparable to the Random Fibre (0.986) (See Section 4.9.2.1)

The simulation results for the average Nusselt number were plotted in Figure 5.22 showing an increasing trend with Reynolds number; it varies almost linearly for all configurations. For larger number of segmentations, higher values of Nusselt number is shown due to the higher values of heat transfer coefficient. For example, Nusselt number equals 8.66 and 13 at Reynolds number of 1700 for the 16- and 32-segmented regenerator respectively. These values of Nusselt number will be used in the next chapter as input porous media parameters in terms of evaluate the overall performance engine.

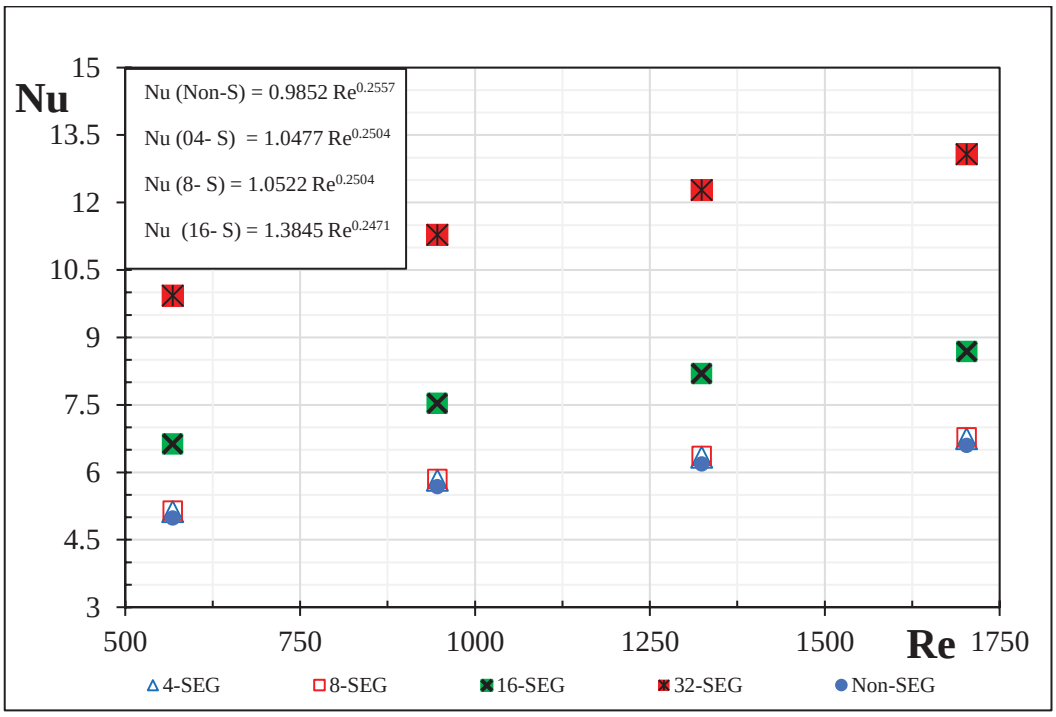


Figure 5.22 Relation between Reynolds number and average Nusselt number for the three segmented-regenerators

5.5 Effect of channels diameter

From the previous section, it was clear that the 32-segmanted micro-channels regenerator performed better than the other segmented regenerators. In this section, the CFD model for the oscillatory flow is used to investigate the effect of changing the channel diameter on the performance of the 32-segmanted micro-channels regenerator in order to perform better thermal effectiveness than the Random fibre matrix. Three diameters 0.50, 1.0 and 1.50 mm are modelled and their respective regenerator's porosity and number of channels per sector are shown in Table 5.1.

Table 5.1 Regenerators configurations and parameters.

Configuration	Tubes/sector	Tubes/annulus	Porosity (%)
0.50mm	~ 273	2186	0.3414
1.00mm	~ 93	749	0.4681
1.50mm	~ 48	385	0.5299

The flow rate was chosen to be at SLPS = 3during run test time of 12 minutes, the valve speed r.p.m =30 and $T_h = 90\ ^0C$. Figure 5.23 , Figure 5.24 and Figure 5.25 show the inlet temperature contours for the three regenerators with three different diameters 0.5, 1.0 and 1.5 mm respectively. As it can be seen, the temperature contours profile decreases with the increasing of diameter.

The 0.5 mm regenerator has the maximum temperature profile (See Figure 5.23) while the 1.5 mm regenerator is the lowest (See Figure 5.25). The average increasing of the solid temperature from the 1.5 mm to the 0.5 mm is about 12 ^0C.

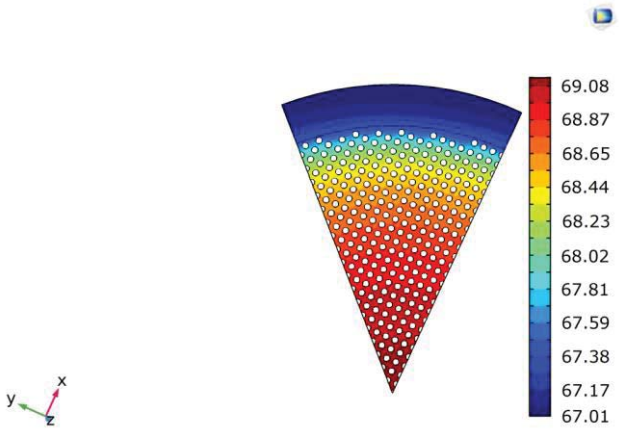


Figure 5.23 Inlet surface temperature contours (^{0}C) for the 0.5 mm regenerator

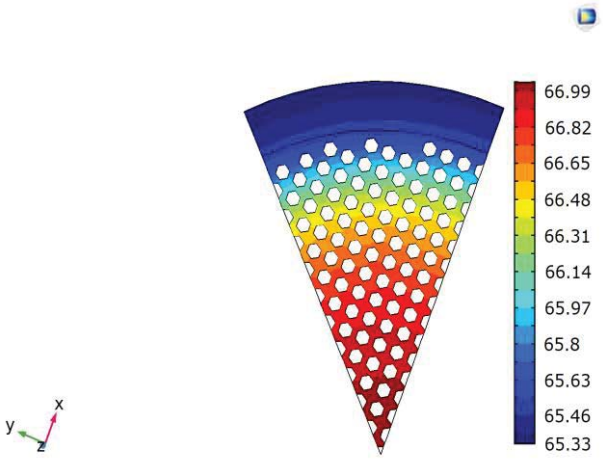


Figure 5.24 Inlet surface temperature contours (^{0}C) for the 1 mm regenerator

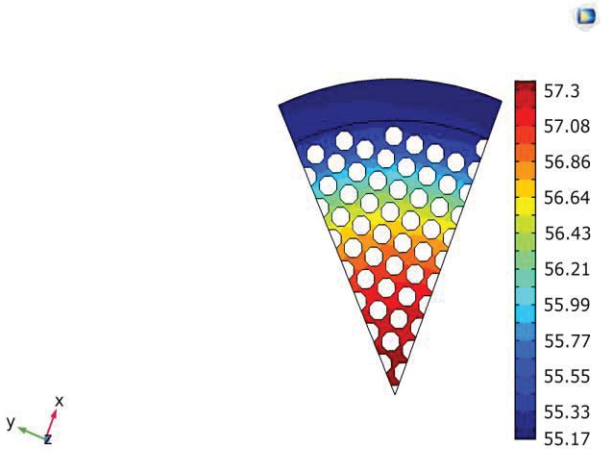


Figure 5.25 Inlet surface temperature contours (^{0}C) for the 1.5 mm regenerator

Figure 5.26 shows the CFD results for the friction factor against Reynolds number for all configurations, it is clear that the friction factor decrease with Reynolds number. The friction factor (pressure drop) for the (0.5 and 1.5 mm regenerators is nearly similar to the friction factor for 1.0 mm which found in Chapter 4 is smaller more than five times of the other two conventional matrixes.

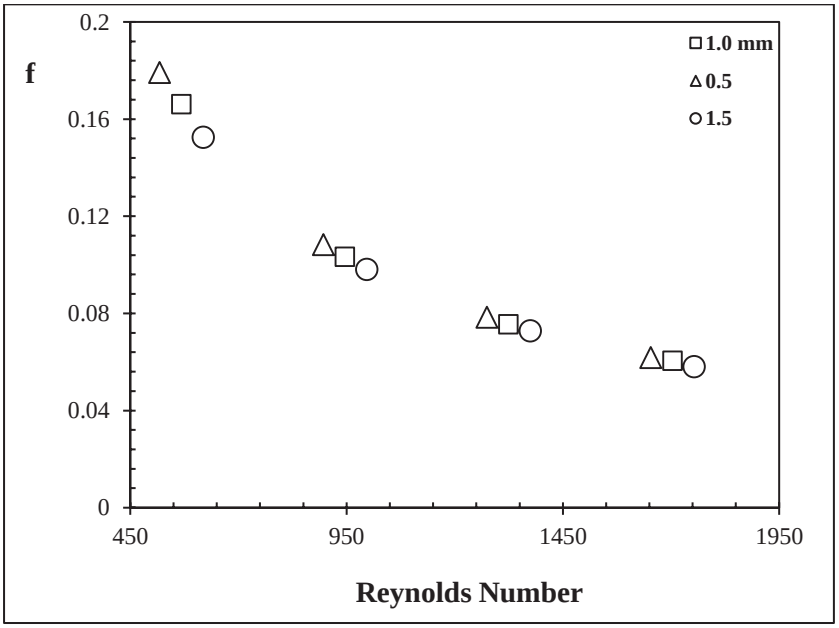


Figure 5.26 Relation between Reynolds number and Friction factor for the three Channels

Figure 5.27 shows a comparison between the air inlet (Th_i) and outlet (Tc_i) temperature for the 32- segmented-regenerator with the three different diameters 0.5, 1.0 and 1.5 mm. It can be seen that the air inlet temperature (**Th_i**) increases as the channel diameter of the segmented regenerator decreases, and the air outlet temperature (**Tc_i**) decreases as the channel diameter of the segmented regenerator decreases. For example, the inlet temperature (**Th_i**) increases from 68.46 ^{0}C to 79 ^{0}C and 80.93 ^{0}C as the channels diameters decreases from 1.5 mm to 1.0 mm and 0.5 mm. For the cold side of the regenerator, the temperature (**Tc_i**) decreases from 47.96 ^{0}C to 37^{0}C and 36.4 ^{0}C as the channels diameter decreases from 1.5 mm to 1.0 mm and 0.5 mm.

The calculated effectiveness (eff) for the 0.5 mm, 1.0 mm and 1.5 mm 32-segemented regenerator configurations are 0.988, 0.981 and 0.961 respectively.

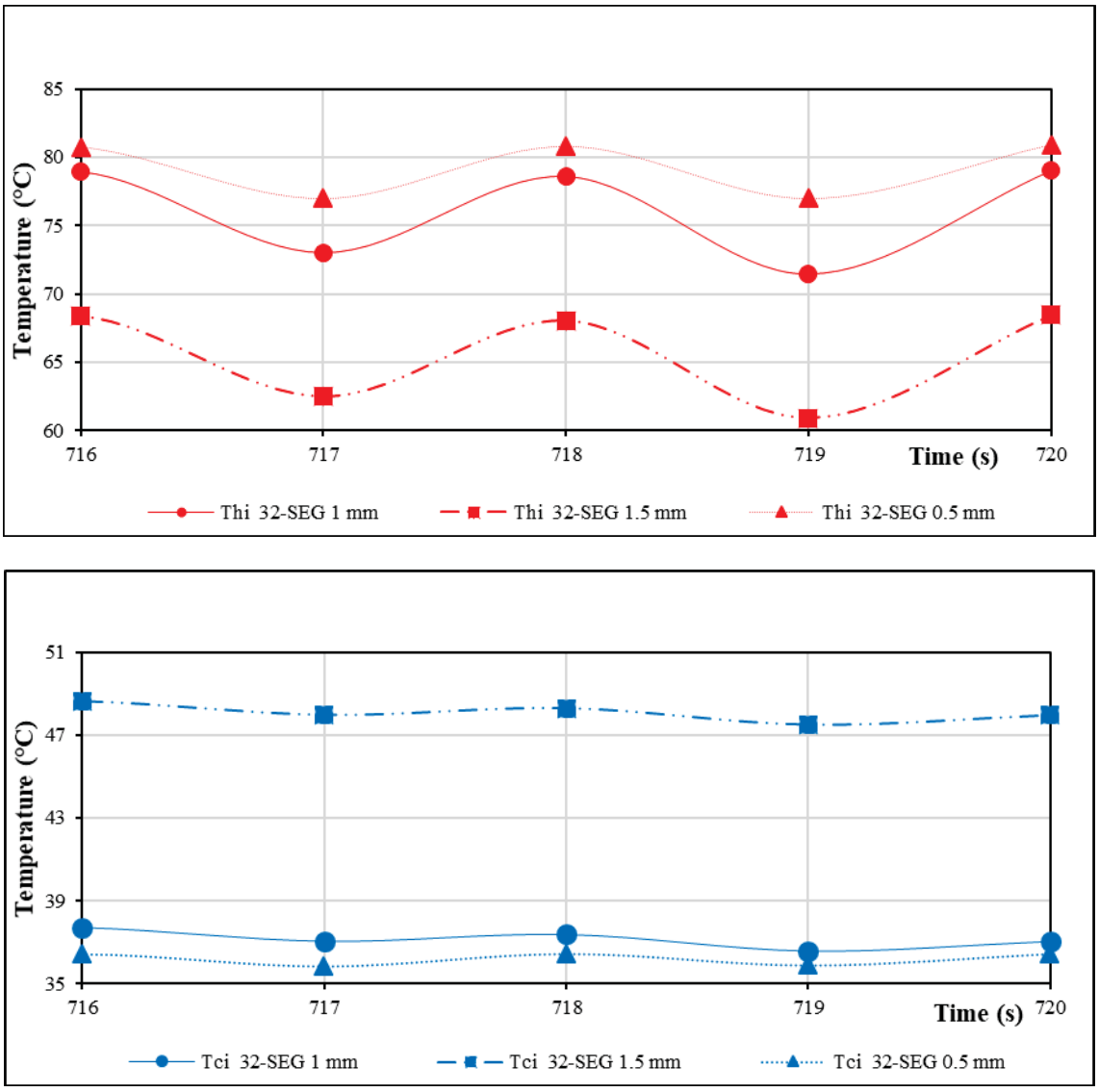


Figure 5.27 Inlet and outlet temperatures (Th_i &Tc_i) from CFD simulations for the 0.5,1 and 1.5mm / 32-segmented-regenerator at SLPS=3 & r.p.m = 30 (cycle 359 & 360)

From the previous figures (Figure 5.26 and Figure 5.27), it can be concluded that the 0.5 mm 32-segemented regenerator configuration is the best choice for this Stirling engine in order to generate power output higher than that produced from using the commercial regenerator such as the Random Fibre that presented in chapter 4.

The simulation results for the average Nusselt number were plotted in Figure 5.28 showing an increasing trend with Reynolds number (fluid velocity), they fluctuate based on the forced convection principles. According to the largest diameter (1.5 mm) in Figure 5.28, which means the highest hydraulic diameters, then it has the highest values of the Nusselt number.

In Figure 5.28, the study range of Reynolds number was chosen to between (100 to 1700) to help for explanation in terms of the thermal responding. The faster thermal reaction is in the small channels diameter (0.5 mm) with small values of Reynolds number (100 to 800) compared to the (1.5 mm) with the range of (100 to 1700). The limitation of heat transfer surface area has a high impact on the heat transfer coefficient, as it can be noticed between the (0.5 mm), which has higher surface area and then higher heat transfer coefficient, and (1.5 mm) which has the lowest surface area and lowest heat transfer coefficient.

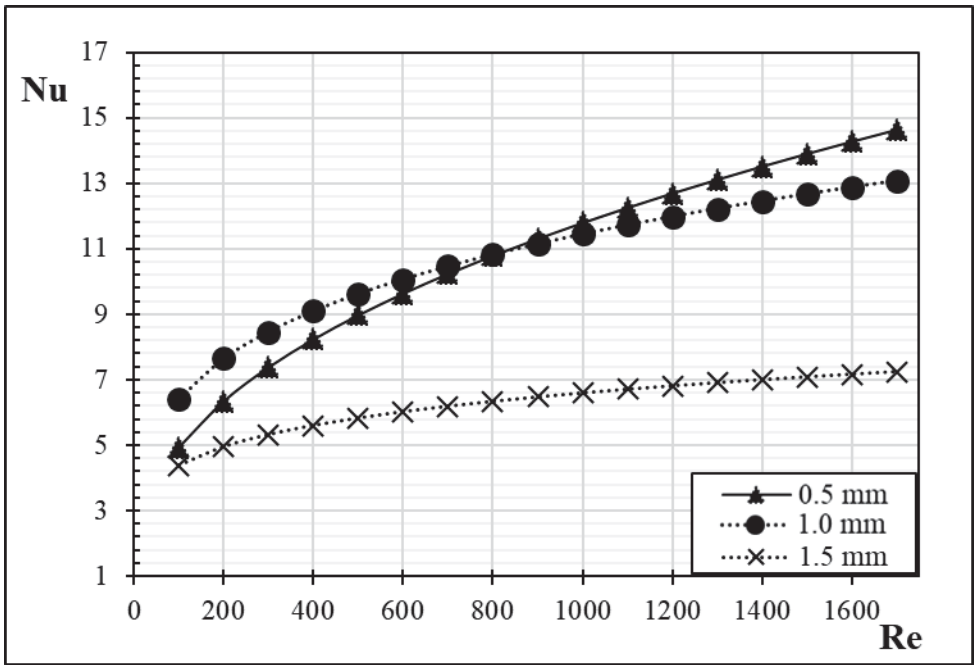


Figure 5.28 Reynolds number vs. average Nusselt number for the three channels regenerators

Table 5.2 summarise the correlations results obtained from the CFD simulation for the different configurations of the segmented micro-channel regenerator matrix (1 × 0.50 mm 4 × 1.0 mm

and 1 × 1.50 mm) which will be used in the next Chapter in terms of engine evaluation as input porous media parameters.

The Forchheimer drag coefficient β_F and the permeability, K was written using Eq. (5.10) and Eq. (5.11) in Section 5.3 as a function of a_1 and a_2 :

Permeability, K (m^2):

$$K = \frac{2{d_h}^2}{a_1 Re^2} \qquad 5.10$$

Forchheimer drag coefficient, β_F (kg/m^4):

$$\beta_F = \frac{1}{2d_h}\,\rho\,(a_2) \qquad 5.11$$

Table 5.2 Equivalent porous media characteristics of segmented micro-channel regenerator matrix

Regenerator type	a_1	a_2	**Nusselt number**
4-segmented (1.00mm)	-9×10^{-5}	0.2047	$1.0477\ Re^{0.2504}$
8-segmented (1.00mm)	-8.8×10^{-5}	0.2032	$1.0522\ Re^{0.2504}$
16-segmented (1.00mm)	-6×10^{-5}	0.2089	$1.3845\ Re^{0.2471}$
32-segmented (1.00mm)	-4.3×10^{-5}	0.2035	$2.0294\ Re^{0.2504}$
32-segmented (0.50mm)	-1×10^{-4}	0.2165	$0.8207\ Re^{0.3861}$
32-segmented (1.50 mm)	-5×10^{-5}	0.1921	$1.9286\ Re^{0.1779}$

5.6 Conclusion

An efficient CFD model for segmented micro-channel regenerator was validated against experimental measurements using unidirectional and oscillatory flows. The validated CFD model was used to carry out an investigation on the effect of increasing the number of segmentations on the regenerator effectiveness. Moreover, the effect of changing the micro channel diameter was also included in this study. The micro- channels regenerator with diameter of 0.5 mm and 32 segmentations (0.5 mm 32-segemented regenerator configuration) performed better than the all configuration in this study including the Random Fibre matrix and can be a good choice for enhancing the performance of the Stirling engine. Correlations for Nusselt number and friction factor for all segmented regenerators that have been investigated in this chapter were developed from the CFD model to be used as porous media parameters in the CFD model of the V alpha-type Stirling engine in the next chapter (6).

CHAPTER 6

DEVELOPMENT OF V-TYPE ALPHA STIRLING ENGINE FROM V-TYPE COMPRESSOR

Part of the work presented in this chapter has already been published in [83] as:

A. K. Almajri, S. Mahmoud, and R. Al-Dadah, "Modelling and parametric study of an efficient Alpha type Stirling engine performance based on 3D CFD analysis," *Energy Convers. Manag.*, vol. 145, 2017.

Almajri is the lead author, he has made the most significant contribution to the research including design, analysis and interpretation of data. He has written and edited a major part of the work, he also takes charge of getting approval from all the other authors and communicating with the journal.

Mahmoud and Al-Dadah fulfil the following criteria: Contribute to the conception, design, analysis and interpretation of data. Participate in drafting and help revising the manuscript for intellectual content. Approve of the version to be published.

6.1 Introduction

With the current global levels of fossil fuel consumption and CO2 emissions, the use of Stirling engines for electrical power generation offers the potential of exploiting the vast amount of waste heat available from industrial processes, thus reducing the use of fossil fuel and carbon emissions. Stirling engines have the advantages of high thermal efficiency, flexibility of using various energy types including renewable sources. Currently, there are few Stirling engine manufacturers worldwide and limited research work for its development. Using 3D CFD

modelling, this chapter investigates the routes to develop V-type alpha Stirling engine from upgrading commercially available V-type compressor, in order to reduce the time and cost for engine development. The correlation of Nusselt number and friction factor for the segmented regenerator that developed in the previous chapter (5) will be used as porous media parameters in the CFD model of the Stirling engine developed in this chapter.

6.2 Engine development from air compressor

Figure 6.1 shows the commercially available V-type compressor used in this work, it is "a versatile heavy duty pump used as a major component in several popular Clarke compressors" [105]. The compressor has twin cylinders (V-shape), with both cylinders having finned walls and

the body of the compressor is made from solid cast iron [105]. The maximum working pressure that can be produced from this compressor is 10 bar and 9 cfm maximum displacement.



Figure 6.1 V-type compressor "Clark Air Compressor Pump 9 CFM- CE20" [105]

Figure 6.2 (a) shows a the 3D drawing for the lower part of the V type compressor used in this work, which is going to be the lower part of the developed engine. It has 88.39 cc swept volume for both pistons (50 mm Stroke and 45 mm Piston Diameter) at a phase angle of 90^0. Figure

6.2 (b) shows a 3D drawing for the full-developed Stirling engine, which consists of the Lower part (pistons assembly), Heater, Regenerator, Cooler and Connecting pipes.

The design was based on the annulus approach to keep the flow with high Reynolds number so that a high heat transfer coefficient can be achieved during cycle operation. The regenerator is a micro-channels matrix placed in a cylindrical housing. The heater and the cooler were placed on the top of the piston assembly of the compressor, with water jacket and heating coil then added around the cooler and heater volumes respectively. Figure 6.3 shows a schematic diagram for the developed engine with its major geometrical parameters.

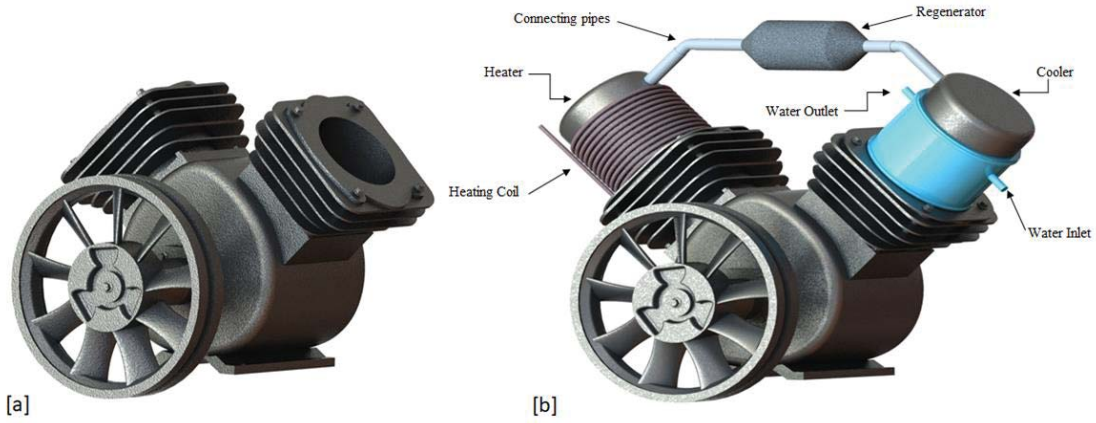


Figure 6.2 [a] V-type compressor [b] Converted Stirling engine

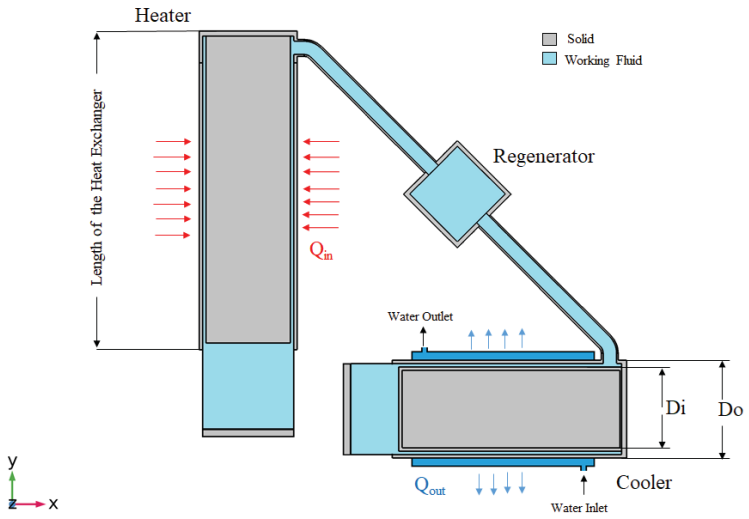


Figure 6.3 Definition of engine geometrical parameters

6.3 Developed engine CFD modelling

The geometrical parts of the developed engine were shaped as a 3D CAD model using SolidWorks and then imported to COMSOL-Multiphysics software (version 5.3). (See Figure 6.4 (a) to (d)). The operating parameters of the developed engine including properties of regenerator, charge pressure, cold and hot temperature values, engine speed, phase angle and other constant parameters were defined in the built-in parameters feature called (Parameter table). The table also contains the geometrical parameters which are used to calculate the dead volumes of the engine. Another built- in table called (Variable table) were filled with the engine variables such as crank angle, pistons' displacements and velocities, expansion and compression volumes.

The Regenerator as in Figure 6.4 (a) was modelled using "Heat Transfer in Porous Media" module, with all parameters and properties were specified in tabular form. The different materials of all engine parts were chosen by using the built-in materials from the software; Air for the working fluid, Copper for the connecting pipes and Steel for the other parts of the engine. (See Figure 6.4 (b) and (c). Following that is applying physics into the different boundaries and domains of the geometry with the boundary condition defined and time dependent equations selected.

Assuming the gas to be ideal, the state equation is,

$$\rho = \frac{p_A}{R_s T} \qquad 6.1$$

Navier-Stokes, Brinkman and continuity equations were used to model the compressible laminar flow and Reynolds number considered to be less than 2000.

The working gas inside the engine is Air where its density is calculated using the state equation Eq. (6.1) while its other thermal properties depend on the pressures and temperatures using in

the CFD simulation. These properties are predefined in COMSOL-Multiphysics using piecewise polynomials covering the temperature variation in the range of 200 to 1600 K [93]. The dynamic viscosity of Air is defined by

$$\mu = -8.38278E^{-7} + (8.35717342E^{-8})T - (7.69429583E^{-11})T^2 + (4.6437266E^{-14})T^3 - (1.06585607E^{-17})T^4 \quad 6.2$$

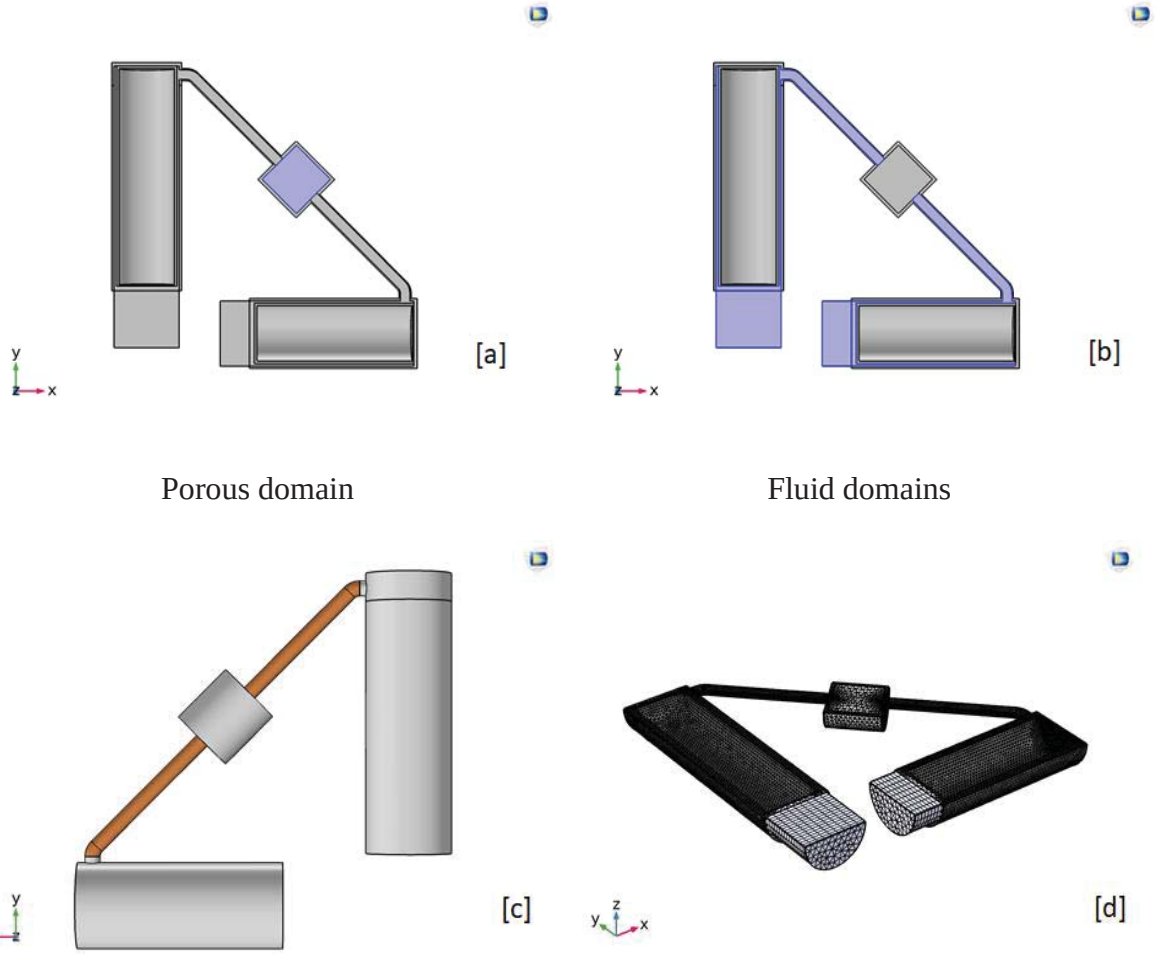
The heat capacity of Air is defined by

$$C_p = 1047.63657 - (0.372589265)T + (9.45304214E^{-4})T^2 - (6.02409443E^{-7})T^3 + (1.2858961E^{-10})T^4 \quad 6.3$$

And finally, Air thermal conductivity is defined by

$$k = -0.00227583562 + (1.15480022E^{-4})T - (7.90252856E^{-8})T^2 + (0.11702505E^{-11})T^3 - (7.43864331E^{-15})T^4 \quad 6.4$$

All fixing walls were set as non-slip boundary conditions while the moving walls were described by velocity equations, these equations were called from the Variable table. The next step is adding the 'moving mesh' physics to set the moving boundaries and the displacement of the parts were defined using a UDF interface. The tetrahedral elements with fine sensitivity were used to suit the engine's dynamic and complex geometry as shown in Figure 6.4 (d). The initial values of the operating conditions are: engine speed 500 R.P.M, charging pressure 2.5 bar, Porosity 0.3414%, hot temperature 327 ^{0}C and cold temperature 27 ^{0}C [60].



Porous domain | Fluid domains

Solid domains (Copper and Steel) | Engine Mesh

Figure 6.4:[a] to [d] Geometry domains and mesh

6.4 Results and discussion

The developed CFD model was used to evaluate the best design geometrical parameters on the engine efficiency and power output. Figure 6.5 to Figure 6.10 show the effect of changing the inner/outer diameters and the length of the heating / cooling volumes. Figure 6.5 and Figure 6.6 show that engine power output increases as the inner diameter increases while the outer diameter and the length were fixed at 50 mm and 120 mm respectively. The power output increased due to the decreasing their dead volumes in their volumes. Figure 6.7 and Figure 6.8 show that power output decreases as the outer diameter increases while fixing the inner

diameter and length at 45 mm and 120 mm respectively Figure 6.9 and Figure 6.10 show that power output increases with increasing the heater and cooler lengths (using $D_0 = 50$ mm and $D_i = 45$ mm). The maximum power from the Heater can be reached at around 185 mm of heater length, then stays constant after that (See Figure 6.9), while maximum power output can be achieved cooler length around 135 mm (See Figure 6.10).

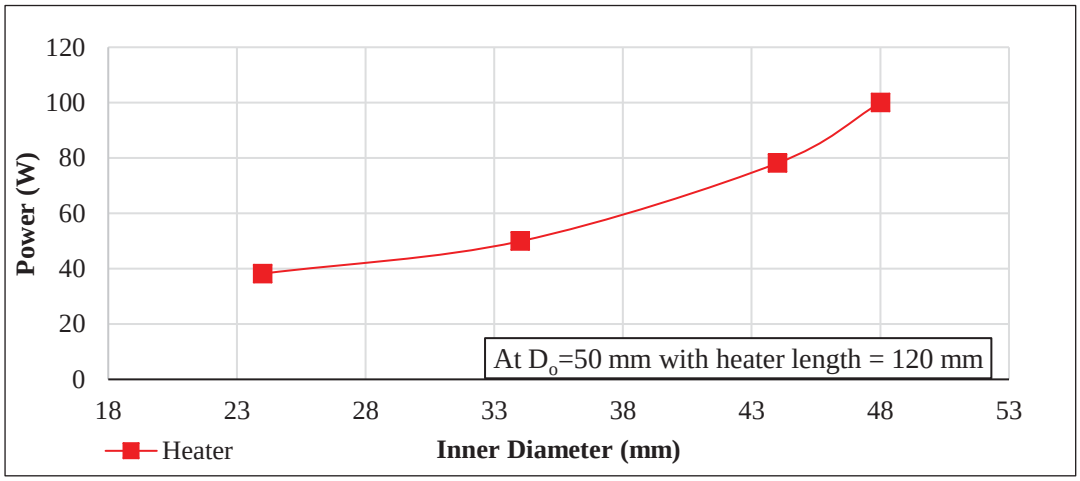


Figure 6.5 Heater inner diameter Vs. Power

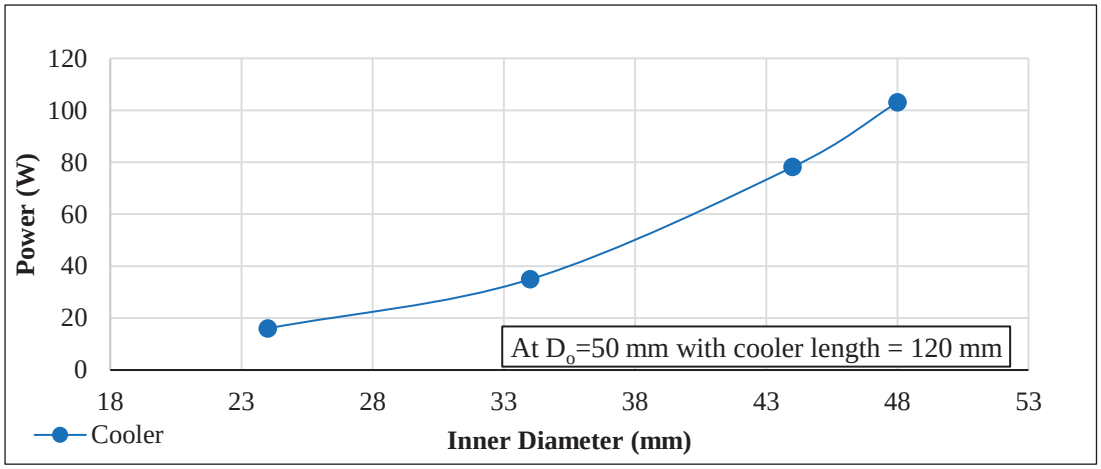


Figure 6.6 Cooler inner diameter Vs. Power

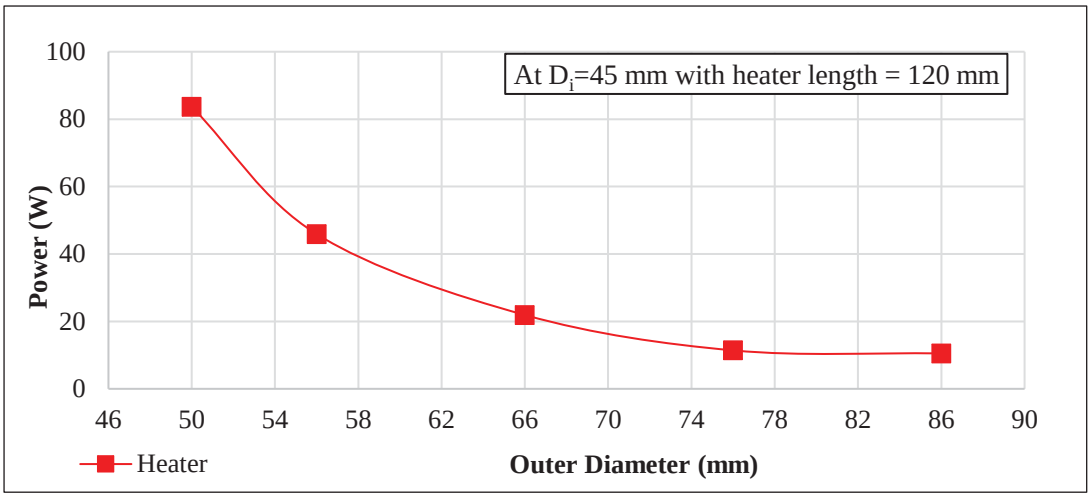


Figure 6.7 Heater outer diameter Vs. Power

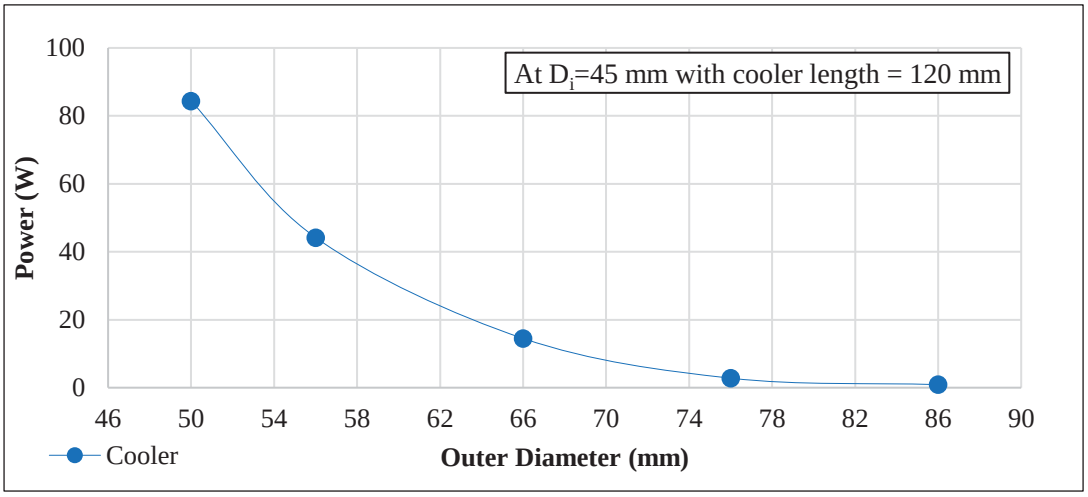


Figure 6.8 Cooler outer diameter Vs. Power

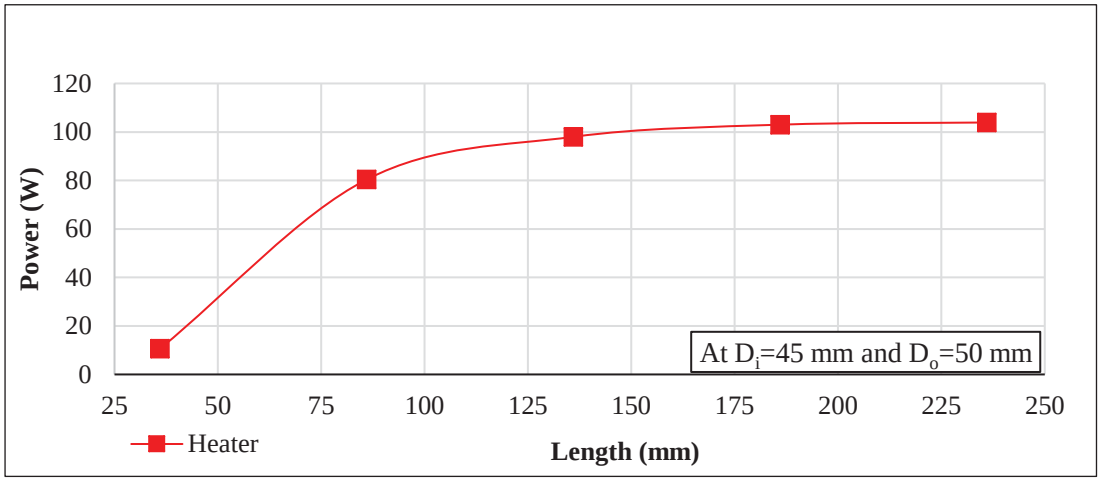


Figure 6.9 Heater length Vs. Power

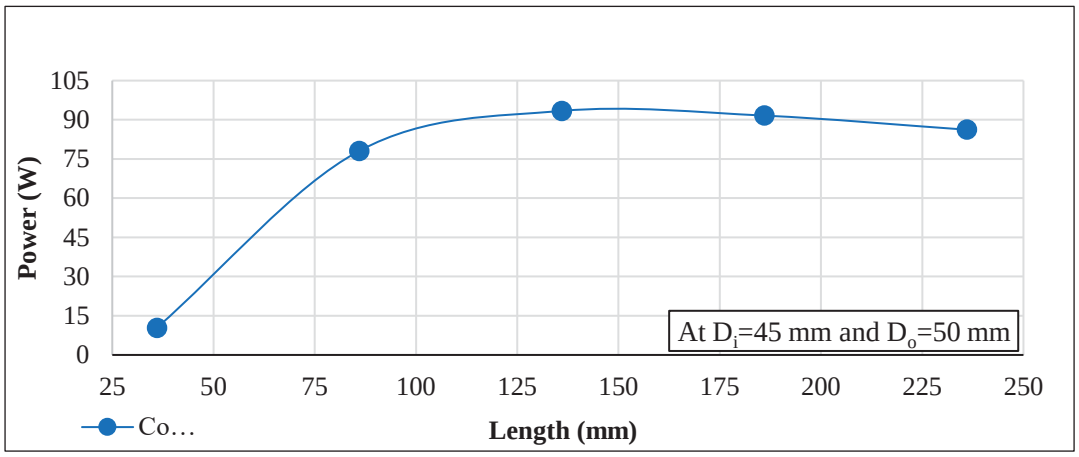


Figure 6.10 Cooler length Vs. Power

Figure 6.11 shows the variation of power output versus the regenerator length, where maximum power can be achieved with regenerator length of 40 mm.

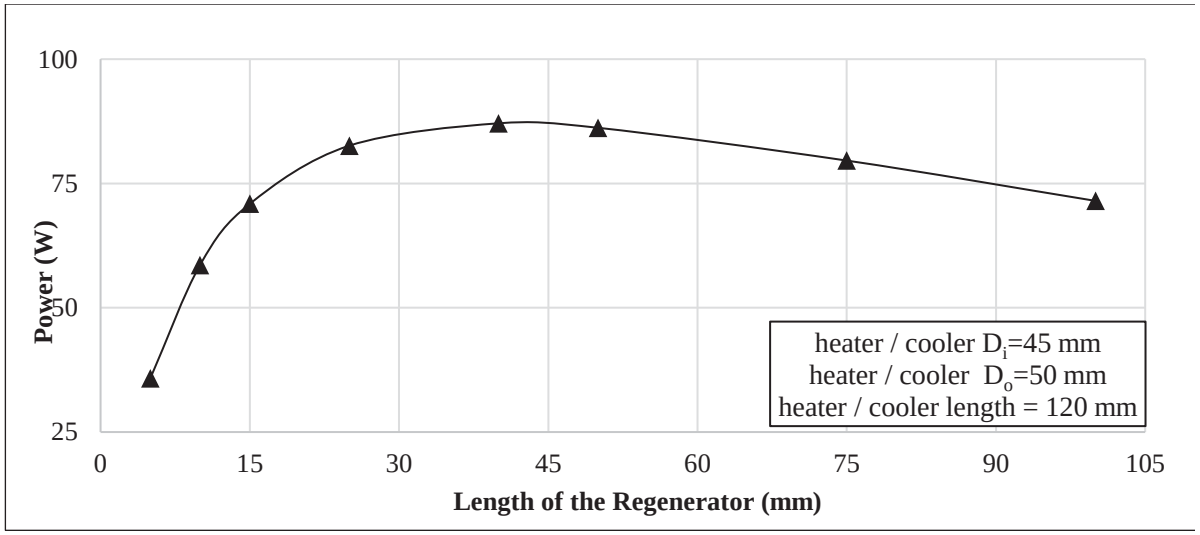


Figure 6.11 Regenerator length Vs. Power

Results from previous figures suggest that using the following geometry of the heater/cooler dimensions of Di= 54 mm, Do= 45 mm, thickness= 4.5 mm, heater length= 186 mm, cooler length= 136 mm with regenerator length= 40 mm and regenerator diameter = 40 mm can produce maximum power output of 110.98 W.

Table 6.1 shows all the dimensions for the engine parts, the engine operating conditions, regenerator properties and other constant parameters used.

Table 6.1 Stirling engine specifications and operating conditions

Parameter	Value
Engine type	Alpha α (V)
Cylinder bore	54.0 mm
Cylinder Stroke	45.0 mm
Swept volume	88.39 cm^3
Phase angle Working gas Air	90 ^{0}
Type of the regenerator's matrix	Micro-Channels
Channel diameter	0.50 mm
Regenerator diameter	40.0 mm
Regenerator length	40.0 mm
Diameter of the connecting pipe	5.00 mm
Length of the connecting pipe	220 mm
Heater/Cooler outer diameter	54.0 mm
Heater/Cooler inner diameter	45.0 mm
Length of the heater	186 mm
Length of the cooler	136 mm
Type of the heater	Heating coil
Type of the cooler	water jacket
Cooling	Water
Engine speed	500 rpm
Charge pressure	2.5 (bar)
Working fluid	Air
Porosity	0.3414%
Inlet water temperature	20 (°C)
Hot source temperature	327 (°C)

Figure 6.12 (a) to (d) present the distribution of temperature inside the whole engine with different crank angle Theta 0^0, 90^0, 180^0 and 270^0 during the 5^{th} cycle. The temperature inside the cooler varies from 20 to 75 ^{0}C, with higher values near the cooler connecting pipe, as the working fluid comes from the hot space in the heater through the regenerator to the cooler. The temperature inside the heater varies from 327 to 367 ^{0}C. The working fluid moves from the cold space in the cooler via the regenerator towards the hot space. The higher temperature values appeared near the heater Top Dead Centre (TDC) position.

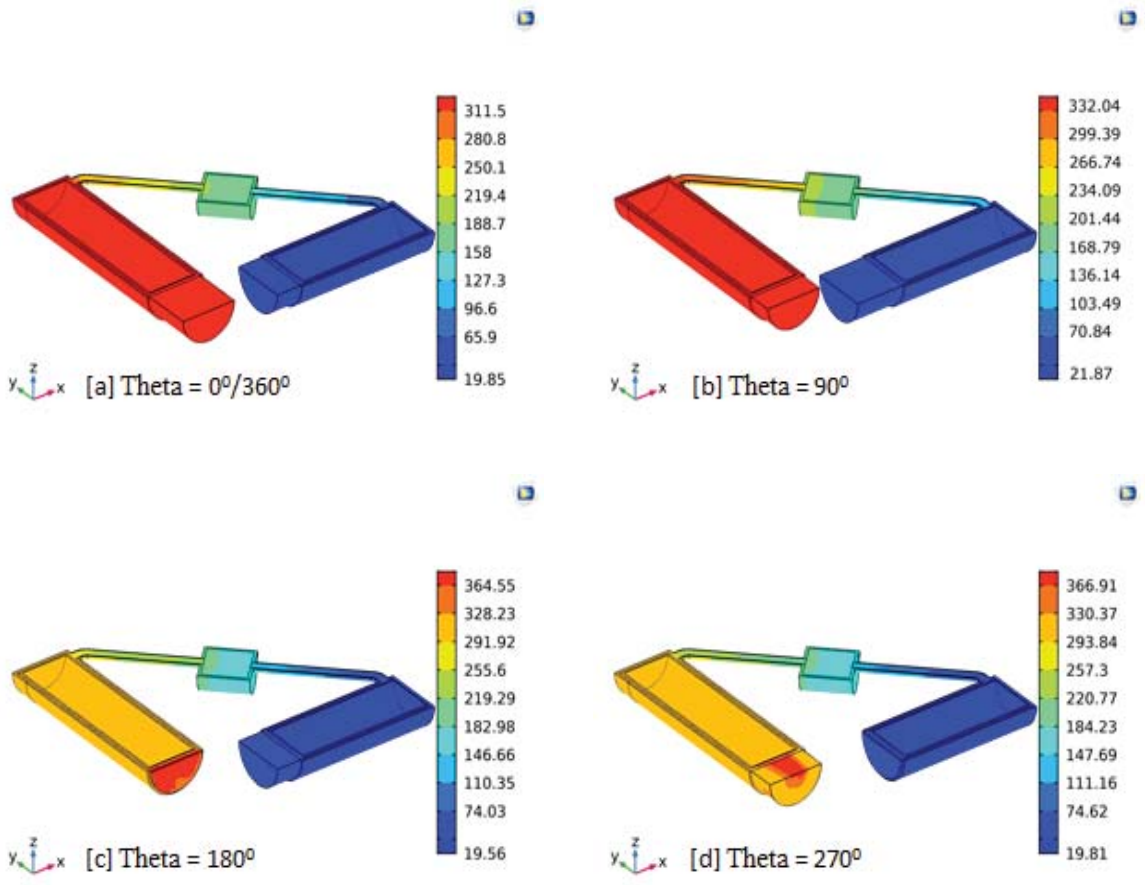
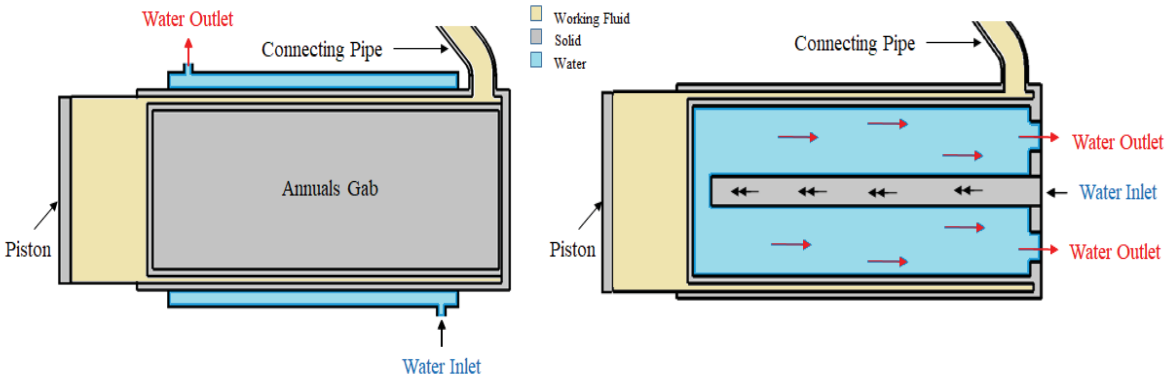


Figure 6.12: [a] to [d] CFD Temperature contours at different [Theta]crank angels during 5^{th} cycle

6.5 Design improvement of the engine cooler

This section presents the CFD modelling for a new cooler design in order to improve the total engine performance. As shown in Figure 6.2 and Figure 6.3, a water-jacket was used to reduce the temperature of the cooler (Figure 6.13 (a)), but this was not very effective since it only reduced the outer surface of the cooler while the annuals gab was left at the ambient temperature. The new concept is based on inserting a pipe with certain length inside the annuals gab (Figure 6.13 (b)), where water is injected as the cooling medium to replace the water-jacket cooling configuration. This will increase the heat output from the cooler as the surface area increases, where the surface area can be defined as the outer surface area of the cooler (covered by the water-jacket) plus the surface area of the annuals gap. (See Figure 6.13 (a) and (b)). This design was chosen based on the use of the annular gap in the centre of the cooler. It is also advisable to insert the tube into the centre of the annulus in order to obtain symmetric and equal vortices along the entire circumference of the annulus gap.



[a] Water-jacket system [b] New cooler configuration

Figure 6.13: [a] and [b] Cooler of Stirling engine cooling system

A CFD model was developed to evaluate this new cooler configuration and to determine the best geometrical parameters including the inner pipe length and diameter, in addition to added

holes and fins to the pipe to increase the turbulences inside the cooler gab as shown in Figure 6.14 and Figure 6.15.

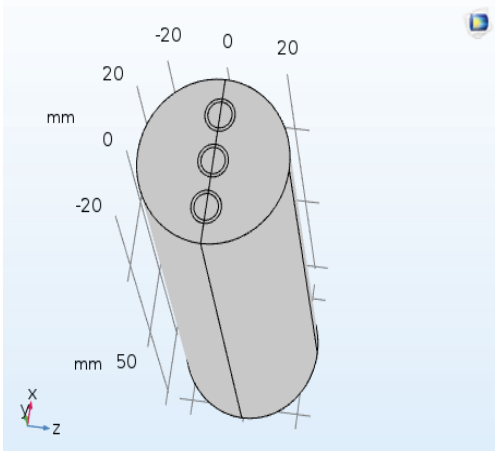


Figure 6.14 Three dimensional view of the finned-cooler

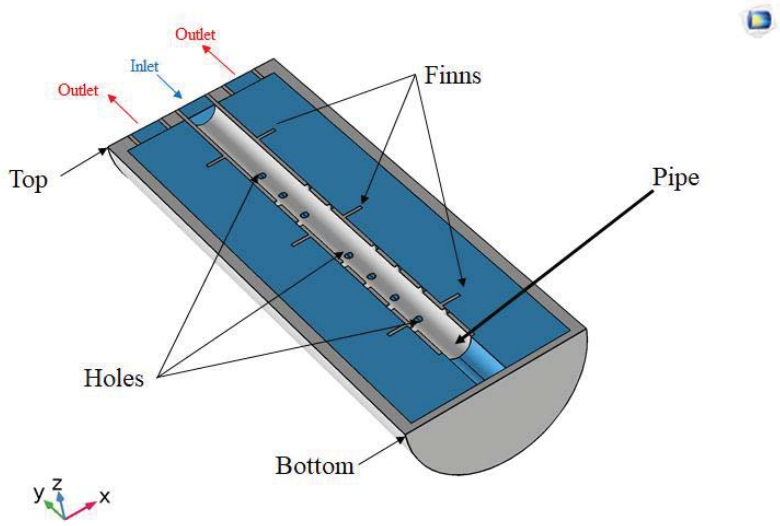
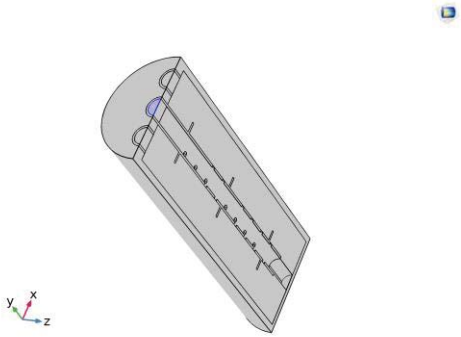
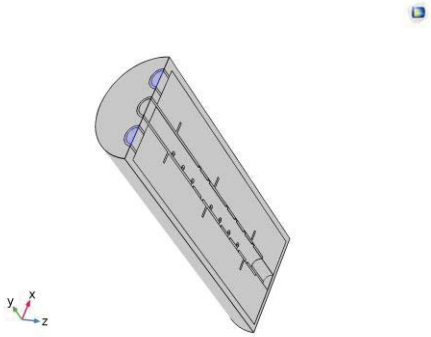


Figure 6.15 Symmetrical view of the finned-cooler

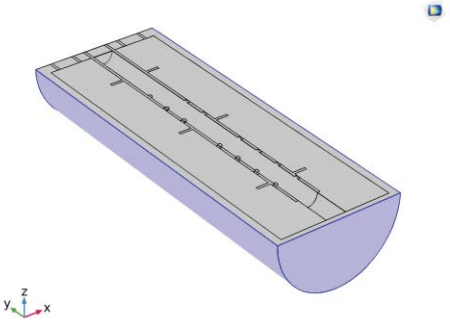
The boundaries of all faces that used in the CFD model of the finned-cooler can be seen on Figure 6.16 and their values are located in Table 6.2.



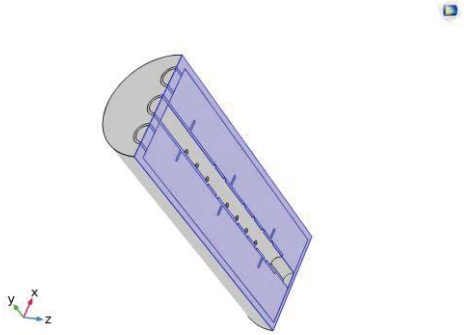
[a] Inlet mass flow rate and temperature



[b] Out flow



[c] Heat flux



[d] Symmetry

Figure 6.16 Boundary conditions of the finned-cooler

Table 6.2 Value of the boundary conditions:

Boundary	**Value**
Mass flow rate	(0.01283/2) kg/s
Inlet temperature	(20) ^{0}C
Heat flux	(11836) W/m^{2}

Figure 6.17 shows the temperature distribution along the cooler height (from top to the bottom) for five pipe lengths of 65, 108, 115, 120 and 124 mm, with inlet and outlet diameters of 10mm.

With pipe lengths of 65 and 108 mm higher temperatures (around 50 ^{0}C) and non-homogenise temperature fluctuations were experienced, like temperature = 50 ^{0}C at the height of 40 mm while the temperature = 27 ^{0}C and 32 ^{0}C at 15 mm and 110 mm respectively. The pipe length of 120 mm produced smooth temperature fluctuations around 32 ^{0}C along the cooler's walls leading to cooler water and almost equal heat flux along the surface of the cooler.

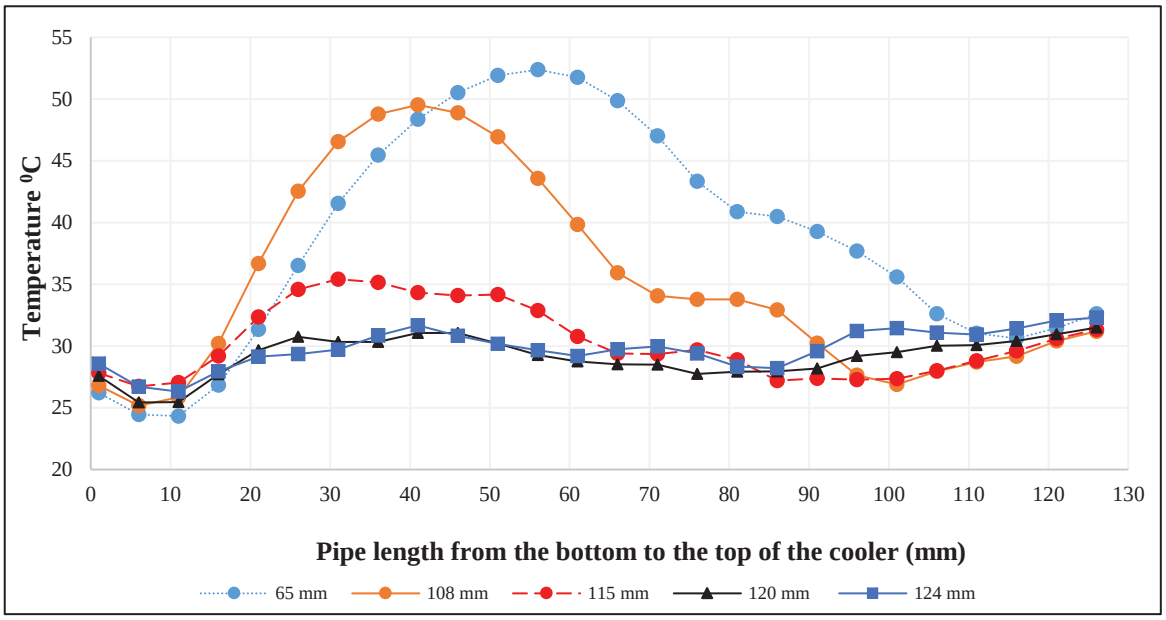


Figure 6.17 Axial temperature for the finned cooler with different lengths

The CFD model for the pipe length of 120 mm was used to evaluate the best inlet and outlet diameters in terms of enhancing the cooler design. Figure 6.18 shows the temperature distribution for inlet and outlet diameter of 6 and 8 mm, with the latter generating less temperature fluctuations and average temperature around 29.17 ^{0}C.

Adding circular fins around the tube can enhance the flow conditions inside the cooler, Figure 6.19 (a) and (b) compares the flow velocity distribution for the non-finned- and finned-cooler,

while Figure 6.20 (a) and (b) illustrate the temperature distribution. The effects of adding fines on the velocity and temperature distribution is clear where more streamlines are generated in the finned pipes leading to reduced average surface temperature.

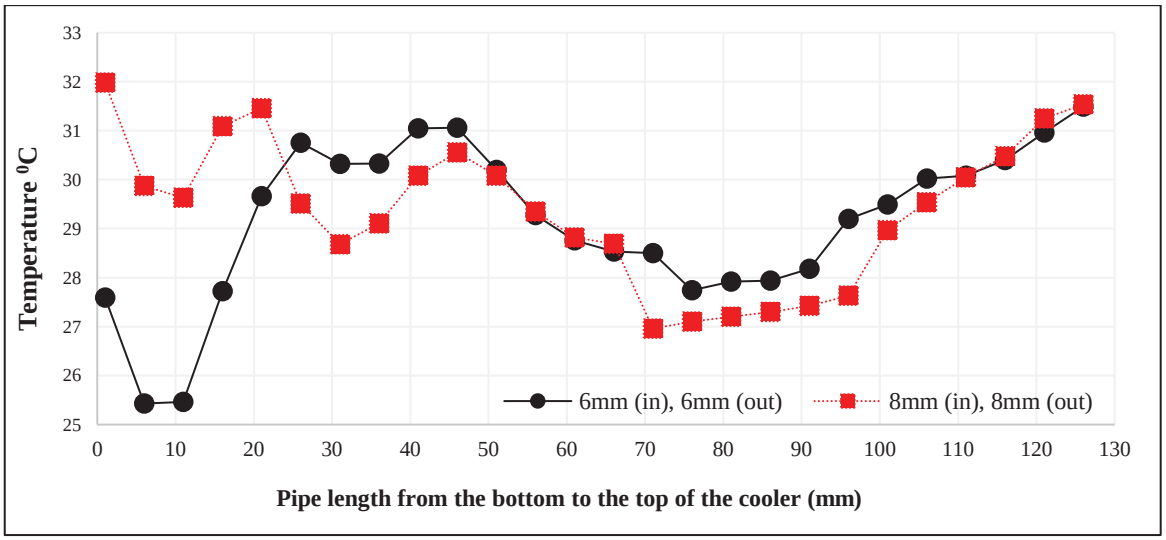


Figure 6.18 Axial temperature for the finned cooler with different diameters

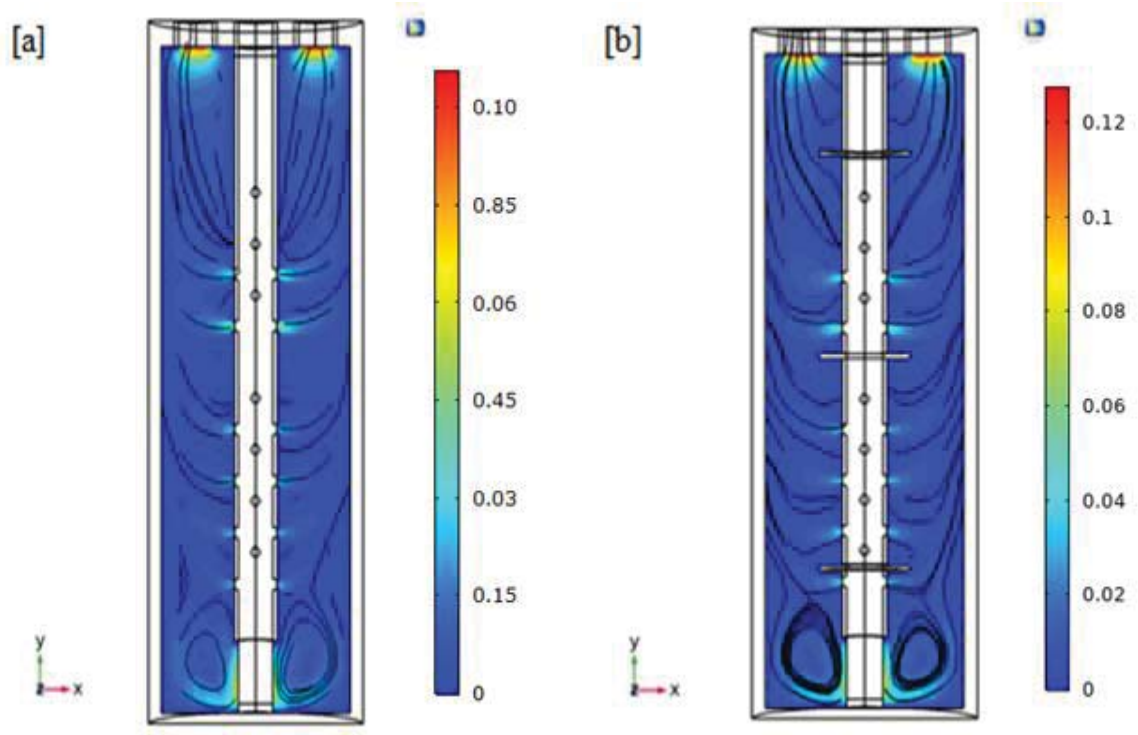


Figure 6.19: Water velocity magnitude (m/s) [a]Non finned and [b]Finned cooler

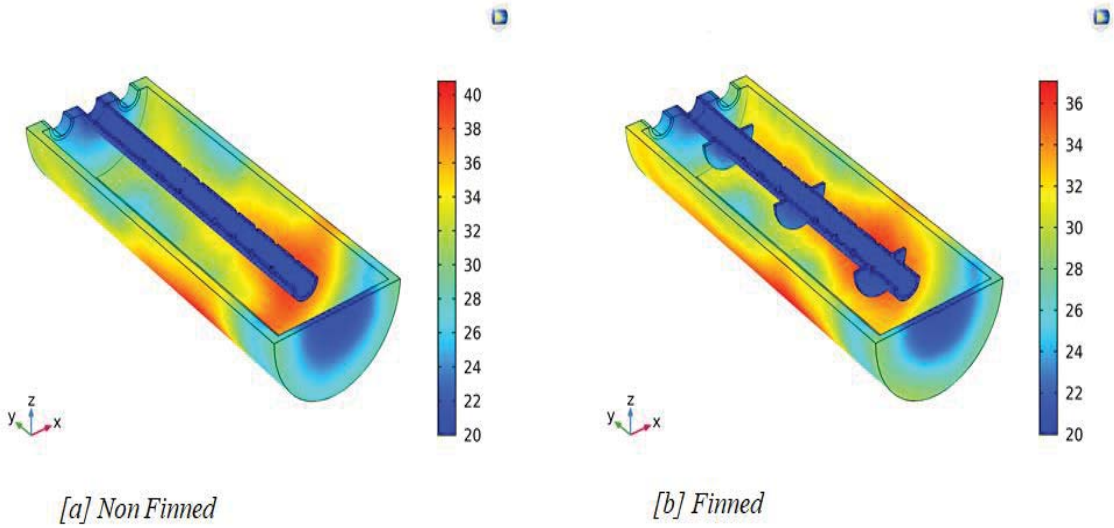


Figure 6.20 [a] and [b] Temperature distribution (^{0}C)

The CFD model of the V-type alpha Stirling engine predicted that by using finned cooler with a pipe length of 120 mm and diameter of 8mm the power output can increase from 110.98 W to 132 W. Figure 6.21. shows the new developed Stirling engine with the finned cooler.

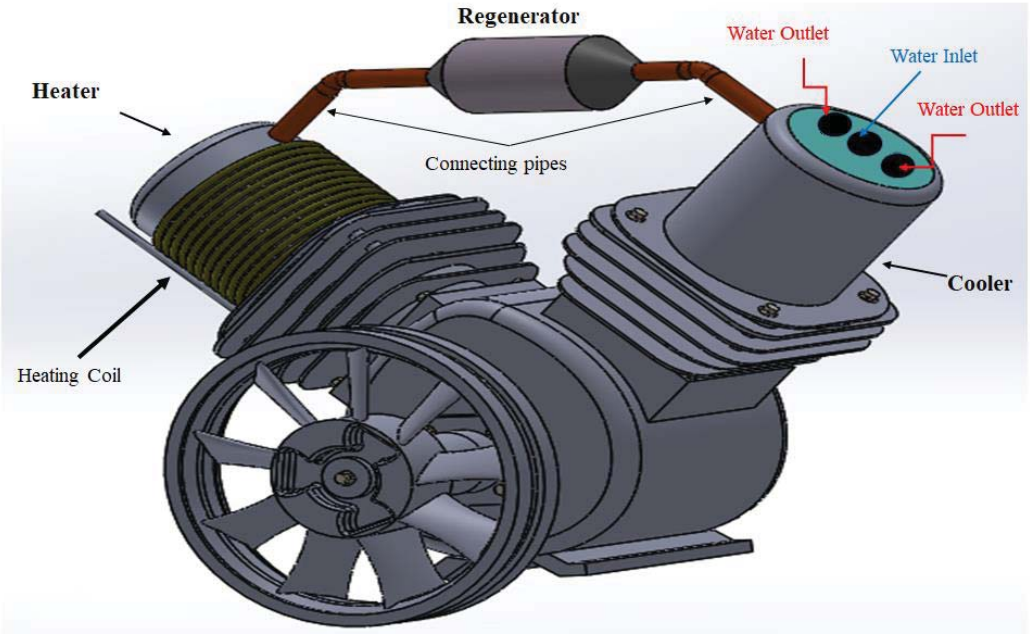


Figure 6.21 V-type alpha Stirling engine with Finned-cooler

The 0.5 mm 32-segemented regenerator configuration developed in chapter (5) was used to evaluate the performance of the developed engine. The correlations data obtained from the developed regenerator were inserted as porous media to the CFD model of the engine and the engine was provided an indicated power of 132 W by using these correlations.

The CFD model of the engine developed in this chapter were used to compare the developed segmented micro-channel regenerator with two commercial matrix regenerators: the Random fibre and the Screen woven matrix which their correlations can be found in [84].

Figure 6.22 illustrates the indicated power of the engine which predicted from the CFD model for the Screen woven, Random fibre woven and the three different developed micro-channels matrixes 0.5 mm, 1.0 mm and 1.5mm 32-segemented regenerator configurations (See section 5.5).

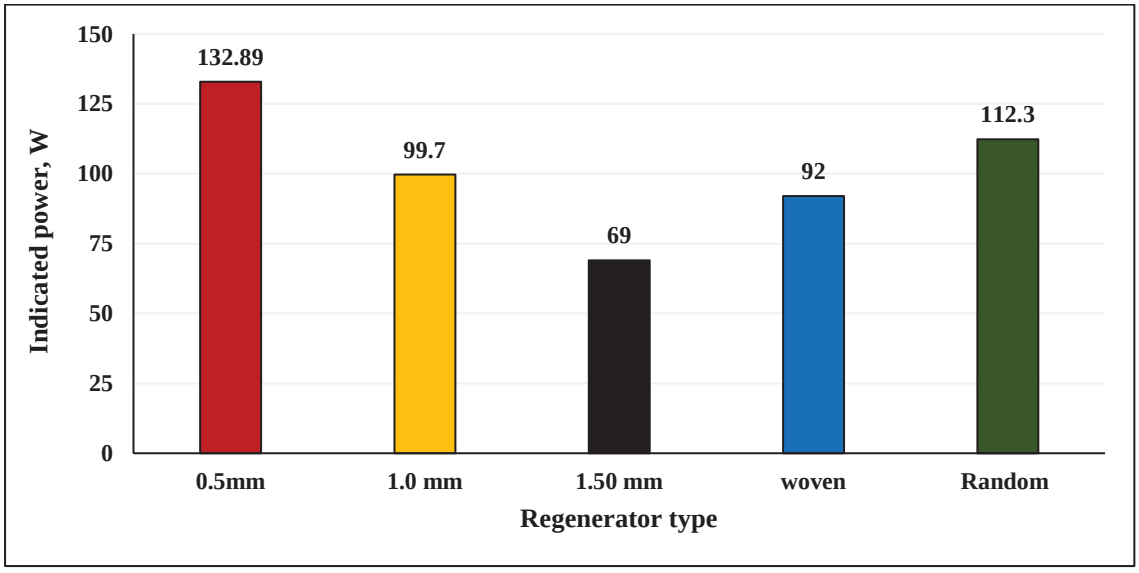


Figure 6.22 Indicated power for channels, Screen woven and random fibre matrix regenerators

The maximum indicated power from the engine was observed from the 0.5 mm regenerator which is (33.28, 92.59, 44.4, and 18.33 %) higher than that of 1.0 mm, 1.5mm, Woven and Random regenerators respectively.

For the 1mm regenerator, as the number of segmentations decreases, the indicated power decreasing of (33.28 %) and further decreasing in the indicated power with just only 69 W for the 1.5 mm regenerator compared to that of the 0.5 mm regenerator (decreasing of 92.59%).

The type of regenerator has a significant impact on the performance of the engine as can be seen also in Figure 6.22, the power of the engine was 132.89 W by using 0.5 mm micro-channels regenerator while the power was 112.3 W and 92 W for the random and screen woven matrixes. The pressure drop in the micro-channels regenerators is very low compare to the random and screen woven matrixes regenerator as was proven experimentally in chapter (4), and then it can be concluded that the pressure drop has the highest influence on the regenerator performance compare to its heat transfer characteristics.

6.6 Conclusion

This work investigated the route to upgrade commercially available V-type compressor to develop V-type alpha Stirling engine through detailed 3D CFD modelling in order to reduce the time and cost for engine development. The correlations of Nusselt number and friction factor for the developed segmented regenerator were used as porous media parameters in the CFD model for the developed Stirling engine. Also, a new concept for the engine cooler design was modelled and integrated in the overall engine model, showing improved performance for the engine due to lower coolant temperature. The maximum indicated power from the developed engine was 132.89, W which was observed by using the 32-segmented regenerator with 0.5 mm micro-channel diameter. It is which is higher 18.33 % and 44.4 % than those of the two commercial matrix regenerators, namely the Random fibre and the Screen woven respectively.

CHAPTER 7

CONCLUSIONS AND RECOMMENDATIONS

7.1 Introduction:

The development of efficient Stirling engines will increase the use of renewable energy sources like solar and geothermal to generate electricity and reduce the need to burn fossil fuels. Also, it will enable the exploitation of the vast resources of industrial waste heat which will lead to major impacts on energy consumption and Co2 emissions.

In this context, this work presents the development of detailed thermodynamic and full 3D CFD models for a V-type alpha Stirling engine using engine prototype and its experimental results from published data in the open literature. New approach of combining the thermodynamic analysis with 3D CFD modelling was developed in order to investigate the performance of the V-type alpha Stirling engine under various operating conditions and design parameters including, regenerator porosity, charge pressure, matrix wire diameter, dead volume and hot/cold ends temperatures on the engine performance in terms of power output, through predicting the PV diagram of the engine. Results showed that power output increased by 180 W when the charge pressure was increased from 1 to 3.5 bar. Also, maximum power output of 155 W was achieved by increasing the regenerator matrix wire diameter to 200 μm. This parametric study concluded that as the cold end temperature decreases, the power output increases reaching 162 W at -20 ^{0}C compared to 146 W at 20 ^{0}C, indicating the potential of using low temperature cooling to enhance the engine power output. Also, it was shown that the design of the heater and the cooler affect the performance of the engine where the power output increased to 200 W by increasing the heater and cooler lengths to maximum value of 140 mm. The power output of V alpha-type Stirling engine increased by up to 65% (from 146 W to 240 W)

when the best new design parameters were applied such as heater length, outer and inner diameters =120 and 44 / 41 mm, cooler length and outer / inner diameters =140 and 30 / 27 mm and the length of the connecting pipes = 155 mm. The best new operating conditions were engine speed = 555r.p.m, charge pressure of 3.5 bar, cold temperature of -20 ^{0}C, hot temperature of 1100 ^{0}C, air as a working fluid and porosity of 80%. This developed model highlights the potential of using 3D CFD modelling to improve the performance of V-type alpha Stirling engine through identifying the best design parameters and operating conditions.

The regenerator design has a major effect on the performance of the Stirling engine since it impacts on the heat transfer and the pressure drops between the regenerator and the working fluid as it oscillates between the hot and the cold ends of the engine. Commercially available regenerators are generally made from Random fibre or Screen woven meshes of various diameters. In this work a new regenerator configuration for the V-type alpha Stirling engine has been developed; it is a parallel-geometry segmented regenerator with circular micro-channels structure. A regenerator with hydraulic diameter of 1 mm was machined at the University of Birmingham using CNC machining technology and consisting of four parts, each part was 10 mm length with 40 mm diameter. The work involved 3D CFD modelling and experimental testing for this regenerator and comparison to other configurations like: The Non-aligned micro-channels, Random fibre regenerators. A detailed description of the test rig facility including the measuring instruments and uncertainty analysis was also included in this work. Results have shown that the Random Fibre regenerator performed better than the other two-segmented regenerators in terms of thermal effectiveness. On the other hand, the pressure drop in the Random Fibre regenerator case was higher than the other segmented regenerators, and that was more obvious in terms of friction factor correlations. It was found that the friction factor in the Micro-channels matrix was smaller than that for the two conventional matrixes namely the Random fibre and Screen woven.

The CFD modelling for the developed segmented micro-channels regenerator was successfully validated with the experimental measurements showing maximum deviation of 10.6% and 6.03% for the unidirectional and oscillatory flows respectively in terms of measuring the outlet temperature. This validated CFD model was used to carry out detailed investigation on the effect of increasing the number of segments on the regenerator effectiveness, it was concluded that as the number of segments increases the heat transfer between the working fluid and the regenerator increases. The calculated effectiveness (eff) for the 1mm micro-channels non-segmented and the 4, 8, 16 and 32-segmented parallel channels regenerators were 0.965, 0.972, 0.973, 0.979 and 0.981 respectively. Based on the effectiveness analysis, the 32-segmented regenerator is superior to the other segmented-regenerators in terms of reducing the amount of heat supplied from the heater and the amount of heat rejected from the cooler. In addition, the effectiveness of the 32-segmented micro-channels matrix (0.980) is comparable to that of the Random Fibre (0.986).

Moreover, the effect of changing the channel diameter was also investigated, where the micro-channels regenerator with diameter of 0.5 mm and 32-segmentations was performed better than the all configuration in this study including the Random Fibre. The effectiveness value of the 0.5 mm and 32-segmented micro-channels matrix was (0.988).

In order to encourage the wide spread implementation of Stirling engines, it is important to explore routes that can reduce the time and cost for the development and manufacturing of Stirling engines. Therefore, this work investigated the route to upgrade of a commercially available V-type compressor to develop V-type alpha type Stirling engine through detailed 3D CFD modelling. The correlations of Nusselt number and friction factor for the developed segmented regenerator were used as porous media parameters in the CFD model of the developed Stirling engine. Also, a new concept for the engine cooler design was modelled and integrated in the overall engine model, showing improved performance for the engine due to

lowering of the coolant temperature. The maximum indicated power observed from the developed engine using the 32-segmented regenerator with 0.5 mm micro-channel diameter was 132.89 W, which is higher by 44.4% and 18.33 % than the indicated power produced by the Random fibre and Screen woven regenerators respectively.

7.2 Conclusion:

The conclusions made from the above described research can be summarised as follows:

- The development of a CFD model for a V-type Alpha Stirling engine using both analytical modelling and experimental results. This model was used to carry out a parametric study to investigate the effects of various design parameters and operating conditions such as, regenerator porosity, charge pressure, matrix wire diameter, dead volume and hot/cold ends temperatures on the engine performance in terms of power output, through predicting the PV diagram of the engine.
- As the regenerator is a fundamental part of the engine, a new parallel-geometry segmented regenerator with circular micro-channels structure was manufactured and developed at the University of Birmingham with its CFD model. The validated CFD model was used to carry out an investigation on the effect of changing the diameter and increasing number of segmentations on pressure drop and heat transfer losses in order to enhance the performance of the regenerator.
- This work highlights the potential of using CFD modelling to investigate the routes to develop V-type Alpha Stirling engine from upgrading commercially available V-type compressor. The work involves the development of detailed CFD modelling and new concept for the cooler design, which improved the performance of the developed engine in terms of its power output.

- A comprehensive comparison between all developed regenerator configurations and two commercial matrix regenerators, namely the Random fibre and the Screen woven on the developed V-type Alpha Stirling engine performance. The performance of the developed engine by using the micro- channels regenerator with diameter of 0.5 mm and 32 segmentations is (44.4, and 18.33 %) higher than that of two commercial matrix regenerators, namely the Random fibre and the Screen woven respectively.

7.3 Recommendations for future work

- A prototype for the developed V-type alpha Stirling engine from a commercially available V-type compressor needs to be manufactured and experimentally tested.
- More research is needed to investigate the effects of using smaller micro holes diameters (less than 0.5 mm), and their manufacturing processes. Also, the manufacturing processes to produce higher numbers of segments of smaller thicknesses.
- Further experimental work is required on the developed regenerator in terms of using higher speeds with turbulent flow conditions.
- Develop experimental measurement techniques to allow for measuring the flow temperature inside the micro channels are needed to increase the range of investigation.

REFERENCES

[1] R. Stirling, “Stirling patent of 1816/1817,” *Philips Stirling engine, Elsevier Sci. Publ. BV, Amsterdam, Netherlands*, 1991.

[2] A. J. Organ and CRC Press., *The air engine : stirling cycle power for a sustainable future*. Woodhead Pub, 2007.

[3] F. Barari, E. M. E. Luna, R. Goodall, and R. Woolley, “Metal foam regenerators; heat transfer and storage in porous metals,” *J. Mater. Res.*, vol. 28, no. 17, pp. 2474–2482, 2013.

[4] A. J. Organ, “The regenerator and the Stirling engine / by Allan J. Organ.” Mechanical Engineering Publications, London, 1997.

[5] M. Ibrahim and R. T. Jr, *Stirling convertor regenerators*, 1st Edition. CRC Press., 2016.

[6] S. C. Costa, H. Barrutia, J. A. Esnaola, and M. Tutar, “Numerical study of the heat transfer in wound woven wire matrix of a Stirling regenerator,” *Energy Convers. Manag.*, vol. 79, pp. 255–264, Mar. 2014.

[7] M. Iasiello *et al.*, “Numerical Analysis of Heat Transfer and Pressure Drop in Metal Foams for Different Morphological Models,” *J. Heat Transfer*, vol. 136, no. 11, p. 112601, Aug. 2014.

[8] A. Ross, *Making Stirling Engines*. Columbus, Ohio: Ross experimental, 1993.

[9] D. G. Thombare and S. K. Verma, “Technological development in the Stirling cycle engines,” *Renew. Sustain. Energy Rev.*, vol. 12, no. 1, pp. 1–38, Jan. 2008.

[10] G. (Graham) Walker, “Stirling engines / by G. Walker.” Clarendon Press, Oxford, 1980.

[11] A. T. Shiferaw *et al.*, “Design of a Stirling Engine for Electricity Generation,” 2014.

[12] W. R. Martini, *Stirling Engine Design Manual*. US Department of Energy, Office of Conservation and Solar Applications, Division of Transportation Energy Conservation, 1978.

[13] C. D. West, “Theoretical basis for the Beale number,” *Intersoc. Energy Convers. Eng. Conf. 16th, Atlanta, GA, August 9-14, 1981, Proceedings. Vol. 2.*, p. 1886, 1981.

[14] W. T. Beale, J. Wood, and B. Chagnot, “Stirling engines for developing countries,” in *Intersociety Energy Conversion Engineering Conference 15*, 1980, pp. 1971–1975.

[15] B. Kongtragool and S. Wongwises, “Investigation on power output of the gamma-configuration low temperature differential Stirling engines,” *Renew. Energy*, vol. 30, no. 3, pp. 465–476, 2005.

[16] C. D. West, “Principles and applications of Stirling engines / C.D. West.” Van Nostrand Reinhold, New York, N.Y., 1986.

[17] G. Schmidt, “Classical analysis of operation of Stirling engine,” *A Rep. Publ. Ger. Eng. union (Original Ger.*, vol. 15, pp. 1–12, 1871.

[18] A. J. Organ, P. J. G. LONG, and L. VASCIAVEO, “Back-to-back test for determining the pumping losses in a Stirling cycle machine,” *IECEC’82*, pp. 1856–1861, 1982.

[19] F. Toda, S. Iwamoto, and K. Nagajima, “Development of Low-Temperature Difference

Stirling engine-Behaviour of the mechanism effectiveness for the performance prediction method," in *Proceeding of 13th international Stirling engine conference*, 2007, pp. 49–51.

[20] A. A. El-Ehwany, G. M. Hennes, E. I. Eid, and E. A. El-Kenany, "Development of the performance of an alpha-type heat engine by using elbow-bend transposed-fluids heat exchanger as a heater and a cooler," *Energy Convers. Manag.*, vol. 52, no. 2, pp. 1010–1019, 2011.

[21] H. Damirchi *et al.*, "Micro Combined Heat and Power to provide heat and electrical power using biomass and Gamma-type Stirling engine," *Appl. Therm. Eng.*, vol. 103, pp. 1460–1469, 2016.

[22] Y. Kato, S. Saitoh, K. Ishimatsu, and M. Iwamoto, "Effect of geometry and speed on the temperatures estimated by CFD for an isothermal model of a gamma configuration low temperature differential Stirling engine with Flat-shaped heat exchangers," *Appl. Therm. Eng.*, vol. 115, pp. 111–122, 2017.

[23] Senviboon, Varit, Silpsakoolsook, Banterng, and Kwankaomeng, Sutapat, "Optimization of geometrical parameter for V-type alpha Stirling engine based on dimensionless analysis," *MATEC Web Conf.*, vol. 192, p. 2044, 2018.

[24] D. Ipci and H. Karabulut, "Thermodynamic and dynamic analysis of an alpha type Stirling engine and numerical treatment," *Energy Convers. Manag.*, vol. 169, pp. 34–44, Aug. 2018.

[25] E. I. Eid, "Effect of using regenerative displacer on the performance of a beta-type heat engine," *AEJ - Alexandria Eng. J.*, vol. 48, no. 1, pp. 25–40, 2009.

[26] E. Eid, "Performance of a beta-configuration heat engine having a regenerative displacer," *Renew. Energy*, vol. 34, no. 11, pp. 2404–2413, Nov. 2009.

[27] R. Li, L. Grosu, and D. Queiros-Condé, "Losses effect on the performance of a Gamma type Stirling engine," *Energy Convers. Manag.*, vol. 114, pp. 28–37, Apr. 2016.

[28] T. Finkelstein, "Analogue simulation of Stirling engine," *Simulation*, vol. 2, 1975.

[29] A. Altman, "SNAP 2002 - A Stirling Numerical Analysis Program A Second Generation Program," *Intersoc. Energy Convers. Eng. Conf.*, no. 20088, pp. 497–502, 2002.

[30] B. Thomas and D. Pittman, "Update on the evaluation of different correlations for the flow friction factor and heat transfer of Stirling engine regenerators," in *Energy Conversion Engineering Conference and Exhibit, 2000.(IECEC) 35th Intersociety*, 2000, vol. 1, pp. 76–84.

[31] R. B. Paula, J. L. Gonçalves, V. R. M. Cobas, and E. E. S. Lora, "THEORETICAL ASSESSMENT OF A STIRLING ENGINE'AMAZON'BY USING PROSA AND MATHCAD," *Rev. Eng. Térmica*, vol. 10, no. 1–2, pp. 32–37, 2018.

[32] J. A. Araoz, M. Salomon, L. Alejo, and T. H. Fransson, "Numerical simulation for the design analysis of kinematic Stirling engines," *Appl. Energy*, vol. 159, pp. 633–650, Dec. 2015.

[33] Y. Timoumi, I. Tlili, and S. Ben Nasrallah, "Design and performance optimization of GPU-3 Stirling engines," *Energy*, vol. 33, no. 7, pp. 1100–1114, Jul. 2008.

[34] Y. Timoumi, I. Tlili, and S. Ben Nasrallah, "Performance optimization of Stirling engines," *Renew. Energy*, vol. 33, no. 9, pp. 2134–2144, Sep. 2008.

[35] C.-H. Cheng, H.-S. Yang, and L. Keong, “Theoretical and experimental study of a 300-W beta-type Stirling engine,” *Energy*, vol. 59, pp. 590–599, Sep. 2013.

[36] R. Gheith, H. Hachem, F. Aloui, and S. Ben Nasrallah, “Experimental and theoretical investigation of Stirling engine heater: Parametrical optimization,” *Energy Convers. Manag.*, vol. 105, pp. 285–293, Nov. 2015.

[37] M. H. Ahmadi, M. A. Ahmadi, F. Pourfayaz, M. Bidi, H. Hosseinzade, and M. Feidt, “Optimization of powered Stirling heat engine with finite speed thermodynamics,” *Energy Convers. Manag.*, vol. 108, pp. 96–105, Jan. 2016.

[38] G. Valenti *et al.*, “Experimental and numerical study of a micro-cogeneration Stirling unit under diverse conditions of the working fluid,” *Appl. Energy*, vol. 160, pp. 920–929, Dec. 2015.

[39] D. M. Berchowitz and I. Urieli, “Stirling cycle engine analysis,” *Adam Hilger Ltd, Bristol*, 1984.

[40] S. Alfarawi, R. AL-Dadah, and S. Mahmoud, “Enhanced thermodynamic modelling of a gamma-type Stirling engine,” *Appl. Therm. Eng.*, vol. 106, pp. 1380–1390, Aug. 2016.

[41] J. M. Strauss and R. T. Dobson, “Evaluation of a second order simulation for Sterling engine design and optimisation,” *J. Energy South. Africa*, vol. 21, no. 2, pp. 17–29, 2010.

[42] T. Finkelstein and A. J. Organ, “Air Engines, the History,” *Sci. Real. Perfect Engine, Am. Soc. Mech. Eng. New York, NY*, 2001.

[43] R. Dyson, S. Wilson, and R. Tew, “Review of computational stirling analysis methods,” in *2nd International Energy Conversion Engineering Conference*, 2004, p. 5582.

[44] D. Gedeon, “Computational techniques for the two-dimensional gasdynamic equations in Stirling engine regenerators and associated manifolds,” in *20th Intersociety Energy Conversion Engineering Conference, Volume 3*, 1985, vol. 3, pp. 3–354.

[45] S. C. Huang, “HFAST-A harmonic analysis program for Stirling cycles,” *IECEC*, San Diego, Aug. 1992.

[46] F. Nepveu, A. Ferriere, and F. Bataille, “Thermal model of a dish/Stirling systems,” *Sol. Energy*, vol. 83, no. 1, pp. 81–89, Jan. 2009.

[47] S. Toghyani, A. Kasaeian, S. H. Hashemabadi, and M. Salimi, “Multi-objective optimization of GPU3 Stirling engine using third order analysis,” *Energy Convers. Manag.*, vol. 87, pp. 521–529, Nov. 2014.

[48] B. Hoegel, D. Pons, M. Gschwendtner, A. Tucker, and M. Sellier, “Thermodynamic peculiarities of alpha-type Stirling engines for low-temperature difference power generation: Optimisation of operating parameters and heat exchangers using a third-order model,” *Proc. Inst. Mech. Eng. Part C J. Mech. Eng. Sci.*, vol. 228, no. 11, pp. 1936–1947, 2014.

[49] K. Mahkamov, “An axisymmetric computational fluid dynamics approach to the analysis of the working process of a solar Stirling engine,” *J. Sol. energy Eng.*, vol. 128, no. 1, pp. 45–53, 2006.

[50] K. Mahkamov, “Design improvements to a biomass Stirling engine using mathematical analysis and 3D CFD modeling,” *J. Energy Resour. Technol.*, vol. 128, no. 3, pp. 203–215, 2006.

[51] W. L. Chen, K. L. Wong, and H. E. Chen, “An experimental study on the performance

of the moving regenerator for a γ-type twin power piston Stirling engine," *Energy Convers. Manag.*, vol. 77, pp. 118–128, 2014.

[52] W.-L. Chen, K.-L. Wong, and L.-W. Po, "A numerical analysis on the performance of a pressurized twin power piston gamma-type Stirling engine," *Energy Convers. Manag.*, vol. 62, pp. 84–92, 2012.

[53] J. L. Salazar and W. L. Chen, "A computational fluid dynamics study on the heat transfer characteristics of the working cycle of a β-type Stirling engine," *Energy Convers. Manag.*, vol. 88, pp. 177–188, 2014.

[54] W.-L. Chen, K.-L. Wong, and Y.-F. Chang, "A computational fluid dynamics study on the heat transfer characteristics of the working cycle of a low-temperature-differential γ-type Stirling engine," *Int. J. Heat Mass Transf.*, vol. 75, pp. 145–155, 2014.

[55] Z. Li, Y. Haramura, Y. Kato, and D. Tang, "Analysis of a high performance model Stirling engine with compact porous-sheets heat exchangers," *Energy*, vol. 64, pp. 31–43, 2014.

[56] W.-L. Chen, Y.-C. Yang, and J. L. Salazar, "A CFD parametric study on the performance of a low-temperature-differential γ-type Stirling engine," *Energy Convers. Manag.*, vol. 106, pp. 635–643, 2015.

[57] S.-C. Costa *et al.*, "Experimental and numerical flow investigation of Stirling engine regenerator," *Energy*, vol. 72, pp. 800–812, Aug. 2014.

[58] S. C. Costa, I. Barreno, M. Tutar, J.-A. Esnaola, and H. Barrutia, "The thermal non-equilibrium porous media modelling for CFD study of woven wire matrix of a Stirling regenerator," *Energy Convers. Manag.*, vol. 89, pp. 473–483, 2015.

[59] S. Alfarawi, R. Al-Dadah, and S. Mahmoud, "Influence of phase angle and dead volume on gamma-type Stirling engine power using CFD simulation," *Energy Convers. Manag.*, vol. 124, pp. 130–140, 2016.

[60] H. Karabulut, H. I. S. YÜCESU, and A. I. KOCA, "Manufacturing and testing of a V-type Stirling engine," *Turkish J. Eng. Environ. Sci.*, vol. 24, no. 2, pp. 71–80, 2000.

[61] C. Çınar, F. Aksoy, H. Solmaz, E. Yılmaz, and A. Uyumaz, "Manufacturing and testing of an α-type Stirling engine," *Appl. Therm. Eng.*, vol. 130, pp. 1373–1379, Feb. 2018.

[62] E. Podesser, "Electricity production in rural villages with a biomass Stirling engine," *Renew. Energy*, vol. 16, no. 1–4, pp. 1049–1052, Jan. 1999.

[63] İ. Batmaz and S. Üstün, "Design and manufacturing of a V-type Stirling engine with double heaters," *Appl. Energy*, vol. 85, no. 11, pp. 1041–1049, Nov. 2008.

[64] B. Demir and A. Güngör, "Manufacturing and testing of a v-type Stirling engine," *Int. J. Electron. Mech. Mechatronics Eng.*, vol. 1, no. 1, pp. 39–44, 2010.

[65] I. M. Yusof, N. A. Farid, Z. A. Zainal, and M. Azman, "Preliminary investigation of a converted fourstroke diesel to alpha v-shaped Stirling engine," *Asian J. Appl. Sci*, vol. 2, no. 2, pp. 101–114, 2009.

[66] ~~N. Ajey, "Experimental and computational studies on an alpha type stirling engine for combined heat and power applications," Indian institute of technology madras.~~

[67] "Regenerator Simple Analysis (updated 1/17/2010)." [Online]. Available: https://www.ohio.edu/mechanical/stirling/simple/regen_simple.html. [Accessed: 15-Oct-2018].

[68] S. Isshiki *et al.*, "The experimental study of atmospheric Stirling engines using pin-fin arrays' heat exchangers," *J. Power Energy Syst.*, vol. 2, no. 5, pp. 1198–1208, 2008.

[69] Y. Kato and K. Baba, "Empirical estimation of regenerator efficiency for a low temperature differential stirling engine," *Renew. Energy*, vol. 62, pp. 285–292, 2014.

[70] N. Umale and D. Thombare, "Theoretical Analysis of Effect of Regenerator Geometry and Material on Stirling Engine Performance," *Proceedings of the 1st National P. G. Conference RIT NCon PG*, India, 2015

[71] R. Gheith, F. Aloui, and S. Ben Nasrallah, "Determination of adequate regenerator for a Gamma-type Stirling engine," *Appl. Energy*, vol. 139, pp. 272–280, Feb. 2015.

[72] M. Tanaka, I. Yamashita, and F. Chisaka, "Flow and heat transfer characteristics of the Stirling engine regenerator in an oscillating flow," *JSME Int. journal. Ser. 2, Fluids Eng. heat Transf. power, Combust. Thermophys. Prop.*, vol. 33, no. 2, pp. 283–289, 1990.

[73] D. Gedeon and J. G. Wood, "Oscillating-Flow Regenerator Test Rig: Hardware and Theory With Derived Correlations for Screens and Felts," *NASA-Lewis Contract. Rep. 198422*, 1996.

[74] S. C. Costa, H. Barrutia, J. A. Esnaola, and M. Tutar, "Numerical study of the pressure drop phenomena in wound woven wire matrix of a Stirling regenerator," *Energy Convers. Manag.*, vol. 67, pp. 57–65, Mar. 2013.

[75] H. Takizawa, N. Kagawa, A. Matsuguchi, and S. Tsuruno, "Performance of new matrix for Stirling engine regenerator," in *Energy Conversion Engineering Conference, 2002. IECEC'02. 2002 37th Intersociety*, 2004, pp. 491–496.

[76] N. Caney, P. Marty, and J. Bigot, "Friction losses and heat transfer of single-phase flow in a mini-channel," *Appl. Therm. Eng.*, vol. 27, no. 10, pp. 1715–1721, Jul. 2007.

[77] S. Alfarawi, R. AL-Dadah, and S. Mahmoud, "Transient investigation of mini-channel regenerative heat exchangers: Combined experimental and CFD approach," *Appl. Therm. Eng.*, vol. 125, pp. 346–358, Oct. 2017.

[78] K. Nam and S. Jeong, "Development of parallel wire regenerator for cryocoolers," *Cryogenics (Guildf).*, vol. 46, no. 4, pp. 278–287, Apr. 2006.

[79] M. Ibrahim, D. Danila, T. Simon, S. Mantell, and L. Sun, "A microfabricated segmented-involute-foil regenerator for enhancing reliability and performance of Stirling engines," Cleveland, OH, United States, 2007.

[80] Y. B. Tao, Y. W. Liu, F. Gao, X. Y. Chen, and Y. L. He, "Numerical analysis on pressure drop and heat transfer performance of mesh regenerators used in cryocoolers," *Cryogenics (Guildf).*, vol. 49, no. 9, pp. 497–503, 2009.

[81] W. T. Beale, "Stirling engine for developing countries," *15th IECEC Seattle*, 1980.

[82] C. D. West, "A fluidyne Stirling engine, report no." AERE, 1981.

[83] A. K. Almajri, S. Mahmoud, and R. Al-Dadah, "Modelling and parametric study of an efficient Alpha type Stirling engine performance based on 3D CFD analysis," *Energy Convers. Manag.*, vol. 145, 2017.

[84] D. Gedeon and J. Wood, "Oscillating-flow regenerator test rig: hardware and theory with derived correlations for screens and felts," *NASA Contractor Report 198442*, Feb., 1996.

[85] W. M. Kays and A. L. London, "Compact heat exchangers," *McGrawhill*, New York

1964.

[86] T. L. Bergman, F. P. Incropera, D. P. DeWitt, and A. S. Lavine, *Fundamentals of heat and mass transfer*. John Wiley & Sons, 2011.

[87] J. R. Senft, *An introduction to Stirling engines*. Moriya Press, 1993.

[88] D. A. Nield, "Effects of local thermal nonequilibrium in steady convective processes in a saturated porous medium: forced convection in a channel," *J. Porous Media*, vol. 1, pp. 181–186, 1998.

[89] J. Schreiber and L. Thieme, "Accomplishments of the NASA GRC stirling technology development project," in *2nd International Energy Conversion Engineering Conference*, 2004, p. 5517.

[90] D. Gedeon, "Sage Stirling-Cycle Model-Class Reference Guide," *Gedeon Assoc. Athens, OH*, 1999.

[91] R. Tew, T. Simon, D. Gedeon, M. Ibrahim, and W. Rong, "An initial non-equilibrium porous-media model for CFD simulation of stirling regenerators," in *4th International Energy Conversion Engineering Conference and Exhibit (IECEC)*, 2006, p. 4003.

[92] D. A. Nield, A. Bejan, and others, *Convection in porous media*, vol. 3. Springer, 2006.

[93] A. B. Comsol, "Comsol Multiphysics Reference Manual." Version, 2018.

[94] R. G. Carbonell and S. Whitaker, "Heat and mass transfer in porous media," in *Fundamentals of transport phenomena in porous media*, Springer, 1984, pp. 121–198.

[95] J. Donea, P. Fasoli-Stella, and S. Giuliani, "Finite element solution of transient fluid-structure problems in Lagrangian coordinates," *Proc. Internat. Meeting on Fast Reactor Safety and Related Physics.*, vol. 3. Chicago 1976, pp. 1327-1435.

[96] J. Donea, P. Fasoli-Stella, and S. Giuliani, "Lagrangian and Eulerian finite element techniques for transient fluid-structure interaction problems," *In Trans. 4th Int. Conf. on Structural Mechanics in Reactor Technology*, Paper B1/2, San Francisco, 1977.

[97] S. K. Andersen, H. Carlsen, and P. G. Thomsen, "Numerical study on optimal Stirling engine regenerator matrix designs taking into account the effects of matrix temperature oscillations," *Energy Convers. Manag.*, vol. 47, no. 7–8, pp. 894–908, 2006.

[98] R. Radebaugh, Y. Huang, A. O'Gallagher, and J. Gary, "Calculated Performance of Low-Porosity Regenerators at 4 K with He-4 and He-3," in *Cryocooler*, 2009, vol. 15, pp. 325–334.

[99] R. Radebaugh and B. Louie, "A simple, first step to the optimization of regenerator geometry," *Proceedings of the 3rd Cryocooler Conference*, NBS special application 698, p. 177–98, 1985

[100] S. Alfarawi, R. AL-Dadah, and S. Mahmoud, "Potentiality of new miniature-channels Stirling regenerator," *Energy Convers. Manag.*, vol. 133, pp. 264–274, 2017.

[101] D. J. Shendage, S. B. Kedare, and S. L. Bapat, "Investigations on Performance of Stirling Engine Regenerator Matrix," *ASME/JSME 2011 8th Therm. Eng. Jt. Conf.*, pp. T20044-T20044-8, 2011.

[102] "Inkbird PID Temperature Controller Thermostat ITC-100VH 230V One SSR Output + One Relay Alarm Output 100V-240V AC for Heater or Cooler Device (ITC-100VH + K Thermocouple + 25A SSR + Heat Sink): Amazon.co.uk: DIY & Tools." [Online]. Available:

https://www.amazon.co.uk/gp/product/B00HVA23CK/ref=oh_aui_detailpage_o00_s00?ie=UTF8&psc=1. [Accessed: 04-Nov-2018].

[103] A. M. Elsayed, "Heat transfer in helically coiled small diameter tubes for miniature cooling systems," *PhD diss.*, University of Birmingham, 2011.

[104] G. Xiao, H. Peng, H. Fan, U. Sultan, and M. Ni, "Characteristics of steady and oscillating flows through regenerator," *Int. J. Heat Mass Transf.*, vol. 108, pp. 309–321, 2017.

[105] "Clarke NH2CVB Air Compressor Pump." [Online]. Available: https://www.machinemart.co.uk/p/clarke-nh2cvb-air-compressor-pump/. [Accessed: 24-Dec-2017].

[106] C. M. (Clifford M. . Hargreaves, *The Philips Stirling engine*. Elsevier, 1991.

[107] Hargreaves and C.M., "The Phillips Stirling engine." New York, NY (United States); Elsevier Science Pub. Co., Inc., 01-Jan-1991.

[108] D. Erol, H. Yaman, and B. Do\ugan, "A review development of rhombic drive mechanism used in the Stirling engines," *Renew. Sustain. Energy Rev.*, vol. 78, pp. 1044–1067, 2017.

[109] "Stirling engine." [Online]. Available:

https://ifisc.uib-csic.es/users/raul/CURSOS/TERMO/Stirling engine.pdf. [Accessed: 10-Jan-2019].

[110] G. Walker, G. Reader, O. Fauvel, and E. Bingham, "The Stirling alternative. Power systems, refrigerants and heat pumps," 1993.

[111] "Thermodynamics performance analysis of solar stirling engines," *downloads.hindawi.com*.

[112] N. Naddaf and others, "Stirling engine cycle efficiency," *Degree Program in Automation Engineering*, University of Applied Scinces, Valkeakoski, 2012.

[113] T. S. Oros, I. Vadan, R. Pop, C. Brad, and others, "Linear Generator for a Free Piston Stirling Engine," *J. Electr. Electron. Eng.*, vol. 7, no. 1, p. 111, 2014.

[114] G. Walker, "Stirling cycle cooling engine with two-phase, two-component working fluid," *Cryogenics (Guildf).*, vol. 14, no. 8, pp. 459–462, 1974.

[115] J. R. Senft and J. R. Senft, *Ringbom stirling engines*, vol. 200. Oxford university press New York, 1993.

APPENDIX A

THE WORKING PRINCIPLES OF STIRLING ENGINE

A.1 Historical Background of Stirling engine

A.1.1 Invention

According to the industrial revolution in the 19th century, which was known as the golden era of the development in science and technology, the management of these industrial applications required a huge need for mechanical engines and thermal energy. Stirling engine was invented by Robert Stirling in 1816 [1], and was one of the engines in competition with the steam engine that used during this time. The initial using of the engine was for pumping water and producing two horse-power and that for almost 2 years [2]. Figure A.1 shows the first engine model and it was using the air as a working fluid.

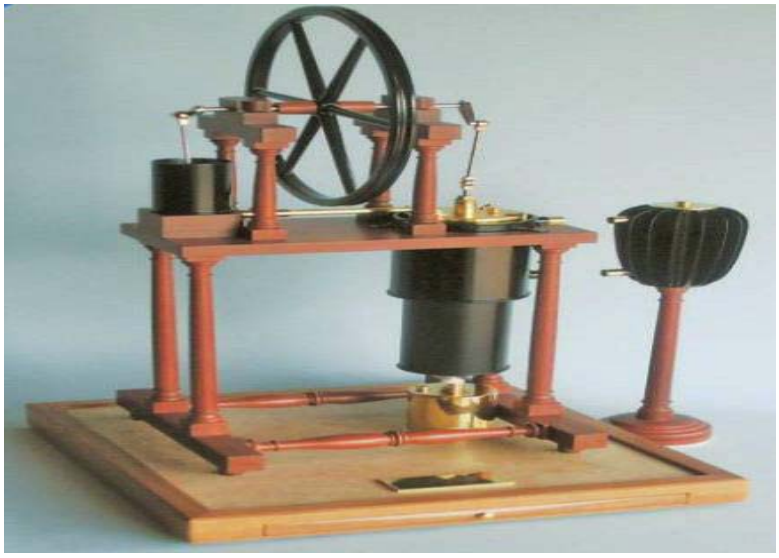


Figure A.1 Air engine model built by Robert Stirling in 1816 [1]

A.1.2 Second engine model

In 1843, Robert Stirling introduced his second model [106] as in Figure A.2. It was designed as a double-acting piston to produce thirty-seven horse-powers.

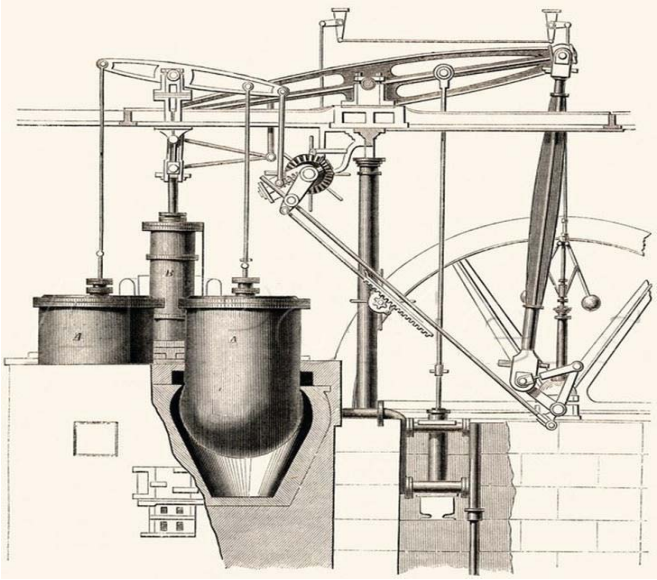


Figure A.2 Stirling's improved engine[106]

Despite the engine was safe and quiet in operation and had a high competitive efficiency than the steam engine, it became forgotten, because still suffered from materials failure, while the steam engine developed and became safer. Moreover, new engines had been developed in that era, such as the electric and the internal combustion engines, and they successfully compete with steam engines.

A.1.3 The Philips Stirling engine

It was 1936, only after the Renaissance in the field of industrial processes and the discovery of more effective metals such as stainless steel [107].

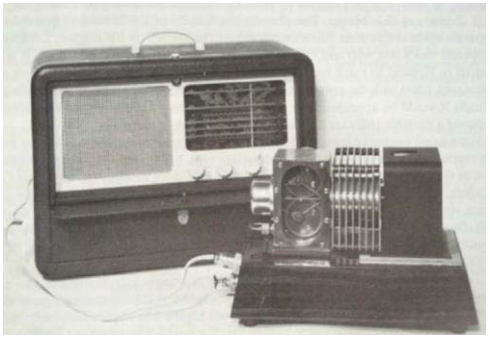


Figure A.3 First Philips Stirling engine [108]

A.1.4 The efficient Stirling engine

Philips continued its development to work in the Stirling engines field and introduced Philips MP1002CA Stirling in 1951 the engine was generating about 200W. In the late 1970's and early 1980's the Government of Japanese started working on the Stirling engines and succeed stationary engines were developed which produced power up to 30 kW.

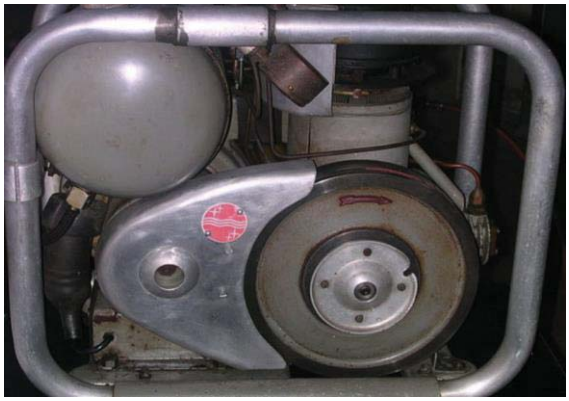
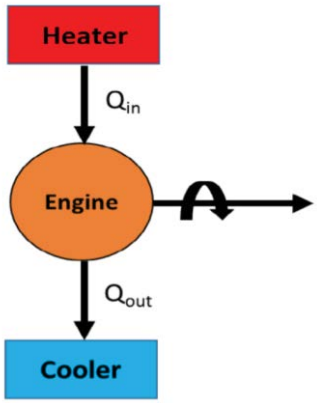


Figure A.4 Philips MP1002CA Stirling generator of 1951[109]

More recent, the research on the space power by NASA involved in the development of the Stirling machines, they have made a free-piston space engine which produced 12 kW.

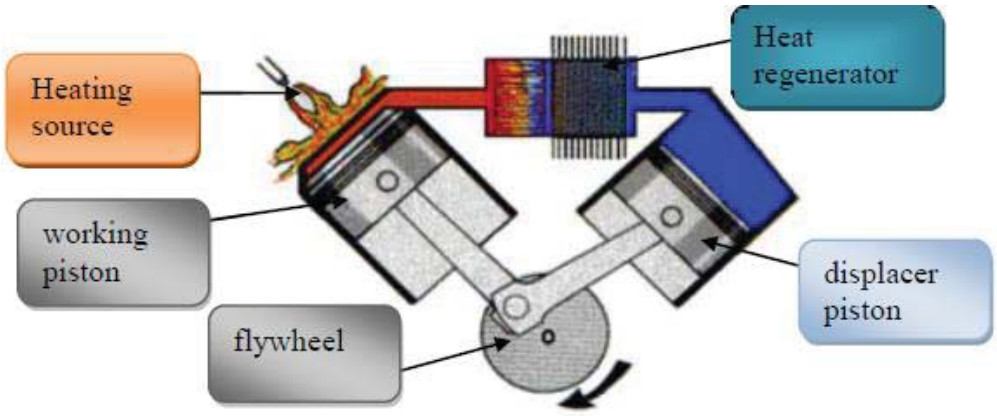
A.2 Working Principles of Stirling Engine

The basic principle of Stirling engine operation, in general, is similar to other heat engines when a portion of the thermal energy is converted from a high-temperature heat source to mechanical energy and then the residual energy is rejected in the lower temperature heat sink. A Simple schematic in Figure A.5 shows the general principle of a heat engine operating between high and low-temperature levels to produce work [110], [111].



FigureA.5 Principle of the heat engine

In a simple shape, as in Figure A.6, the Stirling engine consists of two pistons, three heat exchanges, connecting pipe, working fluid and flywheel. The power piston at the cold end and the displacer at the hot end are the two pistons, while the cooler, heater and regenerator are the three heat exchangers.



FigureA.6 Simple shape of Stirling engine [112]

In general, when any an external heat source is placed on the cylinder at the hot side of the engine, this causes the temperature of the working gas inside the cylinder to rise up and expanding. This expansion drives the piston cylinder to the bottom and thus moves the flywheel.

On the cold side of the engine, the piston moves upward due to the momentum force of inertia of the flywheel, thus the cool gas is pushed back into the hot part of the engine and ready to start a new cycle, and so on.

A.2.1 Theoretical cycle of Stirling Engine

The theoretical cycle, which can be called the ideal thermodynamic cycle of the Stirling engine, has main four processes for the working fluid inside the engine at different levels of temperature as seen in Figure A.7.

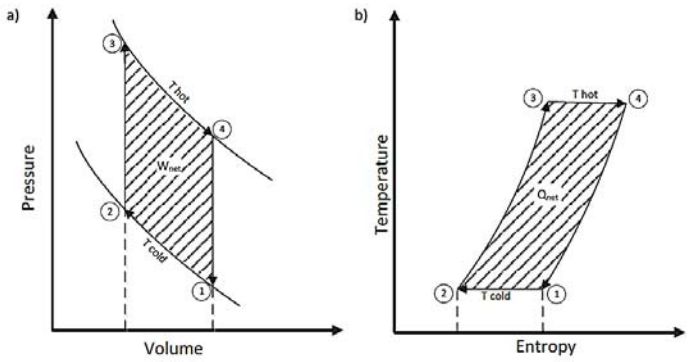


Figure A.7 (a): P-V diagram. (b): T-S diagram [113]

1-2 Isothermal compression

In Figure A.8, the compression-space piston compresses the working fluid and the piston drives to the bottom dead centre (BDC). The heat transfers at a constant gas temperature to an external heat sink. Thus, as seen on the T-S diagram in Figure A.7, as the heat is transferred to the sink the entropy is reduced.

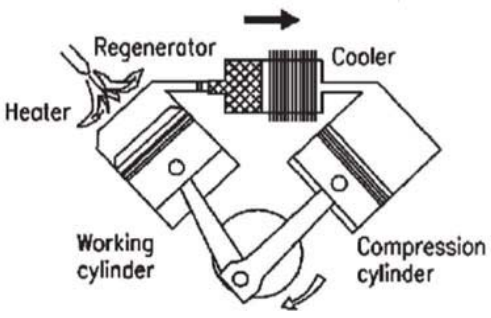


Figure A.8 Isothermal compression stage of Stirling cycle [113]

2-3 Isochoric heat addition

In Figure A.9, the working fluid is compressed to the expansion space via the regenerator matrix, this is due to the joint movement by the flywheel which controls the cold and the hot pistons. During this transformation, the temperature is increased to the maximum temperatures of the cycle, while the volume of the gas is kept constant. The entropy increases due to transferring the heat from the regenerator in this process.

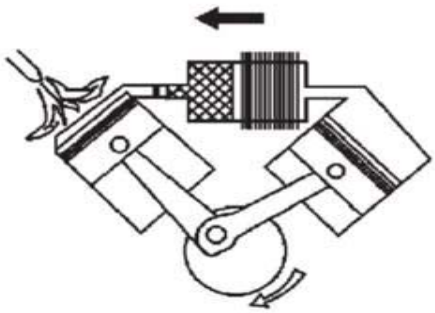


Figure A.9 Isochoric heat addition stage of Stirling cycle [113]

3-4 Isothermal expansion

In Figure A.10, the expansion-space piston expands the working fluid and the piston drives to the top dead centre (TDC). During this process, the heat transfers at a constant gas temperature from an external heat source and the entropy are increased.

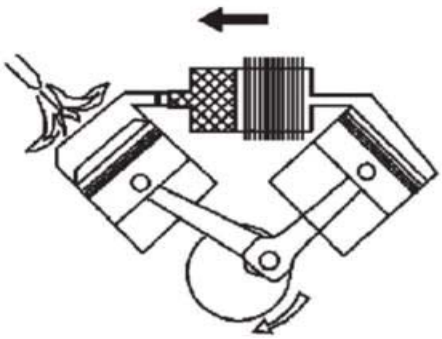


Figure A.10 Isothermal expansion stage of Stirling cycle [113]

4-1 Isochoric heat rejection

In Figure A.11, the working fluid is compressed to the compression space through the regenerator matrix, this is again due to joint movement by the flywheel which controls the cold and the hot pistons. In this process, the temperature is decreased to the minimum temperatures of the cycle, while the volume of the gas is kept constant.

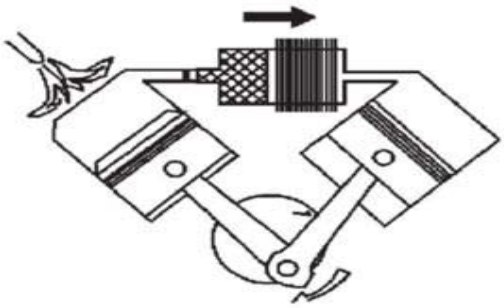


Figure A.11 Isochoric heat rejection stage of Stirling cycle [113]

A.2.2 Carnot and Stirling cycles

Ideally, the process (2-3) when the heat transfers from the surrounding to the engine is equal to the process (4-1) when the heat rejects from the engine to the surrounding. The same as Carnot cycle, these two processes occur at a constant temperature and that meets the requirements of the 2nd law of thermodynamics.

A comparison of the PV and TS diagrams for Stirling and Carnot cycles between the given levels of pressure, temperature and volume are in Figure A.12. The Stirling cycle (1 2 3 4 1) and the Carnot cycle (1 2C 3 4C 1). The increment in the PV diagram area is shown that the cycle of Stirling has a higher work than the cycle of Carnot at lower swept volumes and pressures [114].

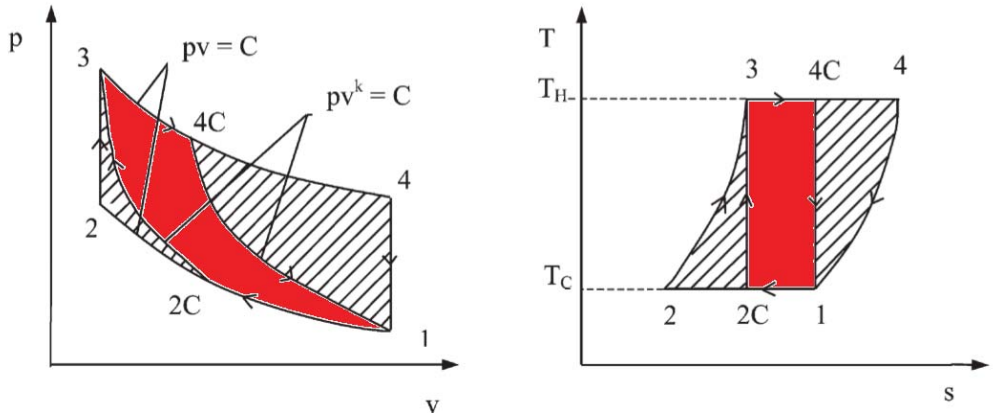


Figure A.12 Stirling and Carnot cycles [115]

A.2.3 Real cycle of Stirling Engine

The real cycle is greatly affected by the inability to be ideal because of the non-ideal mechanisms transport between the different engine components.

The following Figure A.13 is shown the ideal and real time-displacement diagram of a Stirling cycle with the piston arrangement at the terminal points of the cycle at different process of the engine cycle.

The difference between the ideal and real motion led to a decrease in the power output up to 60% [114].

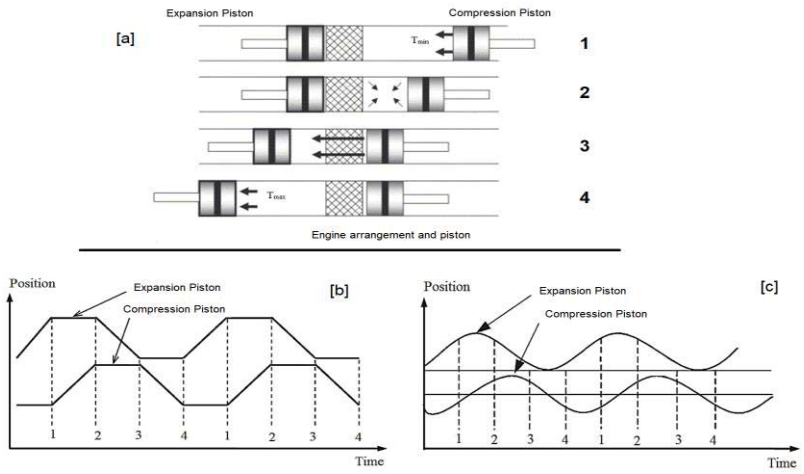


Figure A.13 (a): Piston arrangement at the terminal points of the cycle, (b): Ideal time-displacement diagram, (c): Real time-displacement diagram [115]

APPENDIX B

MATHEMATICAL MODELLING CODE

(MATLAB CODE)

```
% sea (stirling engine analysis) - main program
% this script is based on non-ideal regenerator,heater and cooler
% pumping losses are also included
clc;
clear all;
% Row indices of the var, dvar arrays:
 TC = 1;  % Compression space temperature (K)
 TE = 2;  % Expansion space temperature (K)
 QK = 3;  % Heat transferred to the cooler (J)
 QR = 4;  % Heat transferred to the regenerator (J)
 QH = 5;  % Heat transferred to the heater (J)
 WC = 6;  % Work done by the compression space (J)
 WE = 7;  % Work done by the expansion space (J)
 W  = 8;  % Total work done (WC + WE) (J)
 P  = 9;  % Pressure (Pa)
 VC = 10; % Compression space volume (m^3)
 VE = 11; % Expansion space volume (m^3)
 MC = 12; % Mass of gas in the compression space (kg)
 MK = 13; % Mass of gas in the cooler (kg)
 MR = 14; % Mass of gas in the regenerator (kg)
 MH = 15; % Mass of gas in the heater (kg)
 ME = 16; % Mass of gas in the expansion space (kg)
 TCK = 17; % Conditional temperature compression space / cooler (K)
 THE = 18; % Conditional temeprature heater / expansion space (K)
 GACK = 19; % Conditional mass flow compression space / cooler (kg/rad)
 GAKR = 20; % Conditional mass flow cooler / regenerator (kg/rad)
 GARH = 21; % Conditional mass flow regenerator / heater (kg/rad)
 GAHE = 22; % Conditional mass flow heater / expansion space (kg/rad)
% Size of var(ROWV,COL), dvar(ROWD,COL)
 ROWV = 22; % number of rows in the var matrix
 ROWD = 16; % number of rows in the dvar matrix
 COL = 37; % number of columns in the matrices (every 10 degrees)
%=========================================================================
global tk tr th % cooler, regenerator, heater temperatures [K]
global vk % cooler void volume [m^3]
global vr % regen void volume [m^3]
global vh % heater void volume [m^3]
global vclc vcle % compression,expansion clearence vols [m^3]
global vswc vswe % compression, expansion swept volumes [m^3]
global rgas % gas constant [J/kg.K]
global cp % specific heat capacity at constant pressure [J/kg.K]
global cv % specific heat capacity at constant volume [J/kg.K]
global gama % ratio: cp/cv
global mu0 % dynamic viscosity at reference temp t0 [kg.m/s]
global t0  % reference temp. [K]
global mgas % total mass of gas in engine [kg]
```

```
global pmean % mean (charge) pressure [Pa]
global freq omega % cycle frequency [herz], [rads/s]
global ar % regen internal free flow area [m^2]
global awgr % regen internal wetted area [m^2]
global dr % regen hydraulic diameter [m]
global lr % regenerator effective length [m]
global cqwr % regenerator housing thermal conductance [W/K]
global mu0 % dynamic viscosity at reference temp t0 [kg.m/s]
global t_suth
global alpha % phase angle advance of expansion space [radians]

%=========================================================================
%engine configuration & operating parameters
vclc = 4.313e-06;      %D=52.4 mm ,clearance=2 mm
vcle = 4.313e-06;      %D=52.4 mm ,clearance=2 mm
vswc = 129.39e-6;  %m^3
vswe = 129.39e-6;  %m^3
alpha = (pi/2);
th = 1373;
tk = 293;
tr = (th - tk)/log(th/tk);
N=555;      %RPM
freq = N/60;
omega = 2*pi*freq;
%=========================================================================
%gas type (air or helium)
rgas = 287;
gama = 1.4;
mu0 = 17.08e-6;
t_suth = 112;  % suthnderland temperature used in viscosity to calculated renum= reynolds
number
cv = rgas/(gama - 1);
cp = gama*cv;
t0 = 273;  % reference temperature
prandtl = 0.71;
%=========================================================================
%heat exchangers details
%=========================================================================
%regenerator (tubular type)
dout = 22e-3;
domat = 20e-3;
dimat = 0;
lr = 38e-3;
num = 1;
awgr0 = pi*(dimat + domat)*lr;
amat = num*pi*(domat*domat - dimat*dimat)/4; % regen matrix area
awr = num*pi*(dout*dout - domat*domat)/4; % regen housing wall area
kwr = 11.3; % thermal conductivity [W/m/K]
cqwr = kwr*awr/lr; % regen wall thermal conductance [W/K]
%=========================================================================
%(mesh matrix)
porosity = 0.70;
dwire = 0.100e-3;  % matrix wire diameter
ar = amat*porosity;
vr = ar*lr;
%regenerator=vr
dr = dwire*porosity/(1 - porosity);
```

```
awgr = 4*vr/dr + awgr0;
fprintf(' matrix porosity: %.3f\n', porosity)
fprintf(' matrix wire diam %.2f(mm)\n', dwire*1e3)
fprintf(' hydraulic diam %.3f(mm)\n', dr*1e3)
fprintf(' total wetted area %.3e(sq.m)\n', awgr)
fprintf(' regenerator length %.1f(mm)\n', lr*1e3)
fprintf(' void volume %.2f(cc)\n', vr*1e6)

%=========================================================================
%heater
doh=0.046;
dih=0.04;
dh=6e-3;
lh=100e-3;
numh=1;
ah = numh*pi*(doh^2-dih^2)/4;  % heater cross sectional area
vh = ah*lh;    % heater air volume
awgh = numh*pi*(doh)*lh;  % heater wetted area like as surface area  of heat transfer

%=========================================================================
%kooler
dok=0.032;
dik=0.025;
dk=7e-3;
lk=120e-3;
numk=1;
ak = numk*pi*(dok^2-dik^2)/4; % cooler cross sectional area
vk = ak*lk;    % cooler air volume
awgk = numk*pi*(dok)*lk;   % cooler wetted area like as surface area  of heat transfer
%=========================================================================
%total mass of working gas in engine
% Schmidt analysis
pmean = 2.5*10^5;   % charge pressure
%=========================================================================
VDk=1543.6e-9;                                    % dead volume from the cold side
VDh=1436.6e-9;                                    % dead volume from the hot side
vot = vk/tk+ vr/tr + vh/th+( VDk/tk)+(VDh/th) ;    % total volume (heater+cooler+regenerator)
ve = vcle+0.5*vswe*(1+cos(0));                    % Expansion volume
vc = vclc+0.5*vswc*(1+cos(0-alpha));              % Compression volume
mgas = pmean*(vc/tk + vot + ve/th)/rgas;          % total mass of gas in engine [kg]
%=========================================================================
fprintf('=========================================================\n')
fprintf(' total mass of gas (kg) %.8f\n', mgas);
[var,dvar] = simple;
%=========================================================================
% calculate the mean pressure and compare with the input value
%=========================================================================
avgP = sum(var(P,:))/length(var(P,:));
corr_fact = (pmean-avgP)/avgP;
fprintf(' calculated  mean pressure: %.2f[Pa]\n', avgP);
fprintf(' correction factor: %.2f[Percent]\n', corr_fact*100);
%=========================================================================
```

```
function [var,dvar] = adiab
% ideal adiabatic model simulation
% Returned values:
%   var(22,37) array of variable values every 10 degrees (0 - 360)
```

```
%   dvar(16,37) array of derivatives every 10 degrees (0 - 360)

global tk th % cooler, heater temperatures [K]

% Row indices of the var, dvar matrices, and the y,dy variable vectors:
 TC = 1;  % Compression space temperature (K)
 TE = 2;  % Expansion space temperature (K)
 QK = 3;  % Heat transferred to the cooler (J)
 QR = 4;  % Heat transferred to the regenerator (J)
 QH = 5;  % Heat transferred to the heater (J)
 WC = 6;  % Work done by the compression space (J)
 WE = 7;  % Work done by the expansion space (J)
 W  = 8;  % Total work done (WC + WE) (J)
 P  = 9;  % Pressure (Pa)
 VC = 10; % Compression space volume (m^3)
 VE = 11; % Expansion space volume (m^3)
 MC = 12; % Mass of gas in the compression space (kg)
 MK = 13; % Mass of gas in the cooler (kg)
 MR = 14; % Mass of gas in the regenerator (kg)
 MH = 15; % Mass of gas in the heater (kg)
 ME = 16; % Mass of gas in the expansion space (kg)
 TCK = 17; % Conditional temperature compression space / cooler (K)
 THE = 18; % Conditional temeprature heater / expansion space (K)
 GACK = 19; % Conditional mass flow compression space / cooler (kg/rad)
 GAKR = 20; % Conditional mass flow cooler / regenerator (kg/rad)
 GARH = 21; % Conditional mass flow regenerator / heater (kg/rad)
 GAHE = 22; % Conditional mass flow heater / expansion space (kg/rad)
% Size of var(ROWV,COL), y(ROWV), dvar(ROWD,COL), dy(ROWD)
 ROWV = 22; % number of rows in the var matrix
 ROWD = 16; % number of rows in the dvar matrix
 COL = 37; % number of columns in the matrices (every 10 degrees)
%=========================================================================
fprintf('============Ideal Adiabatic Analysis====================\n')
fprintf('Cooler Tk = %.1f[K], Heater Th = %.1f[K]\n', tk, th);
 epsilon = 1e-06;  % Allowable error in temerature (K)
 max_iteration = 30;  % Maximum number of iterations to convergence
 ninc = 360; % number if integration increments (every degree)
 step = ninc/36; % for saving values in var, dvar matrices
 dtheta = 2.0*pi/ninc; % integration increment (radians)
% Initial conditions:
 y(THE) = th;
 y(TCK) = tk;
 y(TE) = th;
 y(TC) = tk;
 iter = 0;
 terror = 10*epsilon; % Initial error to enter the loop
% Iteration loop to cyclic convergence
 while ((terror >= epsilon)&&(iter < max_iteration))
% cyclic initial conditions
    tc0 = y(TC);
    te0 = y(TE);
    theta = 0;
    y(QK) = 0;
    y(QR) = 0;
    y(QH) = 0;
    y(WC) = 0;
    y(WE) = 0;
```

```
    y(W) = 0;
    fprintf('iteration %d: Tc = %.1f[K], Te = %.1f[K]\n',iter,y(TC),y(TE))
    for i = 1:1:ninc
       [theta,y,dy] = rk4('dadiab',7,theta,dtheta,y);
    end
    terror = abs(tc0 - y(TC)) + abs(te0 - y(TE));
    iter = iter + 1;
 end

if (iter >= max_iteration)
    fprintf('No convergence within %d iteration\n',max_iteration)
end

% Initial var and dvar matrix
var = zeros(22,37);
dvar = zeros(16,37);

% a final cycle, to fill the var, dvar matrices
theta=0;
y(QK)=0;
y(QR)=0;
y(QH)=0;
y(WC)=0;
y(WE)=0;
y(W)=0;
[var,dvar] = filmatrix(1,y,dy,var,dvar);
for i = 2:1:COL
    for j = 1:1:step
        [theta,y,dy] = rk4('dadiab',7,theta,dtheta,y);
    end
    [var,dvar] = filmatrix(i,y,dy,var,dvar);
end
```

```
function [y,dy] = dadiab(theta,y)
% Evaluate ideal adiabatic model derivatives
% global variables used from "define" functions
global vk % cooler void volume [m^3]
global vr % regen void volume [m^3]
global vh % heater void volume [m^3]
global rgas % gas constant [J/kg.K]
global cp % specific heat capacity at constant pressure [J/kg.K]
global cv % specific heat capacity at constant volume [J/kg.K]
global gama % ratio: cp/cv
global mgas % total mass of gas in engine [kg]
global tk tr th % cooler, regen, heater temperatures [K]

% Indices of the y, dy vectors:
 TC = 1;  % Compression space temperature (K)
 TE = 2;  % Expansion space temperature (K)
 QK = 3;  % Heat transferred to the cooler (J)
 QR = 4;  % Heat transferred to the regenerator (J)
 QH = 5;  % Heat transferred to the heater (J)
 WC = 6;  % Work done by the compression space (J)
 WE = 7;  % Work done by the expansion space (J)
 W  = 8;  % Total work done (WC + WE) (J)
 P  = 9;  % Pressure (Pa)
 VC = 10; % Compression space volume (m^3)
```

```
 VE = 11; % Expansion space volume (m^3)
 MC = 12; % Mass of gas in the compression space (kg)
 MK = 13; % Mass of gas in the cooler (kg)
 MR = 14; % Mass of gas in the regenerator (kg)
 MH = 15; % Mass of gas in the heater (kg)
 ME = 16; % Mass of gas in the expansion space (kg)
 TCK = 17; % Conditional temperature compression space / cooler (K)
 THE = 18; % Conditional temeprature heater / expansion space (K)
 GACK = 19; % Conditional mass flow compression space / cooler (kg/rad)
 GAKR = 20; % Conditional mass flow cooler / regenerator (kg/rad)
 GARH = 21; % Conditional mass flow regenerator / heater (kg/rad)
 GAHE = 22; % Conditional mass flow heater / expansion space (kg/rad)
%=========================================================================
% Volume and volume derivatives:
 [y(VC),y(VE),dy(VC),dy(VE)] = sinevol(theta);

% Pressure and pressure derivatives:
 vot = vk/tk + vr/tr + vh/th;
 y(P) = (mgas*rgas/(y(VC)/y(TC) + vot + y(VE)/y(TE)));
 top = -y(P)*(dy(VC)/y(TCK) + dy(VE)/y(THE));
 bottom = (y(VC)/(y(TCK)*gama) + vot + y(VE)/(y(THE)*gama));
 dy(P) = top/bottom;

% Mass accumulations and derivatives:
 y(MC) = y(P)*y(VC)/(rgas*y(TC));
 y(MK) = y(P)*vk/(rgas*tk);
 y(MR) = y(P)*vr/(rgas*tr);
 y(MH) = y(P)*vh/(rgas*th);
 y(ME) = y(P)*y(VE)/(rgas*y(TE));
 dy(MC) = (y(P)*dy(VC) + y(VC)*dy(P)/gama)/(rgas*y(TCK));
 dy(ME) = (y(P)*dy(VE) + y(VE)*dy(P)/gama)/(rgas*y(THE));
 dpop = dy(P)/y(P);
 dy(MK) = y(MK)*dpop;
 dy(MR) = y(MR)*dpop;
 dy(MH) = y(MH)*dpop;

% Mass flow between cells:
 y(GACK) = -dy(MC);
 y(GAKR) = y(GACK) - dy(MK);
 y(GAHE) = dy(ME);
 y(GARH) = y(GAHE) + dy(MH);

% Conditional temperatures between cells:
 y(TCK) = tk;
 if(y(GACK)>0)
    y(TCK) = y(TC);
 end
 y(THE) = y(TE);
 if(y(GAHE)>0)
    y(THE) = th;
 end

% 7 derivatives to be integrated by rk4:
% Working space temperatures:
 dy(TC) = y(TC)*(dpop + dy(VC)/y(VC) - dy(MC)/y(MC));
 dy(TE) = y(TE)*(dpop + dy(VE)/y(VE) - dy(ME)/y(ME));
```

```
% Energy:
 dy(QK) = vk*dy(P)*cv/rgas - cp*(y(TCK)*y(GACK) - tk*y(GAKR));
 dy(QR) = vr*dy(P)*cv/rgas - cp*(tk*y(GAKR) - th*y(GARH));
 dy(QH) = vh*dy(P)*cv/rgas - cp*(th*y(GARH) - y(THE)*y(GAHE));
 dy(WC) = y(P)*dy(VC);
 dy(WE) = y(P)*dy(VE);

% Net work done:
 dy(W) = dy(WC) + dy(WE);
 y(W) = y(WC) + y(WE);
end
```

```
function tgh = hotsim(var,twh,qrloss)
% evaluate heater average heat transfer performance
% Modified  to include regenerator qrloss
% Arguments:
%   var(22,37) array of variable values every 10 degrees (0 - 360)
%   twh - heater wall temperature [K]
%   qrloss - heat loss due to imperfect regenerator [J]
% Returned values:
%   tgh - heater average gas temperature [K]

% Row indices of the var array:
 TC = 1;  % Compression space temperature [K]
 TE = 2;  % Expansion space temperature [K]
 QK = 3;  % Heat transferred to the cooler [J]
 QR = 4;  % Heat transferred to the regenerator [J]
 QH = 5;  % Heat transferred to the heater [J]
 WC = 6;  % Work done by the compression space [J]
 WE = 7;  % Work done by the expansion space [J]
 W  = 8;  % Total work done (WC + WE) [J]
 P  = 9;  % Pressure [Pa]
 VC = 10; % Compression space volume [m^3]
 VE = 11; % Expansion space volume [m^3]
 MC = 12; % Mass of gas in the compression space [kg]
 MK = 13; % Mass of gas in the cooler [kg]
 MR = 14; % Mass of gas in the regenerator [kg]
 MH = 15; % Mass of gas in the heater [kg]
 ME = 16; % Mass of gas in the expansion space [kg]
 TCK = 17; % Conditional temperature compression space / cooler [K]
 THE = 18; % Conditional temeprature heater / expansion space [K]
 GACK = 19; % Conditional mass flow compression space / cooler [kg/rad]
 GAKR = 20; % Conditional mass flow cooler / regenerator [kg/rad]
 GARH = 21; % Conditional mass flow regenerator / heater [kg/rad]
 GAHE = 22; % Conditional mass flow heater / expansion space [kg/rad]

global th % heater temperature [K]
global freq omega % cycle frequency [herz], [rads/s]
global ah % heater internal free flow area [m^2]
global awgh % heater internal wetted area [m^2]
global dh % heater hydraulic diameter [m]
global cp % specific heat capacity at constant pressure [J/kg.K]
global prandtl
% Calculating the Reynolds number over the cycle
for(i = 1:1:37)
   gah(i) = (var(GARH,i) + var(GAHE,i))*omega/2;
   gh = gah(i)/ah;
```

```
   [mu,kgas,re(i)] = reynum(th,gh,dh);
end

% Average and maximum Reynolds number
sumre=0;
remax=re(1);
for (i=1:1:36)
   sumre=sumre + re(i);
   if(re(i) > remax)
      remax = re(i);
   end
end
reavg = sumre/36;
if reavg<2000;
    fr=16;
    fr1=fr
elseif reavg>4000
    fr=0.0791*reavg^0.75;
    fr2=fr
else
    fr=7.343e-4*reavg^1.3142;
    fr3=fr
end
% From Reynolds simple analogy:
ht=fr*mu*cp/(2*dh*prandtl);

tgh = twh - (var(QH,37)+qrloss)*freq/(ht*awgh); % Heater gas temperature [K]

fprintf('============ Heater Simple analysis =============\n')
fprintf(' Average Reynolds number : %.1f\n',reavg)
fprintf(' Maximum Reynolds number : %.1f\n',remax)
fprintf(' Heat transfer coefficient [W/m^2*K] : %.2f\n',ht)
fprintf('heater wall/gas temperatures: Twh = %.1f[K], Tgh = %.1f[K]\n',twh,tgh);
```

```
function tgk = kolsim(var,twk,qrloss)
% evaluate cooler average heat transfer performance
% Modified  to include regenerator qrloss
% Arguments:
%   var(22,37) array of variable values every 10 degrees (0 - 360)
%   twk - cooler wall temperature [K]
%   qrloss - heat loss due to imperfect regenerator [J]
% Returned values:
%   tgk - cooler average gas temperature [K]

% Row indices of the var array:
 TC = 1;  % Compression space temperature [K]
 TE = 2;  % Expansion space temperature [K]
 QK = 3;  % Heat transferred to the cooler [J]
 QR = 4;  % Heat transferred to the regenerator [J]
 QH = 5;  % Heat transferred to the heater [J]
 WC = 6;  % Work done by the compression space [J]
 WE = 7;  % Work done by the expansion space [J]
 W  = 8;  % Total work done (WC + WE) [J]
 P  = 9;  % Pressure [Pa]
 VC = 10; % Compression space volume [m^3]
 VE = 11; % Expansion space volume [m^3]
 MC = 12; % Mass of gas in the compression space [kg]
```

```
 MK = 13; % Mass of gas in the cooler [kg]
 MR = 14; % Mass of gas in the regenerator [kg]
 MH = 15; % Mass of gas in the heater [kg]
 ME = 16; % Mass of gas in the expansion space [kg]
 TCK = 17; % Conditional temperature compression space / cooler [K]
 THE = 18; % Conditional temeprature heater / expansion space [K]
 GACK = 19; % Conditional mass flow compression space / cooler [kg/rad]
 GAKR = 20; % Conditional mass flow cooler / regenerator [kg/rad]
 GARH = 21; % Conditional mass flow regenerator / heater [kg/rad]
 GAHE = 22; % Conditional mass flow heater / expansion space [kg/rad]

global tk % cooler temperature [K]
global freq omega % cycle frequency [herz], [rads/s]
global ak % cooler internal free flow area [m^2]
global awgk % cooler internal wetted area [m^2]
global dk % cooler hydraulic diameter [m]
global cp % specific heat capacity at constant pressure [J/kg.K]
global prandtl
% Calculating the Reynolds number over the cycle
for(i = 1:1:37)
   gak(i) = (var(GACK,i) + var(GAKR,i))*omega/2;
   gk = gak(i)/ak;  % mass flux
   [mu,kgas,re(i)] = reynum(tk,gk,dk);
end

% Average and maximum Reynolds number
sumre=0;
remax=re(1);
for (i=1:1:36)
   sumre=sumre + re(i);
   if(re(i) > remax)
      remax = re(i);
   end
end
reavg = sumre/36;
if reavg<2000;
    fr=16;
    fr1=fr
elseif reavg>4000
    fr=0.0791*reavg^0.75;
    fr2=fr
else
    fr=7.343e-4*reavg^1.3142;
    fr3=fr
end

% From Reynolds simple analogy:reavg>2000 &
ht=fr*mu*cp/(2*dk*prandtl);

tgk = twk - (var(QK,37)-qrloss)*freq/(ht*awgk); % Heater gas temperature [K]

fprintf('============ Cooler Simple analysis ============\n')
fprintf(' Average Reynolds number : %.1f\n',reavg)
fprintf(' Maximum Reynolds number : %.1f\n',remax)
fprintf(' Heat transfer coefficient [W/m^2*K] : %.2f\n',ht)
fprintf('cooler wall/gas temperatures: Twk = %.1f[K], Tk = %.1f[K]\n',twk,tgk);
```

```
function [st,fr] = matrixfr(re)
% evaluate regenerator mesh matrix stanton number, friction factor
% Arguments:
%   re - Reynolds number
% Returned values:
%   st - Stanton number
%   fr - Reynolds friction factor ( = re*fanning friction factor)

global prandtl % Prandtl number

% equations taken from Kays & London (1955 edition)
st = 0.46*re^(-0.4)/prandtl;
%fr = 54 + 1.43*re^0.78;
%%fr = 129/re +2.91*re^-0.103; %new
fr = 32.25 +0.7275*re^0.897; %new
end
```

```
function [ht,fr]=pipefr(d,mu,re)
% evaluate heat transfer coefficient, Reynolds friction factor
% Arguments:
%   d - hydraulic diameter [m]
%   mu - gas dynamic viscosity [kg.m/s]
%   re - Reynolds number
% Returned values:
%   ht - heat transfer coefficient [W/m^2.K]
%   fr - Reynolds friction factor ( = re*fanning friction factor)

global cp % specific heat capacity at constant pressure [J/kg.K]
global prandtl % Prandtl number

% Personal communication with Alan Organ, because of oscillating
% flow, we assume that flow is always turbulent. Use the Blasius
% relation for all Reynolds numbers:
fr=0.0791*re^0.75;
%%fr=16;
% From Reynolds simple analogy:
ht=fr*mu*cp/(2*d*prandtl);
```

```
function dwork = worksim(var,dvar)
% Evaluate the pressure drop available work loss [J]
% Arguments:
%   var(22,37) array of variable values every 10 degrees (0 - 360)
%   dvar(16,37) array of derivatives every 10 degrees (0 - 360)
% Returned value:
%   dwork - pressure drop available work loss [J]

% Row indices of the var, dvar arrays:
 TC = 1;  % Compression space temperature [K]
 TE = 2;  % Expansion space temperature [K]
 QK = 3;  % Heat transferred to the cooler [J]
 QR = 4;  % Heat transferred to the regenerator [J]
 QH = 5;  % Heat transferred to the heater [J]
 WC = 6;  % Work done by the compression space [J]
 WE = 7;  % Work done by the expansion space [J]
 W  = 8;  % Total work done (WC + WE) [J]
 P  = 9;  % Pressure [Pa]
```

```
 VC = 10; % Compression space volume [m^3]
 VE = 11; % Expansion space volume [m^3]
 MC = 12; % Mass of gas in the compression space [kg]
 MK = 13; % Mass of gas in the cooler [kg]
 MR = 14; % Mass of gas in the regenerator [kg]
 MH = 15; % Mass of gas in the heater [kg]
 ME = 16; % Mass of gas in the expansion space [kg]
 TCK = 17; % Conditional temperature compression space / cooler [K]
 THE = 18; % Conditional temeprature heater / expansion space [K]
 GACK = 19; % Conditional mass flow compression space / cooler [kg/rad]
 GAKR = 20; % Conditional mass flow cooler / regenerator [kg/rad]
 GARH = 21; % Conditional mass flow regenerator / heater [kg/rad]
 GAHE = 22; % Conditional mass flow heater / expansion space [kg/rad]
% Size of var(ROWV,COL), dvar(ROWD,COL)
 ROWV = 22; % number of rows in the var matrix
 ROWD = 16; % number of rows in the dvar matrix
 COL = 37; % number of columns in the matrices (every 10 degrees)
%=========================================================================
global tk tr th % cooler, regenerator, heater temperatures [K]
global freq omega % cycle frequency [herz], [rads/s]
global vh % heater void volume [m^3]
global ah % heater internal free flow area [m^2]
global dh % heater hydraulic diameter [m]
global lh % heater effective length [m]
global vk % cooler void volume [m^3]
global ak % cooler internal free flow area [m^2]
global dk % cooler hydraulic diameter [m]
global lk % cooler effective length [m]
global vr % regen void volume [m^3]
global ar % regen internal free flow area [m^2]
global lr % regenerator effective length [m]
global dr % regen hydraulic diameter [m]

dtheta = 2*pi/36;
dwork = 0; % initialise pumping work loss
re =zeros(1,36);
dpkol = zeros(1,36);
dpreg = zeros(1,36);
dphot = zeros(1,36);
dp = zeros(1,36);
pcom = zeros(1,36);
pexp = zeros(1,36);
%=========================================================================
for i = 1:1:36
    %kooler
    gk = (var(GACK,i) + var(GAKR,i))*omega/(2*ak);
    [mu,kgas,re(i)] = reynum(tk,gk,dk);
    fr = 0.0791*re(i)^0.75;%%%%%
    dpkol(i) = 2*fr*mu*vk*gk*lk/(var(MK,i)*dk^2);
%=========================================================================
    %regen
    gr = (var(GAKR,i) + var(GARH,i))*omega/(2*ar);
    [mu,kgas,re(i)] = reynum(tr,gr,dr);
   [st,fr] = matrixfr(re(i));
    dpreg(i) = 2*fr*mu*vr*gr*lr/(var(MR,i)*dr^2);
%=========================================================================
    %heater
```

```
    gh = (var(GARH,i) + var(GAHE,i))*omega/(2*ah);
    [mu,kgas,re(i)] = reynum(th,gh,dh);
    fr = 0.0791*re(i)^0.75;
    dphot(i) = 2*fr*mu*vh*gh*lh./(var(MH,i)*dh^2);
    dp(i) = dpkol(i) + dpreg(i) + dphot(i);
%=========================================================================
    dwork = dwork+dtheta*dp(i)*dvar(VE,i); % pumping work [J]
        pcom(i) = var(P,i);
        pexp(i) = pcom(i) + dp(i);
end
%=========================================================================
dpkol(COL) = dpkol(1);
dpreg(COL) = dpreg(1);
dphot(COL) = dphot(1);
dp(COL) = dp(1);
pcom(COL) = pcom(1);
pexp(COL) = pexp(1);

choice = 'x';
while(~strncmp(choice,'q',1))
        fprintf('Choose pumping loss plot type:\n');
        fprintf('   h - for heat exchanger pressure drop plot\n');
        fprintf('   p - for working space pressure plot\n');
        fprintf('   q - to quit\n');
        choice = input('h)x_pdrop, p)ressure, q)uit: ','s');
        if(strncmp(choice,'h',1))
                figure;
                x = 0:10:360;
                plot(x,dpkol,'b-',x,dphot,'r-',x,dpreg,'g-');
                grid on
                xlabel('Crank angle (degrees)');
                ylabel('Heat exchanger pressure drop [Pa]');
                title('Heat exchanger pressure drop vs crank angle');
        elseif(strncmp(choice,'p',1))
                figure
                x = 0:10:360;
                pcombar = pcom*1e-5;
                pexpbar = pexp*1e-5;
                plot(x,pcombar,'b-',x,pexpbar,'r-');
                grid on
                xlabel('Crank angle (degrees)');
                ylabel('Working space pressure [bar]');
                title('Working space pressure vs crank angle');
        end
end
fprintf('quitting pressure plots...\n');
```

```
function [var,dvar]=filmatrix(j,y,dy,var,dvar)
% Fill in the j-th column of the var, dvar matrices with values of y, dy
% Arguments:  j - column index (1 - 37, every 10 degrees of cycle angle)
%             y(ROWV) - vector of current variable values
%             dy(ROWD) vector of current derivatives
%             var(ROWV,37) - matrix of current variables vs cycle angle
%             dvar(ROWD,37) - matrix of current derivatives vs cycle angle
% Returned values:
%             var(ROWV,37) - matrix of updated variables vs cycle angle
%             dvar(ROWD,37) - matrix of updated derivatives vs cycle angle
```

```
ROWV = 22; % number of rows in the var matrix
ROWD = 16; % number of rows in the dvar matrix

for i = 1:1:ROWV
   var(i,j) = y(i);
end
for i = 1:1:ROWD
   dvar(i,j) = dy(i);
end
```

```
function [st,ht,fr] = foilfr(d,mu,re)
% evaluate regenerator wrapped foil stanton number, friction factor
% Arguments:
%   d - hydraulic diameter [m]
%   mu - gas dynamic viscosity [kg.m/s]
%   re - Reynolds number
% Returned values:
%   st - Stanton number
%   ht - heat transfer coefficient [W/m^2.K]
%   fr - Reynolds friction factor ( = re*fanning friction factor)

global cp % specific heat capacity at constant pressure [J/kg.K]
global prandtl % Prandtl number

if (re < 2000) % normally laminar flow
   fr = 24;
else
   fr = 0.0791*re^0.75;
end
% From Reynolds simple analogy:
st=fr/(2*re*prandtl);
ht=st*re*cp*mu/d;
```

```
function qrloss = regsim(var)
% Evaluate the effectiveness and performance of the regenerator
% modified  to include 'no regenerator matrix'
% Arguments:
%   var(22,37) array of variable values every 10 degrees (0 - 360)
% Returned value:
%   qrloss - regenerator net enthalpy loss [J]

% Row indices of the var array:
 TC = 1;  % Compression space temperature [K]
 TE = 2;  % Expansion space temperature [K]
 QK = 3;  % Heat transferred to the cooler [J]
 QR = 4;  % Heat transferred to the regenerator [J]
 QH = 5;  % Heat transferred to the heater [J]
 WC = 6;  % Work done by the compression space [J]
 WE = 7;  % Work done by the expansion space [J]
 W  = 8;  % Total work done (WC + WE) [J]
 P  = 9;  % Pressure [Pa]
 VC = 10; % Compression space volume [m^3]
 VE = 11; % Expansion space volume [m^3]
 MC = 12; % Mass of gas in the compression space [kg]
 MK = 13; % Mass of gas in the cooler [kg]
 MR = 14; % Mass of gas in the regenerator [kg]
```

```
 MH = 15; % Mass of gas in the heater [kg]
 ME = 16; % Mass of gas in the expansion space [kg]
 TCK = 17; % Conditional temperature compression space / cooler [K]
 THE = 18; % Conditional temeprature heater / expansion space [K]
 GACK = 19; % Conditional mass flow compression space / cooler [kg/rad]
 GAKR = 20; % Conditional mass flow cooler / regenerator [kg/rad]
 GARH = 21; % Conditional mass flow regenerator / heater [kg/rad]
 GAHE = 22; % Conditional mass flow heater / expansion space [kg/rad]

global fr
global ar % regen internal free flow area [m^2]
global awgr % regen internal wetted area [m^2]
global dr % regen hydraulic diameter [m]
global tr % regen temperature [K]
global freq omega % cycle frequency [herz], [rads/s]
global prandtl
% Reynolds number over the cycle
for i = 1:1:37
    gar(i) = (var(GAKR,i) + var(GARH,i))*omega/2;
    gr = gar(i)/ar;
    [mu,kgas,re(i)] = reynum(tr,gr,dr);
end

% average and maximum Reynolds number
sumre = 0;
remax = re(1);
for(i = 1:1:36)
    sumre = sumre + re(i);
    if(re(i) > remax)
        remax = re(i);
    end
end

reavg = sumre/36;

% Stanton number, number of transfer units, regenerator effectiveness
global prandtl % Prandtl number

% for matrix mesh regen
[st,fr] = matrixfr(reavg);
%effectiveness
ntu = st*awgr/(2*ar);
effect = ntu/(ntu + 1);%num of transfer units
% Calculate qrloss
qreg = zeros(1,37);
for i=1:1:37
    qreg(i) = var(QR,i);
end
qrmin = min(qreg);
qrmax = max(qreg);
qrloss = (1 - effect)*(qrmax - qrmin);

% Regenerator simple analysis results:
fprintf('============ Regenerator Simple analysis =============\n')
fprintf('Average Reynolds number: %.1f\n', reavg);
fprintf('Maximum Reynolds number: %.1f\n', remax);
fprintf('Stanton number(Average Re): %.3f\n',st);
```

```
fprintf('Number of transfer units: %.1f\n',ntu);
fprintf('Regenerator effectiveness : %.3f\n',effect);
fprintf('Regenerator net enthalpy loss: %.1f[W]\n', qrloss*freq);
```

```
function [mu,kgas,re] = reynum(t,g,d)
% evaluate dynamic viscosity, thermal conductivity, Reynolds number
% Arguments:
%   t - gas temperature [K]
%   g - mass flux [kg/m^2.s]
%   d - hydraulic diameter [m]
% Returned values:
%   mu - gas dynamic viscosity [kg/m.s]
%   kgas - gas thermal conductivity [W/m.K]
%   re - Reynolds number

global cp % specific heat capacity at constant pressure [J/kg.K]
global mu0 % dynamic viscosity at reference temp t0 [kg.m/s]
global t0 t_suth % reference temperature [K], Sutherland constant [K]
global prandtl % Prandtl number

mu = mu0*(t0 + t_suth)/(t + t_suth)*(t/t0)^1.5;
kgas = cp*mu/prandtl;
re = abs(g)*d/mu;

if(re < 1)
   re = 1;
end
```

```
function [x, y, dy] = rk4(deriv,n,x,dx,y)
%Classical fourth order Runge-Kutta method
%Integrates n first order differential equations
%dy(x,y) over interval x to x+dx

x0 = x;
y0 = y;

[y,dy1] = feval(deriv,x0,y);
for i = 1:n
       y(i) = y0(i) + 0.5*dx*dy1(i);
end
xm = x0 + 0.5*dx;
[y,dy2] = feval(deriv,xm,y);
for i = 1:n
       y(i) = y0(i) + 0.5*dx*dy2(i);
end
[y,dy3] = feval(deriv,xm,y);
for i = 1:n
       y(i) = y0(i) + dx*dy3(i);
end
x = x0 + dx;
[y,dy] = feval(deriv,x,y);
for i = 1:n
       dy(i) = (dy1(i) + 2*(dy2(i) + dy3(i)) + dy(i))/6;
       y(i) = y0(i) + dx*dy(i);
end
```

```
function [var,dvar] = simple
% simple analysis - including heat transfer and pressure drop effects
% Returned values:
%   var(22,37) array of variable values every 10 degrees (0 - 360)
%   dvar(16,37) array of derivatives every 10 degrees (0 - 360)

% Row indices of the var, dvar arrays:
 TC = 1;  % Compression space temperature [K]
 TE = 2;  % Expansion space temperature [K]
 QK = 3;  % Heat transferred to the cooler [J]
 QR = 4;  % Heat transferred to the regenerator [J]
 QH = 5;  % Heat transferred to the heater [J]
 WC = 6;  % Work done by the compression space [J]
 WE = 7;  % Work done by the expansion space [J]
 W  = 8;  % Total work done (WC + WE) [J]
 P  = 9;  % Pressure [Pa]
 VC = 10; % Compression space volume [m^3]
 VE = 11; % Expansion space volume [m^3]
 MC = 12; % Mass of gas in the compression space [kg]
 MK = 13; % Mass of gas in the cooler [kg]
 MR = 14; % Mass of gas in the regenerator [kg]
 MH = 15; % Mass of gas in the heater [kg]
 ME = 16; % Mass of gas in the expansion space [kg]
 TCK = 17; % Conditional temperature compression space / cooler [K]
 THE = 18; % Conditional temeprature heater / expansion space [K]
 GACK = 19; % Conditional mass flow compression space / cooler [kg/rad]
 GAKR = 20; % Conditional mass flow cooler / regenerator [kg/rad]
 GARH = 21; % Conditional mass flow regenerator / heater [kg/rad]
 GAHE = 22; % Conditional mass flow heater / expansion space [kg/rad]
% Size of var(ROWV,COL), dvar(ROWD,COL)
 ROWV = 22; % number of rows in the var matrix
 ROWD = 16; % number of rows in the dvar matrix
 COL = 37; % number of columns in the matrices (every 10 degrees)
%=========================================================================

global freq % cycle frequency [herz]
global tk tr th % cooler, regenerator, heater temperatures [K]
global cqwr % regenerator housing thermal conductance [W/K]

%th = 1323;
%th = 1323;
%tk = 293;
twk = tk; % Cooler wall temp - equal to initial cooler gas temp
twh = th; % Heater wall temp - equal to initial heater gas temp
epsilon = 0.01; % allowable temperature error bound for cyclic convergence
terror = 10*epsilon; % Initial temperature error (to enter loop)

while (terror>epsilon)
   [var,dvar] = adiab;
   qrloss = regsim(var); % included 2/7/2010
   tgh = hotsim(var,twh,qrloss); % new heater gas temperature
   tgk = kolsim(var,twk,qrloss); % new cooler gas temperature
   terror = abs(th - tgh) + abs(tk - tgk);
   th = tgh;
   tk = tgk;
   tr = (th-tk)/log(th/tk);
```

```
end

fprintf('===== converged heater and cooler mean temperatures =====\n');
fprintf('heater wall/gas temperatures: Twh = %.1f[K], Th = %.1f[K]\n',twh,th);
fprintf('cooler wall/gas temperatures: Twk = %.1f[K], Tk = %.1f[K]\n',twk,tk);
% Print out ideal adiabatic analysis results
eff = var(W,COL)/var(QH,COL); % engine thermal efficency
Qkpower = var(QK,COL)*freq;   % Heat transferred to the cooler (W)
Qrpower = var(QR,COL)*freq;   % Heat transferred to the regenerator (W)
Qhpower = var(QH,COL)*freq;   % Heat transferred to the heater (W)
Wpower = var(W,COL)*freq;     % Total power output (W)
fprintf('========== ideal adiabatic analysis results ==========\n');
fprintf(' Heat transferred to the cooler: %.2f[W]\n', Qkpower);
fprintf(' Net heat transferred to the regenerator: %.2f[W]\n', Qrpower);
fprintf(' Heat transferred to the heater: %.2f[W]\n', Qhpower);
fprintf(' Total power output: %.2f[W]\n', Wpower);
fprintf(' Ideal Adiabatic Thermal efficiency: %.1f[%%]\n', eff*100);
fprintf('============= Regenerator analysis results============\n');
fprintf(' Regenerator net enthalpy loss: %.1f[W]\n', qrloss*freq);
qwrl = cqwr*(twh - twk)/freq;
fprintf(' Regenerator wall heat leakage: %.1f[W]\n', qwrl*freq);

% Temperature plot of the simple simulation results
               figure
               x = 0:10:360;
               Tcomp = var(TC,:);
               Texp = var(TE,:);
               plot(x,Tcomp,'b-',x,Texp,'r-');
               hold on
               x = [0,360];
               y = [twk,twk];
               plot(x,y,'b--')
               y = [tk,tk];
               plot(x,y,'b-')
               y = [tr,tr];
               plot(x,y,'g-')
               y = [th,th];
               plot(x,y,'r-')
               y = [twh,twh];
               plot(x,y,'r--')
               hold off
               grid on
               xlabel('Crank angle (degrees)');
               ylabel('Temperature (K)');
               title('Simple Simulation - Wall and Gas Temps vs crank angle');
% Various plots of the ideal adiabatic simulation results
plotadiab(var,dvar);
fprintf('========= pressure drop simple analysis =============\n');
dwork = worksim(var,dvar);
fprintf(' Pressure drop available work loss: %.1f[W]\n', dwork*freq)

IndicatedPower=Wpower;
actWpower = Wpower - dwork*freq;
actQhpower = Qhpower + qrloss*freq + qwrl*freq;
acteff = actWpower/actQhpower;
fprintf(' Indicated power from simple analysis: %.1f[W]\n', IndicatedPower);
fprintf(' Actual power from simple analysis: %.1f[W]\n', actWpower);
```

```
fprintf(' Actual heat power in from simple analysis: %.1f[W]\n', actQhpower);
fprintf(' Actual efficiency from simple analysis: %.1f[%%]\n', acteff*100);
```

```
function [vc,ve,dvc,dve] = sinevol(theta)
% Ross yoke drive volume variations and derivatives
% Argument:  theta - current cycle angle [radians]
% Returned values:
%   vc, ve - compression, expansion space volumes [m^3]
%   dvc, dve - compression, expansion space volume derivatives

global vclc vcle % compression,expansion clearence vols [m^3]
global vswc vswe % compression, expansion swept volumes [m^3]
global alpha % phase angle advance of expansion space [radians]


 ve = vcle + 0.5*vswe*(1 + cos(theta));
 vc = vclc + 0.5*vswc*(1 + cos(theta-alpha));
 dve = -0.5*vswe*sin(theta);
 dvc = -0.5*vswc*sin(theta-alpha);
end
```

```
function plotadiab(var,dvar)
% various plots of ideal adiabatic simulation results
% Arguments:
%   var(22,37) array of variable values every 10 degrees (0 - 360)
%   dvar(16,37) array of derivatives every 10 degrees (0 - 360)

% Row indices of the var, dvar arrays:
 TC = 1;  % Compression space temperature (K)
 TE = 2;  % Expansion space temperature (K)
 QK = 3;  % Heat transferred to the cooler (J)
 QR = 4;  % Heat transferred to the regenerator (J)
 QH = 5;  % Heat transferred to the heater (J)
 WC = 6;  % Work done by the compression space (J)
 WE = 7;  % Work done by the expansion space (J)
 W  = 8;  % Total work done (WC + WE) (J)
 P  = 9;  % Pressure (Pa)
 VC = 10; % Compression space volume (m^3)
 VE = 11; % Expansion space volume (m^3)
 MC = 12; % Mass of gas in the compression space (kg)
 MK = 13; % Mass of gas in the cooler (kg)
 MR = 14; % Mass of gas in the regenerator (kg)
 MH = 15; % Mass of gas in the heater (kg)
 ME = 16; % Mass of gas in the expansion space (kg)
 TCK = 17; % Conditional temperature compression space / cooler (K)
 THE = 18; % Conditional temeprature heater / expansion space (K)
 GACK = 19; % Conditional mass flow compression space / cooler (kg/rad)
 GAKR = 20; % Conditional mass flow cooler / regenerator (kg/rad)
 GARH = 21; % Conditional mass flow regenerator / heater (kg/rad)
 GAHE = 22; % Conditional mass flow heater / expansion space (kg/rad)
% Size of var(ROWV,COL), dvar(ROWD,COL)
 ROWV = 22; % number of rows in the var matrix
 ROWD = 16; % number of rows in the dvar matrix
 COL = 37; % number of columns in the matrices (every 10 degrees)
%=========================================================================
global tk tr th % cooler, regenerator, heater temperatures [K]
global vk % cooler void volume [m^3]
```

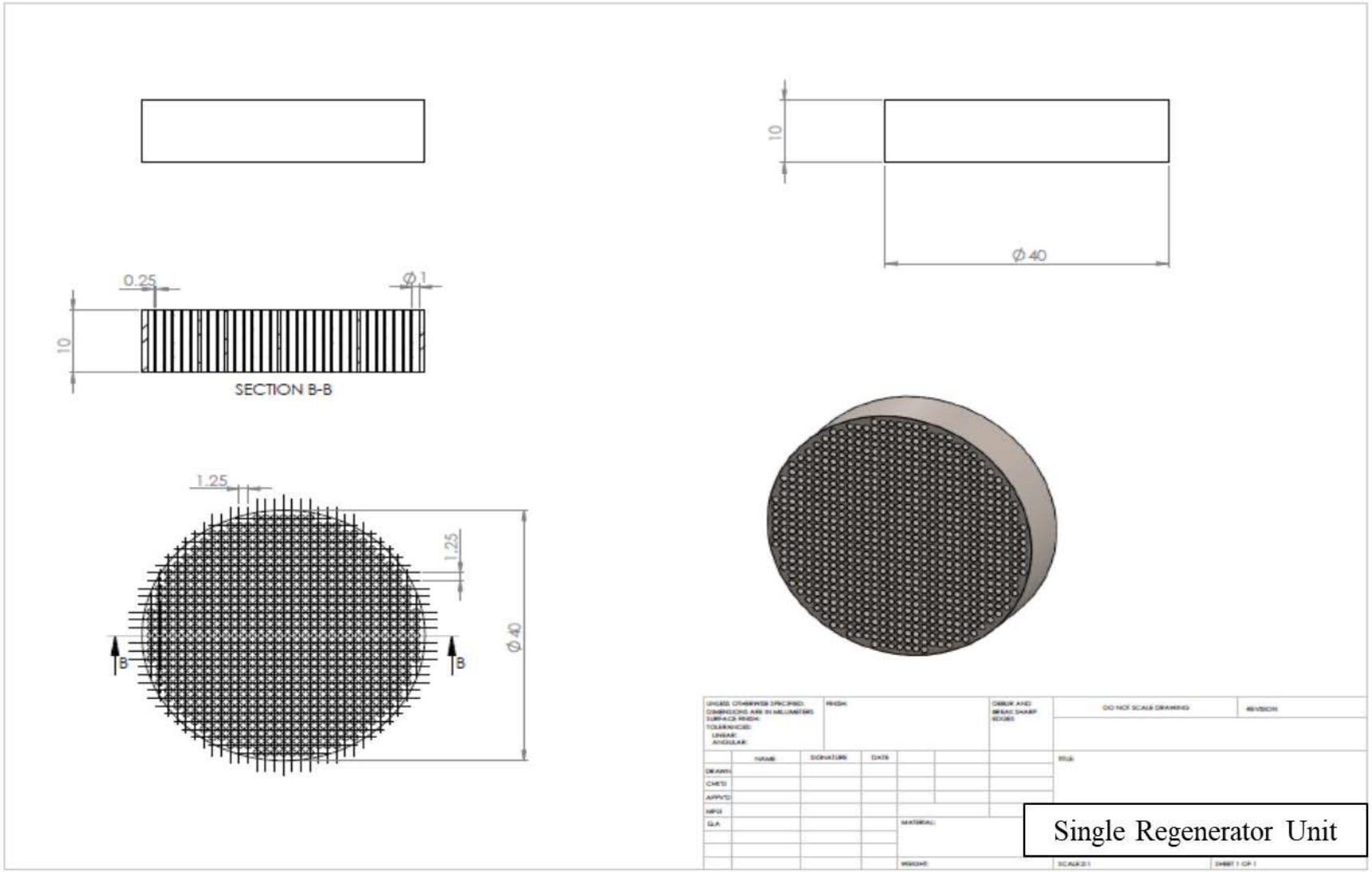
```
global vr % regen void volume [m^3]
global vh % heater void volume [m^3]
global freq  % cycle frequency [herz], [rads/s]
choice = 'x';
while(~strncmp(choice,'q',1))
       fprintf('Choose plot type:\n');
       fprintf('   p - for a PV diagram\n');
       fprintf('   t - for a temperature vs crank angle plot\n');
       fprintf('   e - for an energy vs crank angle plot\n');
       fprintf('   m - for masses vs crank angle plot\n');
    fprintf('   f - for mass flow rate vs crank angle plot\n');
    fprintf('   r - for energy flow rate vs crank angle plot\n');
    fprintf('   q - to quit\n');
       choice = input('p)vdiagram, t)emperature, e)nergy, m)asses, f)low, r)ates, q)uit :
','s');
       if(strncmp(choice,'p',1))
              figure
              vol = (var(VC,:) + var(VE,:))*1e6; % cubic centimeters
              pres = (var(P,:))*1e-6; % MPa
              plot(vol,pres,'k')
              grid on
              xlabel('Volume (cc)')
              ylabel('Pressure (MPa)')
              title('P-v diagram')
       elseif(strncmp(choice,'t',1))
              figure
              x = 0:10:360;
              Tcomp = var(TC,:);
              Texp = var(TE,:);
              plot(x,Tcomp,'b-',x,Texp,'r-');
              hold on
              x = [0,360];
              y = [tk,tk];
              plot(x,y,'b-')
              y = [tr,tr];
              plot(x,y,'g-')
              y = [th,th];
              plot(x,y,'r-')
              hold off
              grid on
              xlabel('Crank angle (degrees)');
              ylabel('Temperature (K)');
              title('Temperature vs crank angle');
       elseif(strncmp(choice,'e',1))
              figure
              x = 0:10:360;
              Qkol = var(QK,:); % [J]
              Qreg = var(QR,:); % [J]
              Qhot = var(QH,:); % [J]
              Work = var(W,:); % [J]
              plot(x,Qkol,'b-',x,Qreg,'g-',x,Qhot,'r-',x,Work,'k-.');
              grid on
              xlabel('Crank angle (degrees)');
              ylabel('Energy [Joules]');
              title('Energy vs crank angle');
    elseif(strncmp(choice,'m',1))
```

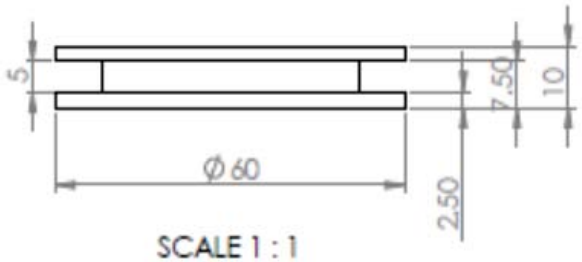
```
                figure
                x = 0:10:360;
                Mcomp = var(MC,:); % [Kg/rad]
                Mcol = var(MK,:); % [Kg/rad]
                Mreg = var(MR,:); % [Kg/rad]
                Mhot = var(MH,:); % [Kg/rad]
                Mexp = var(ME,:); % [Kg/rad]
                plot(x,Mcomp,'b-',x,Mcol,'g-',x,Mreg,'r-',x,Mhot,'k-.',x,Mexp,'b--');
                grid on
                xlabel('Crank angle (degrees)');
                ylabel('masses [Kg/rad]');
                title('Masses vs crank angle');
     elseif(strncmp(choice,'f',1))
        figure
                x = 0:10:360;
                Fcompcol = var(GACK,:); % [Kg/s]
                Fcolreg = var(GAKR,:); % [Kg/s]
                Freghe = var(GARH,:); % [Kg/s]
                Mhetexp = var(GAHE,:); % [Kg/s]
                plot(x,Fcompcol,'b-',x,Fcolreg,'g-',x,Freghe,'r-',x,Mhetexp,'k-.');
                grid on
                xlabel('Crank angle (degrees)');
                ylabel('masses flow rates [Kg/rad]');
                title('Masses flow rates vs crank angle');
     elseif(strncmp(choice,'r',1))
                figure
                x = 0:10:360;
                Q_k = var(QK,:)*freq; % [W]
                Q_r = var(QR,:)*freq; % [W]
                Q_h = var(QH,:)*freq; % [W]
                W_o = var(W,:)*freq; % [W]
        plot(x,Q_k,'b-',x,Q_r,'g-',x,Q_h,'r-',x,W_o,'k-.');
                grid on
                xlabel('Crank angle (degrees)');
                ylabel('Energy [Watts]');
                title('Energy rates vs crank angle');
        end
end
fprintf('quitting ideal adiabatic plots...\n');
```

APPENDIX C

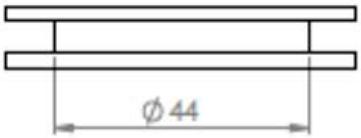
REGENERATOR DRAWINGS

The segmented micro-channel regenerator heat exchanger components were designed and manufactured in the University of Birmingham. The regenerator material was Steel AISI 4340.

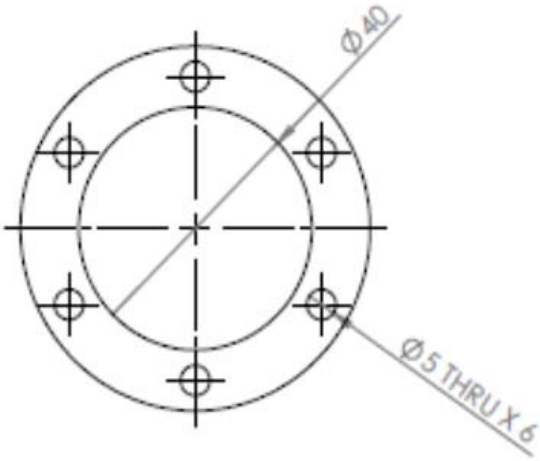

10
Ø 40
0.25
Ø 1
10
SECTION B-B
1.25
1.25
Ø 40
B
B
Single Regenerator Unit



SCALE 1 : 1



SCALE 1 : 1



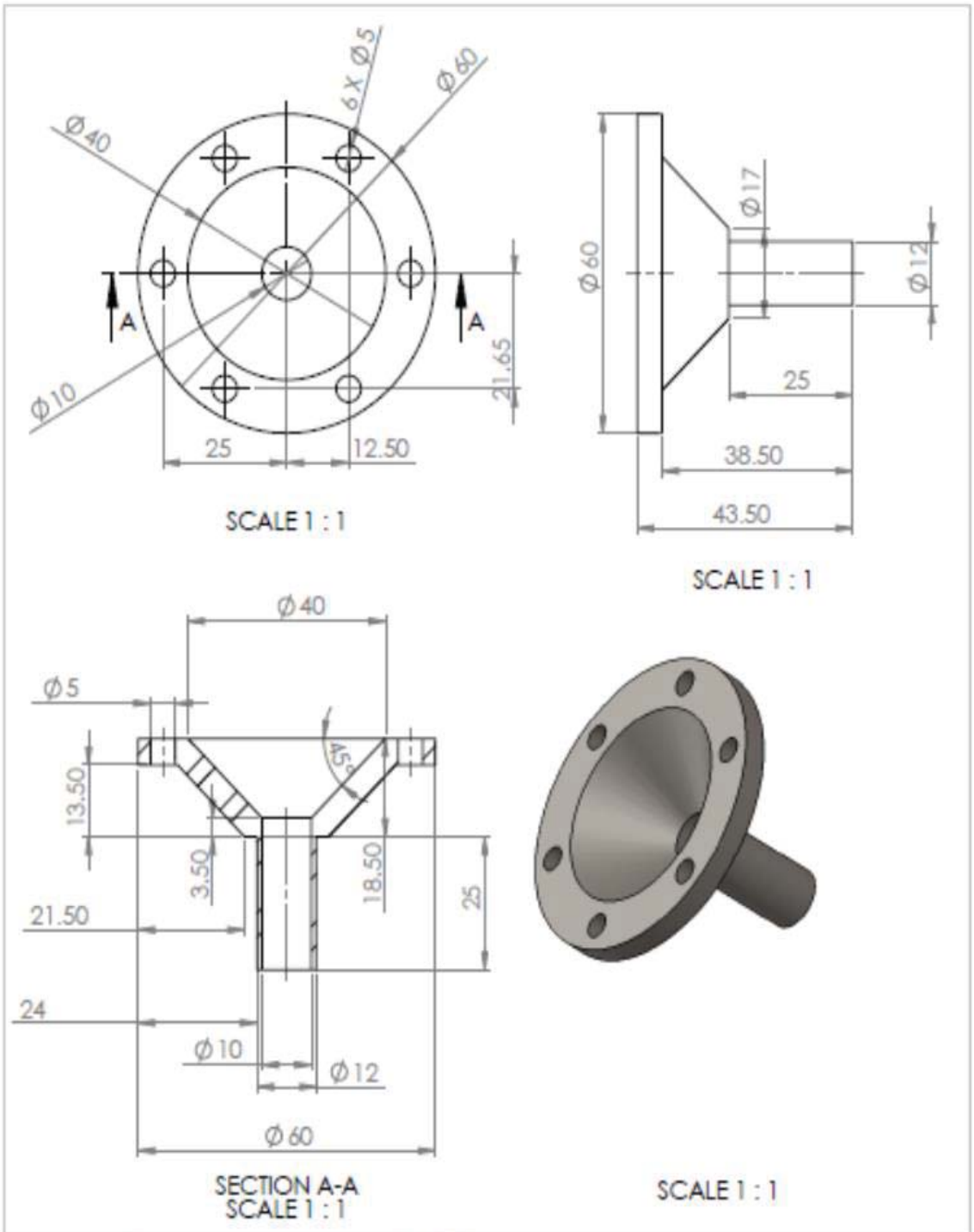
SCALE 1 : 1

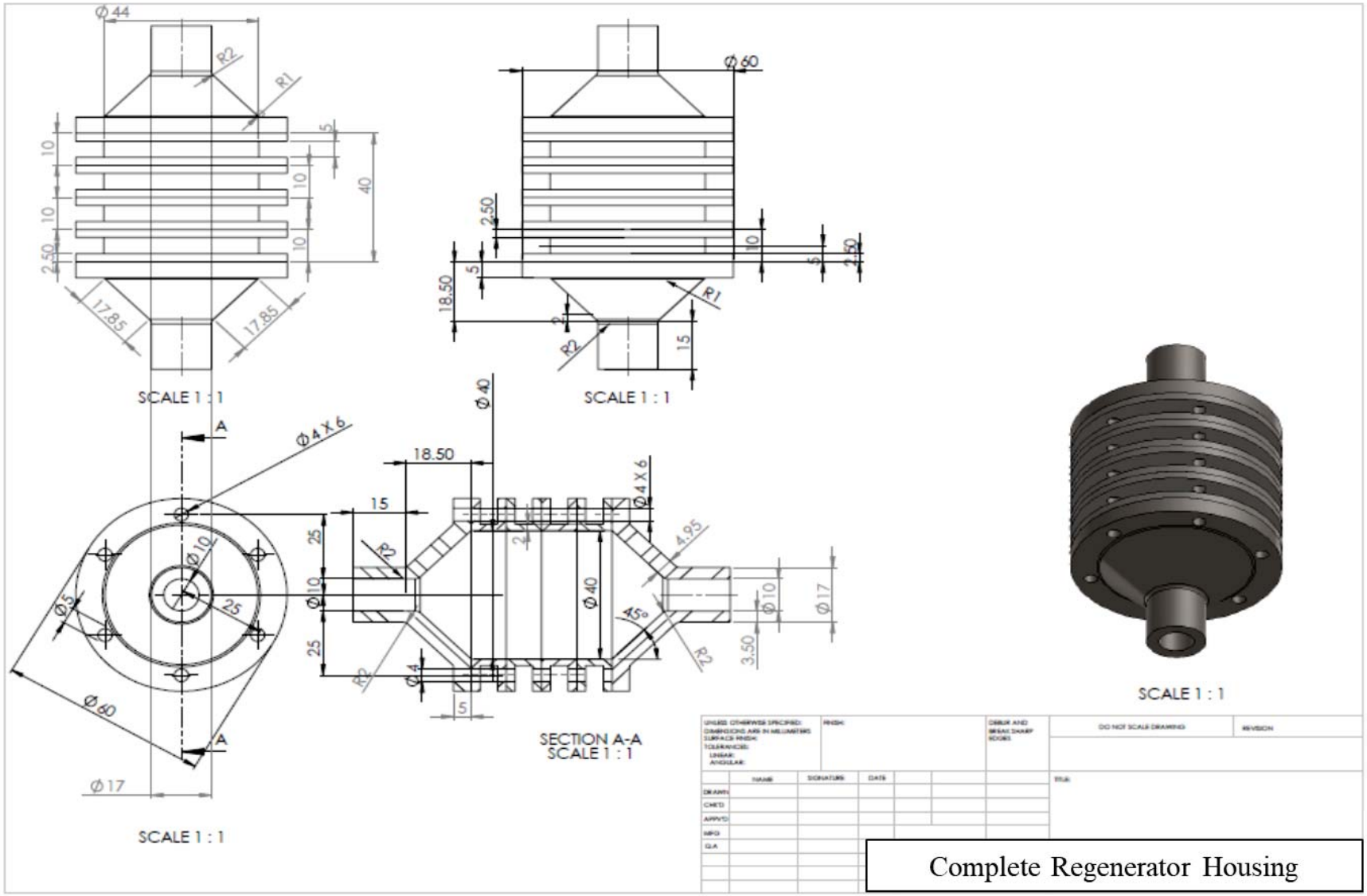


SCALE 1 : 1

UNLESS OTHERWISE SPECIFIED: DIMENSIONS ARE IN MILLIMETERS SURFACE FINISH: TOLERANCES: LINEAR: ANGULAR:				FINISH:		BREAK ALL SHARP EDGES	DO NOT SCALE DRAWING
	NAME	SIGNATURE	DATE				TITLE:
DRAWN							
CHK'D							
APP'D							
MFG							
Q.A				MATERIAL:			
				WEIGHT:		SCALE:1:1	SHEET 1 OF 1

Single Regenerator Housing


6 X Ø5
Ø60
Ø40
A
A
Ø10
21.65
25
12.50
SCALE 1 : 1
Ø17
Ø60
Ø12
25
38.50
43.50
SCALE 1 : 1
Ø40
Ø5
45°
13.50
3.50
18.50
25
21.50
24
Ø10
Ø12
Ø60
SECTION A-A
SCALE 1 : 1
SCALE 1 : 1
DO NOT SCALE DRAWING
REVISION
NAME
SIGNATURE
DATE
DRAWN
CHK'D
APP'VD
MFG
Q.A
MATERIAL:
WEIGHT:
SCALE:1:2
SHEET 1 OF 1
Cone Regenerator Housing


Ø44
R2
R1
10
10
2.50
5
10
10
40
17.85
17.85
SCALE 1 : 1
Ø60
2.50
18.50
5
10
5
2.50
R1
R2
15
SCALE 1 : 1
Ø40
A
Ø4 X 6
18.50
15
Ø4 X 6
25
Ø10
Ø5
25
Ø10
Ø40
4.95
45°
Ø10
Ø17
3.50
25
R2
Ø4
5
Ø60
A
Ø17
SCALE 1 : 1
SECTION A-A
SCALE 1 : 1
SCALE 1 : 1
DO NOT SCALE DRAWING
REVISION
NAME
SIGNATURE
DATE
DRAWN
CHKD
APPVD
MFG
Q.A
Complete Regenerator Housing

APPENDIX D

DEVICES CALIBRATION

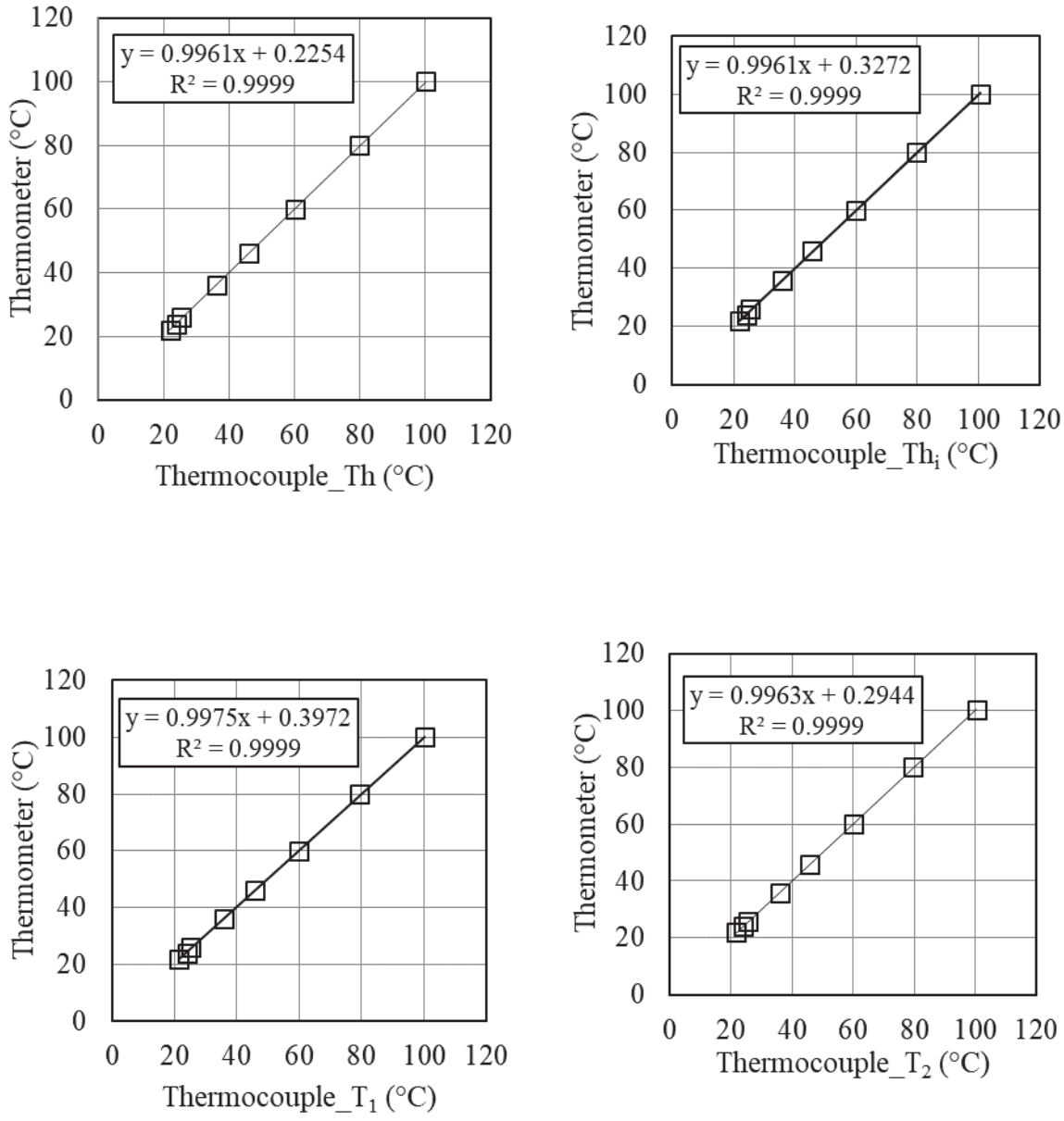


Figure D.1[a]: Thermocouple calibration charts

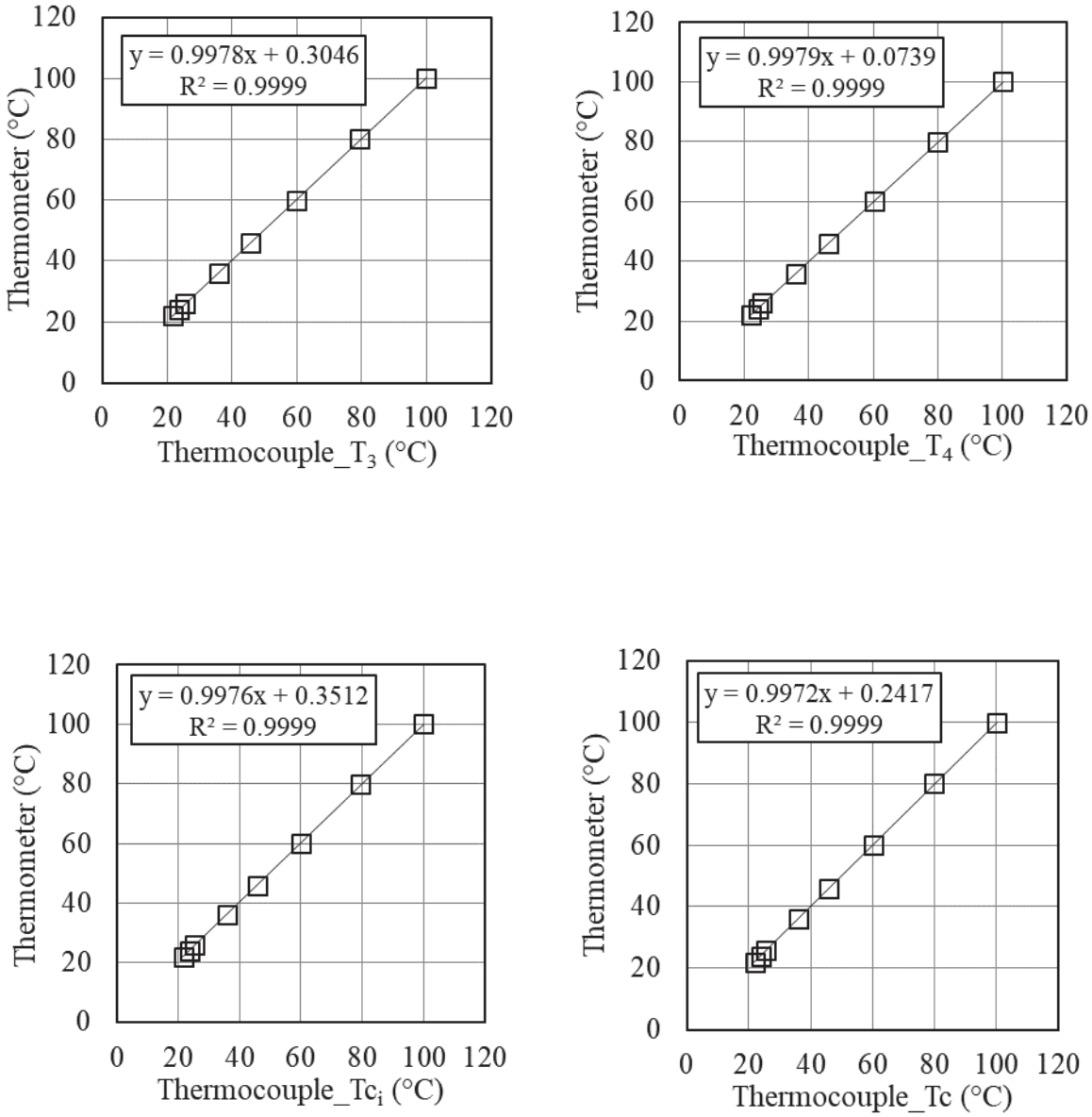


Figure D.1[b]: Thermocouple calibration charts

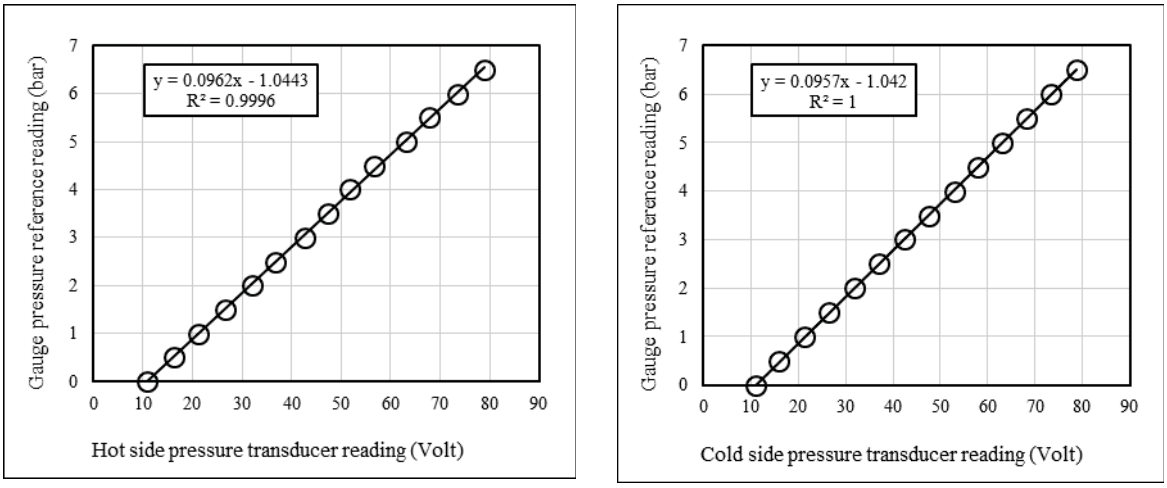


Figure C.2 Relationship between pressure transducer readings and Gauge pressure readings.

APPENDIX E

V- TYPE COMPRESSOR SPECIFICATIONS

"The V-type compressor used in this work is a versatile heavy duty pump used as a major component in several popular Clarke compressors and which can also be supplied separately for replacements and special builds. 9cfm max. displacement - balanced `V`-twin cylinders with finned inter-cooler Maximum working pressure 10bar (150 psi) Multiplied flywheel for effective cooling. Dependable splash feed lubrication. Solid cast iron construction. Twin air intake filters Requires a minimum 1.5 - 2.0hp drive motor." [105]



Figure E.1 "V-type compressor "Clark Air Compressor Pump 9 CFM- CE20" [105]